

THE UNIVERSITY OF ASTON IN BIRMINGHAM

"The study of gamma-rays produced in
the inelastic scattering of neutrons"

Thesis submitted for the degree of Doctor of Philosophy

by

Kevin Anthony Connell

Department of Physics

THESIS

539.1714 CON

27 JUN 72 152012

June, 1972.

SUMMARY

A gamma-ray spectrometer employing a sodium iodide scintillation detector, has been constructed to observe the gamma-rays produced in 14.2 MeV neutron interactions with elemental samples. The predominant gamma-ray production mechanism is inelastic neutron scattering; the source neutrons being produced by the ${}^3\text{H}(d,n){}^4\text{He}$ reaction. The main problem in the design of such a spectrometer is to overcome the large background owing to the sensitivity of sodium iodide to neutrons. This was overcome by using a gamma-ray detector neutron shield and a particle time-of-flight discrimination system. The associated particle time-of-flight method was used. The instant of production of a source neutron is defined by detecting the associated alpha-particle, enabling the subsequent neutron-gamma-ray time-of-flight discrimination. The different particle flight times over the sample to detector flight path are measured electronically and the system used is described.

Three elements for which there have been few or no previous measurements were studied: silicon, sulphur and titanium. Gamma-ray spectra have been observed for each element under 14.2 MeV neutron bombardment, at several scattering angles in the 0° to 90° angular interval. The spectra enabled absolute differential gamma-ray production cross-sections and angular distributions of the resolved gamma-ray lines to be measured. The differential gamma-ray production cross-section, angular distribution and integrated cross-section measurements are compared with the published data where available.

The angular distribution measurements, of the gamma-rays produced in neutron inelastic scattering, for each element are compared with Hauser-Feshbach-Satchler compound nucleus model calculations.

ACKNOWLEDGEMENTS

I thank the Science Research Council for the provision of a grant which enabled the research to be carried out.

I am very much indebted to my supervisor, Dr. A.J. Cox, for his guidance and encouragement throughout the research project and I thank Professor S.E. Hunt, Head of the Physics Department, for his interest in the work.

I wish to acknowledge the members of the Nuclear Physics Group for many useful discussions and to thank the technical staff of the laboratory and workshop for their help.

I am very grateful to Mrs. R. Finch for typing the thesis.

Finally I wish to thank my wife Annwen for her patience and understanding throughout the period.

CONTENTS

		<u>Page No.</u>
<u>Chapter 1.</u>	<u>Introduction</u>	1
1.1	Introduction	1
1.2	The Research Project	6
1.3	Review of Experimental Methods	9
1.3.1	The Open Geometry	9
1.3.2.	The Closed Geometry	11
<u>Chapter 2</u>	<u>Gamma-Ray Detection and Detector Shielding</u>	
2.1	The Sodium Iodide Scintillation Detector	14
2.2	The Lithium Drifted Germanium Detector	21
2.3	Choice of Detection System	25
2.4	The Anti-Coincidence Spectrometer	28
2.5	Sodium Iodide Scintillation Detector Design	29
2.6	Detector Shielding	32
2.6.1	Neutron Shielding Principles and Materials Used	32
2.6.2	Shield Construction	35
2.6.3	Efficiency Test of the Shield	37
<u>Chapter 3</u>	<u>The Experimental Method</u>	39
3.1	The Time of Flight Discrimination Technique	39
3.1.1	The Pulsed Beam Method	40
3.1.2	The Associated Particle Method	41
3.2	The Experimental Arrangement for the Associated Particle Method	42
3.2.2	The Beam Tube and Target Assembly	43
3.2.3.	The Alpha-Particle Detector	44
3.2.4	Alpha-Detector Shielding	47
3.2.5	Scattering Sample Position	48

3.2.6	Laboratory Shielding	50
3.3	Time Resolution	51
3.3.1	Timing with Slow Phosphors	54
3.4	The Electronics	56
3.4.1	The Time of Flight Electronics	56
3.5	The Electronic Setting of Procedure	66
3.6	Time of Flight Spectra	68
3.7	Gamma-Ray Energy Analysis	70
3.7.1	Spectrometer Calibration	70
3.7.2	Energy Resolution	72
<u>Chapter 4</u>	<u>Absolute Differential Cross-Section Measurement</u>	73
4.1	The Differential Cross-Section	73
4.2	The Neutron Source	75
4.2.1	The Angular Range of Source Neutrons	75
4.2.2	The Neutron Yield as a Function of Deuteron Energy	77
4.2.3	The Neutron Beam Profile	80
4.2.4	Assumptions in the Calculation of the Neutron Beam Profile	81
4.2.5	The Neutron Line Shape	87
4.3	Sample Size and Geometry	88
4.3.1	Multiple Scattering	88
4.3.2	Choice of Sample Geometry	90
4.3.3	Gamma-Ray Absorption in the Scattering Sample	91
4.3.4	Sample Thickness	93
4.4	The Integrated Neutron Flux	94
4.5	Gamma-ray Detector Efficiency	100
4.5.1	Peak to Total Ratio and Full Energy Peak Efficiency	102

<u>Chapter 5</u>	<u>Absolute Cross-section Measurement Results</u>	105
5.1	Differential Cross-section Measurement Procedure	105
5.1.1	The need for Stability in the Neutron Source Strength	106
5.2	Silicon	106
5.2.1	The Scattering Sample	106
5.2.2	Gamma-Ray Spectra and Interpretation	107
5.2.3	Differential Gamma-Ray Production Cross-Sections	111
5.2.4	The Angular Distribution and Integrated Cross-Section of the $^{28}\text{Si}(n,n'\gamma)^{28}\text{Si}$ 1.78 MeV γ -ray	115
5.3	Sulphur	118
5.3.1	The Scattering Sample	118
5.3.2	Gamma-Ray Spectra	119
5.3.3	The 2.24 MeV Gamma-Ray	120
5.3.3(i)	Differential γ -ray Production Cross-sections	121
5.3.3(ii)	Angular Distribution and Integrated Cross-section	123
5.3.4	The 1.7 MeV Gamma-Ray	124
5.3.4(i)	Differential γ -ray Production Cross-sections	125
5.3.4(ii)	The Angular Distribution and Integrated Cross-section	126
5.3.5	The 1.27 MeV Gamma-Ray	127
5.3.5(i)	Differential γ -ray Production Cross-sections	127
5.3.5(ii)	Angular Distribution and Integrated Cross-section	129
5.4	Titanium	129
5.4.1	The Scattering Sample	129
5.4.2	Gamma-Ray Spectra and Interpretation	130
5.4.3	Differential Gamma-Ray Production Cross-Sections	131

5.4.4	Angular Distributions and Integrated Cross-sections of the $^{48}\text{Ti}(n,n'\gamma)^{48}\text{Ti}$ 0.99 MeV and 1.31 MeV γ -rays	133
<u>Chapter 6</u>	<u>Theoretical Comparison of Results</u>	134
6.1	The Optical Model	134
6.2	The Compound Nucleus Theory	139
6.3	The Use of the Programme MANDY at 14 MeV Neutron Energy	143
6.4	Results	144
<u>Chapter 7</u>	<u>Conclusions and Recommendations</u>	150
<u>Appendix 1</u>		154
<u>Appendix 2</u>		156
<u>Appendix 3</u>		161
<u>References</u>		167

CHAPTER 1.Introduction1.1 Introduction

The investigation of neutron reactions with matter is a major part of neutron physics which is broadly concerned with the production, interaction and detection of neutrons. A measure of the probability of a neutron reacting with a nucleus is expressed as the cross-section. As the neutron carries no electrical charge, there is no Coulomb repulsion to prevent its interaction with nuclei. There is, consequently, an enormous energy range (10^{-3} eV to 10^8 eV) over which neutrons exhibit appreciable interactions with matter.

Of the many neutron interactions there is relatively little data on the γ -rays produced in fast neutron reactions (neutron energies greater than 0.5 MeV) and little information on the reaction mechanisms. The reactions are of the type $A(n, x \gamma)B$, where A is the target nucleus, n is the incident neutron, x is the emitted particle or particles, and B is the product nucleus. If B is formed in an excited state then it normally decays to its ground state, either directly or by a cascade process with the emission of γ -rays.

In neutron interactions with light and medium mass nuclei (atomic mass number $A \lesssim 80$), at energies of the order of a few MeV, usually the only γ -ray production mode is inelastic scattering in which the scattered neutron transfers some of its kinetic energy to the nucleus raising it to an excited state. The (n, γ) reaction, in which γ -radiation is emitted following neutron absorption, is energetically possible but normally it has a negligible cross-section at energies of the order MeV. As the neutron energy increases charged particle reactions become possible, particularly the (n, p) and (n, α) reactions which have thresholds of approximately 5 MeV for medium mass nuclei though this may vary considerably for individual nuclei. The threshold

for the $(n,2n)$ reaction is normally above 10 MeV neutron energy for medium mass nuclei. Up to neutron energies of 15 MeV however, the predominant non-elastic reaction is inelastic scattering.

Most of the work to date on γ -ray production measurements has been done at neutron energies less than 7 MeV. The work in this energy range has been reviewed by Day⁽¹⁾, Ferguson⁽²⁾ and McEllistrem⁽³⁾. There is a large energy gap in the easily available neutron source spectrum from ~ 10 MeV to 14 MeV since neutrons from the $D(d,n)^3\text{He}$ reaction are not monoenergetic because of deuteron break up. The $^3\text{H}(d,n)^4\text{He}$ reaction provides an abundant source of 14 MeV neutrons.

In the 14 MeV to 15 MeV energy interval, Deuchars and Dandy⁽⁴⁾ observed γ -ray energy spectra following neutron interactions with several medium and heavy weight nuclei to obtain spectroscopic data of their excited level structures. Although they were able to make energy assignments to many excited levels, due to the complicated spectra containing very many γ -ray lines, the assignments tended to be rather more uncertain than can be made at lower neutron energies. The spectra also gave information about the excited level decay schemes. Because of the complicated spectra the work done at 14 MeV has concentrated on the measurement of differential γ -ray production cross-sections of resolved lines identified on the basis of published level structure data. The predominant lines correspond to transitions from the first few levels which are intensified by cascade contributions from higher levels. A differential cross-section is a measure of the probability of radiation being emitted into a small solid angle, $d\Omega$, at an angle, θ , to the incident beam direction.

Differential γ -ray production cross-sections for 14 to 15 MeV neutrons, have been measured for many elements, particularly the light and medium mass nuclei. Examples of extensive analysis are the work of Engesser and Thompson⁽⁵⁾, Bocharov and Nefedov⁽⁶⁾ and of the Texas

Nuclear group⁽⁷⁻¹¹⁾ as part of a cross-section measurement programme. The measurements are usually made at a 90° scattering angle with an angular resolution of $\pm 20^\circ$. In γ -ray spectra containing many unresolved lines, the Texas Nuclear group⁽⁹⁾ were able to measure differential γ -ray production cross-sections in $\frac{1}{2}$ MeV energy intervals with the aid of an anti-coincidence spectrometer (section 2.4); for example, they measured the γ -ray differential production cross-section for the 2 to 2.5 MeV γ -ray energy interval.

Gamma-ray angular distributions, which give the variation of the differential cross-section per steradian with scattering angle θ , are often anisotropic. The anisotropy decreases with increasing neutron energy; however marked anisotropies have been observed in γ -ray angular distributions following the interaction of 14 MeV neutrons. Distribution measurements have been reported by Anderson et al.⁽¹²⁾, Benetskii et al.⁽¹³⁾, Martin and Stewart^{(14),(15)}, Benveniste et al.⁽¹⁶⁾ and Morgan et al.⁽¹⁰⁾ for γ -rays produced in 14 MeV to 15 MeV neutron interactions. The measurements of the prominently excited γ -rays followed neutron interactions with nuclei ranging from ^{12}C to ^{56}Fe . The predominant reaction was inelastic scattering, but Morgan et al.⁽¹⁰⁾ attributed some γ -ray production modes to $(n,p\gamma)$, $(n,d\gamma)$ and $(n,\alpha\gamma)$ reactions. Because of the anisotropy in the distributions, the angular distribution is essential in the integration of the differential cross-section to obtain the γ -ray production cross-section.

The study of these reactions is of interest from both the practical and theoretical point of view. On the practical side, the energy distribution of γ -rays, production cross-sections and angular distributions following fast neutron interactions are useful in the design of safety shielding for nuclear reactors and other intense neutron flux devices. On the theoretical side, besides the spectroscopic data of the nuclear level structure, a comparison of theoretical and experimental

γ -ray angular distributions and excitation functions (the variation of the cross-section with energy) provides a test of the theoretical description of the reaction mechanism.

Two theoretical models widely used to describe fast neutron interactions are the statistical compound nucleus and direct interaction models. In the compound nucleus theory the reaction proceeds by a comparatively long lived, approximately 10^{-16} s, intermediate stage involving one or more states of a compound nucleus with many degrees of freedom. The direct interaction process has few degrees of freedom and is characterised by short reaction times, approximately 10^{-21} s which is the transit time of the neutron across the nucleus. Both models essentially represent simplifications of the as yet insoluble many body problem: the compound nucleus approach constitutes one simplified mathematical extreme and the direct interaction the other. The compound nucleus mechanism is considered to predominate at lower neutron energies (less than 6 MeV) and the direct interaction mechanism at higher energies. 14 MeV is an interesting intermediate region between wholly compound nucleus and wholly direct interaction mechanisms.

Both models are incomplete without specifying the interaction potential. The particle-nucleus interaction can be described by a complex or "optical" potential in which all the complexities of the individual nucleon-nucleon interactions and of the nucleus itself are replaced by a potential that depends only on the radial distance, r , between the nucleon and the nucleus. Elastic scattering is described in the main by the real part of the optical potential, although some is associated with the imaginary part. The imaginary part principally has the effect of absorbing particles from the incident beam and these particles are the ones that initiate non-elastic processes.

The compound nucleus theory of fast neutron interactions is due to Hauser and Feshbach⁽¹⁷⁾ and it has been extended by Satchler⁽¹⁸⁾

to predict γ -ray angular distributions following inelastic scattering. The theory is commonly referred to as the Hauser-Feshbach-Satchler theory. There are several computer programmes based on this theory available for the calculations of γ -ray production cross-sections and angular distributions. One of the most general of these is the programme Mandy due to Sheldon and Gantenbein⁽¹⁹⁾ and further extended by Sheldon and Strang⁽²⁰⁾ to include, at option, modifications to the theory due to Moldauer⁽²¹⁾. No published computer code, based on a direct interaction mechanism, was found that takes account of γ -rays produced in fast neutron interactions. Hence, all comparisons of theoretical and experimental results have used the compound nucleus model.

The Hauser-Feshbach-Satchler theory, with the Moldauer correction, has had considerable success in predicting γ -ray production cross-sections and angular distributions at lower neutron energies, vide Mathur et al.⁽²²⁾, Sheldon⁽²³⁾ and Day⁽¹⁾. This has enabled excited nuclear level spins and decay schemes to be determined by comparing theoretical and experimental γ -ray angular distributions. In a review of the theory with particular emphasis on γ -ray production in reactions, Sheldon⁽²³⁾ has shown that the shape and anisotropy of an angular distribution is not particularly sensitive to the parity of the level decaying, and for a definite determination of parity it is necessary to make angular correlation measurements. Examples of the determination of level spins and the confirmation of uncertain spin assignments of excited states of medium mass nuclei are given by Mathur et al.⁽²²⁾, Benjamin et al.⁽²⁴⁾ and Sheldon⁽²³⁾. The spin assignment of a level is most definite when a γ -ray originating at the excited level is of a single multipolarity (e.g. a transition to a level with spin 0), because the shape of the distributions corresponding to different spin assignments are then most varied. Mathur et al.⁽²²⁾ have also shown that although the shapes of γ -ray distributions remain unaltered, the magnitudes of the

production cross-sections are significantly sensitive to the choice of level parities and in many cases can lead to reliable parity assignments.

At higher neutron energies, at which the theory is less applicable, approximations are required because the number of compound nucleus decay reaction channels is very large and there is insufficient level structure data to account for them all. However, calculations of γ -ray angular distributions at 14 MeV neutron energies using the Hauser-Feshbach-Satchler theory have been reported by Drake⁽²⁵⁾ and Martin and Stewart⁽¹⁴⁾.

Besides the difficulties in the theoretical treatment of γ -ray production cross-sections in reactions at higher neutron energies (approximately 14 MeV) the main reason for the small amount of work is the poor signal to background ratio which results from the neutron sensitivity of γ -ray detectors and the large neutron induced background. Experimental work has therefore involved the development of techniques to overcome this problem.

1.2. The Research Project

The principal objective of the present work was to investigate the de-excitation γ -rays produced in fast neutron reactions, particularly in inelastic scattering, with the view of increasing the experimental and theoretical information on these reactions. The ${}^3\text{H}(d,n){}^4\text{He}$ reaction was used to provide a source of 14 MeV neutrons.

The first and a major part of the project was to construct a spectrometer capable of observing the prompt γ -ray energy spectra produced in the interaction of source neutrons with elemental scattering samples. The principal considerations in the design of the spectrometer were that it should (i) have a good γ -ray spectral response with good energy resolution, (ii) overcome the normally unworkable signal to background ratio and (iii) have a good angular resolution to facilitate γ -ray angular distribution measurements.

The spectrometer was used to obtain spectra of γ -rays emitted from several elements after bombardment with 14 MeV neutrons. The spectra were used for absolute differential γ -ray production cross-section, angular distribution and integrated cross-section measurements of resolved spectral lines identified on the basis of published level structure data. Silicon, sulphur and titanium were selected for study. They were chosen for several reasons. They are all common elements being three of the most abundant elements of the earth's crust. The common isotopes of each element, namely ^{28}Si , ^{32}S and ^{48}Ti , have isotopic abundances of 92%, 95% and 74% respectively and are all even mass nuclei. Measured angular distributions of even mass nuclei, excited in 14 MeV neutron inelastic scattering have shown anisotropies of up to a factor of two, see references (10, 12 - 16), particularly for the first excited level to ground state transitions. The Hauser-Feshbach-Satchler theory⁽²³⁾ predicts that γ -ray transitions from an excited level with spin zero, following a reaction, have isotropic distributions. The three nuclei, ^{28}Si , ^{32}S and ^{48}Ti , each have ground state spins of 0^+ and first excited state spins of 2^+ and the distributions for these transitions may, therefore, be expected to be anisotropic. The samples were also selected because at 14 MeV neutron energies there have been relatively few measurements of their γ -ray production cross-sections, and where more than a single measurement has been made there are discrepancies in the results.

Differential γ -ray production cross-section measurements, at 90° have been reported for silicon by the Texas Nuclear group⁽⁸⁻⁹⁾, Engesser and Thompson⁽⁵⁾ and Caldwell et al.⁽²⁶⁾. They made measurements for several resolved γ -ray lines of which the most intense was a 1.78 MeV γ -ray attributed to inelastic scattering. The values for the 1.78 MeV γ -ray differential production cross-section are 23.8 ± 7 mb/st, 26.2 ± 4.4 mb/st and 31.5 ± 7 mb/st. There is only a single angular distribution measurement reported and this is for the 1.78 MeV γ -ray

and it was measured by Martin and Stewart⁽¹⁵⁾. They do not, however, give any of their spectra or differential cross-section results obtained at any scattering angles, but only give a Legendre Polynomial expression obtained by a least squares fit to their results. Using this angular distribution equation the 90° differential cross-section was calculated as 33.6 mb/st which is larger than the above values. Benetskii⁽¹³⁾ has reported measuring the total 1.78 MeV γ -ray production cross-section.

Gamma-ray energy spectra produced in 14 MeV neutron interactions with sulphur have been observed at a single scattering angle, 90° , by the Texas Nuclear group⁽⁹⁾, Engesser and Thompson⁽⁵⁾, Bocharev and Nefedov⁽⁶⁾ and Caldwell et al.⁽²⁶⁾. Several γ -rays were resolved of which the most intense was a 2.24 MeV γ -ray. The values of the 90° differential production cross-section for this γ -ray range from 16.1 ± 1.7 mb/st to 31 mb/st. The only angular distribution measurement for sulphur is due to Martin and Stewart⁽¹⁵⁾. They measured the differential production cross-section for the 2.24 MeV γ -ray at four scattering angles in the 0° to 90° angular interval. The 90° differential cross-section for this γ -ray, calculated from the least squares fit equation to their measurements, has a value of 14.7 mb/st which is lower than the other reported values.

The only work reported for titanium at 14 MeV is by Engesser and Thompson⁽⁵⁾. They observed only a 90° γ -ray spectrum and measured differential production cross-sections for several lines of which the most intense, a 0.99 MeV γ -ray attributed to inelastic scattering, had a large cross-section of 70.1 ± 6.8 mb/st. No γ -ray angular distribution measurements at 14 MeV neutron energies have been reported for titanium.

Finally, a comparison of the angular distribution measurements of the γ -rays resulting from neutron inelastic scattering was made with the theoretical predictions. In the absence of a suitable direct interaction theory computer programme, the comparison was made with the

Hauser-Feshbach-Satchler theory. This served as a test of the applicability of the compound nucleus theory. To make this comparison the programme Mandy⁽²⁰⁾ was used.

1.3. Review of Experimental Methods

The experimental methods used for measuring differential γ -ray production cross-sections in fast neutron interactions can be broadly classified under the headings of open and closed geometries. These refer to whether a minimum amount of shielding is used or whether fairly massive shielding is used around either the neutron source or the detector or both.

1.3.1. The Open Geometry

Open geometry experiments need to be carried out in a large room keeping the apparatus as far as possible from the walls and floor to reduce the scattered background in the detector. The most extensively used open geometry method is that employing a large scattering sample in the form of an annulus. Figure 1.1 shows a typical arrangement, the detector to source distance is about 0.4 m. Typically sample rings have outside diameters of up to 300 mm and are several centimetres thick. The inside diameter depends on the detector size. The main advantage of the method is that the annular sample enables a larger mass of scatterer to be placed in close proximity to the detector than is otherwise possible without introducing a large self absorption of γ -rays in the scatterer. The large sample is required to give a workable signal to background ratio.

This rather simple approach has many disadvantages in the measurement of γ -ray differential production cross-sections. The main problem is the background produced in the detector due to both prompt neutron detection and activation of the detector. The spectrum background cannot be corrected for very accurately as a large fraction of the background is due to neutrons scattered into the detector by the sample.

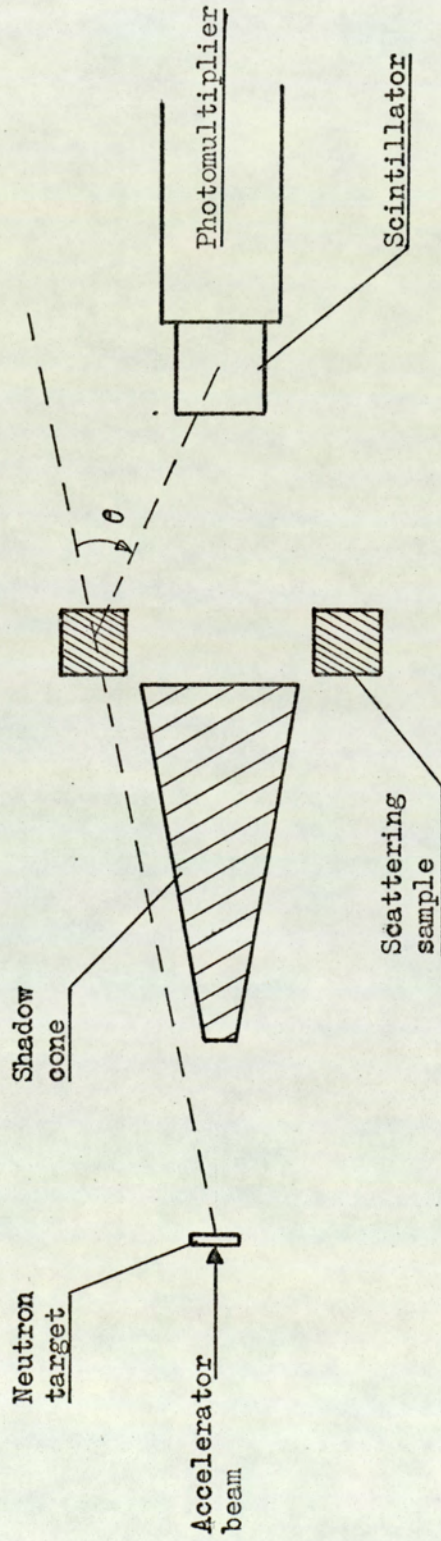


Figure 1.1. Plan view of a ring geometry method.

Due to the compactness of the system the angular resolution is poor. The scattering angle is changed by moving either the detector or the scattering ring along the axis of the system. This, however, results in a change in the geometry which consequently changes the detector efficiency. If the scattering angle is changed by moving the ring, the neutron flux and energy at the sample undergo a substantial change. Also, the angular range over which measurements can be made is limited.

In absolute cross-section measurements the detector efficiency is required and it can only be calculated with a poor accuracy for the case of an extended ring source surrounding a cylindrical detector. Some researchers⁽²⁷⁾ have tried to overcome this difficulty by measuring the efficiency with calibrated isotope sources in the shape of ring samples.

Finally, because of the large sample volume, there is a high probability of neutron multiple scattering, which tends to increase the γ -ray yield. The data has to be corrected for this process and this correction is also a function of scattering angle.

The method has been extensively used at lower neutron energies (less than 7 MeV) particularly by Day⁽²⁷⁾ and Van Patter⁽²⁸⁾, both of whom used sodium iodide scintillation detectors. A similar simple open geometry method has been used at 14 MeV neutron energy by Caldwell et al⁽²⁶⁾. Instead of a ring sample Caldwell used two rectangular block samples with one placed either side of the detector. This method has similar limitations and advantages to the ring geometry, except that multiple neutron scattering and γ -ray self absorption are rather more marked.

The extreme penetrability of higher energy neutrons severely reduces the signal to background ratio with the open geometry method and the simple method tends to be less satisfactory. Bocharov and Nefedov⁽⁶⁾ in their work with 14 MeV neutrons used a ring geometry, but

to reduce the neutron background they used a stilbene organic crystal employing pulse shape discrimination. The more common method of reducing the neutron background problem at 14 MeV neutron energies is to employ a time of flight technique. The time of flight method is used to discriminate between signal γ -rays and scattered neutrons and it requires the detector to be withdrawn the order of 1m from the scattering sample. The method is discussed in section 3.1. Benveniste et al.⁽¹⁶⁾, Anderson et al.⁽¹²⁾ and Deuchars and Dandy⁽⁴⁾ used this method with the open ring geometry at 14 MeV neutron energies with sodium iodide scintillation detectors. Although this technique improves the background problem the method still suffers from the other disadvantages given above for the simple ring geometry.

1.3.2. The Closed Geometry

In a situation where it is not possible to have the neutron source well away from thick walls and the floor, the scattered neutron flux in the room can cause very serious background problems in an unshielded arrangement. If only limited space is available to conduct the experiment then a closed geometry has to be used. An advantage of the closed geometry arrangement is that very much smaller scattering samples are used than in the ring geometry method.

Although either the neutron source or the γ -ray detector can be shielded it is usual to shield the γ -ray detector. Neutrons above 10 MeV are very penetrating and a massive shield is required to absorb the source neutrons and γ -rays produced in neutron reactions with the shielding material. The size of the shield requires the detector to be withdrawn more than 1m from the scattering sample. To obtain a reasonable signal to background ratio the sample, at the detector collimator entrance, has to be placed close to the source. The large solid angle subtended by the sample at the target gives the method poor angular resolution. Differential cross-section measurements in this case are usually limited

to one angle because the amount of shielding required around the detector makes it immobile.

As was the case with the simple ring geometry method, the background correction for neutrons scattered into the detector is a source of error. In the closed geometry case though the effect is not so serious for two reasons. Firstly, it accounts for a smaller fraction of the background, and secondly, measurements are usually only made at an angle of 90° and at this angle there are less elastically scattered neutrons, as elastic scattering is very forward peaked. A disadvantage of both the simple open and closed geometry methods is that γ -rays resulting from fast neutron activation of the sample can be detected. Whether this is troublesome is very dependant on the nature of the sample, i.e. whether it has a large cross-section for say the (n,p) or (n,α) reactions and whether the unstable reaction products have short half-lives.

The simple closed geometry arrangement was used to observe the prompt γ -rays resulting from 14.7 MeV neutron interactions with many elements by Engesser and Thompson⁽⁵⁾. They heavily shielded a large sodium iodide crystal detector to view a small sample placed close to the neutron source. The shield measured 2.5 m long with a diameter of 1.85 m and with the fixed position shield differential cross-section measurements could only be made at one scattering angle, 90° , with an angular resolution of $\pm 25^\circ$.

The most common geometry now used is the closed geometry with the γ -ray detector shielded. The shielding is limited though, so that the detector can be easily rotated about the scattering sample, Figure 1.2. Good angular resolution is obtained by using small scattering samples positioned between 100 mm to 300 mm from the source. The resolution is defined by the angle subtended at the source by the sample as the detector is considerably further removed from the sample. With this arrangement a time of flight neutron discrimination technique has to be

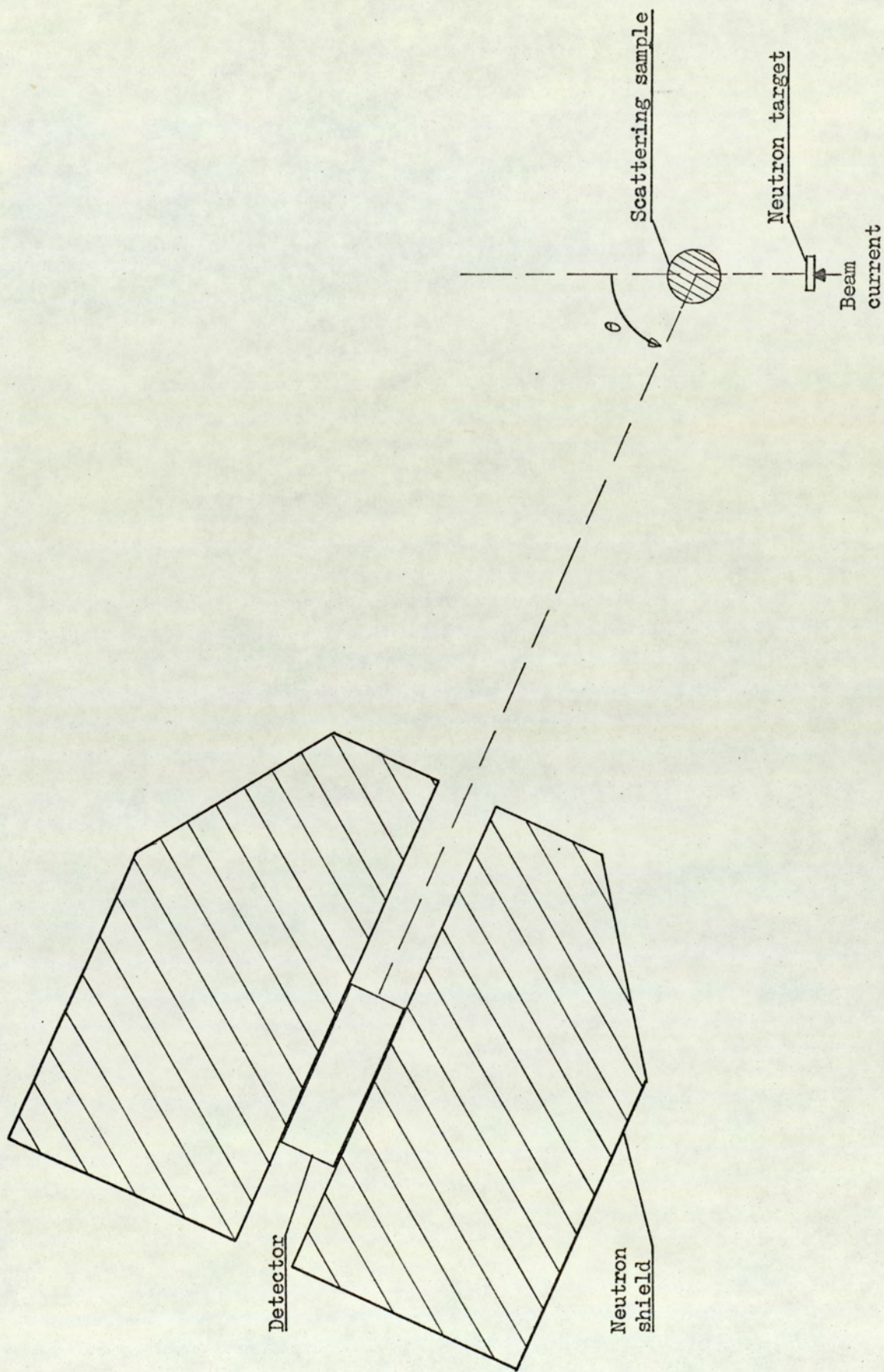


Figure 1.2. Plan view of a closed geometry method.

used to obtain a workable signal to background ratio. This method overcomes many of the disadvantages associated with the ring geometry method. As with the ring geometry method employing time of flight discrimination the background spectrum can be readily reproduced as neutrons scattered into the detector by the sample are discriminated by their flight time. Additionally, the detector efficiency can be accurately calculated for the time of flight closed geometry method and altering the scattering angle does not change the geometry or the neutron flux at the sample. Finally, the γ -ray absorption in the sample and neutron multiple scattering present a smaller problem. This method lends itself then to absolute differential cross-section and angular distribution measurements. The single disadvantage it has compared with the ring geometry is that data acquisition is much slower.

Differential cross-section measurements have been made by this method over a wide spectrum of neutron energies. In particular, the Texas Nuclear group⁽⁷⁻¹⁰⁾ and Martin and Stewart^{(14), (15)} have used this approach with 14 MeV to 15 MeV neutrons using sodium iodide detectors. Morgan et al.⁽¹¹⁾ have made similar measurements with 15 MeV neutrons using a lithium drifted germanium detector. This method was used for the present work.

CHAPTER 2 .Gamma-Ray Detection and Detector Shielding

The two most useful detectors for γ -ray spectroscopy are the sodium iodide thallium activated, NaI(Tl), scintillation detector and the lithium drifted germanium, Ge(Li), semiconductor detector. In the detection of γ -rays produced in fast neutron interactions the organic scintillator, stilbene, has been used⁽⁶⁾ but because of its very poor detection efficiency and spectral response it was not considered for the present work. The properties to be considered in the choice of a suitable detector are listed as follows:

1. the detector efficiency,
2. the spectral response,
3. the energy resolution,
4. the response time,
5. the neutron response.

These properties are discussed for the two systems considered leading to a choice of detector. Finally the detector neutron shield is described.

2.1. The Sodium Iodide scintillation Detector

The detection efficiency of sodium iodide crystal primarily depends on the absorption coefficient for γ -ray interactions producing secondary ionising electrons. The interaction processes are the photoelectric effect, Compton scattering and pair production. The photoelectric absorption coefficient, at photon energies above the K-shell binding energy, is proportional to $NZ^5 E^{-3.5}$ where N is the number of atoms per unit volume, Z is the atomic number and E is the photon energy. This coefficient then increases rapidly with atomic number but decreases rapidly with photon energy. The Compton linear absorption coefficient is proportional to NZ and it decreases with increasing photon energy. For pair production to occur the photon energy must exceed the rest energy of the electron and positron, $2mc^2$, which is 1.02 MeV. At energies

near the threshold, the coefficient is proportional to $NZ^2(E - 2mc^2)$. The higher energy dependence becomes logarithmic and it is proportional to $NZ^2 \log_e E$. In each case the pair production coefficient is proportional to the square of the atomic number of the absorbing material.

The atomic numbers of sodium, iodine and thallium are 11, 53 and 81 respectively, but thallium is only present in NaI(Tl) in a very small proportion, 0.1%. As discussed above, the absorption coefficients are very dependent on atomic number, so the iodine in the crystal makes it a very good γ -ray absorbing material. For this reason and as NaI is a very dense material, $3,670 \text{ Kg m}^{-3}$, it has a very good intrinsic γ -ray detection efficiency. The efficiency is a function of the crystal size as the probability of γ -ray detection increases with increasing depth of crystal the radiation has to penetrate. Large efficient NaI(Tl) crystals are readily available with dimensions up to 150 mm in diameter and 150 mm thick.

The γ -ray interaction processes give rise to a complicated response function for the NaI(Tl) scintillator. Even a single mono-energetic γ -ray can produce a response whose line shape may contain several peaks plus a continuum. The complexity is essentially due to the detector output pulse being proportional to the total energy of the electrons which are liberated in the crystal, instead of being directly related to the energy of the γ -ray.

As shown above the absorption coefficients are energy dependent. Gamma-rays in the energy range from several hundred KeV to slightly in excess of 1 MeV interact in the crystal by the photoelectric effect and Compton scattering. The line shape then contains a full energy absorption peak, due to photoelectric and multiple processes, plus a step shape Compton distribution. At higher energies pair production begins to compete with the other interaction processes and it becomes more and more predominant as the energy increases. The line shape may then contain a

full energy peak, one or two escape peaks and a continuum. The escape peaks which are 0.511 MeV and 1.02 MeV down from the full energy peak are produced when either one or two annihilation quanta escape the crystal following the annihilation of the positron. The relative amplitudes of the full energy peak and escape peaks depend on the γ -ray energy and crystal size. The probability of the annihilation quanta escaping the crystal decreases with increasing crystal size causing an increase in the relative full energy peak amplitude. For a 76.2 mm (3 in) crystal the first escape peak becomes larger than the full energy peak at between 3 MeV to 4 MeV γ -ray energy.

The energy resolution of a γ -ray detector is usually defined as the ratio of the full width at half maximum height of a full energy peak to the peak energy. The quantity is expressed as a percentage. The operation of the NaI(Tl) scintillation counter involves five consecutive processes and statistical fluctuations in the probability of each of these influence the overall energy resolution. These are:

- (i) Excitation and ionisation along the track of the radiation.
- (ii) Conversion of energy of excitation into light energy by the process of fluorescence.
- (iii) Transfer of light through the crystal and onto the cathode of the photomultiplier tube.
- (iv) Absorption of light at the photocathode with emission of photoelectrons.
- (v) Electron multiplication at successive dynodes of the photomultiplier.

Probably the most significant factor effecting the line width, i.e. the energy resolution, is the photocathode sensitivity. If all the other factors were negligible then the pulse height resolution would vary as the inverse square root of the γ -ray energy as this line width contribution is normal (or Gaussian). The other sources of line width are not necessarily normal. For γ -ray energies above several hundred KeV the energy resolution of the NaI(Tl) detector does vary as the inverse square root

of the γ -ray energy. The resolution is also a function of the crystal size. Light collection at the photocathode deteriorates for larger crystals giving poorer resolution. Typically a 76.2 mm (3 in) diameter by 76.2 mm thick crystal has a resolution of 8% at 0.66 MeV.

The response time of NaI(Tl) is a function of the sodium iodide, the activator and the crystal temperature. The intensity $n(t)$ (in photons per sec.) in the scintillation emission is given by:

$$n(t) = \frac{N}{\lambda_D - \lambda_R} \left[\exp\left(-\frac{t}{\lambda_D}\right) - \exp\left(-\frac{t}{\lambda_R}\right) \right]$$

where N is the total number of photons emitted in the scintillation, and λ_D and λ_R are the decay time and rise time constants respectively. The light pulse then is described by two terms corresponding to an exponential rise in light emission and an exponential decay. Eby and Jentschke⁽²⁹⁾ measured the rise time constant for NaI(Tl) at room temperature as 60 ns and the decay constant as 230 ns for excitation by α -particles. In addition to the main 0.23 μ s decay component Robertson and Lynch⁽³⁰⁾ observed a further decay components in NaI(Tl) excited by γ -rays of 1.5 μ s. For γ -ray excitation the effective decay time constant is increased to about 0.35 μ s. Nicholson and Snelling⁽³¹⁾ reported a value of the decay time constant for γ -ray excitation of NaI(Tl) as 0.34 μ s. The relatively slow light output of NaI(Tl) is the principal factor governing the photomultiplier anode pulse shape.

In addition the sodium iodide detector is sensitive to neutrons. Neutrons are detected by the ionising products of a neutron reaction. Neutron reactions producing ionising radiation can be listed as follows:

- (i) Radiative capture, (n, γ) . The product nucleus is usually unstable.
- (ii) Inelastic scattering, $(n, n' \gamma)$.

(iii) Charged particle emission reactions.

(iv) The (n,2n) reaction. Detection only results if the product nucleus is unstable.

The neutron response is very energy dependent because of the variation of neutron reaction cross-sections with energy. It is important to consider the response to a wide spectrum of neutron energies because a neutron source spectrum can be greatly modified by detector shielding material. The response is considered for two wide neutron energy ranges labelled as follows; slow neutrons, i.e. from 0.01 eV to 0.5 MeV and fast neutrons i.e. from 0.5 MeV to 15 MeV.

The slow neutron response is dominated by the radiative capture process. Table 2.1 gives the radiative capture cross-sections at two neutron energies for the crystal constituents taken from the Barn book⁽³²⁾.

Table 2.1

Element	Energy 0.025 eV $\sigma(n,\gamma)$	0.1 MeV $\sigma(n,\gamma)$
²³ Na	0.525b	1.3b
¹²⁷ I	7.0b	0.43b
Tℓ	3.5b	-

The major response is from neutron capture in the iodine. ¹²⁸I is formed, and because it has a large level density even for low lying levels, the prompt γ -ray emission consists of many γ -rays due to cascade transitions between the many levels. The resulting pulse height spectrum is almost continuous with a maximum pulse height corresponding to 6.71 MeV which is the binding energy of a neutron in ¹²⁸I.

Less than 10% of the slow neutron response of NaI(Tℓ) is due to capture in the sodium. The sodium capture γ -ray spectrum has been observed by Groshev⁽³³⁾. Many capture γ -rays were observed due to cascade transitions between the levels of ²⁴Na. Again the spectrum is

almost continuous with a maximum energy of 6.96 MeV which is the neutron binding energy in ^{24}Na .

Thallium accounts for less than 0.1% of the capture γ -radiation because it is only present in very small quantities.

Prompt neutron detection by inelastic scattering from the iodine is possible for neutrons above 0.059 MeV. Iodine has four levels that can be excited by neutrons below 0.5 MeV. The cross-sections for inelastic scattering in this energy region are smaller than for the radiative capture process.

The radiative capture process with iodine and sodium results in a build up of long lived activity in the crystal. Neutron capture by the iodine produces unstable ^{128}I which has a 25 min half-life. It can decay to ^{128}Xe by β^- emission, or by electron capture or β^+ emission to ^{128}Te . The prominent decay mode is by β^- emission, Figure 2.1. The pulse height spectrum resulting from ^{128}I activity is similar to that of a usual β -decay spectrum. The spectrum is continuous rising to a maximum at about 1 MeV and falling smoothly to zero at 2.12 MeV. The maximum energy, 2.12 MeV, corresponds to the difference in binding energy of ^{128}Xe and ^{128}I . The build up of activity in a NaI(Tl) crystal due to the production of ^{128}I is given by the activation equation,

$$N(t) = \frac{dN}{dt} \left(1 - e^{-\lambda t} \right) / \lambda$$

where $N(t)$ is the number of active isotope nuclei present at time t , $\frac{dN}{dt}$ is the rate of production of the active isotope and λ is the decay constant of the isotope. For a constant neutron flux the rate of production of the ^{128}I is constant, so the amount of ^{128}I present increases exponentially to a maximum value given by $\frac{dN}{dt} / \lambda$. In the irradiation of a NaI(Tl) crystal in a constant neutron flux 88% of the maximum ^{128}I activity is produced after three half-lives exposure, i.e. 75 min. The capture cross-section for sodium is much smaller, but results in the

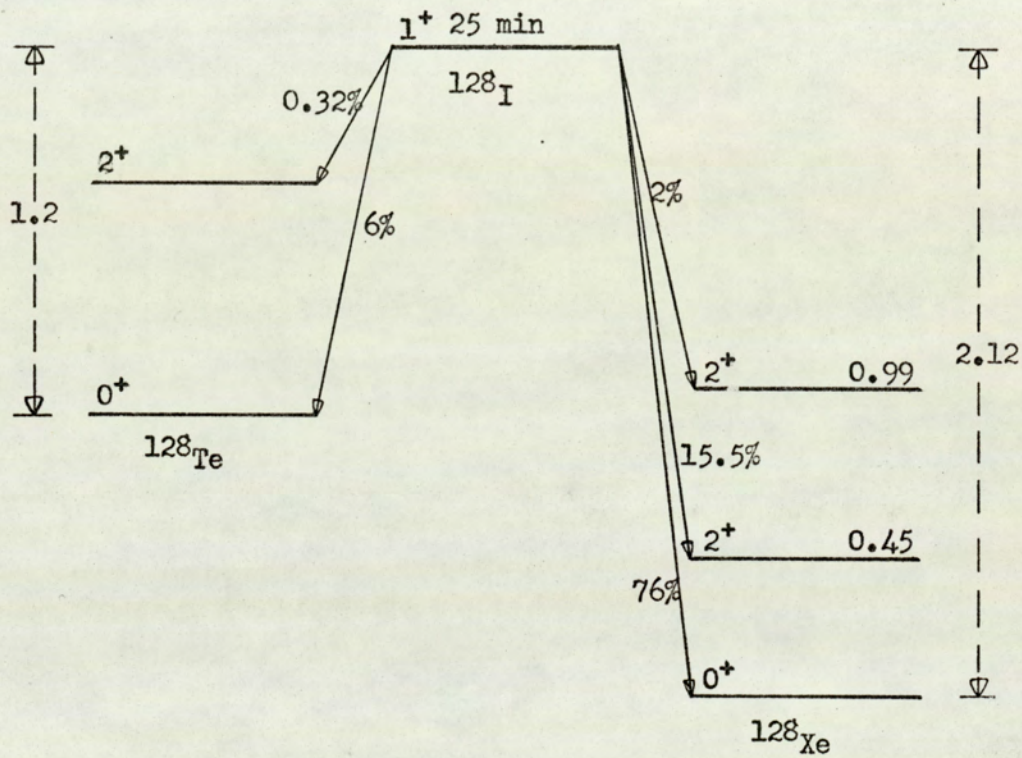


Figure 2.1. The decay scheme for ^{128}I .

production of 15 hour half-life ^{24}Na . Because of the longer half-life the activity induced takes very much longer than the iodine to reach equilibrium.

In the fast neutron energy range the radiative capture reaction becomes less significant. Shafroth et al.⁽³⁴⁾ have shown that in NaI(Tl) fast neutron capture is significant for neutron energies up to about 1 MeV where the radiative capture cross-section for iodine is 88 mb and for sodium it is only 0.23 mb. The spectrum shape is essentially as for slow neutron capture except that the maximum pulse height corresponds to the neutron binding energy, 6.7 MeV in ^{128}I , plus the kinetic energy of the neutron.

The predominant neutron detection mechanism in the fast neutron energy range is by inelastic scattering. Day⁽²⁷⁾ and Van Loef⁽³⁵⁾ have studied the $(n, n'\gamma)$ process in NaI(Tl) crystals for neutron energies in the range 0.52 to 3.15 MeV. The peaks in the spectra correspond to the excited levels of sodium and iodine. As the neutron energy increases new peaks arise as higher levels are excited. For neutron energies of 10 MeV and higher the pulse height spectrum becomes almost continuous due to the large number of levels excited. Throughout the energy range the inelastic scattering cross-section for iodine is larger than for sodium. Van Loef gives the inelastic scattering cross-sections for iodine and sodium at 1 MeV as 1.53 and 0.4 barns respectively (only one level of ^{23}Na can be excited at this neutron energy).

At higher neutron energies charged particle reactions and the $(n, 2n)$ reaction become energetically possible. The cross-sections for the main reactions at 14.5 MeV are given in table (2.2), taken from the Barn book⁽³²⁾

Table 2.2

$E_n = 14.5 \text{ MeV}$	(n,2n)	(n, α)	(n,p)
^{127}I	1.3b	1 mb	230 mb
^{23}Na	20mb	180 mb	38 mb

As at lower neutron energies neutron reactions with iodine predominate. Neutrons are promptly detected by the charged particle emitting reactions but these reactions as in the case of the (n,2n) reaction cause long lived activity in the crystal. The most common reactions of this type are the (n,2n) and (n,p) reactions with the iodine. The ^{127}I (n,2n) reaction produces ^{126}I which has a 13 day half life decaying to ^{126}Te by β^+ emission and to ^{126}Xe by β^- emission. The (n,p) reaction on ^{127}I produces ^{127}Te which has a half life of 9.3 hours and decays to ^{127}I by β^- emission. The pulse height spectra due to the decay of these isotopes are similar in shape to that described for the decay of ^{128}I . The long half-lives, relative to that of ^{128}I , cause a slow build up of activity.

Fast neutron interactions in NaI(Tl) scintillator are then dominated by the inelastic scattering process, giving rise to prompt detection, but at either end of this energy range reactions take place introducing long lived activity into the crystal. At the lower energies the induced activity is mainly due to the (n, γ) reaction with the iodine, and at the high energy end of the range the induced activity results mainly from the (n,2n) and (n,p) reactions with the iodine.

2.2. The Lithium Drifted Germanium Detector

The lithium drifted germanium, Ge(Li), detector, which is essentially the solid state version of the ionisation chamber, is increasingly used for γ -ray spectroscopy. Germanium has an atomic number of 32 and consequently the detector has a poor detection efficiency relative to NaI(Tl). Besides having a low intrinsic detection efficiency,

the efficiency of the solid state detector further suffers because at present it can only be manufactured with a small sensitive volume. A detector volume of 30 cm^3 was the usual maximum obtainable at the time of the start of the project. It is also difficult to manufacture the detector as a coaxial cylinder.

The general spectral response of the semi-conductor detector is as described for the NaI(Tl) detector. However, the ratio of the full energy peak counts to the total spectrum counts for a mono-energetic γ -ray, i.e. the peak to total ratio, is rather poor because of the dependence of the photo-electric and pair production absorption coefficients on the fifth and second powers of the atomic number respectively. For high energy γ -rays interacting in the detector by the pair production process there is a high probability of both annihilation quanta escaping detection because of the small detector volume. Consequently the full energy peak is very small and both the first and second escape peaks are larger than the full energy peak.

The important advantage of the Ge(Li) detector is its excellent energy resolution. A 30 cm^3 detector typically has a resolution of about 0.5% to 0.66 MeV. The excellent resolution results from the direct detection mechanism where simply all the charges liberated in ionisation are collected and in that only about 3 eV is necessary to create an electron-hole pair. For comparison, in the NaI(Tl) detector 300 eV is required to release one photo-electron. The resolution of the semi-conductor detector is theoretically given by $2.355 \frac{\sqrt{F\epsilon}}{\sqrt{E}}$ where E is the γ -ray energy in KeV, ϵ is the average energy in eV necessary to create an electron-hole pair, and F is the Fano factor (0.13 to 0.16). The experimental resolution obtained is considerably inferior to that expected from the above expression mainly because of the limitations of the associated electronics.

The Ge(Li) detector has a very fast response time. Typically

pulse rise times are 20 ns making the detector ideally suited for fast timing applications timing from the leading edge of the pulse.

The detector is very sensitive to neutrons, particularly fast neutrons. Neutrons are detected by the ionising products of a neutron reaction. The main detection mechanism for slow neutrons, i.e. energies below about 0.5 MeV down to thermal energies, is by the radiative capture process. The (n, γ) cross-section for germanium is 2.45 b for thermal neutrons⁽³⁶⁾. There is very little information on the variation of this cross-section with energy. The energy released in a single capture reaction in each of the germanium isotopes is about 9 MeV and due to the density of excited nuclear levels, even the low lying levels, many γ -rays are emitted in a single capture reaction. There are five stable isotopes of germanium and the capture process with ^{70}Ge (20.6%), ^{74}Ge (36.5%) and ^{76}Ge (7.7%) gives unstable products. Of these three, the radiative capture cross-sections are largest for ^{70}Ge and ^{74}Ge and are 0.06b and 0.16b⁽³²⁾ respectively (weighted for isotopic abundance). ^{71}Ge decays with an eleven day half-life by electron capture to ^{71}Ga and the disintegration energy is 0.24 MeV. ^{75}Ge decays by β^- emission to ^{75}As with an 82 min half-life. The disintegration energy is 1.18 MeV and 13% of the decays are accompanied by one or more γ -rays of total energy less than 0.63 MeV. Lithium is present in a very small proportion and so its contribution to neutron detection is negligible. ^{73}Ge has its first excited level at 0.0135 MeV and has three other levels below 0.5 MeV. Neutrons exciting these levels by inelastic scattering can be detected by the γ -rays produced in their subsequent decay. The isotopic abundance of ^{73}Ge is only 7.8%.

The main fast neutron (energies above 0.5 MeV) detection processes are by the $(n, n'\gamma)$, (n, p) and (n, α) reactions. All the germanium isotopes have closely spaced excited nuclear levels, so consequently very many different energy γ -rays are produced by the

inelastic scattering of neutrons of only a few MeV. Aitken and Dixon⁽³⁷⁾ have studied the (n, α) reaction in germanium by bombarding a Ge(Li) detector with 14 MeV neutrons. The pulse height spectrum was almost continuous up to energies of about 13 MeV. The spectrum extended to approximately 17 MeV because the $^{73}\text{Ge} (n, \alpha) ^{70}\text{Zn}$ has a positive Q-value of 3.79 MeV. The pulse-height of the recoil zinc nuclei, produced with energies around 1 MeV by the (n, α) reaction, was found to be low by about 0.4 MeV. There is very little information available on the cross-sections for these reactions. The non-elastic cross-section has been measured as 2 barns⁽³²⁾ for 3.66 MeV neutrons. The (n, p) and (n, α) reactions, besides causing prompt neutron detection, generally produce unstable reaction products. The (n, p) reaction on the three most abundant germanium isotopes produces ^{70}Ga , ^{72}Ga and ^{74}Ga with half-lives of 21 min, 14.1 min and 8 min respectively. The isotopes decay by β^- emission accompanied by several prominent γ -rays in each case. The (n, α) reaction on germanium can produce two unstable isotopes of zinc, ^{69}Zn and ^{71}Zn which both decay by β^- emission with half-lives of 5.5 min and 2.5 min respectively. These reactions cause a build up of long lived activity in the detector following fast neutron bombardment. Fast neutrons can to some extent be detected by the recoil nucleus in an elastic scattering reaction. The recoil nucleus energy varies from zero to a maximum given by $\frac{4A}{(A+1)^2} E_n$ where A is the atomic number of the scattering nucleus and E_n is the neutron energy. The maximum recoil nucleus energy is about 0.7 MeV for 14 MeV neutrons and assuming there is a detection threshold of 0.4 MeV as observed by Aitken⁽³⁷⁾ for the recoil zinc nucleus, this process produces counts from zero to 0.3 MeV.

The Ge(Li) detector is very susceptible to damage caused by continued exposure to fast neutrons. Fast neutrons produce crystal defects such as the displacement of atoms from their equilibrium sites leaving vacancies and interstitial atoms in the lattice. Neutron

reactions can also cause transmutation of the constituent nuclei. Radiation damage results in an appreciable worsening of the detector energy resolution and eventually causes a double peaking effect. Mann and Yntema⁽³⁸⁾ give a figure of 10^{11} neutrons/cm² as a typical allowable integrated fast neutron exposure for the Ge(Li) detector. Significant damage was observed to set in at this dose. However, Ortec, manufacturers of Ge(Li) detectors, state that significant damage causing a rapid deterioration in energy resolution and timing characteristics is produced by a fast neutron exposure of only 10^8 neutrons/cm².

2.3. Choice of Detection System

Both the NaI(Tl) and Ge(Li) detectors are sensitive to neutrons which also cause a build up of activity in the detectors. The large reaction cross-sections for iodine make NaI(Tl) the more sensitive of the two detectors to neutrons. However, regardless of the choice of detector a time of flight discrimination technique must be employed to reduce this background to manageable proportions for the observation of the prompt γ -rays emitted in 14 MeV neutron scattering.

The two most significant points favouring the use of the Ge(Li) detector are its excellent energy resolution and fast rising output pulses well suited to fast timing. The energy resolution of the Ge(Li) detector is superior to the NaI(Tl) crystal by greater than an order of magnitude and its excellent energy resolution gives the semi-conductor system a superior spectral response. The Ge(Li) detector's fast timing properties enable a shorter sample to detector flight path to be used, so that the detector can be brought closer to the scattering sample to subtend a larger solid angle at the sample (time resolution is discussed in section 3.3.)

The high efficiency of the NaI(Tl) crystal is its most favourable property. The detector manufacturers quote the peak efficiency of a 30 cm³ Ge(Li) detector as being 3% that of a 76.2 mm (3") NaI(Tl)

crystal for a point 1.33 MeV γ -ray source 250 mm from the detector face. The peak efficiency gives the fraction of source γ -rays incident on the detector depositing all their energy in the detector (efficiency is discussed more fully in section 4.5). This comparative efficiency is a function of the solid angles subtended by the detectors and of their intrinsic peak efficiencies. The different detector sizes were taken into account and the intrinsic peak efficiency, at 1.33 MeV, of a 76.2 mm NaI(Tl) crystal was estimated as 8.2 times greater than for a 30 cm³ Ge(Li) detector.

The timing information published in the Ortec Catalogue suggests that a 0.5 m flight path should be possible with a 30 cm³ Ge(Li) detector. The flight path required with a NaI(Tl) crystal depends on the complexity of the electronics used to improve its poor timing characteristics, but a flight path of 1 m to 1.5 m is usual. The product of the solid angle subtended at the sample by the detector and the intrinsic peak efficiency was used as a figure of merit and a 76.2 mm NaI(Tl) crystal was estimated as being ten times as efficient as a 30 cm³ Ge(Li) detector with the crystal 1 m from the sample and 4.5 times as efficient with the crystal 1.5 m from the sample.

The flux of γ -rays produced by the scattering sample under neutron irradiation was calculated as being very weak, so it was considered that high detection efficiency was of prime importance in the choice of detector. The data acquisition time would have to be increased by a factor of 5 to 10 for a 30 cm³ Ge(Li) detector compared with a 76.2 mm NaI(Tl) crystal for the same peak intensity at an energy of 1.33 MeV. However, for a peak sitting on a continuous spectrum, fewer counts would be required in the peak obtained with the Ge(Li) detector for the same experimental error, because for a sharp peak fewer counts have to be subtracted from the total counts in

the region of the peak to obtain the peak intensity. It is difficult to quantify this factor, however, in view of the expected very low signal count rate, it was considered that the improved energy resolution of the Ge(Li) detector would not permit a reduction of a factor of five in the peak intensity. Also the error in the total counts in the region of a peak increases as the number of counts is reduced, due to poorer spectrum statistics.

Since the pair production attenuation coefficient depends on the square of the atomic number (see section 2.1), the efficiency of the Ge(Li) detector further deteriorates at higher γ -ray energies compared with the NaI(Tl) detector.

One further disadvantage of the Ge(Li) detector is the damage caused by neutron exposure. For a typical source strength of $5 \cdot 10^7$ neutrons/s, with a flight path of 500 mm and assuming that shielding provides a factor of 10 reduction in the neutron flux at the detector, the calculated time for the detector to receive an integrated exposure of 10^8 n/cm² is only ~ 200 h. Although a deterioration in resolution would not be particularly troublesome the time resolution would deteriorate and this is unacceptable. After this period the detector could have its performance restored by having it redrifted. Neutron damage would not prohibit the use of the detector, but having to return the detector to the manufacturers for a period of several months for redrifting would be very inconvenient.

It was decided to sacrifice energy resolution for high efficiency and a NaI(Tl) crystal was chosen.

As a high detection efficiency was required, particularly for high energy γ -rays a large crystal was necessary. Large crystals however have poorer energy resolution. As a compromise between efficiency and resolution a 76.2 mm (3 in) diameter by 76.2 mm thick crystal was chosen. The crystal was supplied by Nuclear Enterprises.

2.4 The Anti-Coincidence Spectrometer

The complex γ -ray response of both the NaI(Tl) and Ge(Li) detectors would be greatly improved if only events, in which the full γ -ray energy is deposited in the detector, were counted. This would be so if interactions by pair production, when the full γ -ray energy is not deposited, and by Compton scattering were rejected. This more ideal response can be largely achieved with the anti-coincidence spectrometer.

The Trail and Raboy anti-coincidence spectrometer ⁽³⁹⁾ has two NaI(Tl) scintillators. A 61 mm diameter by 152 mm thick crystal is surrounded by an annular shaped scintillator measuring 63.5 mm i.d. by 203 mm o.d. by 305 mm long. The centre crystal is viewed by a single photomultiplier and the annulus by six photomultipliers. If a γ -ray interacts in the centre crystal by a Compton or pair production process, a scattered or annihilation γ -ray escaping the crystal has a high probability of being detected in the surrounding annulus. The outputs of the six annular viewing photomultipliers are summed and fed into an anti-coincidence circuit with a second input from the centre crystal photomultiplier; if a pulse in the centre crystal is coincident with an annulus pulse the centre detector pulse is rejected. In this way, only events in the centre crystal which deposit the full γ -ray energy are counted. The response of the Trail and Raboy spectrometer to ^{24}Na γ -rays (1.37 and 2.75 MeV) is shown in Figure (2.2) and it is compared with the response of a single 89 mm crystal.

Anti-coincidence spectrometers of the Trail and Raboy type have been used for γ -ray detection following neutron reactions by Nichols et al.⁽⁴⁰⁾ and Ashe et al.⁽⁴¹⁾. Morgan et al.⁽¹¹⁾ have reported the construction of a spectrometer with the centre crystal replaced by a 13 cm^3 Ge(Li) detector

An anti-coincidence spectrometer of the above type was not used as the large and difficult to manufacture annular shaped

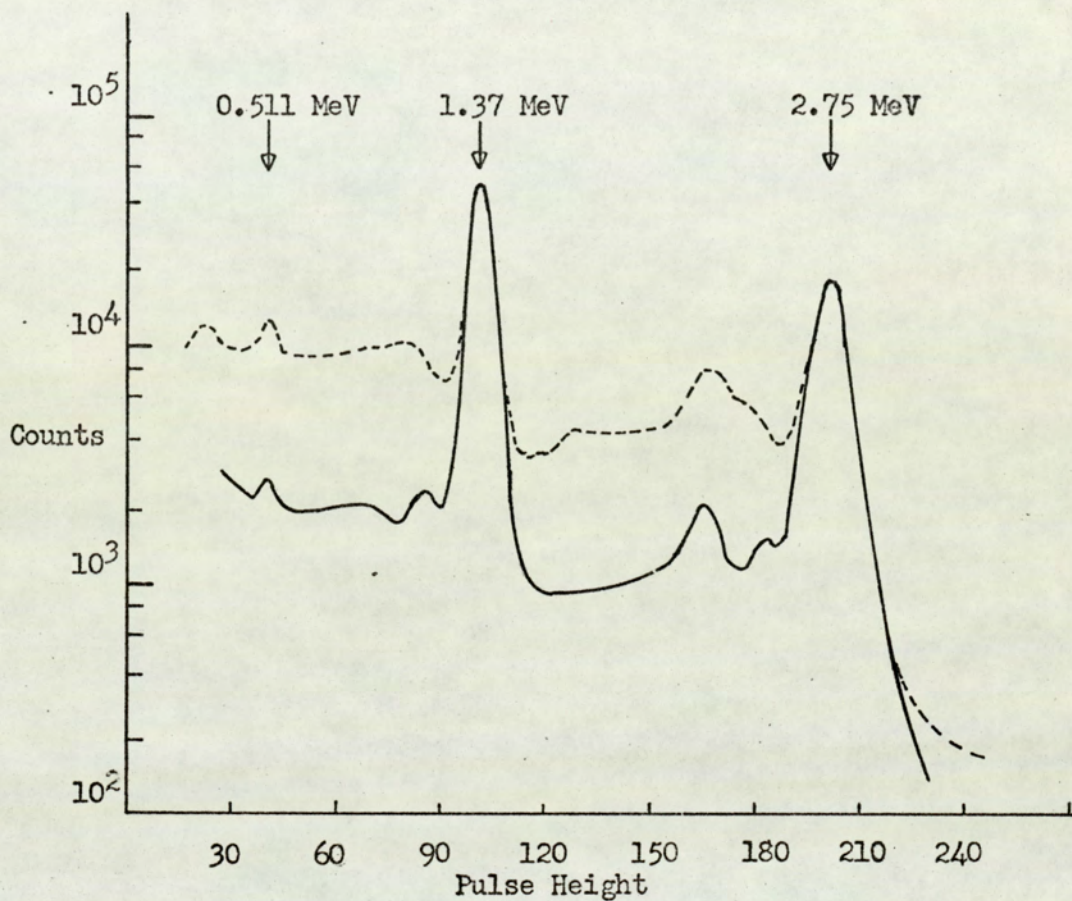


Figure 2.2. The response of the Trail and Raboy⁽³⁹⁾ anticoincidence spectrometer to 2.75 MeV and 1.37 MeV gamma-rays from ^{24}Na compared with the response of a 3.5in crystal.

—— Anticoincidence spectrometer.

----- 3.5in crystal.

scintillator is prohibitively expensive. The use of an annulus of plastic scintillator instead of NaI(Tl) was considered as it is readily available with the large volume required. Plastic scintillator being an organic material with low Z number constituents has a very poor γ -ray detection efficiency and therefore it has a reduced probability of detecting the Compton scattered and annihilation γ -rays escaping the centre crystal. Plastic scintillator is an efficient detector of fast neutrons and as the γ -rays of interest were accompanied by a large neutron background the probability of a full energy γ -ray pulse from the centre crystal being coincident with a neutron background event in the annulus is enhanced and if it cannot be shielded adequately it is best not to have it. The use of an anti-coincidence annulus requires using a small diameter centre crystal which has a lower detection efficiency and low spectrum counts was a particular handicap of the present work. For these reasons the use of a single 76.2 mm NaI(Tl) scintillator was considered the most satisfactory.

2.5 Sodium Iodide Scintillation Detector Design

The factors for consideration in the design of the scintillation detector are the crystal size, choice of photomultiplier tube and the environment. As discussed above, for the present work, a 76.2 mm diameter by 76.2 mm thick crystal was chosen. The type of photomultiplier used is governed by the particular experimental requirements.

Photomultiplier tubes employing the venetian blind or box and grid dynode structures are generally preferred for γ -ray spectrometry as they give the best pulse height resolution. However, for a γ -ray and neutron time of flight measurements, a suitable photomultiplier tube must have a fast transit time with good time resolution. This requirement limits the choice of tube to one with a focused dynode structure as this type has a much smaller spread in electron transit time than both the venetian blind and box and grid structures. There is a very limited variety of focused tubes manufactured. A 76.2 mm diameter photocathode

tube is not manufactured and the nearest size available is a slightly smaller 50.8 mm diameter tube. The tube used was a Philip's 56 AVP. This is a high gain linear focused tube with excellent time resolution having an electron transit time spread of less than 0.5 ns.

To ensure maximum light collection by the photocathode great care must be taken with the optics of the system. As the crystal used had a larger diameter than the photomultiplier tube a light pipe was constructed to make an efficient optical coupling.

In designing a light guide it is important to minimize light loss, which occurs in two ways (i) by absorption in the guide and (ii) through the sides of the guide. Light absorption is usually only significant for light pipes greater than about half a metre. No light is lost through the sides of a guide for transmission by total internal reflection. In the construction of a guide converging from the crystal to the phototube, the angle of convergence should be kept as small as possible so as to encourage total internal reflection. The sides of the guide must be regular and highly polished.

Perspex was chosen as a suitable material for the construction of the light pipe. It has a reasonably low absorption for blue light and is easy to machine. A 76.2 mm diameter rod of perspex was machined on a lathe so that it tapered at one end to a diameter of 46 mm. The angle of convergence was 9° which was the minimum angle possible with the lathe used. The light pipe was 100 mm long. Great care was taken in the polishing of the guide so as to limit light loss. The machined surfaces were polished with progressively finer grades of abrasive paper. The initial polishing was done on a lathe, but the final polishing using very fine abrasive paper down to perspex polish was done by hand. Circumferential ridges cause a marked deterioration in the performance of a light pipe and care was taken in the polishing to avoid them.

If a guide functions correctly, any reflective coating applied

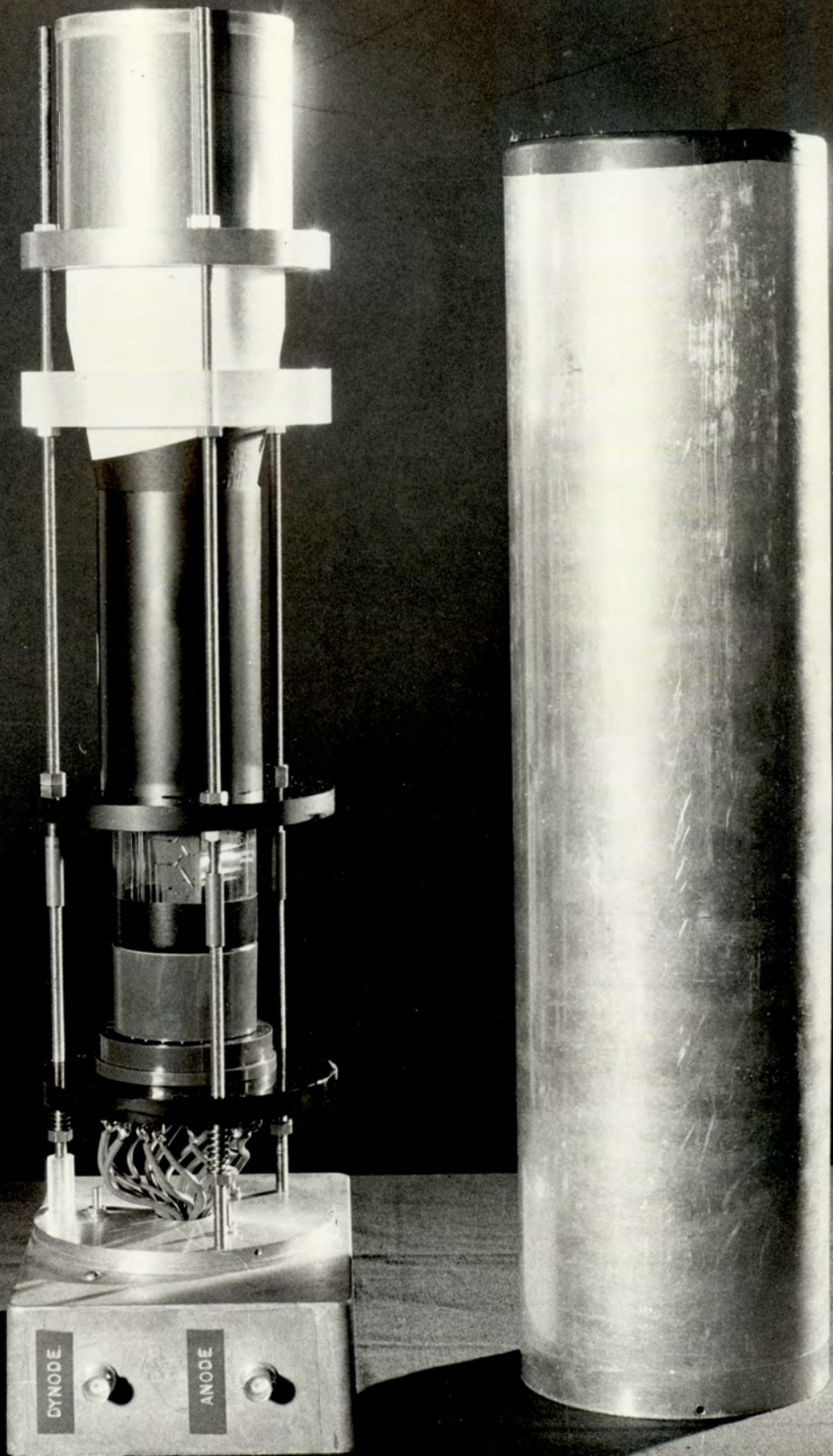
to the surface would be redundant. In the case of a converging guide some light must inevitably strike the surface at an angle less than the critical angle, so that in this case a reflective coating would prove advantageous. For this reason the sides of the guide were coated with titanium dioxide reflecting paint. The reflectivity of titanium dioxide has been compared with that of evaporated aluminium by Swank⁽⁴²⁾. At wavelengths above about 400 nm titanium dioxide is the better reflector, but its relative efficiency falls off at shorter wavelengths. The emission spectrum of NaI(Tl) at room temperature extends from 350 nm to 500 nm peaking at 420 nm⁽⁴³⁾ so that titanium dioxide is a suitable reflector.

The performance of photomultiplier tubes is sensitive to magnetic fields. Tubes with a focused dynode structure are particularly sensitive to magnetic fields. The effect has been reported by Engstrom⁽⁴⁴⁾ and Connor⁽⁴⁵⁾. They have shown that even weak magnetic fields can cause a marked reduction in gain. The earth's magnetic field is not usually troublesome if the tube is operated in a fixed position throughout an experiment. In the present work it was required to rotate the detector about the sample so that shielding from the earth's field was essential for stable performance.

The electron trajectories from the cathode to the first dynode are most sensitive to magnetic fields. The photomultiplier tube was therefore placed inside a cylindrical mu-metal magnetic shield so that the first dynode stages and the photocathode were adequately shielded. The magnetic shield completely corrected a reduction in gain greater than ten per cent observed when the detector was rotated about the scattering sample. The use of a mu-metal shield, besides giving optimum tube gain, gives minimum transit time spread.

The construction of the detector assembly and housing is shown in Figure 2.3. The optical contacts between the crystal, light pipe and

Figure 2.3 The gamma-ray scintillation detector.



photomultiplier were made with non-drying silicon immersion oil. The detector assembly can window was made of thin aluminium sheet, 0.28 mm thick, so as to absorb very little incident γ -radiation. Many investigations have been made of the temperature dependence of photomultipliers. More recently, Murray and Manning⁽⁴⁶⁾ have shown that at temperatures near room temperature there is a decrease in photomultiplier sensitivity with an increase in temperature. The high gain focused tube used in the detector required a large dynode chain current. The heat dissipated by the dynode resistors was nearly ten watts. As shown in Figure 2.3 the voltage divider chain was not mounted directly onto the base of the photomultiplier but screened from the tube to avoid any rise in temperature of the tube.

The detector performance is described in section 3.72 after the associated electronics has been described.

2.6. Detector Shielding

2.6.1. Neutron Shielding Principles and Materials Used

Adequate detector shielding is essential because of the sensitivity of NaI(Tl) scintillator to neutrons. A measure of detector shielding from a neutron source is provided by the use of a "shadow bar". This reduces the number of source neutrons incident on the detector, but neutrons are also scattered into the detector from the floor and walls of a room, so that the shield must subtend a large solid angle at the detector. In the present work the source was a point source of 14 MeV neutrons, so that the detector had to be shielded from the direct flux of 14 MeV neutrons and from the scattered neutrons of lower energies.

A shield should attenuate fast neutrons producing a minimum of secondary penetrating γ -radiation and without causing a build up of activity in the shielding material. Only slow neutrons (0 to 1000 eV) are easily captured. Fast neutrons (above 0.5 MeV) must, therefore, be slowed down, or moderated, before they can be efficiently absorbed.

A neutron shield then has three stages of operation which can be listed as follows:

- (i) moderation of fast neutrons
- (ii) absorption of slow neutrons
- (iii) absorption of secondary penetrating radiation, e.g. γ -rays.

The only way to moderate fast neutrons is to cause them to lose energy in a large number of scattering collisions, by placing a sufficient thickness of material in their path. Fast neutrons may lose energy by inelastic scattering, exciting the scattering nucleus which subsequently emits γ -radiation from which the detector must be shielded. They may also lose energy by elastic scattering, and this is essentially the only process by which slow and intermediate (1 to 500 KeV) neutrons can be moderated. The energy lost by the neutron appears as translational energy transferred to the scattering nucleus. The average loss of energy in an elastic collision is greatest when a neutron is scattered by a hydrogen nucleus, and least for the heaviest nuclei. This follows from the laws of mechanics. Hydrogenous material is the most efficient fast neutron moderator and as the inelastic scattering process does not occur with hydrogen it has a low secondary γ -ray production. The elastic scattering cross-section for hydrogen is relatively large but decreases with increasing neutron energy. Suitable hydrogenous materials are water and paraffin wax, $C_n H_{2n+2}$. Paraffin wax was chosen as the moderate for the shield used in the present work to avoid the construction of a suitably shaped leak proof water tank. In using paraffin wax inelastic scattering by carbon produces 4.43 MeV γ -rays, but the cross-section for this reaction is very much less than for elastic scattering by hydrogen and carbon.

Materials suitable for the absorption of moderated neutrons should have the following three properties: (i) a large neutron cross-section for the absorbing reaction, (ii) easily shieldable reaction

products such as α -particles and β -particles and (iii) a stable reaction product nucleus or if the nucleus is unstable it should decay without the emission of penetrating γ -radiation. There are three widely used materials for slow neutron absorption. They are cadmium, lithium and boron.

Cadmium is a very efficient neutron absorber in the energy range 0.01 eV to 1 eV. The absorption is by radiative capture but the many hard γ -rays emitted in a single capture process make it unacceptable for use in a neutron shield requiring a low γ -ray background.

Both lithium, Li, and boron, B, have large cross-sections for the (n, α) reaction. The (n, α) reaction on ${}^6\text{Li}$ meets the above requirements producing tritium ${}^3\text{H}$, without γ -emission. The unstable tritium decays, by β^- -emission with a 12.3 year half life, to helium again without γ -emission. The cross-section for the ${}^6\text{Li}(n, \alpha){}^3\text{H}$ reaction is 945 barns at thermal neutron energies (0.025 eV) and varies as the inverse of the neutron velocity to 2.5 barns at 10^4 eV. A disadvantage of the use of lithium is that ${}^6\text{Li}$ has an isotopic abundance of only 7.4%. The (n, γ) and neutron scattering cross-sections for natural lithium are negligible in comparison.

The (n, α) reaction cross-section on ${}^{10}\text{B}$ is 3,840 barns for 0.025 eV neutrons and varies as the inverse of the neutron velocity to 6 barns for 10^4 eV neutrons. This is the dominant neutron reaction on natural boron in this energy range. ${}^{10}\text{B}$ has an isotopic abundance of 19.7%. The product nucleus for the (n, α) reaction is ${}^7\text{Li}$ which is stable, but in 94% of the reactions the nucleus is formed in an excited state giving rise to a 0.474 MeV γ -ray.

For handling and constructional reasons boron and lithium are generally used in the form of a compound. Some suitable compounds are lithium carbonate LiCO_3 , borax $\text{Na}_2\text{B}_4\text{O}_7 \cdot 10\text{H}_2\text{O}$, and boric oxide B_2O_3 .

The slow neutron absorber can either be a separate layer of the shield between the moderator and detector or it can be mixed in with the moderator. The later case tends to cause a reduction in capture processes with the moderator material. Thermal neutron capture by hydrogen produces a single γ -ray of 2.23 MeV. The cross-section for this reaction is 330 mb for thermal neutrons. Ashe et al.⁽⁴¹⁾ mixed lithium carbonate with paraffin wax, but a mixture must be rich in lithium carbonate for a substantial reduction in γ -radiation from neutron capture in the hydrogen. However this reduces the density of hydrogen in the shield and consequently the neutron shield is less efficient per unit thickness. As the shield used for the present work had to be mobile for γ -ray angular distribution measurements it was decided to use pure paraffin wax with a layer of suitable boron compound between the moderator and the detector. A boron compound was chosen in preference to a lithium compound because of the larger cross-section and isotopic abundance of the relevant isotope. Boric oxide was used as it has the largest proportion of boron of all the readily available compounds. The 0.47 MeV γ -ray produced in the $^{10}\text{B}(n,\alpha)^7\text{Li}$ reaction can largely be absorbed by the γ -ray shield.

The innermost part of a shield consists of a suitable γ -ray absorbing material. Invariably lead is used for this purpose because of its density and high atomic number. It shields the detector from γ -rays produced by reactions in the shielding material and from the general γ -ray background.

2.6.2. Shield Construction

A cross-section of the constructed shield is shown in Figure (2.4). A limiting factor in the construction of the shield was the fact that it had to be mobile. This tended to limit the size and weight. The weight of the assembled shield was about 225 kg. The lead γ -ray shield was 55 mm thick at the side of the detector and had a maximum thickness of 125 mm in front of the crystal. The attenuation

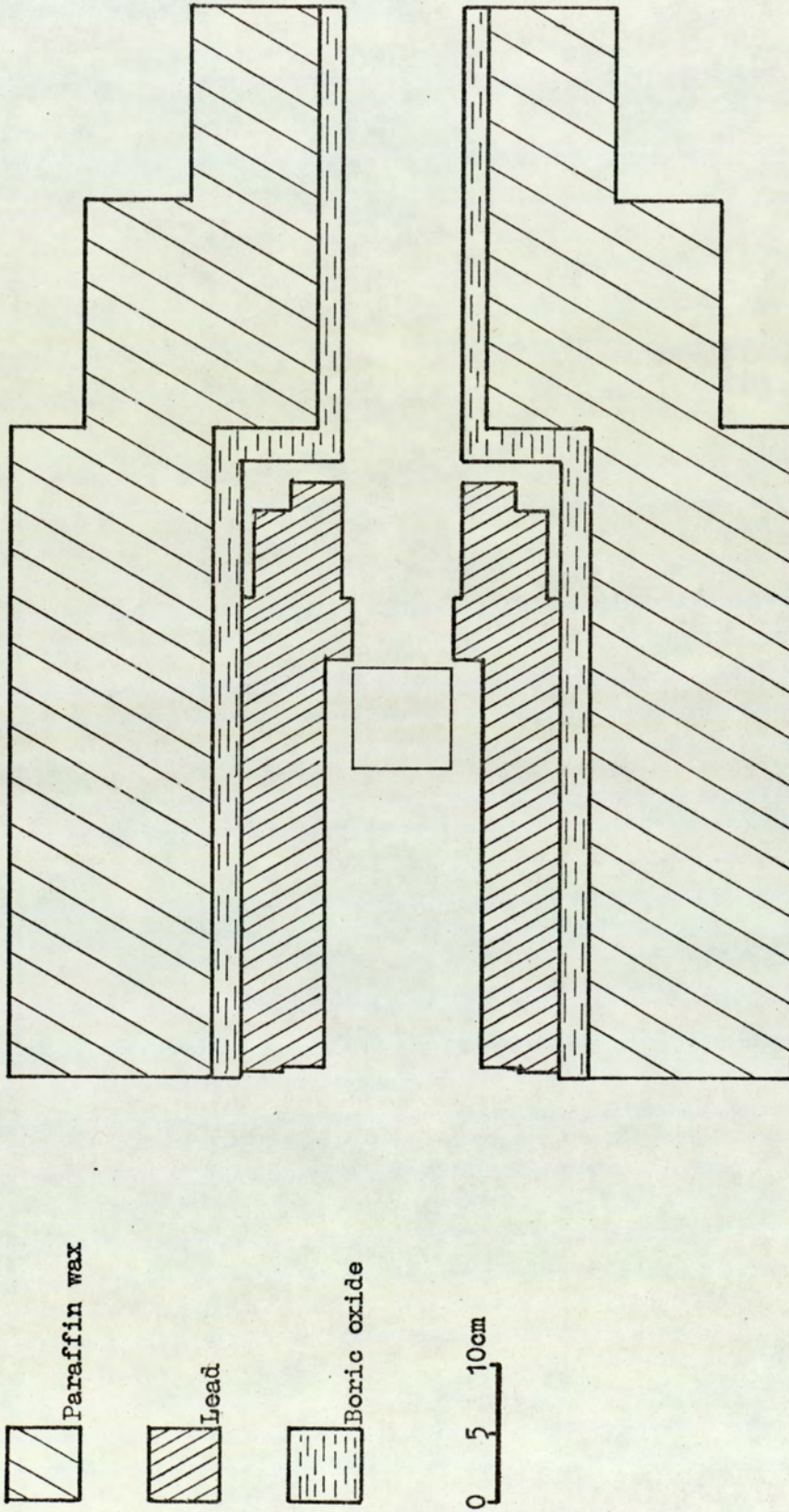


Figure 2.4. Cross-section of the neutron shield.

of γ -rays by lead is a function of γ -ray energy. Figure (2.5) shows the thickness of lead required to attenuate a γ -ray flux by a half. It was calculated from absorption coefficients tabulated by Grodstein⁽⁴⁷⁾. The half thickness values were calculated by the simple exponential absorption law and assumed that scattered γ -rays, degraded in energy, do not reach the detector. The curve shows that 3.5 MeV γ -rays are the most penetrating. The half thickness in this case is 15 mm so that the minimum thickness of lead was nearly four times the half thickness value.

The lead shield was surrounded by a 20 mm thick slow neutron shield. This consisted of a double walled cylinder made from tin plated iron sheet, packed with boric oxide powder. The vessel was sealed off at both ends. The boric oxide powder was packed into the vessel with an effective density of 1200 kg m^{-3} (boric oxide has a density of $1,840 \text{ kg m}^{-3}$). This thickness of boric oxide absorbs 100% of a neutron flux up to a neutron energy of about 1 eV. Figure (2.6) shows the fraction of neutrons absorbed by the (n, α) reaction in the neutron energy range 0.1 eV to 10 KeV for the shield used. The cross-section values used to calculate this curve were taken from the Barn book⁽³²⁾.

The moderator consisted of paraffin wax with a thickness of 150 mm to the side of the crystal and a maximum thickness of 300 mm in front of the crystal. The front of the shield was tapered so as to subtend a smaller solid angle at the neutron source. Kreger and Mathur⁽⁴⁸⁾ state that 200 mm of paraffin is considered enough to absorb most high energy neutrons. The collimator of the neutron shield also contained a lining of boric oxide powder to absorb thermal neutrons. The boric oxide was packed into a sealed double walled cylinder and had a thickness of 15 mm. A steel frame was imbedded in the wax to support the lead and boric oxide shields, preventing them from sinking into the wax. Figure 2.7 shows the shield mounted on its mobile stand.

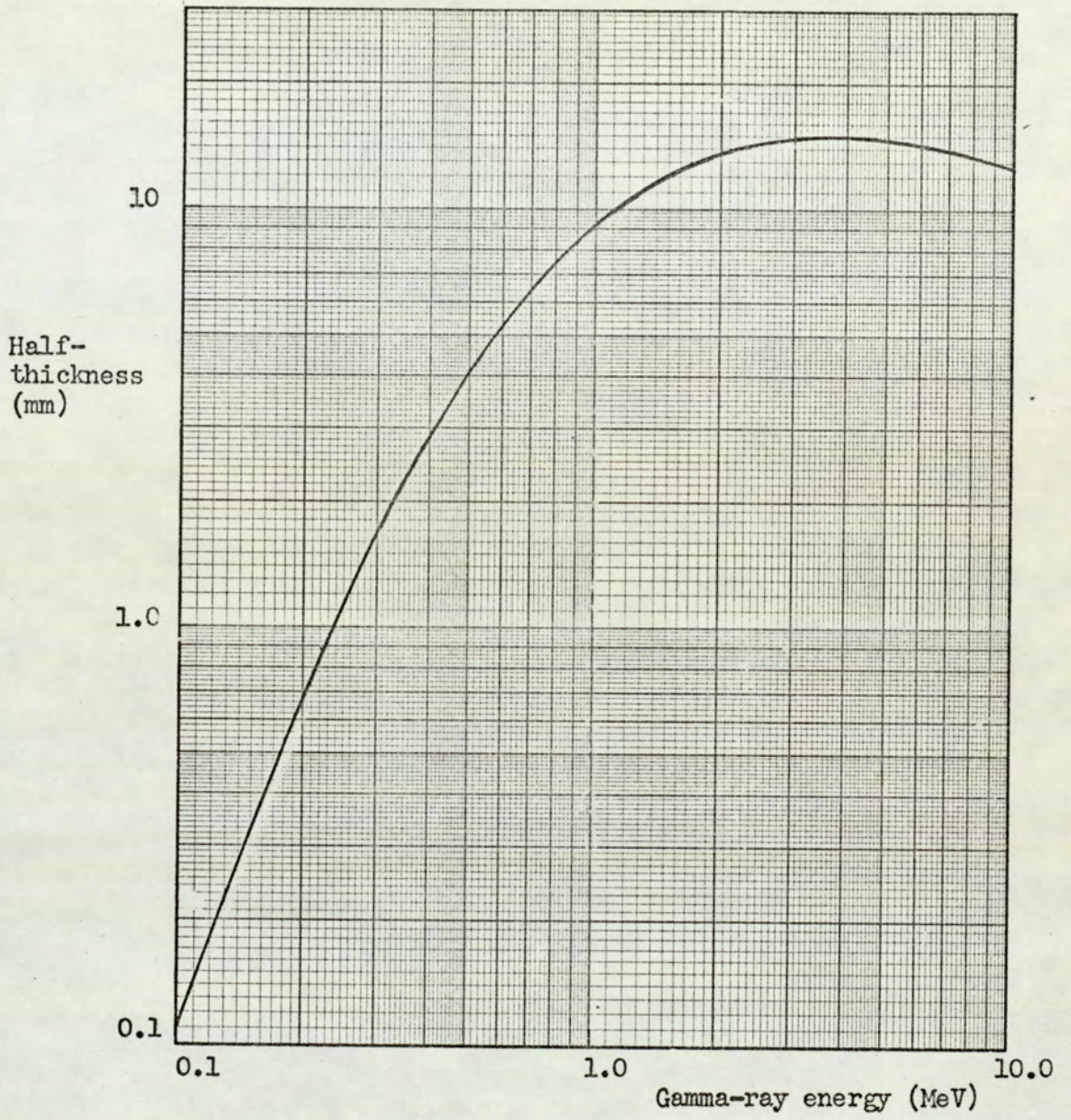


Figure 2.5. The half-thickness of lead vs. gamma-ray energy.

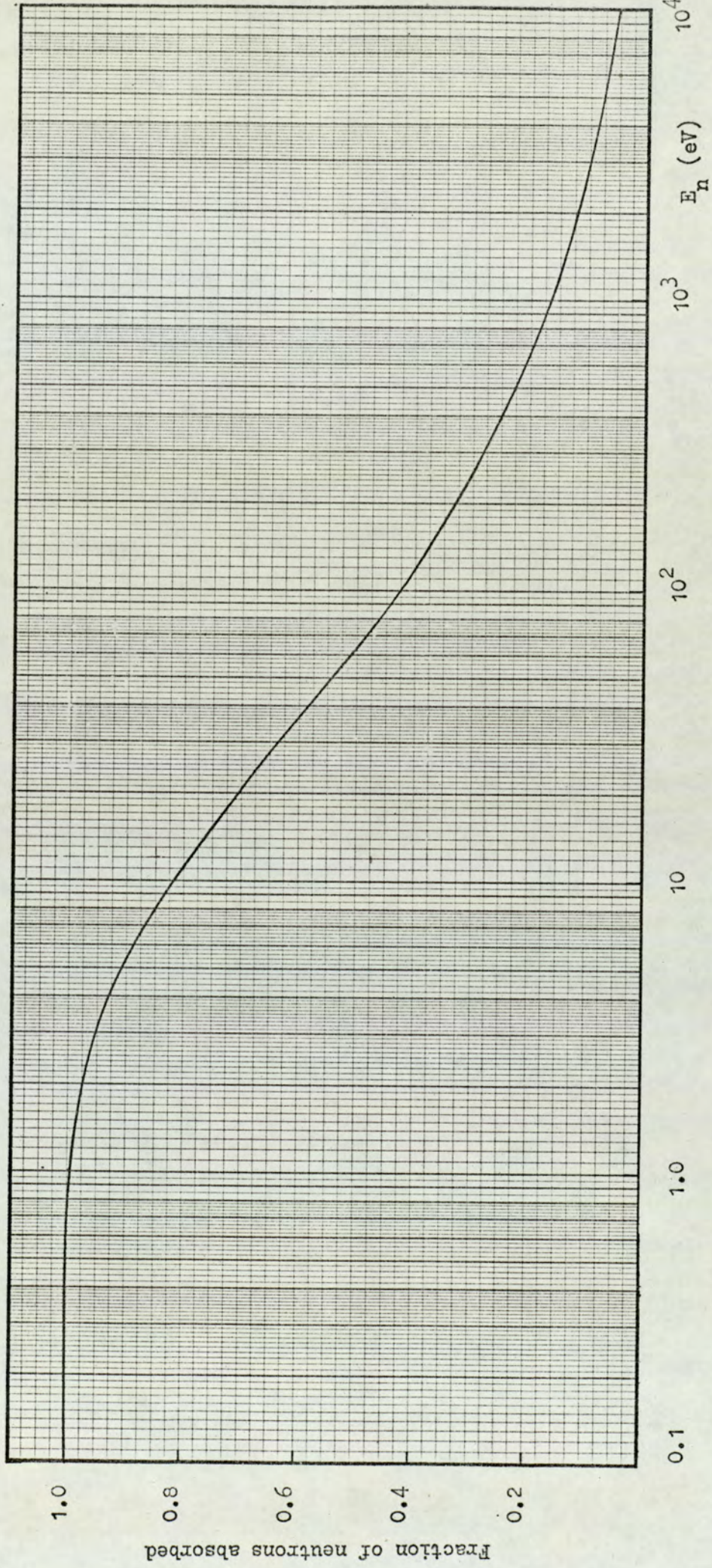


Figure 2.6. The fraction of neutrons absorbed by the B_2O_3 shield vs. neutron energy.

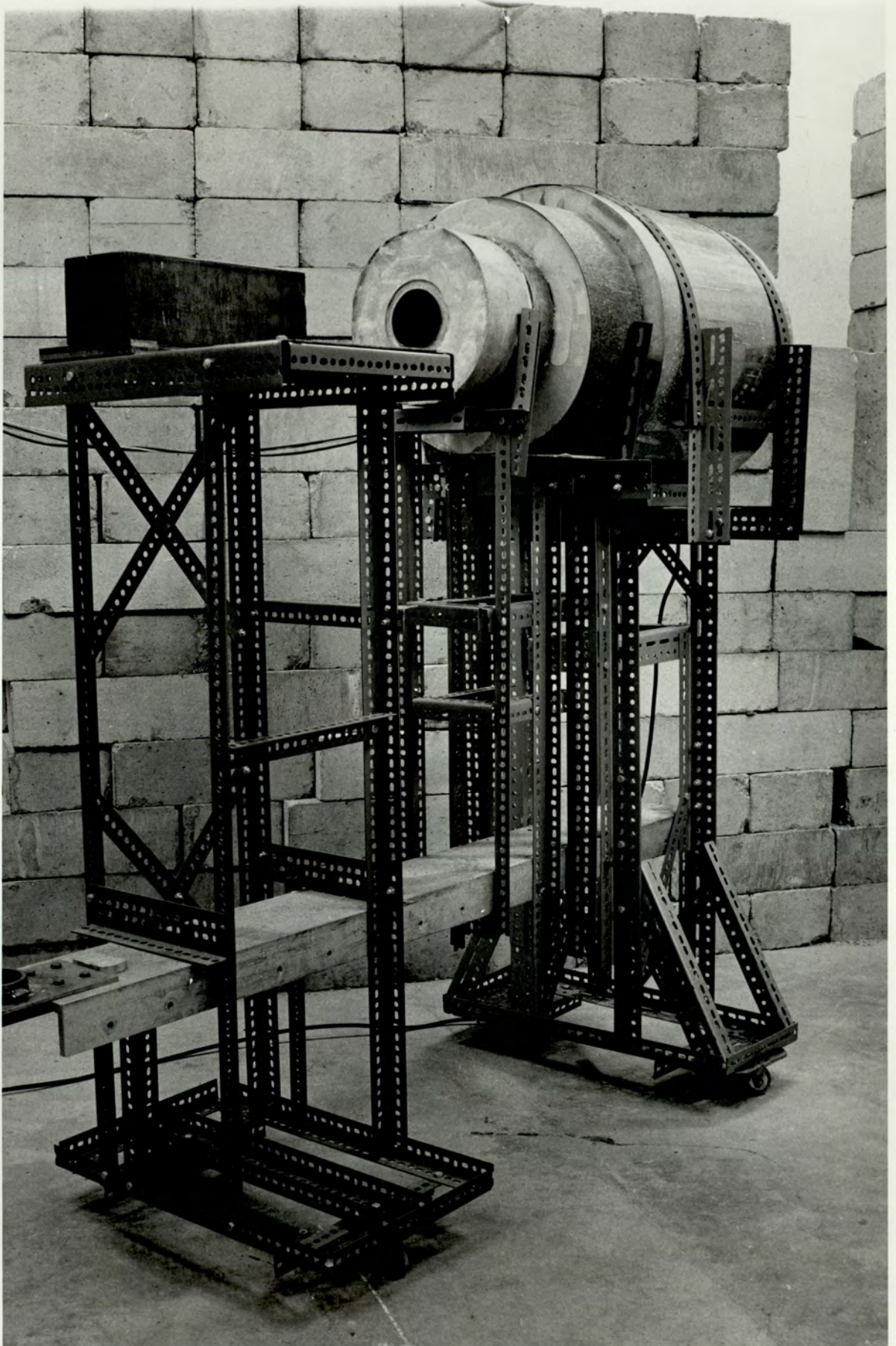


Figure 2.7. The mobile gamma-ray detector shield.

A further measure of shielding was provided by the use of a shadow bar. Neutron target shadow bars are usually made of a heavy metal or in some cases hydrogenous material. The elastic differential cross-sections for heavy metals are very sharply forward peaked and for attenuation purposes the entire elastic cross-section can be neglected. The non-elastic processes either absorb or degrade in energy the incident neutrons, but generally produce hard γ -rays in doing so. Hydrogen, however, provides on average a 50% energy degradation per elastic collision and it is more appropriate in this case to use the total elastic cross-section for attenuation estimates. Materials suitable for shadow bars have been investigated by Hopkins et al⁽⁴⁹⁾. They compared the macroscopic non-elastic cross-sections for several metals and the total macroscopic cross-section for hydrogen in polythene over the range 0.5 to 20 MeV. For neutrons above 6 MeV materials in order of merit were tungsten, copper, iron, lead and polythene. (For lower neutron energies polythene was the most efficient). It was decided to use iron as it is more easily obtainable than the other materials and it is also a very good γ -ray shielding material. Thus secondary γ -rays produced by neutron interactions in the iron are well shielded. The shadow bar was a regular block of mild steel measuring 129 mm square by 385 mm long. The 14 MeV non-elastic cross-section for iron is 1.5 barns⁽³²⁾. Therefore 99% of neutrons travelling the length of the bar will be absorbed or attenuated.

2.6.3. Efficiency Test of the Shield

To test the efficiency of the shielding the following experiment was carried out. The detector was placed $1\frac{1}{2}$ m from the 14 MeV neutron source. The shielded detector was positioned so that the source was off the axis of the detector, i.e. the source was out of the line of vision of the collimated detector. The detector response was recorded for a fixed neutron yield for the following three cases (i) with full shielding, (ii) with the shadow bar removed, (iii) with no shielding at all. The

three spectra obtained are shown in Figure (2.8). The response was recorded for γ -ray energies from 0 to 5 MeV. Curves labelled A, B and C correspond to the above cases in the stated order. The neutron shield gave a 75% to 80% reduction in counts, but with the shadow bar this was improved to a 90% reduction. In the shielded cases the spectra vary smoothly except for peaks at 0.47 and 2.23 MeV γ -ray energies. The lower energy peak results from the $^{10}\text{B} (n, \alpha) ^7\text{Li}$ reaction. The 2.23 MeV peak results from slow neutron capture by hydrogen, though this peak was present, but not as pronounced, in the unshielded case showing that a γ -ray of this energy was present in the general room background. A source of γ -rays of this energy was the wooden beams and water tank serving as shielding above the neutron target. The above spectra show the prompt neutron response. The spectra were recorded in short runs before the crystal had time to become active.

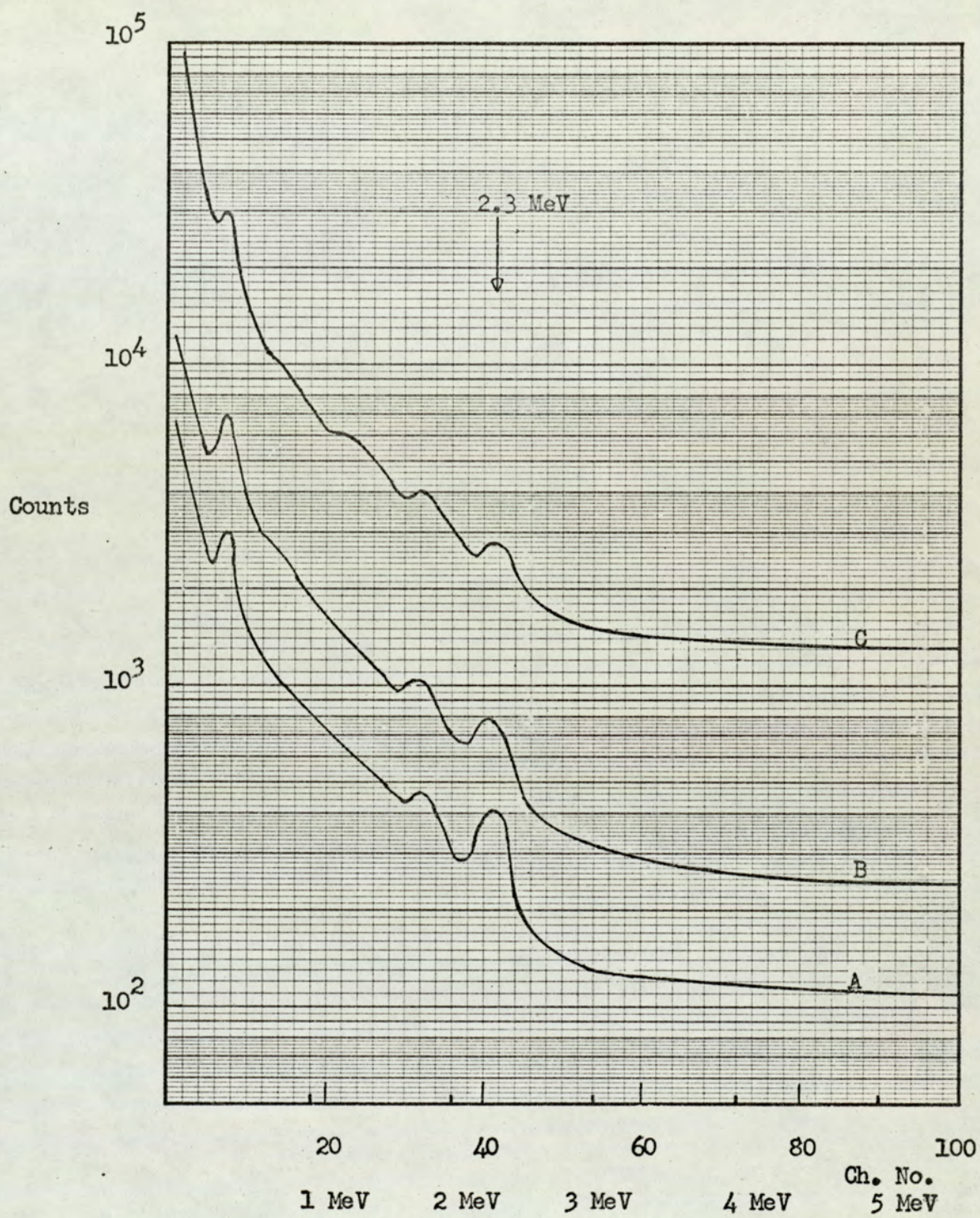


Figure 2.8. The prompt neutron induced background in the gamma-ray detector with various degrees of shielding.

CHAPTER 3THE EXPERIMENTAL METHOD3.1. The Time of Flight Discrimination Technique

Neutron velocity measurement is a well known method of neutron spectroscopy. The neutron's energy is determined by measuring its flight time over a fixed flight path. The application of time of flight techniques to the separation of γ -ray and neutron events, in the observation of γ -rays produced by neutron inelastic scattering, was first suggested by Cranberg⁽¹⁾.

To measure a time interval, t , each end of the time interval must be precisely defined, i.e. a start and a stop signal must be obtained for each neutron of interest. To illustrate the precision required in these timing experiments the flight times per metre of 14 MeV neutrons and γ -rays are 19.3 ns and 3.34 ns respectively. Therefore, with a 1m flight path the time separation of elastically scattered neutrons and γ -rays is approximately 16 ns.

There are two different approaches possible to neutron time-of-flight measurements with low energy accelerators. These methods, which are called the pulsed beam method and the associated particle method, differ in the manner in which the start pulse is obtained. In each case the stop signal is produced when a γ -ray or neutron is detected. The time interval between the start and stop pulses is measured electronically.

The application of the time of flight method to γ -ray detection following fast neutron inelastic scattering brings about a marked improvement in the signal to background ratio. Essentially γ -ray detector events are only stored if the radiation arrives at the detector in a certain short time interval after the production of

the incident neutron. In this way neutrons scattered into the detector by the sample are not detected as they arrive after the γ -rays and also the time independent background is reduced.

3.1.1. The Pulsed Beam Method

This is the most common method used for time of flight work with low energy accelerators in the production of neutrons by positive ion bombardment of a target. The time of origin of the neutron is defined with a small time uncertainty, δt_b , by pulsing the accelerator ion beam so that the target is exposed to short ion bursts of duration δt_b . The two main methods of ion beam pulsing are beam chopping and bunching.

In the beam chopping method a steady beam is passed between a pair of deflection plates. A high frequency, high voltage signal is supplied to the deflection plates so that the beam is swept rapidly across an aperture in front of the target. Typically a 5 MHz signal, with a peak voltage of several kilovolts is used to sweep the beam. With this method neutron bursts of one or two nanoseconds duration can be produced. The method has the advantage that in addition to defining the production time of a neutron to within 1 ns., it provides a time interval of ~ 100 ns during which the beam is held off the target for the scattering and possible subsequent detection of a γ -ray or neutron. A disadvantage of this method is the low duty cycle which can be as low as 1%. This method was largely developed by Cranberg⁽⁵⁰⁾. The Texas Nuclear group⁽⁷⁾ used Cranberg's method to pulse a 2 MeV Van de Graaff accelerator, (the sweeping frequency was 2.54 MHz), for their γ -ray work with 15 MeV neutrons.

The beam chopping method described above is of the post-acceleration type. Pre-acceleration beam pulsing has been developed at the Oak Ridge⁽⁵¹⁾ and Brookhaven⁽⁵²⁾ laboratories. In the pre-acceleration method the beam is chopped before it leaves the high voltage terminal of an electrostatic accelerator. This method is more efficient and greater ion burst peak currents are achieved, but the

duration of the bursts is longer than for post acceleration beam chopping.

Very intense short ion bursts can be produced by the ion bunching technique. First the beam is chopped by either the pre or post-acceleration methods to produce relatively long ion bursts of about 30 ns duration. The ion bursts are then bunched into intense short bursts of about 1 ns duration by either a Mobley-type magnet⁽⁵³⁾ or a Klystron buncher. Stelson et al.⁽⁵⁴⁾ have described a klystron buncher for use with a Cockroft-Walton accelerator. In this system a 250μ A deuteron beam is chopped into bursts of 30 ns duration at a frequency of 4.5 MHz. The beam is then velocity modulated in a klystron tube to less than 2 ns duration with a peak pulse intensity of between 3mA and 4mA.

3.1.2. The Associated Particle Method

This method is not as generally applicable as the pulsed beam method and can only be used with the ${}^3\text{H}(d,n){}^4\text{He}$ and ${}^2\text{H}(d,n){}^3\text{He}$ neutron producing reactions. In these positive Q-value reactions neutron production is accompanied by an energetic helium particle. The instant of production of the source neutron is defined by detecting the associated helium particle, i.e. the neutron start pulse is given by the detection of the helium particle which can be detected with 100% efficiency. The angle between the helium particle and the neutron is fixed by momentum and energy considerations. Consequently the solid angle subtended at the target by the helium particle detector defines a corresponding cone of useful neutrons. It is considerably more difficult experimentally to use the associated particle method with the lower Q-value (3.26 MeV) D,D reaction because the ${}^3\text{He}$ particles produced have low energies. The target geometry must be carefully designed so that the helium particles can escape the target. The helium particles have also to be separated from scattered deuterons, which may have comparable energies to the ${}^3\text{He}$ particles in the case of the D,D reaction.

In the D,T reaction the uncertainty in the neutron production

time is usually less than 1 ns. The timing uncertainty is a function of the energy loss of the α -particles in escaping the target and the time resolution of the α -particle detector. The associated particle method has two distinct advantages: (i) a d.c. accelerator beam is used; and (ii) with the scattering sample positioned so that it subtends all of the defined neutron beam, a neutron start pulse is only obtained when a neutron penetrates the sample and this gives an excellent signal to background ratio. A disadvantage of the method is the low neutron yield which is restricted by the high count rate in the α -particle detector.

The first reported work using the D,T associated particle method was by Scherrer et al⁽⁵⁵⁾, but they were unable to separate scattered neutrons from γ -rays produced in the sample. The method has been used by Martin and Stewart⁽¹⁴⁾ to observe γ -rays in the inelastic scattering of 14 MeV neutrons.

The factor of prime importance in the pulsed beam method is that the target current burst should have a high peak value to give a workable γ -ray signal to background ratio. The production of intense, approximately 1 ns, ion bursts requires sophisticated apparatus. As neither space nor facilities were available for the present work, the only feasible time of flight discrimination technique was the associated particle method and this method was adopted.

3.2. The Experimental Arrangement for the Associated Particle Method

In this section the particle accelerator, the neutron producing target with the alpha-particle detection system and the experimental geometry are described.

3.2.1. The SAMES Accelerator

A titanium tritide target was bombarded with 140 KeV deuterons produced by a SAMES type J accelerator, illustrated in Figure 3.1. The SAMES electrostatic generator is housed in a hermetically sealed unit in

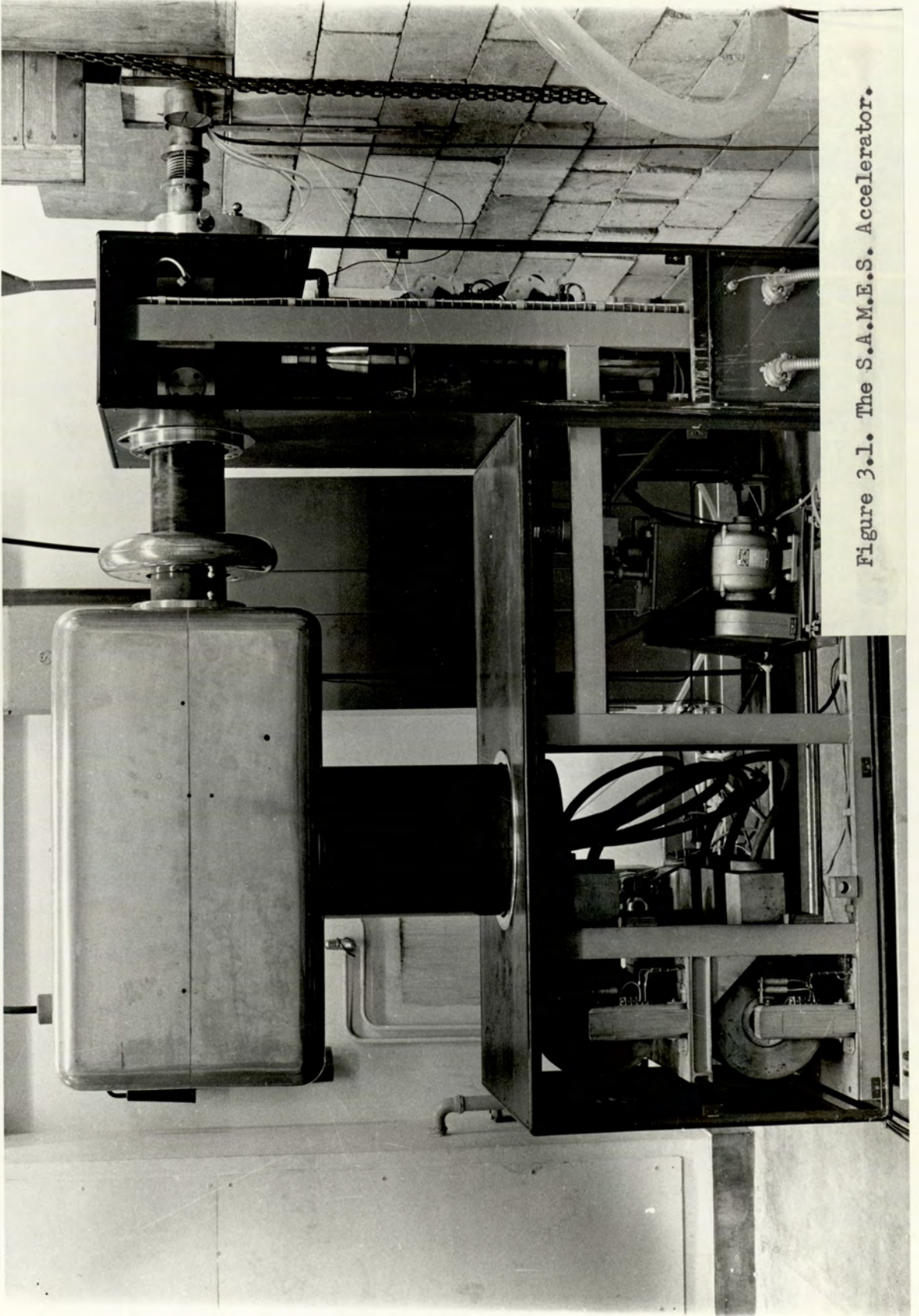


Figure 3.1. The S.A.M.E.S. Accelerator.

a hydrogen atmosphere at 15 atmospheres pressure. The generator can deliver 2mA at +150 kV with a stability of 1%. The accelerator ion source is a 100 MHz radio-frequency source supplied with deuterium gas through a palladium leak. The maximum output current from the ion source is 0.6mA and is extracted by a potential variable from 0 to +6 kV. The extracted beam has a two stage potential drop to earth potential; the intermediate potential, the focus electrode, is adjustable from 0 to +50 kV. The power for the focus lens is provided by an oil immersed Cockroft-Walton generator housed inside the high voltage terminal of the accelerator. The control of the ion source deuterium gas leak, beam extraction and beam focusing inside the high voltage terminal is via 150 kV isolation transformers.

3.2.2. The beam tube and target assembly

Due to the limited space available in the laboratory a long beam tube had to be used to bypass other experimental facilities. The beam tube was made in a 2m section of 101.6mm (4 in) diameter brass pipe bolted together with O-ring seals between the end flanges to make good vacuum seals. The beam tube was evacuated to a pressure of 0.27 nNm^{-2} (2.10^{-6} torr). The main pumping stage was part of the SAMES, but because of the volume of the drift tube, an auxiliary stage was provided at the target end of the tube. The pumps consisted of backed oil diffusion pumps with liquid nitrogen refrigerated baffles. A liquid nitrogen cold finger was positioned above the auxiliary pumping stage to maintain a good vacuum in the target assembly and to stop oil etc., depositing on the target.

Extra beam focusing was required because of the length of the beam tube. A pair of electrostatic quadrupole lenses was used to focus the beam. The focusing has been described by Baynham⁽⁵⁶⁾. Figure 3.2. shows the beam tube length and the positioning of the lenses. The quadrupoles gave optimum focusing with potentials of ± 2.2 kV. A pair of electrostatic deflector plates, shown in Figure 3.2 enabled the target current to be optimized (a typical deflector plate voltage was 500 v).

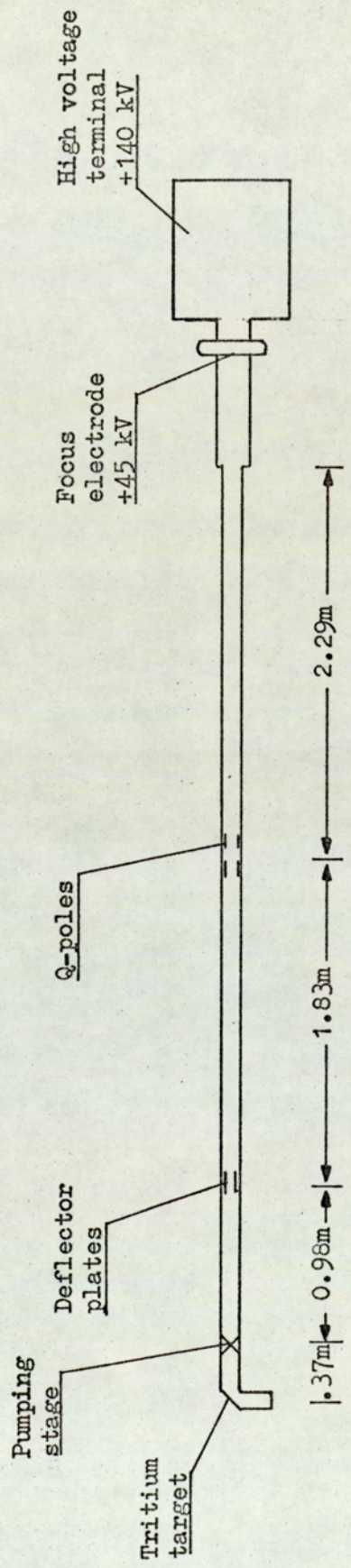


Figure 3.2. The accelerator beam tube.

The 90° branched, stainless steel target assembly was supplied by Multivolt Ltd., and it housed an annular shaped target that could be rotated at 60 r.p.m. by a small electric motor. The target, 143 mm o.d. and 31.8mm wide, originally had 6.2 mCi of tritium per mm², though due to previous use it was not very uniform. The titanium tritide layer was 2,000 nm thick and was backed by a thin copper plate. The target assembly is shown in Figure 3.3. The area of the target bombarded by the beam was restricted by an aperture plate to define a small diameter, approximately point neutron source. The aperture plate was split, see Figure 3.3., to enable efficient pumping of the target assembly. The target and diaphragm were water cooled. Typical target and diaphragm currents were only 1 μA and 10 μA respectively.

Energetic positively charged deuterons eject electrons from the target and diaphragm. To prevent these electrons back streaming to the accelerator the diaphragm and target were self-suppressed, i.e. the electrons were prevented from escaping the target and diaphragm by raising the target and diaphragm potentials to +200 volts. As shown in Figure 3.3, the target, the aperture flange and the main beam tube were insulated by araldite spacing flanges so as to maintain the suppression potentials which were produced by taking the target and diaphragm currents to earth via large resistors. Microammeters in series with the diaphragm and target suppression resistors enabled the currents to be monitored. However, the meter readings could not be taken as the absolute currents, as the target and diaphragm were each found to have a 20 M Ω coupling to earth through the cooling water supplies.

The alpha-particle detector was positioned in the arm of the target assembly at right angles to the main beam tube.

3.2.3. The Alpha-Particle Detector

Alpha-particles being heavy, doubly charged particles are highly ionising and can be detected with 100% efficiency. Either a

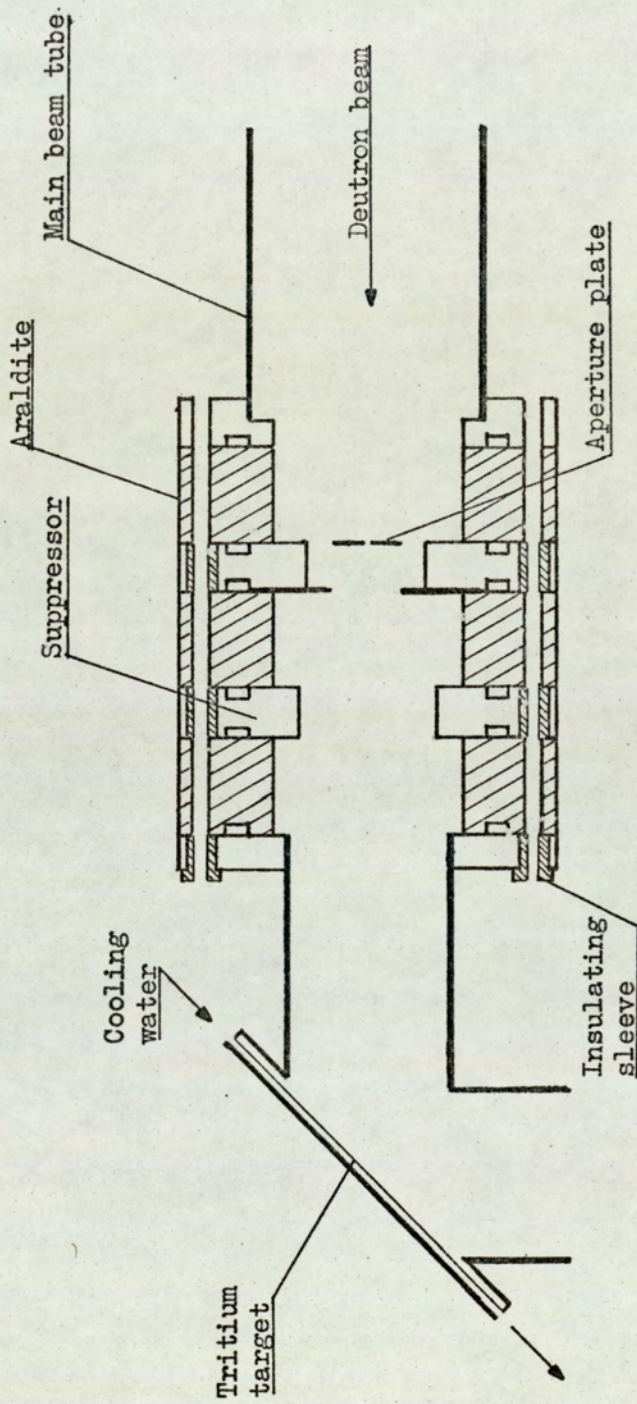


Figure 3.3. The target assembly.

scintillation detector or a semi-conductor detector can be used. For the present application the detector must have the following three properties:

- (i) an excellent α -particle detection efficiency,
- (ii) a low neutron and γ -ray detection efficiency,
- (iii) a fast response time for nanosecond time of flight measurements.

Organic plastic scintillator NE 102a, closely meets these requirements. It is readily available in thin sheets, thus having a low neutron detection efficiency and being an organic material with low Z number constituents it is an inefficient γ -ray detector. Plastic scintillator has a very fast response time; its time decay constant is 2 ns, so used in conjunction with a focused dynode tube with a small transit time spread it meets the timing requirements.

The silicon surface barrier semi-conductor detector is widely used for alpha-particle detection in the D,T reaction. It has a relatively low response to both neutrons and γ -rays and has a fast response time.

Of these detectors there are two advantages in using plastic scintillator in preference to the silicon surface barrier detector. The use of plastic scintillator with a high gain focused photomultiplier tube dispenses with a pulse amplifier which is required with the semi-conductor detector. Secondly the scintillation detector is less sensitive to radiation damage than the semi-conductor detector. Radiation damage in the semi-conductor detector is mainly due to α -particles which are a hundred to a thousand times more damaging than fast neutrons. Mann and Yntema⁽³⁸⁾ state that an integrated alpha particle flux of 10^{10} per cm^2 causes significant damage to the silicon surface barrier detector. For a detector placed 90 mm from a source producing 10^7 neutrons per second the allowable alpha-particle exposure suggested by Mann and Yntema is reached in only 280 h. To reduce the

scintillation efficiency of plastic scintillator by a half, Rozman and Zimmer⁽⁵⁷⁾ give a value of $6 \cdot 10^8 \text{ J} \cdot \text{m}^{-3}$ for the energy of the incident α -radiation dissipated per unit volume. Under the same conditions as described for the semi-conductor detector, plastic scintillator would receive this dose after $6 \cdot 10^4 \text{ h}$ exposure. Significant change in plastic scintillator light output is not expected after 10^4 h exposure; this value was calculated from the results of Birk's work on anthracene and using his estimate that plastic scintillator has a radiation stability of fifty times that of anthracene.

Plastic scintillator was chosen in preference to the semi-conductor detector for the present work. The scintillator used was Nuclear Enterprise's type N.E. 102A. The sensitivity of plastic scintillator to neutrons and γ -rays is discussed in section 4.4.

In the D,T reaction the alpha particles emitted at 90° to the deuteron beam have an energy of approximately 3.5 MeV, (section 4.2.4). The range of a 3.5 MeV alpha-particle in NE 102A is 0.025 mm (taken from the manufacturer's data sheet), so this thickness of plastic scintillator would be 100% efficient. The scintillator used was 0.5 mm thick as NE 102A sheet of this thickness was at hand. A Philip's 56 AVP photomultiplier tube was used. The tube has a transit time spread of less than 0.5 ns making it ideal for fast timing work.

To avoid the problem of housing the photomultiplier tube inside the evacuated target assembly a similar system to that reported by O'Neill⁽⁵⁹⁾ was used. The thin plastic scintillator sheet was attached to a perspex light pipe with the perspex light pipe forming the vacuum sealing flange. The photomultiplier viewed the side of the perspex flange outside the vacuum system. Figure 3.4 shows the alpha-detector arrangement. The scintillator was positioned 90 mm from the centre of the target, i.e. the neutron source point of the target. The scintillator was 30 mm square and it was attached to the perspex flange

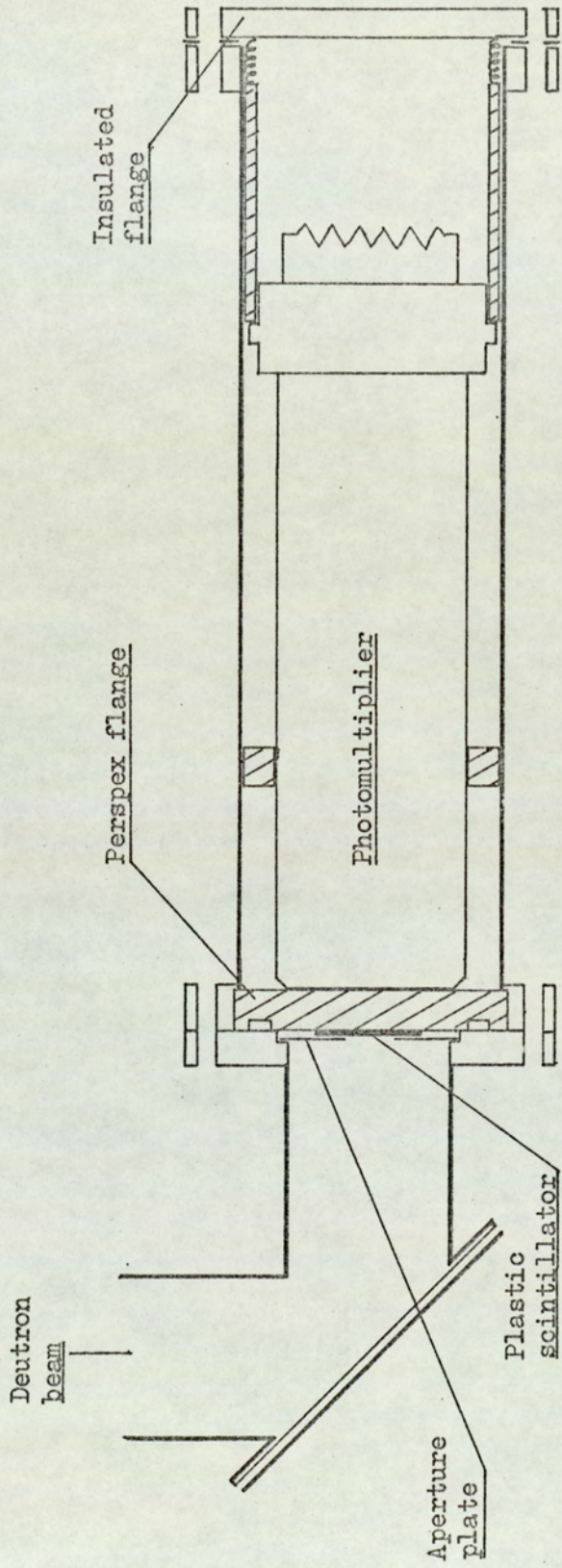


Figure 3.4. The alpha-detector system.

by NE 580 optical cement which is a clear colourless epoxy resin having a refractive index close to that of NE 102A ($\mu = 1.58$). An O-ring vacuum seal was made between the 12.7 mm thick perspex flange and the target assembly flange. The photomultiplier was spring loaded onto the flange using silicon immersion oil to make a good optical contact between the perspex flange and the photocathode. The base flange of the α -detector system was insulated from the main body of the detector and target assembly by using insulating spacers and nylon bolts. This was to keep the base flange at earth potential as the target assembly was self suppressed and its potential rose to about +200 volts under deuteron bombardment.

3.2.4. Alpha-Detector Shielding

The alpha-detector had to be shielded from two sources of radiation. These were β 's emitted by the tritium target and deuterons scattered by the target.

Tritium is unstable and decays by β^- emission with a 12.3 year half-life to ^3He ; the decay is unaccompanied by γ -ray emission. The total energy released is 18.6 KeV and this represents the maximum β -particle energy, though the average β -particle energy is 5.7 KeV. The target with 0.62 Ci cm^{-2} emitted an intense flux of β -particles. Although the β -particles were of a much lower energy than the α -particles of interest and could have been discriminated, they would have caused an exceptionally high count rate in the photomultiplier being detected with a 100% efficiency. The range of 18.6 KeV β -particles in aluminium is $0.0022 \text{ mm}^{(60)}$ so this thickness of aluminium would completely shield the plastic scintillator.

Deuterons scattered through 90° into the alpha-detector have an energy less than 140 KeV. Data on the range of deuterons in aluminium can be obtained by scaling proton range data. The range, $R_d(E)$, of a deuteron of energy, E , and mass, m_d , is given by:

$$R_d(E) = \frac{m_d}{m_p} R_p \left(\frac{m_p}{m_d} E \right)$$

where m_p is the proton mass and R_p is the proton range, i.e. the deuteron range is twice the range of a proton with the same velocity. Mean proton ranges in aluminium have been tabulated by Whaling⁽⁶¹⁾. A 100 KeV proton has a range in aluminium of 0.26 mg/cm^2 (minimum proton energy tabulated), so a 200 KeV deuteron has a range in aluminium of 0.52 mg/cm^2 (0.002 mm).

An aluminium foil was used to shield the scintillator from both sources of radiation. The foil used was 0.0044 mm thick. This completely shielded the β 's and deuterons but did not stop the α -particles. The range of a 3.5 MeV α -particle in aluminium is 4.5 mg/cm^2 (0.017 mm)⁶¹. An added advantage of the foil was that it made the scintillator light tight.

The exposed area of the α -scintillator was restricted by an aperture plate placed directly in front of the scintillator in a slot in the target assembly flange. The aperture plate was 1.5 mm thick with a rectangular hole cut out of its centre so that only an area 24.5 mm by 12.6 mm of the scintillator was exposed to α -particles. This limited the angular acceptance of α -particles in the horizontal plane to $90^{\circ} \pm 4^{\circ}$, so the effective scintillator width was then 12.6 mm. The α -detector scintillator light pipe, aperture plate and photomultiplier are shown in Figure 3.5.

3.2.5. Scattering Sample Position

The angular range of the neutrons, corresponding to the alpha-particles detected at $90^{\circ} \pm 4^{\circ}$ to the deuteron beam, was calculated by the principles of energy and momentum conservation. From the results given in section 4.2, the 8° α -detector defined a cone of neutrons extending from 78° to 92° to the deuteron beam direction (in the

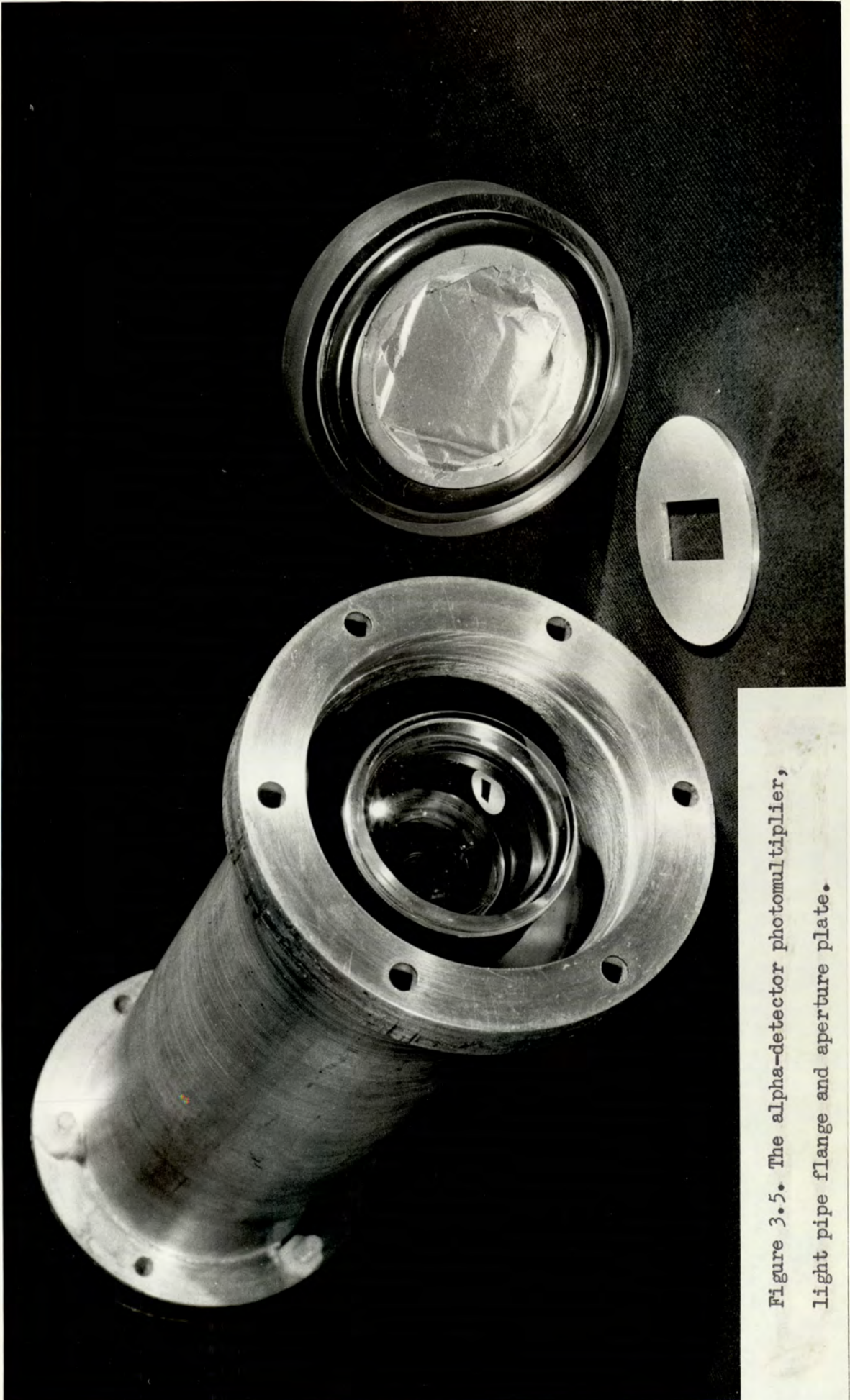


Figure 3.5. The alpha-detector photomultiplier,
light pipe flange and aperture plate.

laboratory frame of reference). The most intense part of the neutron beam was at an angle of 83° to the deuteron beam direction so the scattering sample was centred on this angle. The variation of the neutron yield with angle is discussed in detail in section 4.2.

The scattering sample was positioned so that it completely intercepted the neutron beam defined by the associated alpha-particles. As the defined neutron cone diverged from the target the required sample size depended on the neutron target to sample distance. Withdrawing the sample from the target has the advantage that the γ -ray detector can be more efficiently screened from the neutron source by the shadow bar, particularly at forward scattering angles, thus reducing the random background. A shadow bar should not only shadow the γ -ray detector, but it should also shield the throat of the collimator from the source and this requires a source to sample distance of at least 150 mm. As a compromise between efficient shielding and large sample size the scattering sample was positioned 250 mm from the target. At this distance the cross-sectional area of the neutron beam, defined by the 8° α -detector, was 68 mm high by about 50 mm wide.

The position of the sample spot 250 mm from the target at an angle of 83° to the beam was located by a positioning jig which was bolted onto the target assembly main beam tube flange. The jig had a pointer which located the sample position to within 1 mm. The target assembly was bolted to the shielding roof above the target so that the sample position was permanently fixed.

The sample stand had a steel base fixed to the laboratory floor. The sample platform was a flat brass disc 57 mm in diameter and 1.8 mm thick and it was soldered to a 25.4 mm diameter brass tube. The brass tube fitted into the steel base and the height of the sample platform was adjustable. Small brass stops were slotted into holes in the sample platform enabling the scattering sample to be replaced in exactly the

required position. Figure 3.6 shows the target assembly with a scattering sample in position.

The shielded γ -ray detector was mounted on wheels. An aluminium beam vertically below the detector and parallel to the axis of the collimator was clamped to a bearing on the base of the sample stand enabling the shielded detector to be rotated about the sample, Figure 2.7. The face of the NaI(Tl) crystal was then positioned 1.39 m from the centre of the scattering sample platform. Figure 3.7 shows a plan view, in the reaction plane, of the target, scattering sample and γ -ray detector.

Due to the limited experimental area available in the laboratory, the scattering angle range was limited to angles between 0° and 90° . The scattering angle was calibrated over this range by means of an extra attachment to the sample positioning jig. A horizontal arm was pivoted on the jig; the pivot was at the sample position. The arm was set at a given scattering angle by means of a protractor and then the collimator of the detector shield was aligned with the arm using a telescope inside the collimator. When the collimator was aligned the scattering angle was marked on the laboratory floor. In this way the detector position was calibrated from 0° to 90° .

3.2.6. Laboratory Shielding

Adequate shielding of personnel was provided from the neutron source by means of concrete shielding walls. The neutron source strength was $\sim 10^7$ neutrons s^{-1} but in the shielding considerations this was increased by a factor of five. A dose of 2.5 m rem h^{-1} is one maximum permissible level, 1 m.p.l., and this corresponds to a fast neutron flux of $10 \text{ neutrons cm}^{-2} \text{ s}^{-1}$.

The laboratory was situated in the basement of the building so that shielding from the neutron target was only required for three walls and the ceiling of the room. Figure 3.8 shows a plan view of the experimental area. Where insufficient neutron source attenuation was

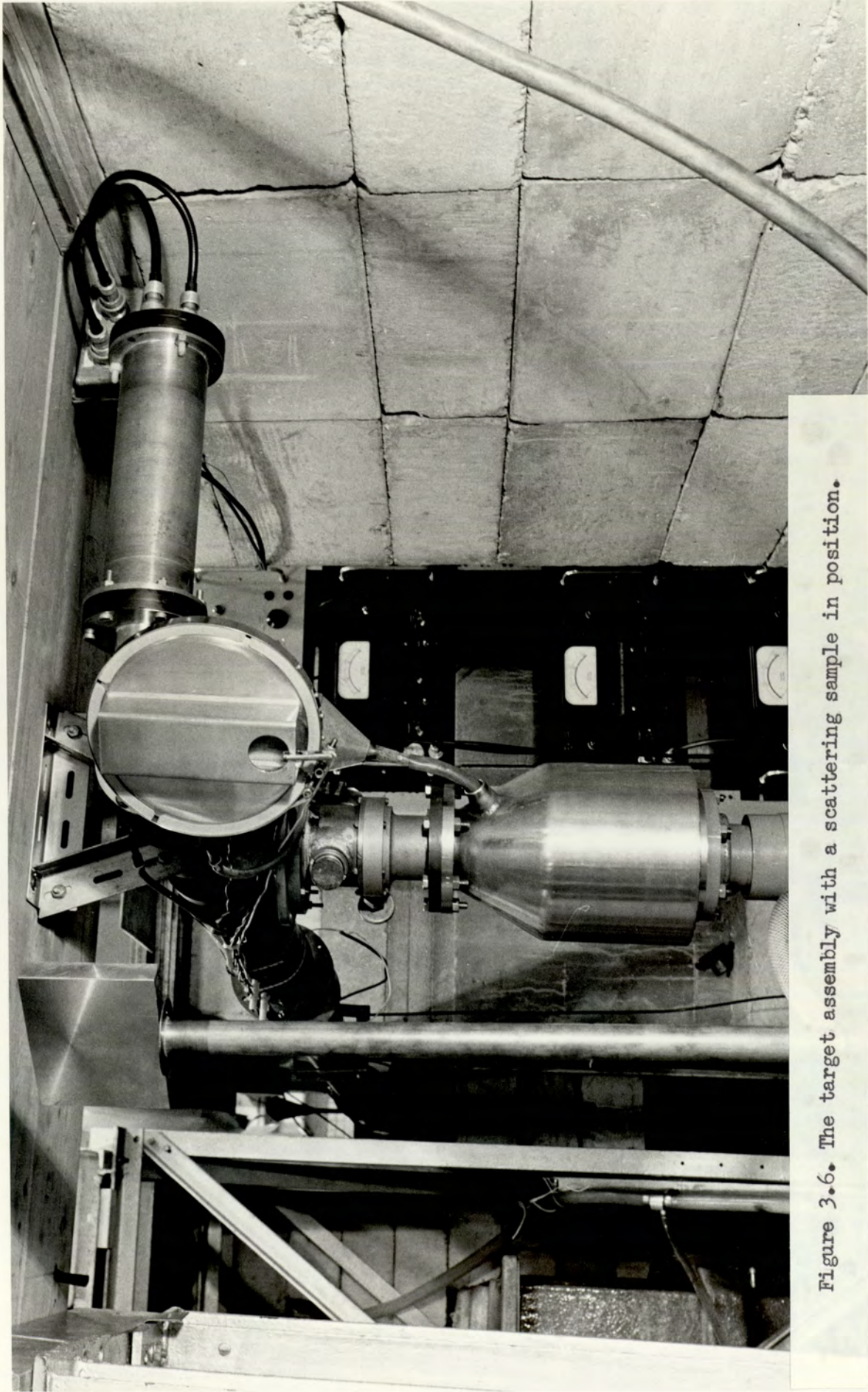


Figure 3.6. The target assembly with a scattering sample in position.

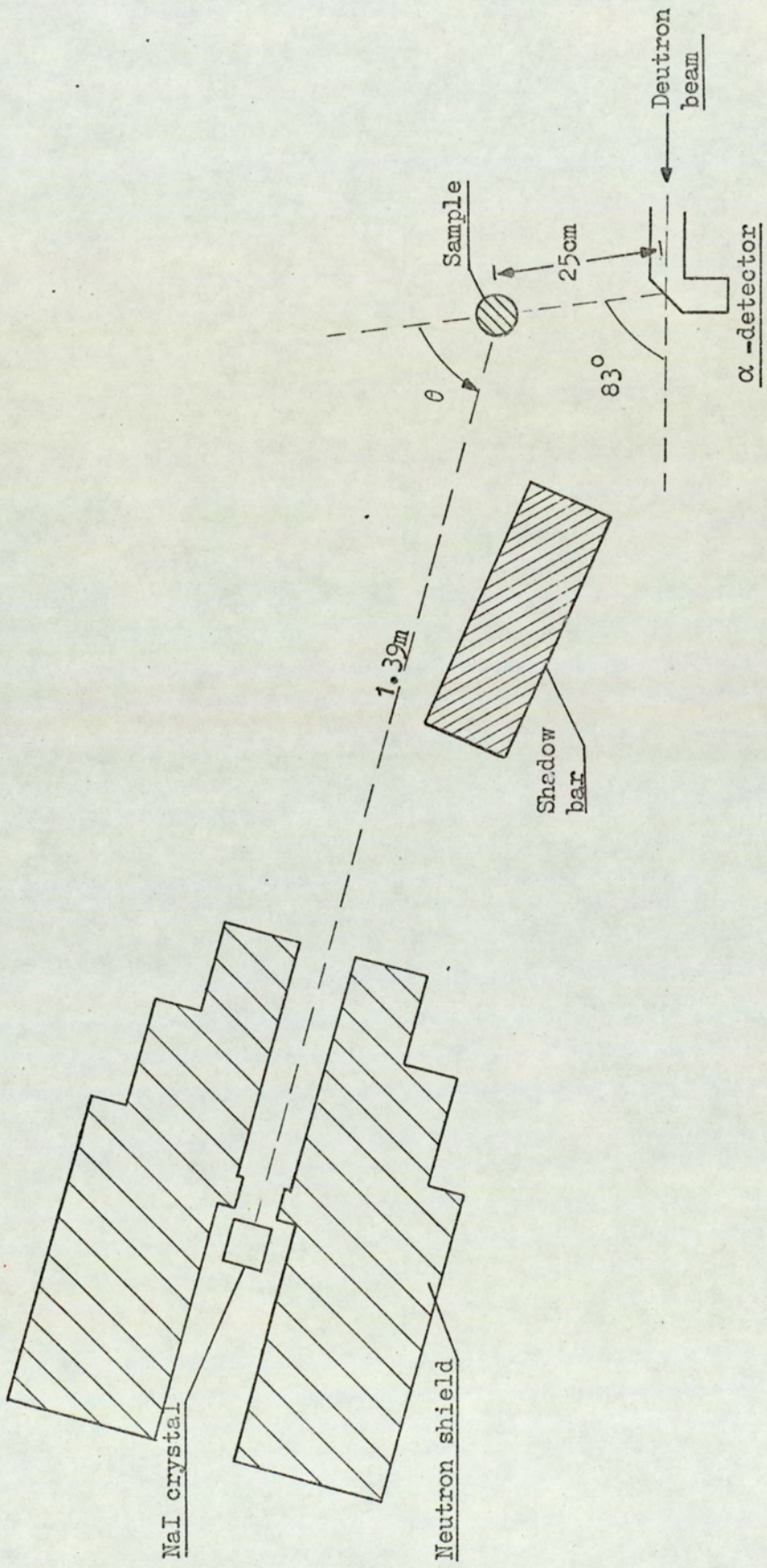


Figure 3.7. A plan view of the experimental geometry.

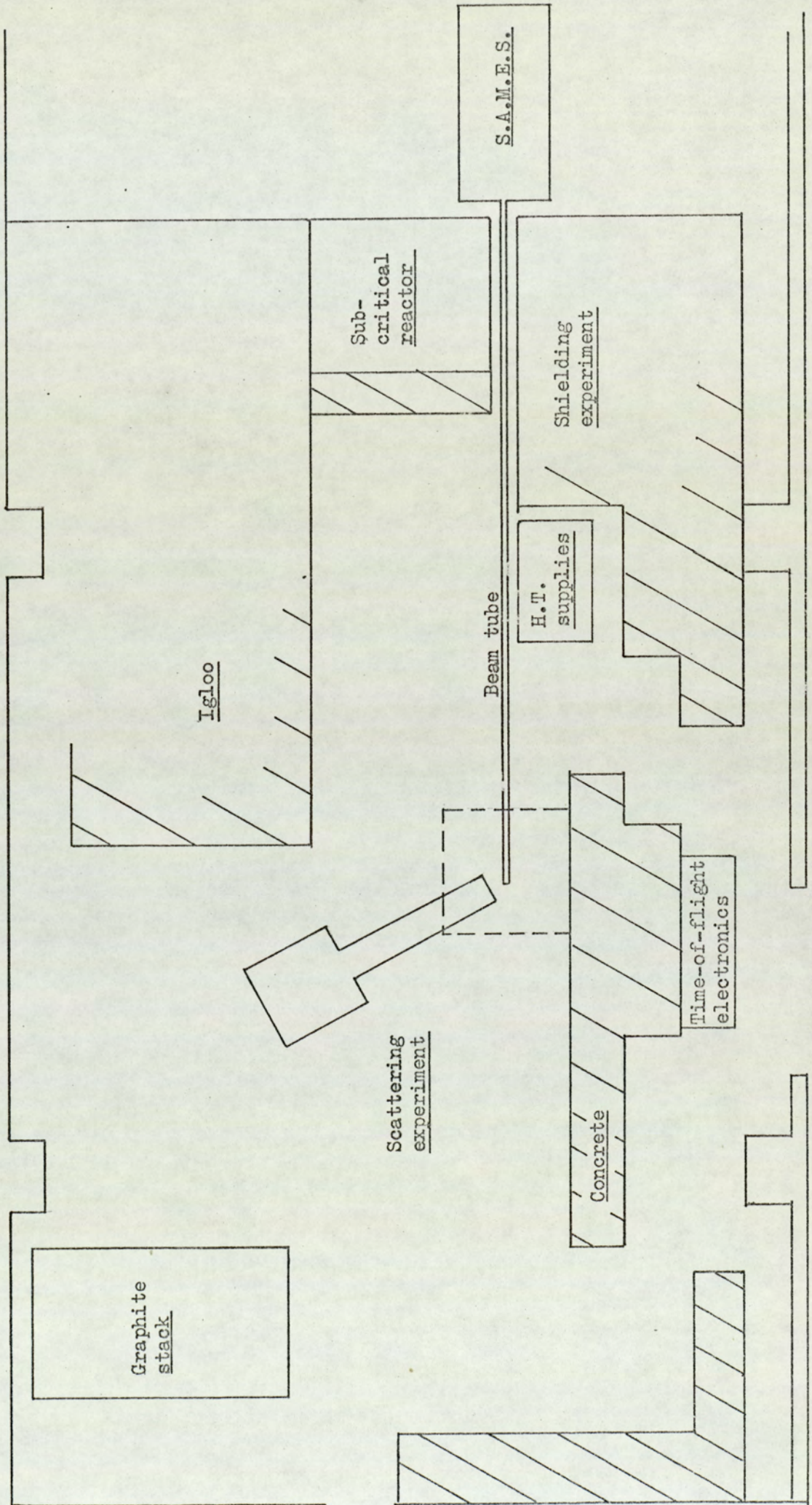


Figure 3.8. Laboratory shielding.

provided by the inverse square law walls of concrete blocks were built. These are shown in Figure 3.8. The attenuation of 14.7 MeV neutrons in concrete has been measured by Strain⁽⁶²⁾ and using his attenuation factors the shielded target flux was estimated. The maximum dose in the corridor was calculated as 0.1 m.p.l. A water tank was situated directly above the neutron target to shield the ground floor room above. The tank was filled to a depth of 0.5 m. The water provided an attenuation factor of 90,⁽⁶²⁾ and the calculated neutron level at the ceiling was 0.1 m.p.l.

Producing neutrons under normal conditions the radiation levels in the corridor and in the ground floor room above were checked with fast neutron and γ -ray monitors. In each case the monitor readings were less than 0.1 m.p.l.

3.3. Time Resolution.

The function of the electronics was to build up a spectrum of γ -ray detector events which arrived in the correct time interval after the production of a source neutron. The electronics required to do this can be divided into two parts. The first, the timing line, deals with time analysis of detector events and the second, the linear line, deals with energy analysis of events. The timing line is used to gate the linear line.

The timing line is basically a time of flight spectrometer. The most important characteristic of such a spectrometer is its time resolution. The time resolution is the factor that governs the sample to detector distance for particle time of flight discrimination. The flight path is chosen so that γ -ray and elastically scattered neutron events are completely resolved in time. Clearly, the time resolution is very important as the better the resolution the closer the detector can be placed to the sample with a consequent improvement in the signal to background ratio.

There are three factors governing time resolution, these are:

- (i) the uncertainty in the neutron production time,
- (ii) the uncertainty in the detection time, and
- (iii) the electronic resolving time.

With the associated particle method the neutron production time can be determined with a very small uncertainty. The contributing factors are the spread in the alpha-particle energies and the time resolution of the alpha detector. The important time resolution of the detector is really electronic as it is determined by the transit time spread of the photomultiplier. The γ -ray detection time is also uncertain due to the photo tube transit time spread. For scattered neutrons detected by the γ -ray detector there is a timing error due to the uncertainty in the sample to detector flight path as the detection medium has a finite thickness. An important electronic timing error known as "time walk" results in timing from the leading edge of slow rising pulses.

Figure 3.9

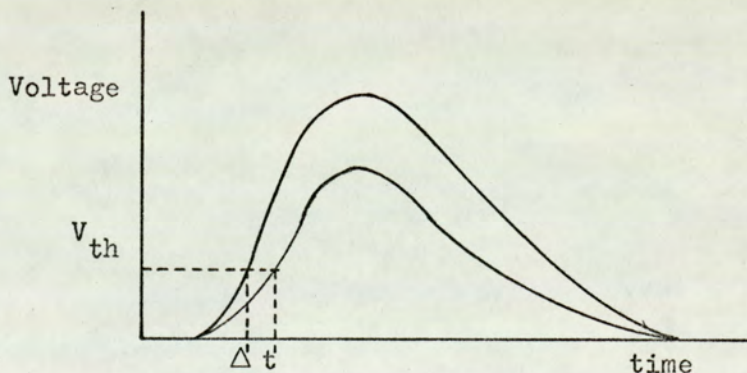


Figure 3.9 shows different amplitude pulses having otherwise identical characteristics, as say produced by a NaI(Tl) detector; if a threshold voltage V_{th} is required to trigger a timing circuit, then a time jitter or walk is introduced into the timing as illustrated.

In the present work the major timing uncertainty was due to the slow γ -ray detector pulses; the other contributions are considered for completeness. The alpha-particles at production had a small energy spread as the detector only subtended an eight degree angular range and

as the maximum deuteron energy was 140 KeV. The energy of the alpha particles at production was 3.5 MeV with an energy spread of less than 50 KeV, (section 4.2). However, alpha particles produced inside the target, by lower energy deuterons, lose energy in escaping the target and the effective alpha-particle energy range was 3.25 MeV to 3.55 MeV (section 4.2). This energy range resulted in a time spread of 0.3 ns over the 90 mm target to α -detector flight path.

The error resulting from the uncertainty in the flight path for elastically scattered 14 MeV neutrons was 1.3 ns in the 76.2 mm detector crystal.

Both photomultiplier tubes were 56 AVP's which have a stated transit time spread of 0.5 ns. Time walk of the alpha-detector pulses was negligible for two reasons. Plastic scintillator has a 2.2 ns decay time constant and the pulses produced had very sharp rise times ideal for timing from the leading edge. Secondly the dynamic pulse range was limited due to the small energy spread of the alpha-particles.

As discussed in section 2.1 the light output of NaI(Tl) has a time constant of 60 ns. and a time decay constant of 340 ns so that the output pulses necessarily had poor rise times. Typical output pulses took 150 ns to reach a maximum. Timing from these slow rising pulses was the over-riding factor in the time resolution of the system; the other terms contributed less than 1 ns to the γ -ray time resolution. The time resolution is given by the square root of the sum of the squares of the individual timing uncertainties and this is equal to the full width at half maximum height of a timing peak in a time of flight spectrum.

Several electronic techniques can be used to overcome the timing problem, but invariably the resulting time resolution is inferior to that obtained with the fast organic phosphors. Time resolutions of between 5 ns and 10 ns have been reported by several groups (14,16,41) working

with slow NaI(Tl) scintillators for use with 14 MeV to 15 MeV neutrons. The time resolution of the system built for the present work was ~ 12 ns; this is discussed in the following sections.

3.3.1. Timing with Slow Phosphors

There are basically two techniques used to overcome time walk for fast timing with slow scintillators. The techniques can be described as linear and non-linear methods.

The non-linear method is to produce a fast rising timing pulse at a time related to the first few photoelectrons emitted in a detection event. Assuming the scintillator has a single decay time constant τ , then the number of photoelectrons, Q , emitted in a time t is given by:

$$Q = N (1 - e^{-t/\tau}) \dots \dots \dots (3.1)$$

where N is the total integrated number of photoelectrons in an event.

If $t \ll \tau$, then $Q = \frac{Nt}{\tau}$

Morton⁽⁶³⁾ has shown that the standard deviation in the time of emission Q photoelectrons, $\alpha(t_Q)$, is given by

$$\alpha(t_Q) \approx \frac{\tau}{N} Q^{1/2} \dots \dots \dots (3.2)$$

A more precise calculation by Post⁽⁶⁴⁾ valid for all t , gives the standard deviation in the time of emission of Q photoelectrons as

$$\alpha(t_Q) = \frac{\tau}{N} Q^{1/2} (1 + 2(Q+1)/N \dots)^{1/2} \dots \dots \dots (3.3)$$

From equations 3.2 and 3.3 it can be seen that the resolution improves with the fewer photoelectrons, Q , required to trip the timing circuit.

In the linear method a timing pulse is produced at a time related to the centroid of the integrated photoelectron current pulse.

Using equation 3.3 the standard deviation in timing by a linear method is given by the timing error in the emission of N photoelectrons, i.e.

$$\alpha(t_N) = \tau \left(\frac{3}{N} \right)^{1/2} \dots \dots \dots (3.4)$$

Numerical evaluations of equations (3.2) and (3.4) suggested that the non-linear method gives a time resolution a factor of three superior to the linear method. This was so for cases in which up to one third of the photoelectron output was required to trigger the timing circuit.

In the present work systems employing both of these methods were developed so as to obtain the best time resolution. In the linear method the anode output pulse of the γ -ray detector photomultiplier was amplified and double delay line shaped to produce a bipolar pulse. The time of the cross-over of the pulse was independent of the pulse amplitude. The bipolar pulse was fed into a cross-over point analyser which produced a standard fast rising pulse accurately timed to the cross-over point of the input pulse. The analyser also incorporated an adjustable pulse amplitude threshold discriminator to reduce the dynamic range of the input pulses. With this method the resolution in terms of the full width at half maximum height of a γ -ray timing peak was 25 ns discriminating off γ -rays below 1 MeV.

The basic principle of the non-linear method employed was to differentiate the photomultiplier output pulse and then amplify the differentiated pulse to produce a fast rising pulse. The amplifier didn't behave in a linear manner but produced a fast timing pulse whose leading edge was related in time to the first few photoelectrons of a detection event. To reduce the dynamic pulse range lower energy γ -ray pulses were discriminated off by a second slow timing circuit. By using a separate circuit for event discrimination the problem of time walk with

the fast timing pulses was reduced. This system is known as the "fast-slow coincidence method". The non-linear method had a resolution a factor of two better than the linear method, i.e. ~ 12 ns, and so the non-linear method was used and it is described in detail in the following section.

3.4. The Electronics

The two parts of the electronics arrangement, the timing line and the energy analysis line are described.

3.4.1. The Time of Flight Electronics

Figure 3.10 shows a block circuit diagram of the time of flight electronics employing a fast-slow coincidence system. The overall operation of the system is briefly outlined before the circuits are described.

The anode pulses of the α -particle and γ -ray photomultipliers were fed into long coaxial cables via emitter follower circuits. Both signals then passed through discriminators and the suitably shaped pulses were fed into a slow coincidence gating circuit with a coincidence time of approximately 400 ns. If an α -pulse was in coincidence with a γ -ray pulse, then the α -pulse provided the stop signal to the time to pulse height converter. The start signal for the time to pulse height converter came from the 14th dynode of the γ -ray photomultiplier, the time walk problem being reduced by the "fast" amplifier. The output pulses of the time converter were fed into a multichannel pulse height analyser to build up a time of flight spectrum.

The Photomultiplier Dynode Chains

The 56 AVP is a high gain photomultiplier tube, with a current gain of 10^8 , capable of producing peak anode currents up to 1A. The manufacturers state that to achieve a stability of 1% the ratio of the current through the voltage divider chain to that through the heaviest loaded part of the tube should be 100:1. For moderate intensities of

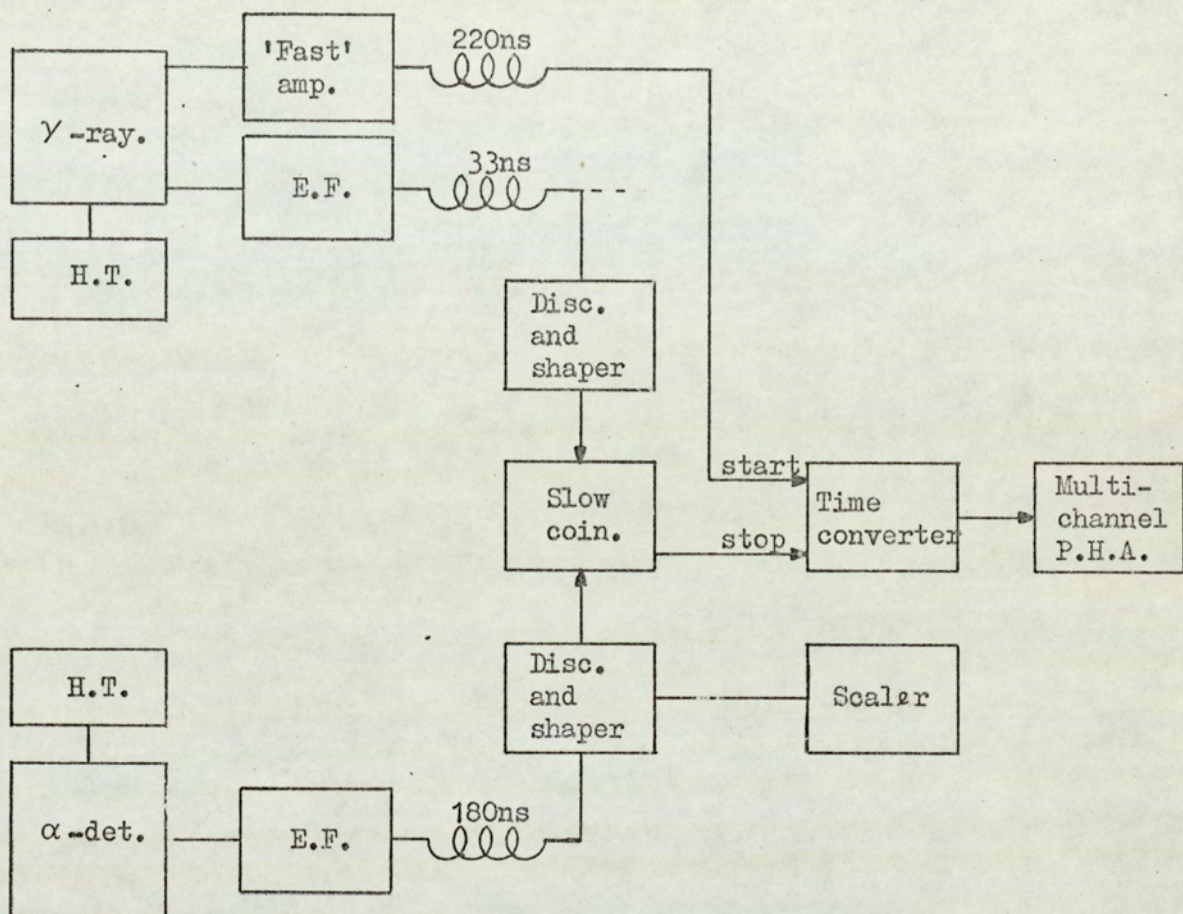


Figure 3.10. Block diagram of the time-of-flight system.

radiation this requires a dynode chain current of 3 mA. Dynode chain currents of 6mA though have been used by Gupta and Nath⁽⁶⁵⁾ and Cernigoi⁽⁶⁶⁾.

The manufacturers recommend two voltage divider chains; type (i) has an equal voltage across the last twelve dynode stages and type (ii) has progressively increasing voltages across the last nine dynode stages. Voltage divider type (i) gives a higher gain, but a higher anode current with better time characteristics can be obtained with divider type(ii). Divider (ii) reduces space charge effects around the latter dynodes. The last dynodes are decoupled with capacitors to stabilize the dynode potentials.

A dynode chain of type (ii) was used for the γ -ray detector. The resistor chain is shown in Figure 3.11(a). Focused tubes are more sensitive to fluctuations of individual dynode potentials than unfocused tubes, so high stability 1 watt metal oxide resistors were used. The current through the dynode chain was 3 mA at an operating voltage of 2kV. A current of 3mA was the maximum current delivered by the H.T. unit, Isotope Developments type 1617A, used. The capacitors used to decouple the last dynode stages are shown in the figure. The manufacturers recommend a value for the capacitor across the last stage given by

$$C_1 = 100q \sqrt{\frac{V}{30}}$$

where q is the quantity of charge transported by the anode and V is the voltage across the tube. Capacitors across earlier stages decrease by a factor of 3 at each stage. For the maximum output signals a value of $C_1 = 0.1 \mu f$ was calculated as being more than adequate.

As shown two output signals were taken from the γ -ray detector photomultiplier. The linear signal for energy analysis and for the slow coincidence circuit was taken off the anode. With the anode output

circuit shown, γ -rays of energies up to 5 MeV produced output signals of up to -4 V amplitude. The output pulse length was 1μ s with a rise time of approximately 0.1μ s. A positive going timing pulse was obtained by inserting a resistor between the 14^{th} dynode and the dynode chain. The output resistor and capacitor were chosen to have a small RC time constant; the values were 470Ω and 22 pf. The differentiated timing pulses were a factor of 3 down on the amplitude of the anode pulses but had rise times of 40 ns.

The α -detector photomultiplier dynode chain was of type (i). The dynode chain is shown in Figure 3.11(b). The dynode chain current was 3 mA at the normal operating voltage of 1900 V. A single output was taken from the anode across a 680Ω load resistor. The output pulses for 3.5 MeV α -particles had an amplitude of -4 V and the pulse duration was 100 ns with a rise time of 10 ns.

Detector Preamplifiers

The γ -ray detector linear signal fed both the slow coincidence circuit and the main amplifier of the linear circuit. The main electronics were removed from the experimental area as shown in Figure 3.8. Approximately 7 m of coaxial cable was required to reach the electronics from the detector. To avoid reflections in this long cable the anode signals were matched into the cable via an emitter follower at the base of the photomultiplier. The single transistor emitter follower circuit is shown in Figure 3.12. The negative anode signal was applied to the base of the pnp transistor, with an input impedance of $\sim 10K \Omega$. The current amplified signal appeared across the 100Ω load resistor with unity voltage gain. The output impedance of the circuit was $\sim 50 \Omega$, and matched the negative pulses into the 70Ω impedance coaxial cable. The coaxial cable introduced a time delay of 33 ns and when the cable was correctly terminated no distortions or reflections were observed.

The α -detector photomultiplier signal was matched into a

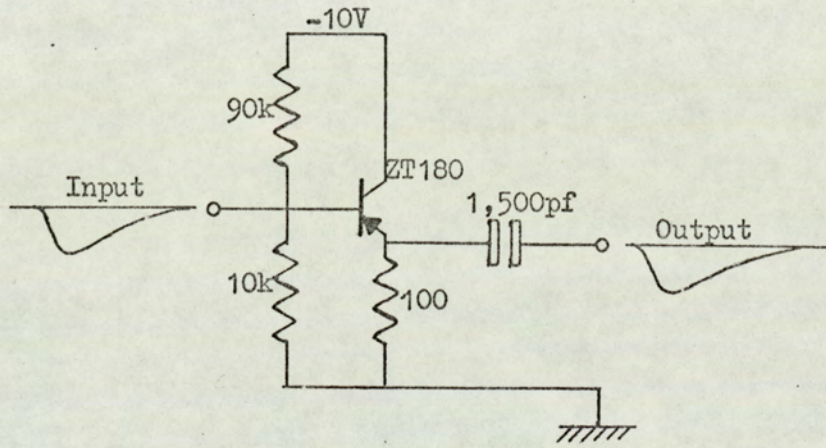


Figure 3.12. Gamma-ray photomultiplier anode pulse emitter follower.

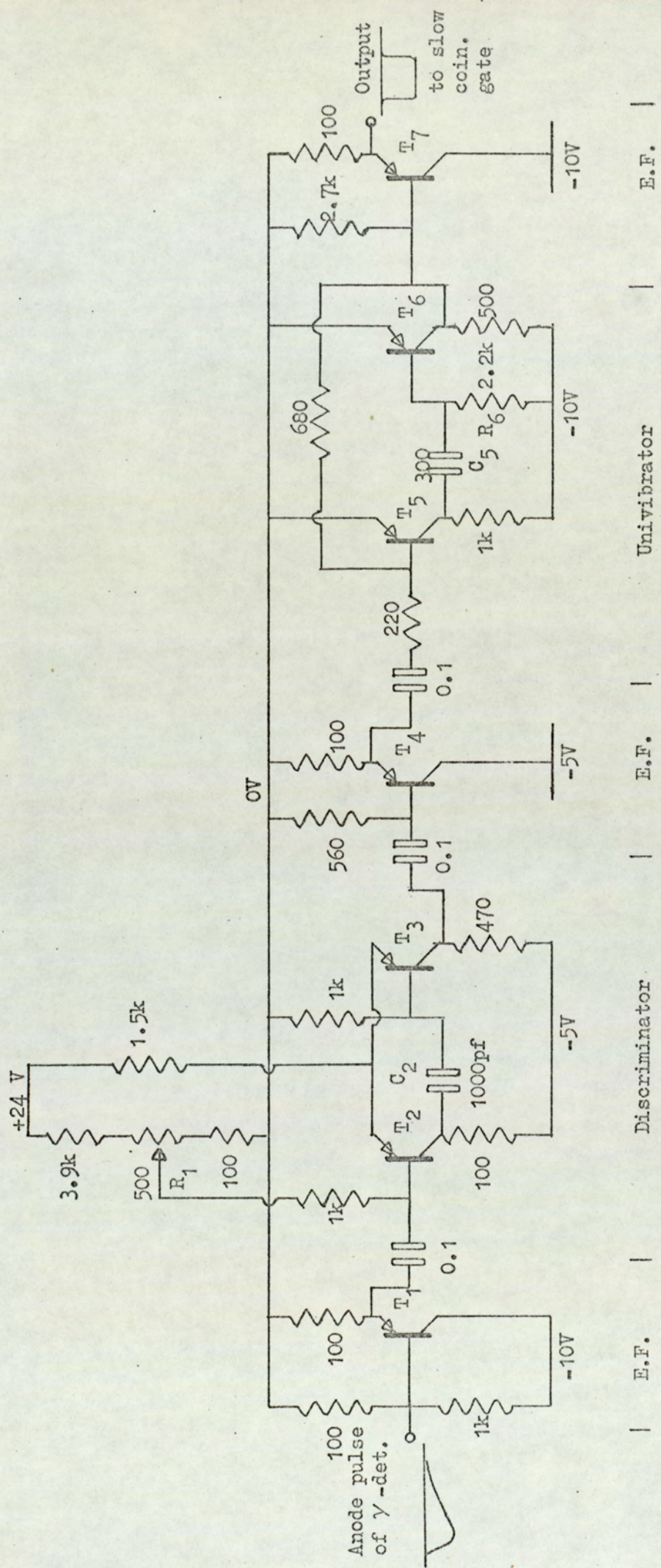
long coaxial cable by a similar emitter follower circuit. The cable was 35 m long and had a delay of 180 ns, but to increase the delay by 40 ns fixed lengths of cable were switched in series with the main cable.

The γ -ray Discriminator and Pulse Shaper

The 33 ns γ -ray delay cable fed both the linear amplifier for γ -ray energy analysis and the discriminator. Figure 3.13 shows the circuit diagram of the discriminator and pulse shaper.

Transistor T_1 , Figure 3.13, formed an emitter follower, with an input impedance of about 100Ω so that the long feeding cable was correctly terminated. The purpose of the emitter follower was to isolate the discriminator from the linear amplifier which had a parallel input. Transistors T_2 and T_3 formed the discriminator. The circuit was an a.c. coupled Schmitt trigger with the base of T_2 held slightly positive by the bias supplied through the variable resistor R_1 , which controlled the discrimination level. T_2 was normally non-conducting and T_3 was conducting. When a negative pulse of sufficient amplitude was applied to the base of T_2 it conducted. A positive pulse was then produced at the collector of T_2 which through the a.c. coupling of C_2 reduced the conduction current of T_3 . This caused more current to be taken by T_2 so the circuit regeneratively switched over to the state of T_2 conducting and T_3 non-conducting. The circuit remained in this condition until the amplitude of the input pulse fell below the hysteresis level. A *positive* going pulse was produced at the collector of T_2 with a 3V amplitude and 20 ns rise time; the pulse length was a function of the input pulse amplitude. The discriminator output was fed into the pulse shaping circuit via an emitter follower which isolated feedback from the pulse shaping circuit to the discriminator.

A standard timing pulse was produced by the monostable multivibrator, transistors T_5 and T_6 . T_5 was biased normally non-conducting and T_6 was biased fully conducting. The negative going



Transistors T₁, T₄, T₅, T₆, T₇ are type ZT180.
 Transistors T₂, T₃ are type BSX29.

Figure 3.13. The gamma-ray pulse discriminator and pulse shaper.

discriminator pulse applied to the base of T_5 switched T_5 on producing a positive pulse at the collector of T_5 . The collector pulse of T_5 was coupled to the base of T_6 via the capacitor C_5 giving a negative going pulse at the collector of T_6 . The duration of the output pulse was determined by the RC of the coupling stage C_5 and R_6 . The RC time constant was 660 ns and produced a standard 500 ns duration output pulse, i.e. independent of the input pulse. The amplitude of the output pulse was -4 V with a 20 ns rise time.

The output stage was an emitter follower, transistor T_7 , with an output impedance of less than 100 Ω .

α - Discriminator and Pulse Shaper

The α -particle pulse discriminator circuit was identical to the one used for the γ -ray pulses. The discriminator introduced negligible time walk in the α -detector pulses.

Two outputs were taken from the discriminator; one to provide a suitably shaped pulse for the coincidence gate and the other to provide the scalar pulse. Figure 3.14 shows the pulse shaping circuits fed by the α -discriminator output. The coincidence gate pulse was first shaped by a monostable multivibrator, transistors T_1 and T_2 . The monostable was as described in the γ -ray line except that the feedback resistor from the collector of T_2 to the base of T_1 was increased to 2.2 K Ω . This increased the amplitude of the output pulse to -10 V. After passing through an emitter follower, T_3 , the large negative going pulse was sharply differentiated. The differentiation time constant was 0.2 ns. This produced a negative going spike 3 V in amplitude and 50 ns long. The positive spike resulting from the differentiation of the trailing edge of the square pulse was less than 1 V due to the slower fall time of the input pulse.

The second α -discriminator output pulse was shaped to feed the scalar monitor. The discriminator pulses were too large for the scalar

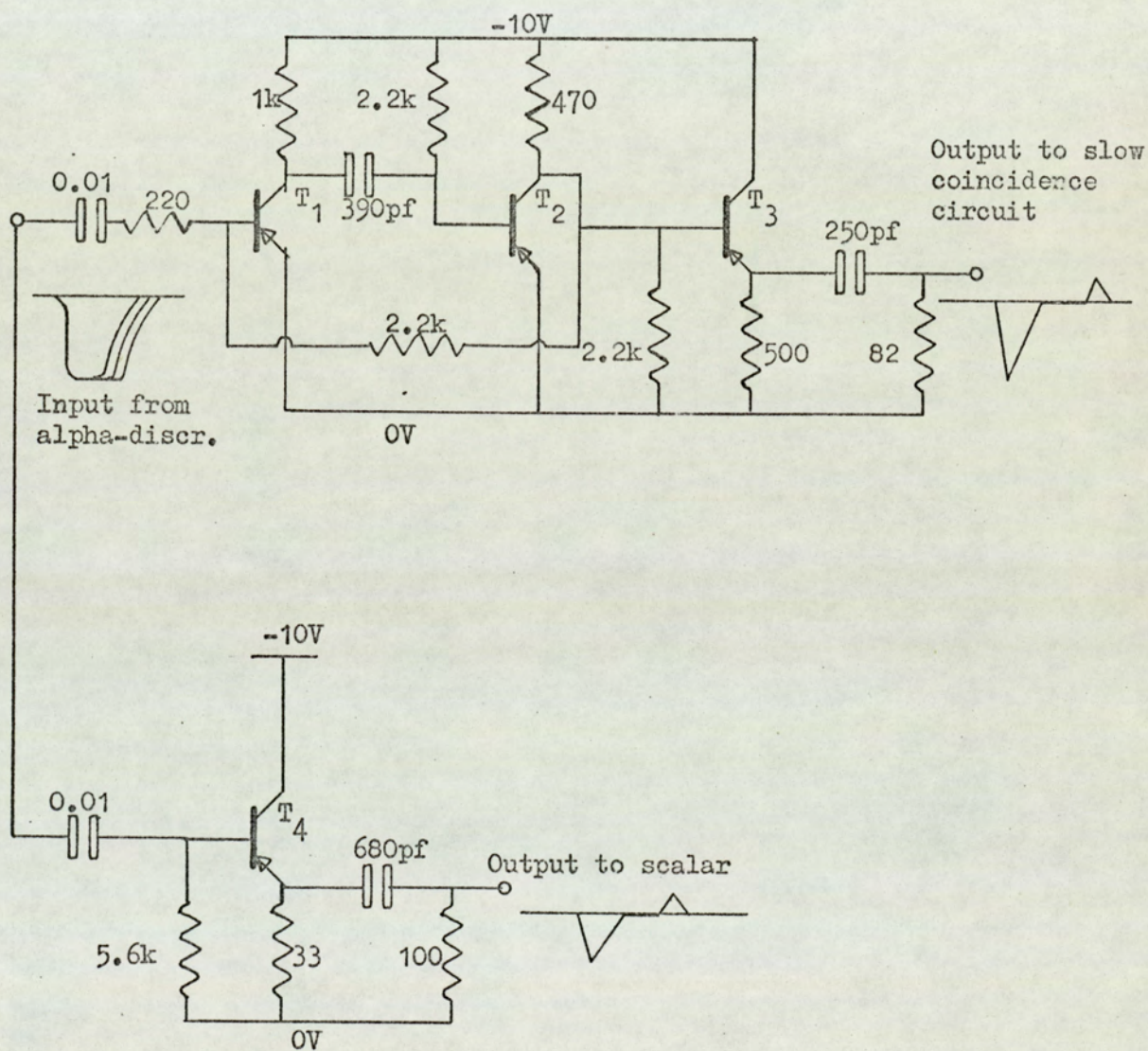


Figure 3.14. The alpha-particle pulse shaping.

which required negative pulses of between 2 V and 4 V amplitude. The discriminator pulses were isolated by the emitter follower T_4 and differentiated to produce short pulses of 2 V amplitude. Only the negative pulses triggered the scalar which was a Nuclear Enterprises, NE 5078, eight decade counter.

The Slow Coincidence Gate

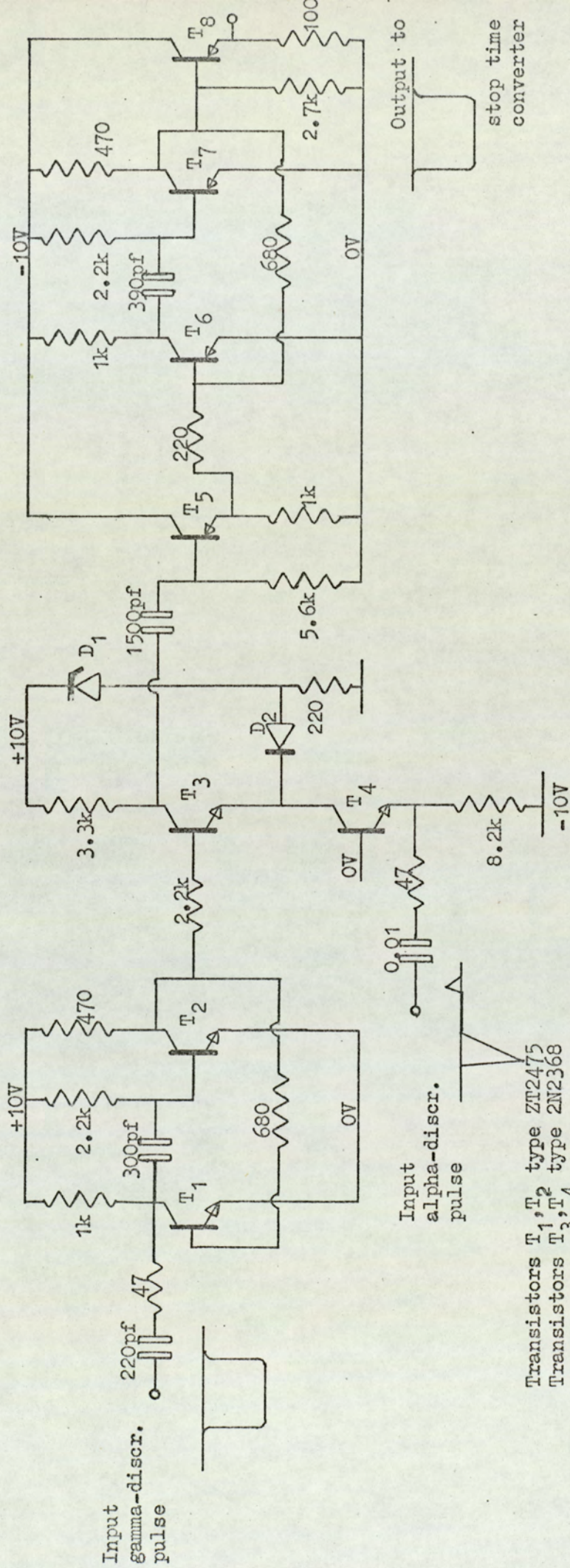
The coincidence gating circuit is shown in Figure 3.15. Essentially the γ -ray pulse was used to gate the α -detector pulse. The gating circuit comprising transistors T_3 and T_4 was designed by Oliver et al⁽⁶⁷⁾.

Transistors T_1 and T_2 formed a monostable multivibrator which inverted the negative input pulse. T_1 was biased non-conducting and T_2 was fully on so that the collector voltage of T_2 was zero volts. A negative γ -ray input pulse applied to the collector of T_1 caused T_1 to conduct and switched T_2 off producing a fast rising positive going pulse of 6 V amplitude at the collector of T_2 with a duration of 400 ns. This provided the gating pulse through a 2.2 K Ω resistor to the base of T_3 . Thus, for the duration of the gating pulse, the base of T_3 was raised to a potential of 5.5 volts.

The α -particle pulses were matched into the grounded base transistor T_4 causing it to saturate, i.e. only for the negative going spike. These produced short negative pulses of 1½ V amplitude at the collector of T_4 (which was the emitter of T_3).

Transistor T_3 was operated as a series gate. With the base of T_3 at +5 V the gate was open and with a zero base potential the gate was closed. An amplified 6 V negative spike was only obtained at the collector of T_3 if the α -particle and γ -ray pulses were coincident. The 400 ns coincidence time was defined by the relatively long γ -ray gating pulse.

The gate output fired the output monostable which produced a



- Transistors T₁, T₂ type ZT2475
- Transistors T₃, T₄ type 2N2368
- Transistors T₅, T₆, T₇, T₈ type ZT180
- Diode D₁ type BZY96C8
- Diode D₂ type FD100

Figure 3.15. The slow coincidence gate.

standard timing pulse, -4 V amplitude with a 10 ns rise time and 0.5 μ s duration. This was the stop pulse for the time to pulse height converter.

The gate output pulse was accurately timed to the α -particle detection event, as the time walk in the γ -ray gating pulse did not alter the time output of a coincident α -pulse. A most important point was to ensure that for two related α -particle and γ -ray pulses the γ -ray gating pulse arrived at the gate before the α -pulse.

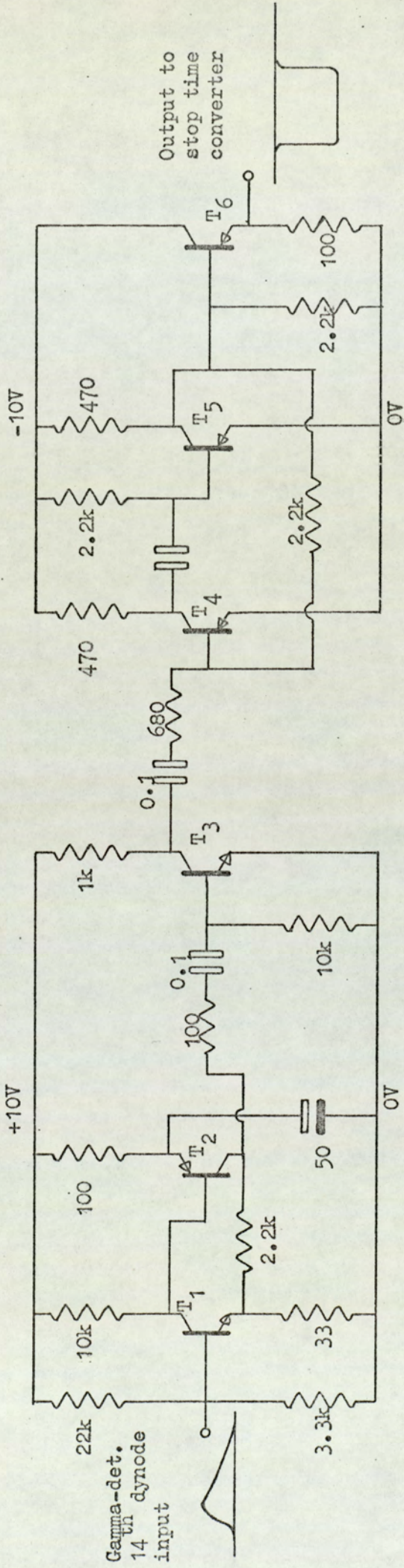
An added advantage in using the coincidence gate was that it blocked the high repetition rate of the α -pulses from the time converter input.

The "Fast" Amplifier and Pulse Shaper

Figure 3.16 shows the amplifier and pulse shaping circuit used for the fast timing pulses taken off the 14^{th} dynode of the γ -ray detector phototube. The circuit was housed at the base of the photomultiplier so that a minimum length of cable was required to feed the pulses to the circuit.

The amplifier had two stages of amplification. The first stage consisted of transistors T_1 and T_2 . The positive input signal was fed onto the base of T_1 and an amplified positive going pulse was produced at the collector of T_2 . A 3 V maximum output pulse was produced at the collector of T_2 for a 0.5 MeV γ -ray input pulse. The pulse was inverted by the common emitter amplifier, T_3 . Again this stage operated in a non-linear manner producing a negative going saturation pulse of 4 V amplitude, with a rise time of 20 ns and a duration of approximately 300 ns.

The fast timing pulse had to be delayed while the corresponding slow pulse passed through the discriminator and coincidence gating stages. The pulse was delayed by a 40 m length of 70 Ω coaxial cable. A standard fast timing pulse was produced to feed into the long delay cable



Transistors T₁, T₃ type 2N2368
 Transistors T₂, T₄, T₅, T₆ type ZT180

Figure 3.16. 'Fast' amplifier and pulse shaper.

by the monostable multivibrator, transistors T_4 and T_5 . The standard pulse had an amplitude of -4 V, a 20 ns rise time and a 500 ns pulse length. The pulse was matched into the cable via an emitter follower, T_6 , with a 50Ω output impedance. The coaxial cable introduced a delay of 220 ns before feeding the signal into the start input of the time converter.

The Time to Amplitude Converter

Short time intervals can be measured by converting them into quantities more readily measured using conventional techniques. The time converter generates an output pulse whose amplitude is proportional to the time interval between start and stop input pulses allowing measurements to be made in the nanosecond range. The basic principle of operation is as follows: When a start input pulse is applied a capacitor starts to charge from a constant current source and when a stop pulse arrives the charging is halted. Thus the voltage across the capacitor is proportional to the time interval between the arrival of the start and stop input pulses. The output pulses of the time converter may then be analysed by a single or multichannel analyser giving a spectrum directly related to the original time intervals being measured.

The time converter used was a Nuclear Enterprises type NE 6250. The shaping of the start and stop input pulses was carefully designed to meet the input specifications of the time converter. The input impedance of both inputs was $1 \text{ K}\Omega$. The start input pulse was fed through 40 m of 70Ω cable from a low output impedance source. The $1 \text{ K}\Omega$ input impedance of the time converter caused a reflection in the cable due to the poor termination. However, ideal matching was achieved if an 82Ω resistor was put in parallel with the time converter input. 82Ω resistors were used across both the start and stop inputs.

The time converter output pulse range was 0 to +10 V and corresponded to time ranges of 0 to 50, 100, 200, 500 or 1000 ns as set

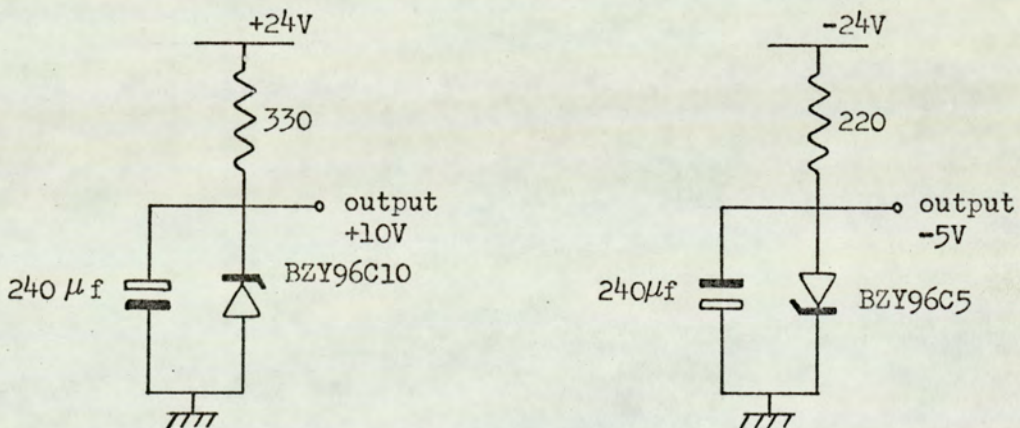
by the range switch. Timing was from the leading edge of the input pulses. In the absence of a stop input pulse, after a start signal, the instrument automatically reset itself with no output pulse being produced.

To obtain a time of flight spectrum the 0 to +10 V time converter output pulses were analysed by a 100 channel pulse height analyser, a T.M.C. Gammascopie II.

The Low Voltage Power Supplies

Two Nuclear Enterprises low voltage supplies, type NE 5383 were used, each having a +24 V and a -24 V output giving a maximum current of 1A from each output.

The five and ten volt low voltage supplies, required for the circuits described above were produced with Zener diodes from the 24 volt supplies. The circuits were as follows:



The maximum output from the 10 V supply was 40 mA and from the 5 V supply was 95 mA. In all 4 ten volt Zener diodes and 2 five volt diodes were required. Smoothing capacitors, $16\mu f$, were used across the voltage rails of the circuits as the supply unit was separate from the circuit units. These capacitors were found to improve the shape of the timing pulses.

3.4.2. The γ -ray Energy Analysis Electronics

A block circuit diagram of the complete electronics, including the linear line, is shown in Figure 3.17. The γ -ray photomultiplier

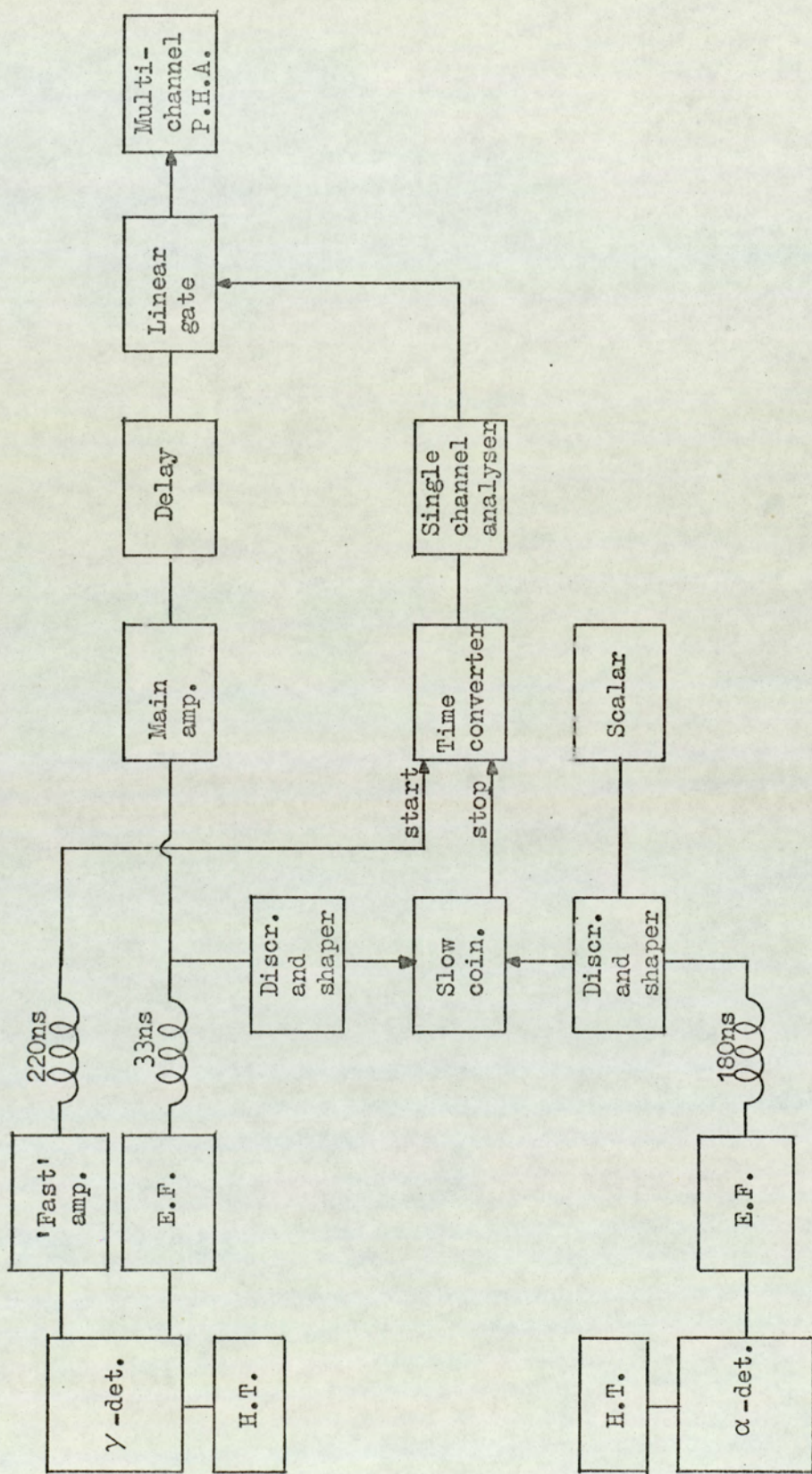


Figure 3.17. Block diagram of the full electronic system.

anode pulses were shaped by the main amplifier and fed, via a delay unit and a linear gate, to a multichannel analyser to build up a pulse height spectrum. The gating pulse, which opened the linear gate, came from a single channel analyser set to view the correct time interval of the time of flight spectrum.

The Main Amplifier

The main γ -ray pulse amplifier was a Nuclear Enterprises type NE 5259. It had a parallel input with the γ -ray discriminator. The amplifier was used in a double differentiation mode of operation, with $1 \mu s$ time constants. The gain was set to give pulses with the positive cycle of the bipolar pulses up to 10 V and the duration of the positive half of the pulse was $1 \mu s$.

The Delay Unit and Linear Gate

While the time analysis of an event was being made in the time of flight circuits the linear γ -ray signal was delayed by a Nuclear Enterprises delay unit, type NE 5262. The signal was delayed without distortion or loss of amplitude and the delay time was adjustable in $0.7 \mu s$ steps up to a maximum of $2.1 \mu s$. A delay unit was used in preference to a length of coaxial cable for two reasons. Firstly, to produce a delay of $2.1 \mu s$ 450 m of cable is required and secondly, the output impedance of the main amplifier, 500Ω , was too high to match the signal into the cable without distorting the signal.

The delayed signal was fed into the linear gate, type NE 5730. The gate was normally closed and it was opened with a gating signal from the single channel analyser. The gate open time could be set at 1, 2, 5 or $10 \mu s$. Normally the delay unit was set at $2.1 \mu s$ and the gate open time was $5 \mu s$. The gate output was fed into the 100 channel pulse height analyser.

The Single Channel Analyser

The single channel analyser, type NE 5159C, was used in a

differential mode of operation. Upper and lower voltage levels were set so that the analyser only gave an output signal for time converter pulses with amplitudes inside this voltage window. The window was set to correspond to the γ -ray peak in a time of flight spectrum, i.e. to the time interval in which the γ -ray events arrived. The negative analyser output pulse provided the gating signal for the linear gate. In this way the pulse height analyser input was gated so that it only received pulses meeting the timing requirements.

The Nuclear Enterprises, Edinburgh series units used in the linear line were compatible, so there was no difficulty with pulse matching particularly as short cables were used between the units. The data accumulated by the multichannel analyser was printed out on paper tape. Figure 3.18 shows the rack mounted time of flight and energy analysis electronics.

3.5. The Electronic Setting up Procedure

Discriminators:

The spectra of both the γ -ray and α -particle detectors were displayed on the multichannel analyser by suitably shaping the pulses with the main amplifier. To check the discriminator setting for both detectors the apparatus was arranged as shown in Figure 3.19. The negative discriminator output pulses provided suitable gating pulses for the linear gate. With the apparatus arranged as shown, the pulses below the discriminator level were blocked from the multichannel analyser.

Figure 3.20 shows a pulse height spectrum of 3.5 MeV

α -particles produced in the deuteron bombardment of the target. The discriminator level as determined by the above method is shown in the figure.

Linearity of Timing System:

To check the time linearity of the time converter and that the slow coincidence circuit was functioning correctly, the following

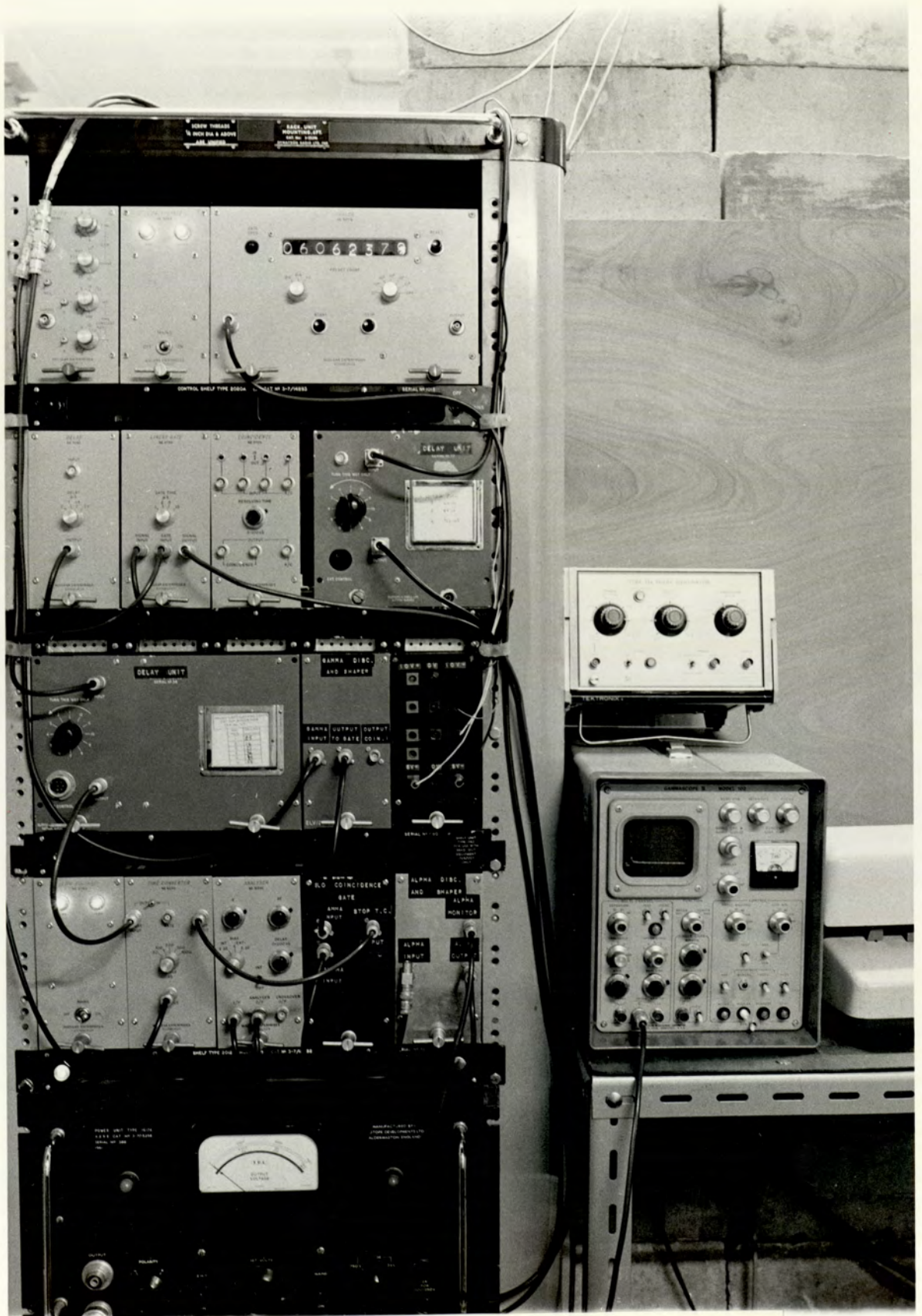


Figure 3.18. The electronics arrangement.

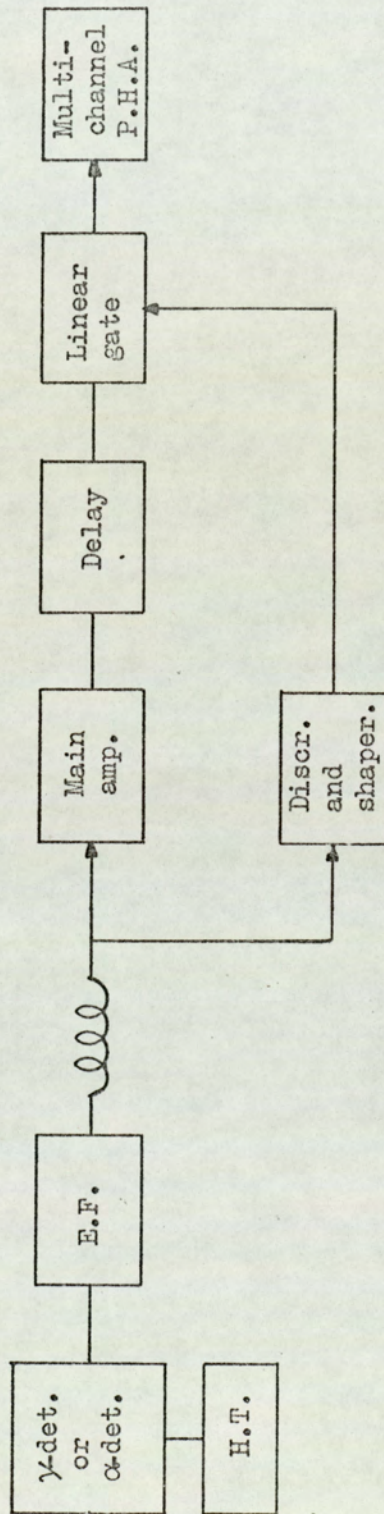


Figure 3.19. Block diagram of the discriminator setting procedure.

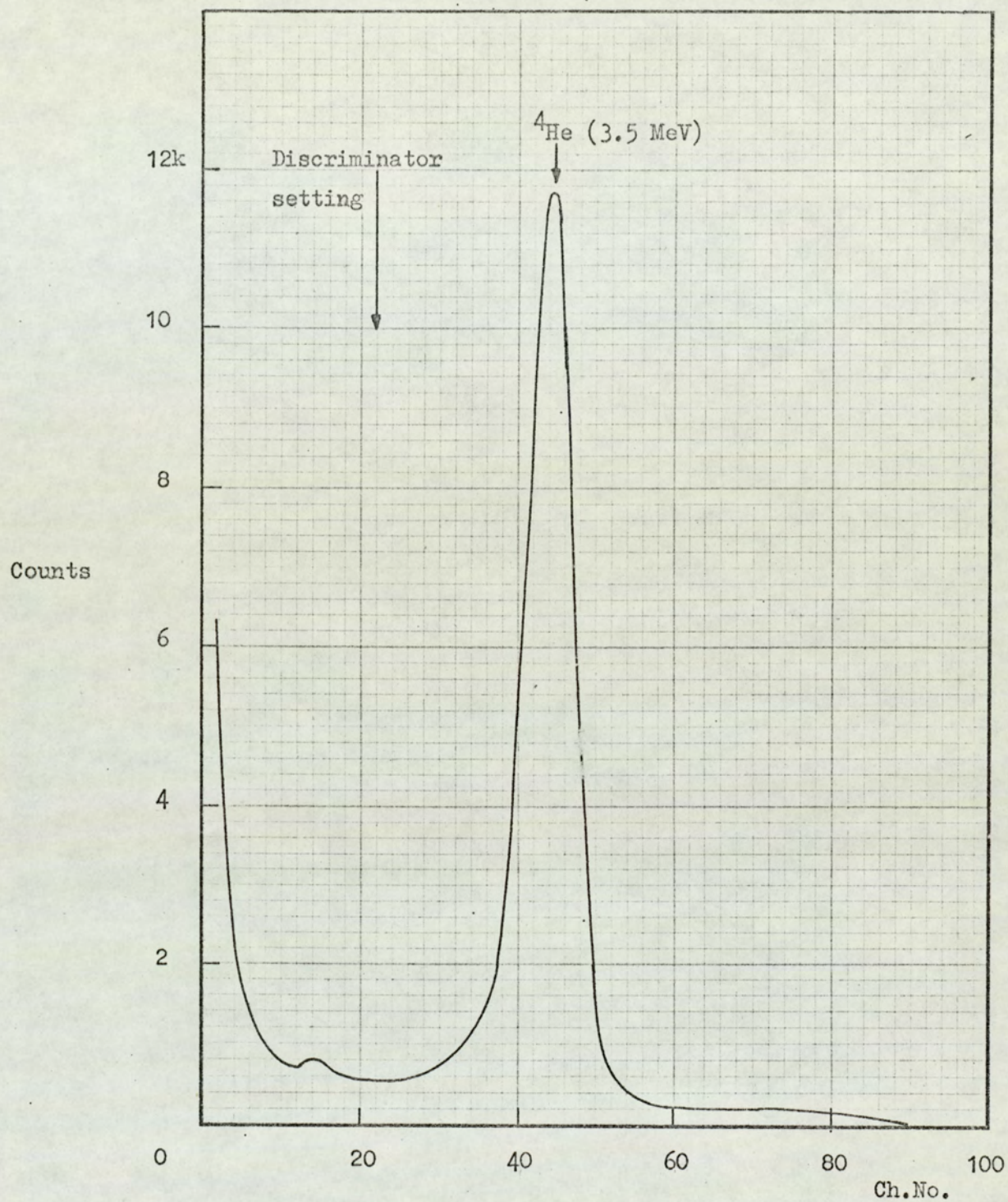


Figure 3.20. The alpha-particle pulse height spectrum from the ${}^3\text{H}(\text{d},\text{n}){}^4\text{He}$ reaction.

experiment was carried out. A random time spectrum was accumulated in the multichannel analyser using a pulse generator and a ^{60}Co γ -ray source with the apparatus arranged as shown in Figure 3.21. The two signals, from the pulse generator and the γ -ray detector, were randomly related in time so that an equal number of counts should be stored in each channel of the analyser, all channels having equal width. Figure 3.22 shows the random time spectrum obtained. The pulse generator was set at 100 KHz s^{-1} and the time converter was set on the 200 ns range so that each channel of the analyser represented 2 ns time duration. The start of the slow coincidence gate plateau was in channel number eight; for lower channels the generator pulses arrived when the gate of the coincidence circuit was closed. The total length of the gate plateau was 400 ns, but only the first half could be displayed by the multichannel analyser with the time converter range used. There was poor time linearity for the first 25 ns after the start of the coincidence gate. The region used is shown in the figure and in this region the maximum differential timing non-linearity was $\pm 3.5\%$, corrected for the statistical error. The manufacturers stated maximum differential non-linearities in the time converter of $\pm 2\%$ and in the pulse height analyser of $\pm 2\%$. Using these values the differential timing non-linearity of the coincidence circuit was calculated as $\pm 2\%$. For the present application, the linearity in the region used was very satisfactory.

Delay Lines:

The delay time of the γ -ray discriminator pulse was set by the minimum length of cable required to reach the electronics from the detector. As mentioned above it was important that the α -detector pulse reached the slow coincidence unit after the corresponding γ -ray gating pulse. To find the delay required in the α -detector line to meet this requirement the apparatus was arranged as shown in Figure 3.21 except that the pulse generator was replaced by the normal α -detector

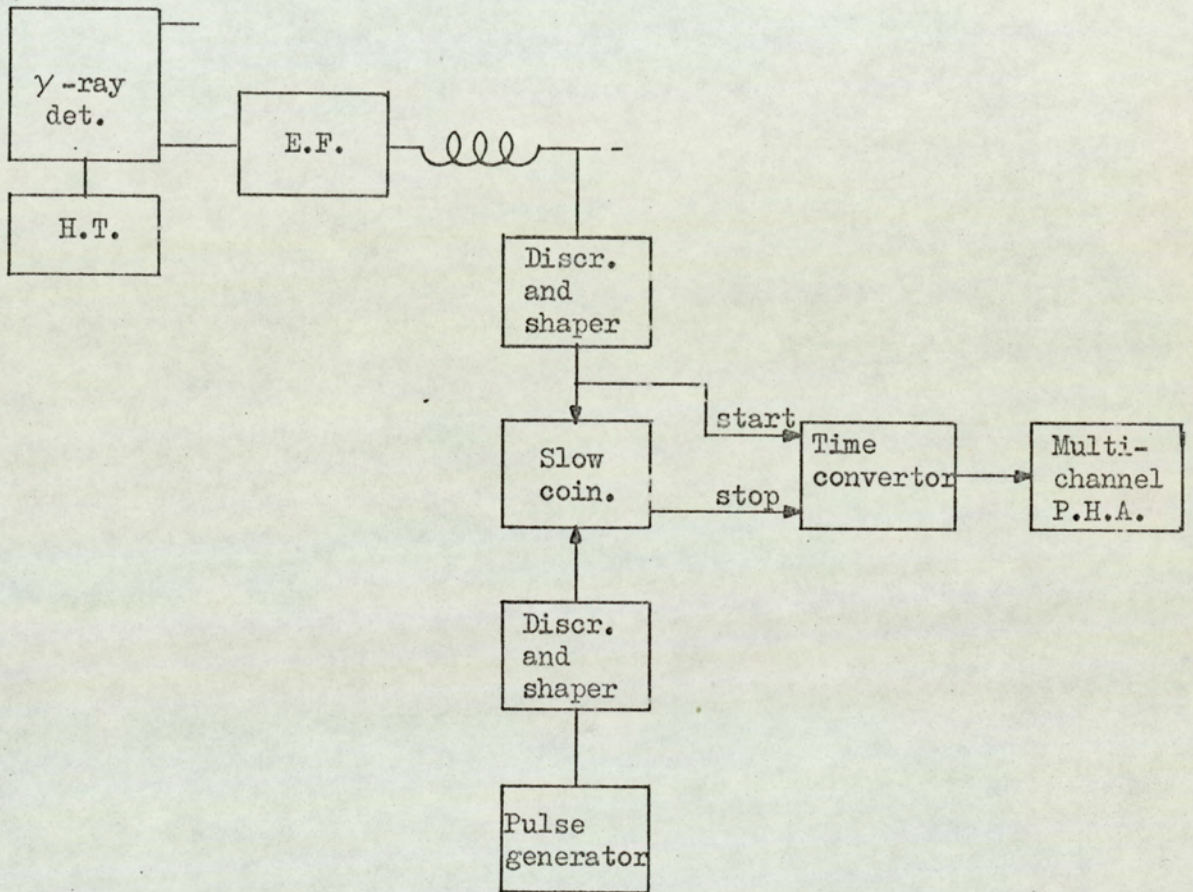


Figure 3.21. Block diagram for testing the time linearity of the system.

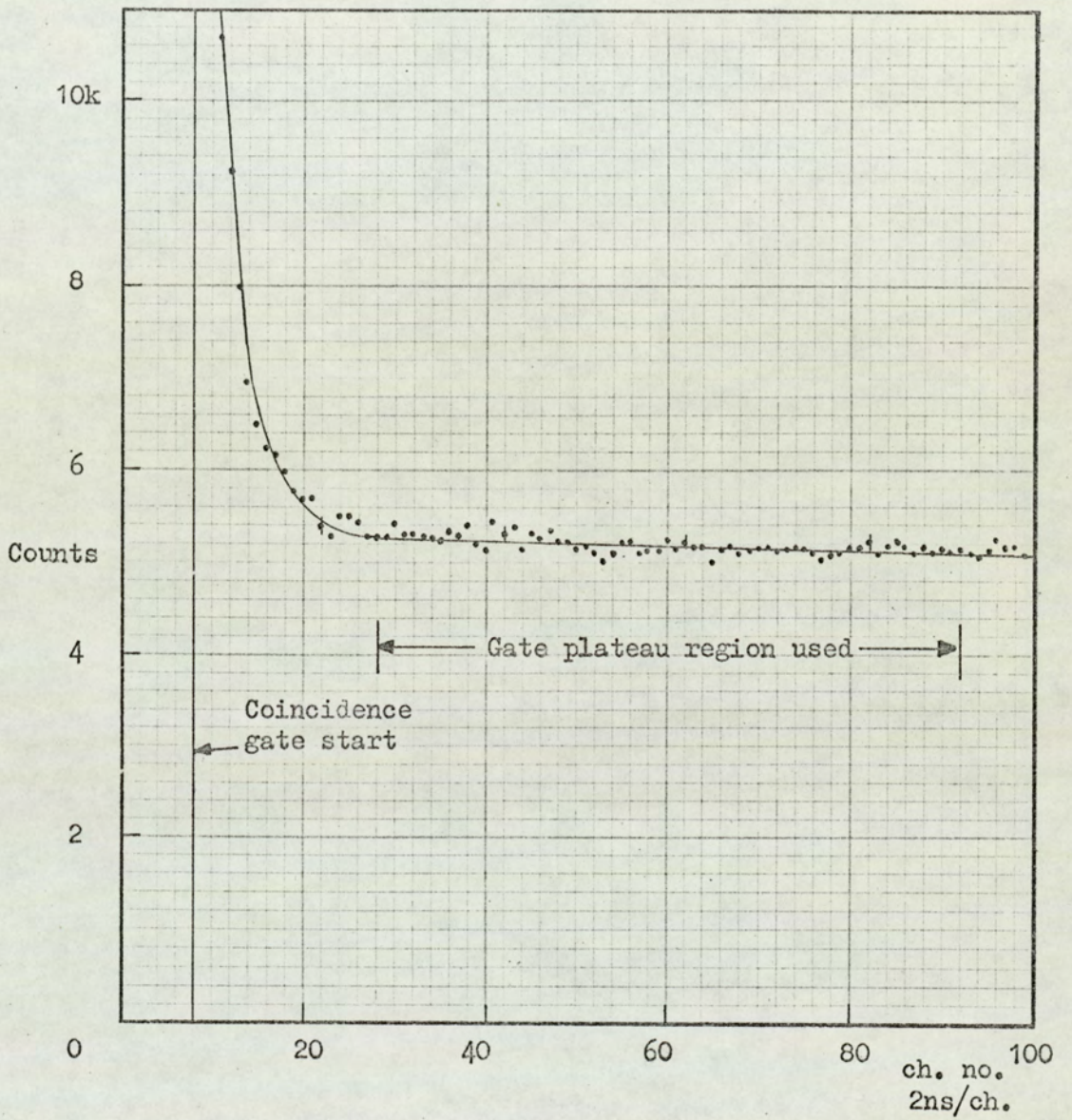


Figure 3.22. A random pulse time spectrum to test the differential timing linearity of the system.

input. Figure 3.23 shows a time of flight spectrum taken with this arrangement. For this spectrum the γ -ray detector was positioned at a 25° scattering angle viewing a titanium scattering sample. The γ -ray discriminator was set at 0.7 MeV. The spectrum shows the unresolved γ -ray and scattered neutron events from the sample. The delay in the α -line was adjusted, by altering the length of coaxial cable, until the spectrum was accumulated in the right pulse height region of the multichannel analyser. The poor resolution was of course due to the walk of the γ -ray pulses.

The γ -ray delay cable in the fast timing line, see Figure 3.10 was similarly set by displaying the time of flight spectrum on the multichannel analyser. With too short a cable in the fast timing line there was a long time separation between the start and stop pulses, this was displayed by using the time converter on the $1\mu s$ range.

Finally the delay of the NE 5262 delay unit was set at $2.1\mu s$. This delayed the linear signal more than the time required by the time converter and the single channel analyser to complete the time analysis. The manufacturers stated a delay in the time converter of $1.1\mu s$ (after the start input pulse) and the delay in the single channel analyser was measured as $0.7\mu s$. Thus the linear gate was opened by the timing pulse several hundred nanoseconds before the linear signal arrived at the gate, which was opened for $5\mu s$.

3.6. Time of Flight Spectra

A time of flight spectrum using the fast-slow coincidence system (Figure 3.10) was always observed to set up the single channel analyser prior to any cross-section measurement.

Figures 3.24(a) to 3.24(d) show typical time of flight spectra accumulated with different γ -ray discriminator settings with scattering samples of carbon, sulphur and titanium. The spectra shown were observed at a forward scattering angle, 25° , to show an intense neutron

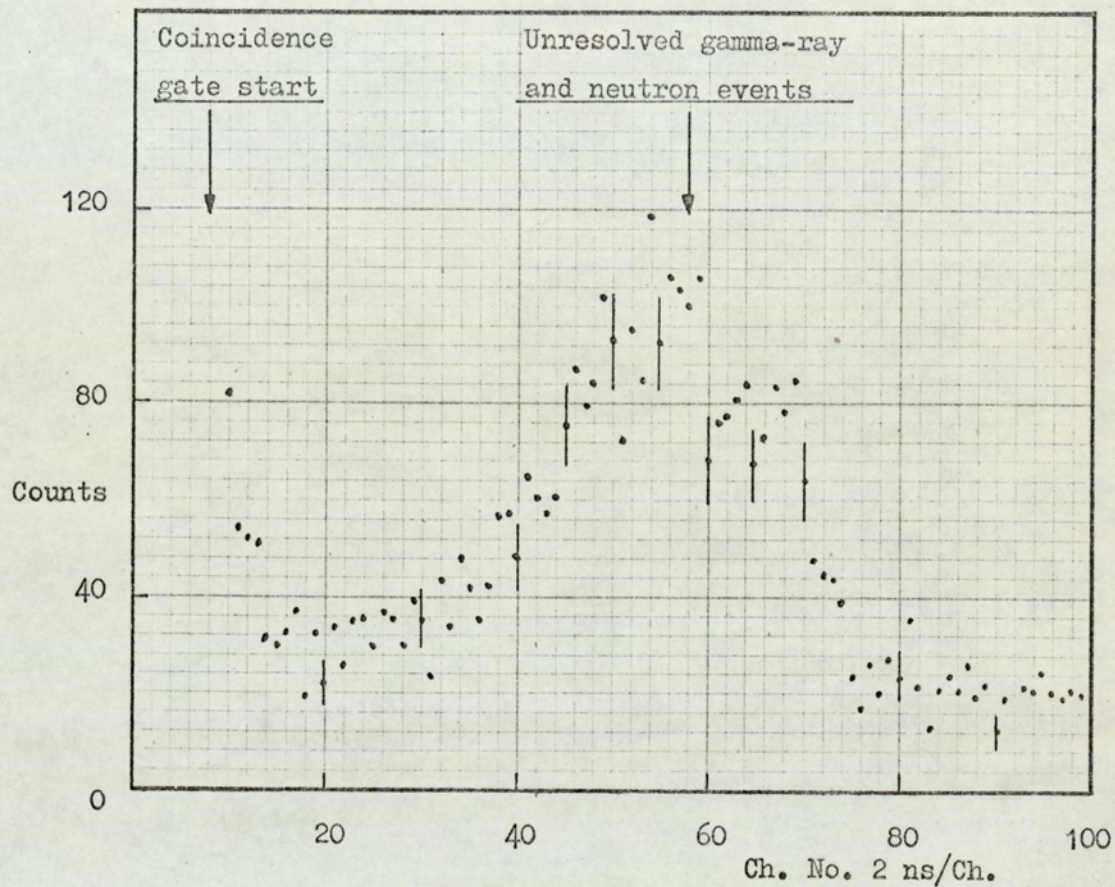
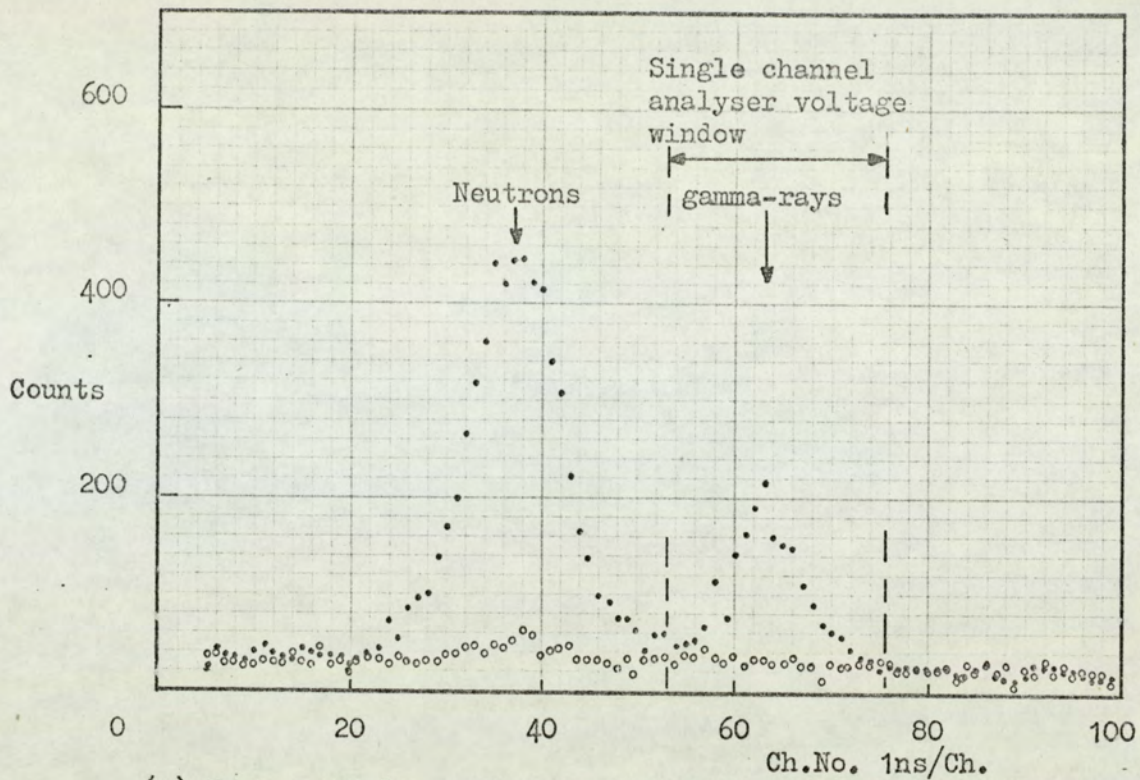
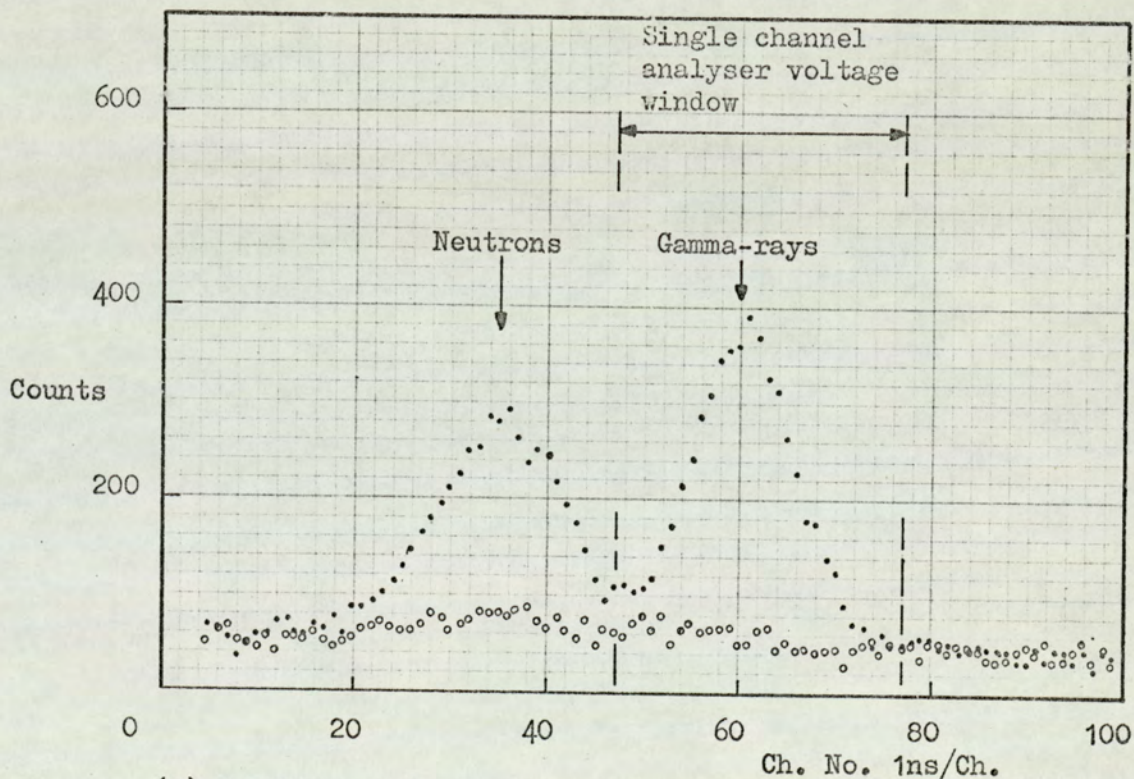


Figure 3.23. Time-of-flight spectrum with a Ti sample at a 25° scattering angle without the fast-slow system.

Gamma-ray discrimination level 0.7 MeV.



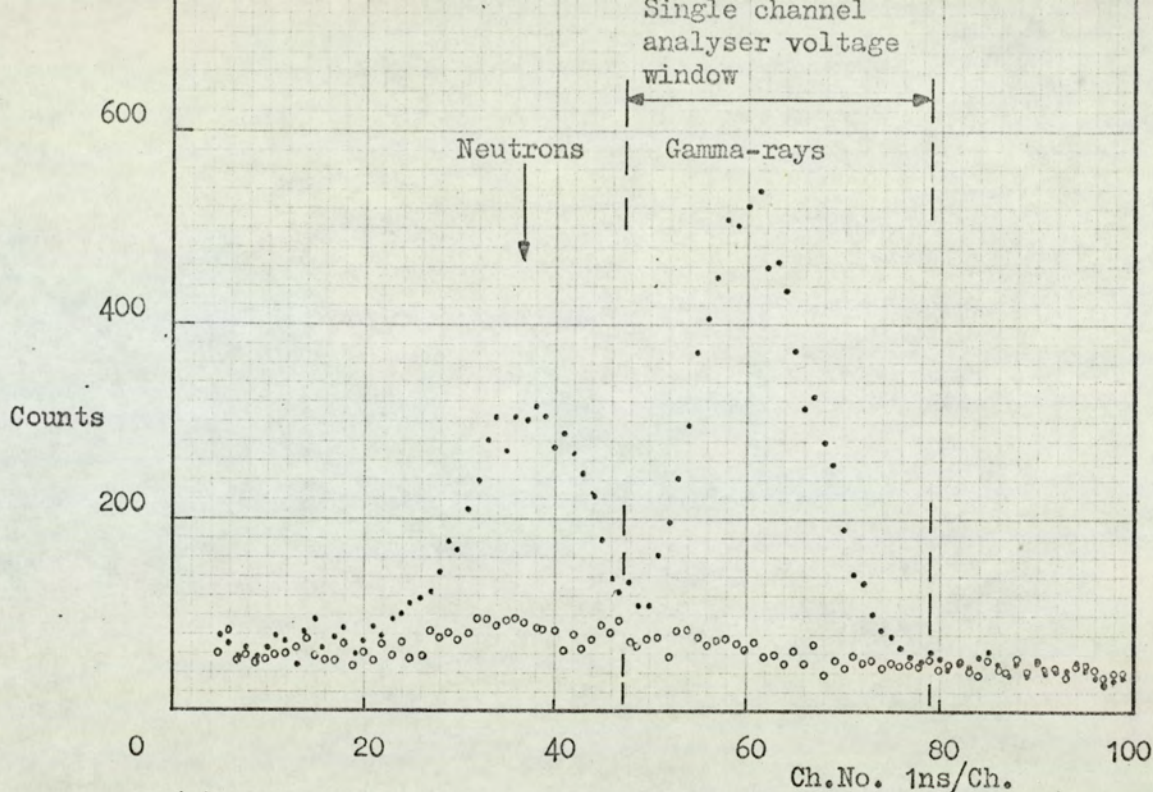
(a) Carbon sample, gamma-ray discrimination level 1.4 MeV.



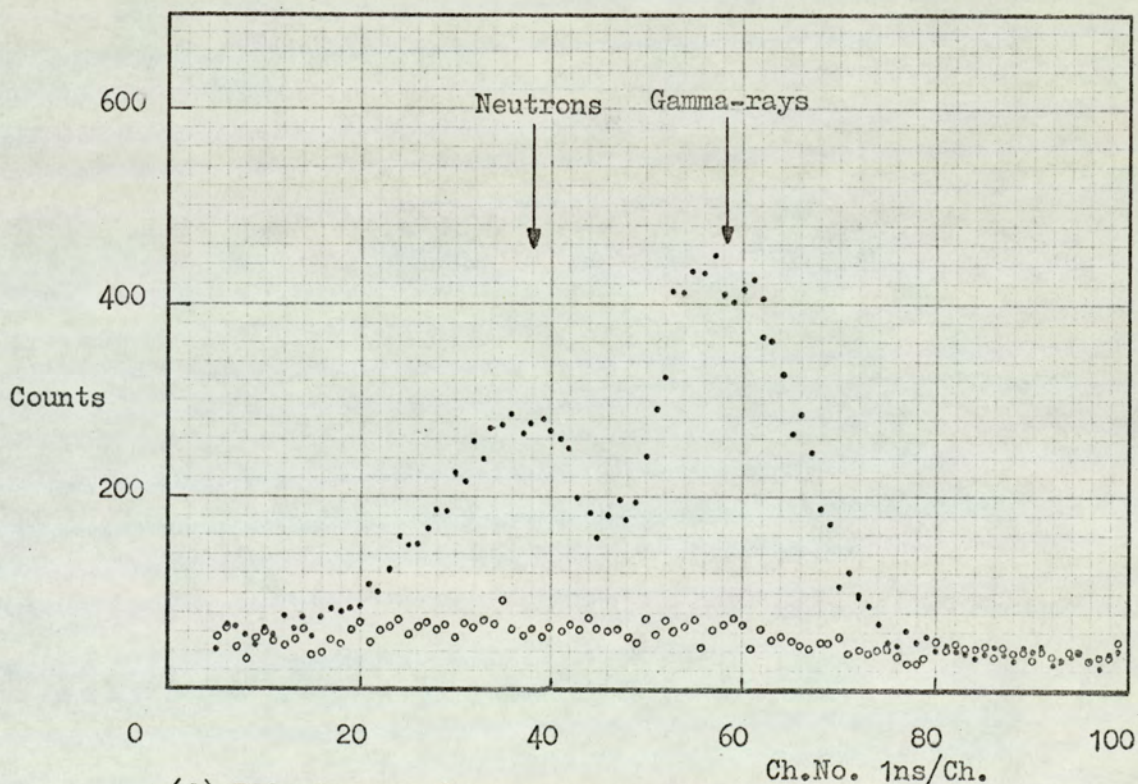
(b) Sulphur sample, gamma-ray discrimination level 1.0 MeV.

Figure 3.24. Time-of-flight spectra (scattering angle 25°).

- Scattering sample in.
- Background with sample removed.



(c) Titanium sample, gamma-ray discriminator level 0.7 MeV.



(d) Titanium sample, gamma-ray discriminator level 0.5 MeV.

Figure 3.24 cont. Time-of-flight spectra (scattering angle 25°)

- Scattering sample in.
- Background with sample removed.

peak as elastic neutron scattering is very forward peaked. Time increases from right to left of the spectra because the γ -ray detector pulse was used to start the time converter. The time converter was on the 100 ns range so one channel interval of the analyser represented 1 ns. The spectra clearly show two peaks, one corresponding to scattered neutron events and the other corresponding to the γ -rays produced in neutron reactions. The two peaks of events produced by the scattering sample sit on a random background spectrum. For each of the spectra shown a background spectrum was accumulated with the scattering sample removed and this is also plotted. The sample in and the sample out spectra were accumulated for the same integrated neutron yield as determined by the α -monitor. The peak identification was confirmed by observing the time shift of the peaks when the flight path was increased by a metre, as the γ -ray peak moves by only 3.3 ns and the neutron peak moves by 19 ns. This also served as a test of the time interval per channel of the analyser.

Figures 3.24 (a-d) show that the time resolution improved as the dynamic γ -ray pulse range was reduced by increasing the discriminator level. Table 3.1 shows the time resolution of the γ -ray peak in terms of the full width at half maximum height for different γ -ray discriminator levels.

Table 3.1

γ -ray discriminator level	Resolution F.W.H.M.
1.4 MeV	7 ns
1.0 MeV	11.5 ns
0.7 MeV	13.5 ns
0.5 MeV	17.0 ns

The 1.39 m flight path was sufficient to completely resolve the γ -ray and scattered neutron peaks with a γ -ray discrimination level of 0.7 MeV, though with a discrimination level of 0.5 MeV the peaks were

just resolved and the spectrometer could certainly be used at this discrimination level. The majority of counts in the neutron peak were due to elastically scattered neutrons because at larger scattering angles the neutron event peak became very small, i.e. consistent with the sharp fall off of the differential elastic cross-section with scattering angle.

The voltage window of the single channel analyser was set as shown on the time of flight spectra. The analyser voltage levels could be set to within a single channel. With the single channel analyser window set as shown, the signal to background ratio was about 4:1, though this value depended on the sample size and the reaction cross-section for the sample, the geometrical factors being fixed. The time taken to accumulate each spectrum was approximately five hours, i.e. 2½ h with the sample in and 2½ h for the background with the sample removed.

No time instability in the time spectrum was observed. Provided the conditions were not altered, for example by altering a discriminator level, the time peaks were consistently reproduced in the same position over a period of several months.

3.7. Gamma-Ray Energy Analysis

3.7.1. Spectrometer Calibration

The γ -ray energy range of interest was from 0.5 MeV to about 5 MeV. The spectrometer had, therefore, to be calibrated over this energy range.

Long lived isotopic sources emitting γ -rays of known energies gave useful calibration energies up to 1.3 MeV. The sources used had activities of $1\ \mu\text{Ci}$. The sources and the γ -ray energies are listed below.

<u>Source</u>	<u>Energy of γ-ray</u>
^{137}Cs	0.662 MeV
^{54}Mn	0.835 MeV
^{60}Co	1.173 MeV
	1.332 MeV
^{22}Na	0.511 MeV
	1.28 MeV

For calibration points at higher energies three γ -ray lines at 1.78, 2.75 and 4.43 MeV were used. The two lower energy γ -rays were obtained from ^{28}Al and ^{24}Na respectively, produced by the irradiation of samples of silicon and magnesium with 14 MeV neutrons. The $^{28}\text{Si}(n,p)^{28}\text{Al}$ reaction has a large cross-section 260 mb for 14 MeV neutrons. ^{28}Al is unstable with a half life of 2.3 min and it decays by β^- emission to the first excited level of ^{28}Si producing a single 1.78 MeV γ -ray. So a 5 min irradiation of a few grains of silicon produced a strong source of 1.78 MeV γ -rays.

The 2.75 MeV line was produced by irradiating magnesium rods with 14 MeV neutrons producing ^{24}Na by the $^{24}\text{Mg}(n,p)^{24}\text{Na}$ reaction. The reaction has a cross-section of 175 mb and ^{24}Na has a 15 h half life. With the laboratory's Van de Graff accelerator which could produce a neutron flux in excess of 10^9 neutrons s^{-1} a calibration source was produced with a sample irradiation of about 2 h. The ^{24}Na isotope decays by β^- emission to the second level of ^{24}Mg giving two γ -rays of energies 2.75 and 1.369 MeV.

The 4.43 MeV γ -ray was produced by an $^{241}\text{Am}/^9\text{Be}$ neutron source. ^{241}Am is a long lived α -particle source giving a 5.49 MeV α -particle. The two isotopes are intimately mixed so that the α -particles can initiate the $^9\text{Be}(\alpha,n)^{12}\text{C}$ reaction. The carbon nucleus can be formed in the ground state or first or second excited levels. The second excited level decays by α -particle emission to ^8Be in 100% of its transistions and the first level decays by γ -ray emission to the ground state giving a 4.43 MeV γ -ray.

The calibration of the pulse heights as displayed by the multichannel analyser was linear with energy to within $\pm 1\%$ for the above sources, provided that the count rate in the detector was similar for each source. The variation of detector output pulse height with count rate has been reported by Gutpa and Nath⁽⁶⁵⁾ for the 56 AVP

photomultiplier tube; the amplitude of the output pulse increases with count rate and the variation is lower for higher dynode chain currents. In the detector used no gain variation was observed for count rates below 2,000 counts per second and in experimental runs the detector always worked at a lower count rate.

An instability in the detector gain was observed due to slight variations in the H.T. power supply. The effect was greatly reduced by using a mains stabilizing transformer with the H.T. unit. However, the drift in the gain was up to $\pm 3\%$ over a period of several hours.

3.7.2. Energy Resolution

The energy resolution of the γ -ray detector was measured as 14% at 0.66 MeV. The resolution improved with energy and it was observed to vary as the inverse square root of the γ -ray energy. At 1.3 MeV the resolution was 12% and the 1.17 MeV and 1.33 MeV γ -rays of ^{60}Co were just resolved. The resolution measurements were made using the apparatus as shown in Figure 3.19, i.e. with the signal pulses passing through the delay unit and the linear gating circuit. Only a very marginal improvement in resolution resulted if the linear delay and gating units were bypassed.

The resolution was rather poorer than the anticipated 10% at 0.66 MeV. The poor resolution was due to two reasons; firstly because a converging light pipe was used and secondly because the photomultiplier tube, while having excellent timing characteristics, has poor pulse height resolution. Poor energy resolution with a 56 AVP photomultiplier tube has been reported by Gupta and Nath⁽⁶⁵⁾ and their NaI(Tl) detector also had a resolution of 14% at 0.66 MeV. To improve the resolution a larger diameter phototube would have to be used to dispense with the light pipe. The next size focused tube available is the 58 AVP with a 127 mm (5 in) diameter photocathode.

Absolute Differential Cross-Section Measurement4.1. The Differential Cross-Section

The total neutron cross-section, σ_T , of a nucleus is a measure of the reaction probability for all interaction processes: elastic and non-elastic processes. If I_0 is the neutron flux incident normally on a slab of material of thickness x , having N nuclei per unit volume, then the undegraded neutron flux, I , after passing through the sample is given by the exponential law $I = I_0 e^{-N\sigma_T x}$. The number of interactions in the sample per unit time is given by:

$$I_0 - I = I_0 (1 - e^{-N\sigma_T x})$$

The present measurements were concerned with γ -ray production cross-sections, σ_γ , in neutron inelastic scattering. The total γ -ray yield, G , from neutron inelastic scattering is given by:

$$G = \phi \left(1 - e^{-N\sigma_T x}\right) \sigma_\gamma / \sigma_T \dots \dots \dots 4.1$$

where ϕ is the time integrated neutron flux over the surface area of the sample, i.e. the total number of neutrons incident on the sample in a given time.

The differential cross-section, which is a measure of the probability of radiation being emitted into an element of solid angle $d\Omega$ at an angle θ to the incident beam direction, is given by, $d\sigma = \sigma(\theta)d\Omega$. The quantity $\sigma(\theta) = \frac{d\sigma}{d\Omega}$ gives the angular distribution of the radiation; it is commonly described as the differential cross-section, but strictly it is the differential cross-section per unit solid angle. By integrating the differential

cross-section over 4π solid angle the reaction cross-section is obtained,

i.e.

$$\sigma = \int_{4\pi} \sigma(\theta) d\Omega = \int_{\Phi=0}^{2\pi} \int_{\theta=0}^{\pi} \sigma(\theta) \sin\theta d\theta d\Phi$$

If the differential cross-section is independent of azimuth, Φ , about the incident beam direction the reaction cross-section is given by

$$\sigma = 2\pi \int_0^{\pi} \sigma(\theta) \sin\theta d\theta \dots \dots \dots 4.2$$

The gamma-ray yield, $G'(\theta)$, in a solid angle $d\Omega$ at an angle θ to the incident neutron beam direction is given by

$$G'(\theta) = \phi (1 - e^{-N\sigma_T x}) \frac{\frac{d\sigma_\gamma}{d\Omega}}{\sigma_T} d\Omega \dots \dots \dots 4.3$$

where $\frac{d\sigma_\gamma}{d\Omega}$ is the differential γ -ray production cross-section per unit solid angle. In the absolute measurement of a differential cross-section the γ -ray detector count has to be corrected for the detector efficiency and for the absorption of γ -rays by the sample to obtain the absolute γ -ray yield. Equation 4.3 then becomes,

$$\frac{d\sigma_\gamma}{d\Omega} = \frac{\sigma_T G(\theta)}{\phi (1 - e^{-N\sigma_T x}) \Delta\Omega \epsilon(E_\gamma) S(E_\gamma, \theta)} \quad 4.4$$

where $G(\theta)$ is the detected γ -ray count; $\epsilon(E_\gamma)$ is the detector efficiency $\Delta\Omega$ is the solid angle subtended by the detector and $S(E_\gamma, \theta)$ is the correction term for γ -ray absorption in the sample. $S(E_\gamma, \theta)$ is the fraction of γ -rays escaping the sample and it can be a function of both γ -ray energy and scattering angle. Other corrections arise for the neutron flux term ϕ , and the sample thickness x , because with a point neutron source the incident neutrons on the sample do not form a parallel beam but a diverging beam and different parts of the beam

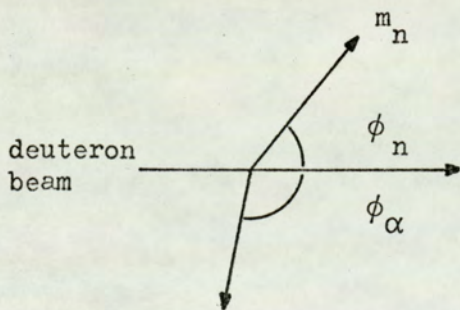
see different sample thicknesses.

In the following sections the neutron source is discussed in detail with particular emphasis on the neutron beam profile, as defined by the α -particle detector, as this is an important factor when considering several terms of equation 4.4. Subsequently, each term of equation 4.4 and the factors affecting them are discussed in detail to enable the evaluation of the absolute differential γ -ray production cross-sections.

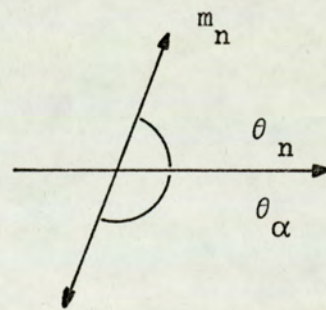
4.2. The Neutron Source

4.2.1. The Angular Range of Source Neutrons

The angular range of neutrons defined by α -particles emitted at $90^\circ \pm 4^\circ$ to the deuteron beam in the D,T reaction can be calculated from the reaction kinetics. The deuteron, mass m_d , is incident on the triton, mass m_t , which is at rest in the laboratory frame of reference; after an interaction an α -particle and a neutron of masses m_α and m_n respectively, emerge at angles ϕ_α and ϕ_n as shown in the following diagram:



Laboratory System



Centre of Mass System

Angles θ_n and θ_α are the corresponding angles in the centre of mass system of co-ordinates. The following expression, given by Benveniste and Zenger⁽⁶⁸⁾, relates the neutron and alpha-particle angles of emission in the laboratory system.

$$\tan\phi_{\alpha} = \frac{\frac{1}{2}\sin\phi_n + \sin\phi_n \left(\frac{1}{\gamma^2} - \sin^2\phi_n \right)^{\frac{1}{2}}}{-\sin^2\phi_n + \cos\phi_n \left(\frac{1}{\gamma^2} - \sin^2\phi_n - \frac{m_{\alpha}}{m_n} \right)^{\frac{1}{2}}} \dots 4.5$$

$$\frac{1}{\gamma^2} = \frac{m_{\alpha}}{m_n} \frac{(m_d + m_t)}{m_d} \left[\frac{m_t}{(m_d + m_t)} + \frac{Q}{E_d} \right] \dots 4.6$$

where E_d is the deuteron energy in the lab. system, and Q is the energy released in the reaction given by $(m_t + m_d - m_{\alpha} - m_n)c^2 = 17.586$ MeV

The tritium target used was a "thick" target. A thick target is one in which the range of deuterons in the target is less than the target thickness and consequently deuterons of all energies from the bombarding energy to zero yield neutrons. Equations 4.5 and 4.6 show that the relationship between the neutron and alpha-particle angles of emission, ϕ_n and ϕ_{α} , depends on the deuteron energy. Figure 4.1 shows the relationship between ϕ_n and ϕ_{α} in the angular range of interest, calculated by equations 4.5 and 4.6 for deuteron energies ranging from 140 KeV to zero energy. Figure 4.1 shows that alpha-particles detected at $90^{\circ} \pm 4^{\circ}$ define a neutron beam over the angular range $\phi_n = 78^{\circ}$ to $\phi_n = 94^{\circ}$. Angular straggling of the deuteron and the alpha-particle in the target have been neglected in the above calculations. These assumptions are considered in section 4.2.4.

The neutron yield, as defined by a $90^{\circ} \pm 4^{\circ}$ alpha-detector, is not uniform over the angular range $\phi_n = 78^{\circ}$ to $\phi_n = 94^{\circ}$. This is because the ${}^3\text{H}(d,n){}^4\text{He}$ reaction cross-section is a function of the deuteron energy and the energy range of deuterons producing neutrons varies with ϕ_n . For example, from Figure 4.1 at $\phi_n = 78^{\circ}$ the neutron yield as defined by the α -detector is due only to deuteron interactions with energies from 140 KeV to 105 KeV and at $\phi_n = 86^{\circ}$ neutrons can be produced by deuterons with energies from 0 to 140 KeV.

To determine the neutron beam profile, i.e. the relative

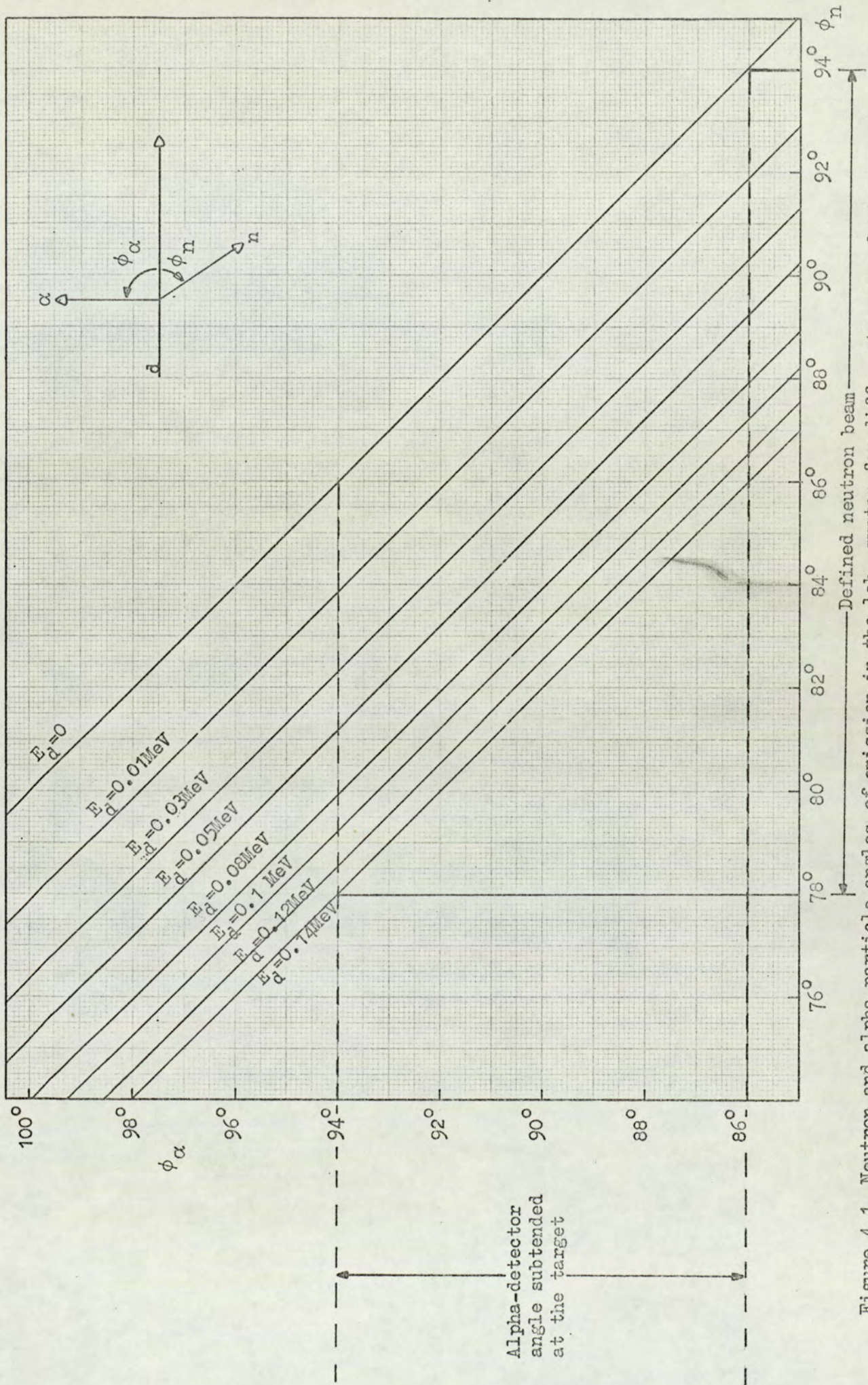


Figure 4.1. Neutron and alpha-particle angles of emission in the lab. system for different energy deuterons.

neutron yield over the angular range $\phi_n = 78^\circ$ to 94° , the variation of the neutron yield with deuteron energy must be calculated.

4.2.2. The Neutron Yield as a Function of Deuteron Energy

The neutron yield in the D,T reaction cannot be calculated by equation 4.1 because the reaction is initiated by a range of deuteron energies and the reaction cross-section is a function of energy. The neutron thick target yield, Y , per incident deuteron is given by

$$Y = \int_0^{E_{dmax}} \frac{\sigma(E_d) N}{\frac{dE_d}{dx}} dE_d$$

where $\sigma(E_d)$ is the reaction cross-section at a deuteron energy E_d , N is the number of tritium atoms per unit volume, and $\frac{dE_d}{dx}$ is the stopping power of the deuteron in the TiT target. This expression assumes that the incident particle flux is constant throughout the target. This is a good approximation as only a very small fraction of the beam interacts with the target tritium.

The neutron yield, $Y(\theta)$, per incident deuteron per unit solid angle at a neutron angle ϕ_n is given by

$$Y(\theta) = \int_0^{E_{dmax}} \frac{\frac{d\sigma}{d\omega} N}{\frac{dE_d}{dx}} dE_d \quad \dots \quad 4.7$$

where $\frac{d\sigma}{d\omega}$ is the differential cross-section per steradian at a deuteron energy E_d and neutron angle ϕ_n .

The ${}^3\text{H}(d,n){}^4\text{He}$ cross-section

The differential neutron production cross-section of the D,T reaction has been found to be isotropic in the centre of mass system for deuteron energies up to 200 KeV by Allen and Poole⁽⁶⁹⁾ and Bame and Perry⁽⁷⁰⁾. Several measurements of the variation of the differential cross-section with deuteron energy are given by Benveniste and Zenger⁽⁶⁸⁾ for the energy range 10 KeV to 500 KeV.

The measurements of the differential cross-section per steradian (given in the centre of mass system) are in good agreement and the curve used for the present calculations is given in Figure 4.2.

The anisotropy factor, $\frac{d\omega^*}{d\omega}$ is required to convert the centre of mass differential cross-section to the lab. frame of reference, (ω is a solid angle in the lab. system and the primed quantity is in the centre of mass system). The anisotropy is given by:

$$\frac{d\omega^*}{d\omega} = \frac{\sin\theta_n d\theta_n}{\sin\phi_n d\phi_n}$$

The relationship between the centre of mass angle θ_n and the lab. angle ϕ_n is given by⁽⁶⁸⁾

$$\cos\theta_n = -\gamma\sin^2\phi_n + \cos\phi_n (1 - \gamma^2\sin^2\phi_n)^{\frac{1}{2}} \quad \dots 4.3$$

where γ is as defined previously. Differentiating and rearranging gives,

$$\frac{d\omega^*}{d\omega} = \frac{\gamma\left(\cos\phi_n + \left(\frac{1}{\gamma^2} - \sin^2\phi_n\right)^{\frac{1}{2}}\right)}{\left(\frac{1}{\gamma^2} - \sin^2\phi_n\right)^{\frac{1}{2}}} \quad \dots 4.8a$$

The neutron anisotropy is plotted against the neutron angle, ϕ_n , for deuteron energies of 0, 100 KeV and 200 KeV in Figure 4.3. Figure 4.3 shows that for neutrons emitted between 78° to 94° the anisotropy is a slowly varying function of energy and it can be considered as constant to within 1%.

Stopping Power of Deuterons in TiT:

The rate of energy loss of deuterons in TiT can be calculated as the sum of the energy losses in the constituents and it is given by

$$\frac{dE_d}{dx} = \frac{48}{48 + 3n} \left(\frac{dE_d}{dx}\right)_{Ti} + \frac{3n}{48 + 3n} \left(\frac{dE_d}{dx}\right)_T \quad \dots 4.9$$

where $\left(\frac{dE_d}{dx}\right)_{Ti}$ is the rate of energy loss of deuterons in normal titanium and $\left(\frac{dE_d}{dx}\right)_T$ that in tritium, both quantities must be measured

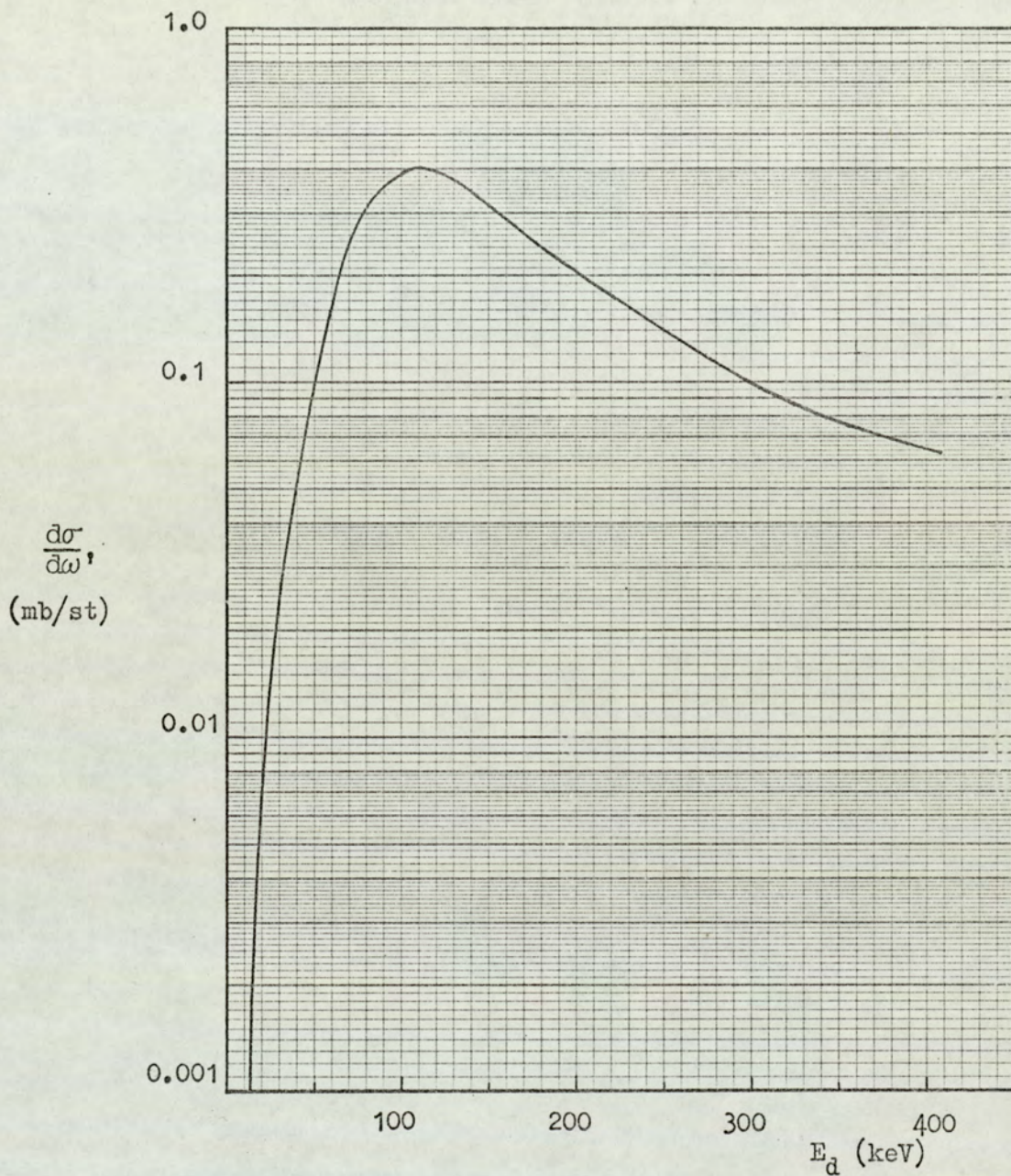


Figure 4.2. The differential cross-section for the ${}^3\text{H}(d,n){}^4\text{He}$ reaction vs. deuteron energy.

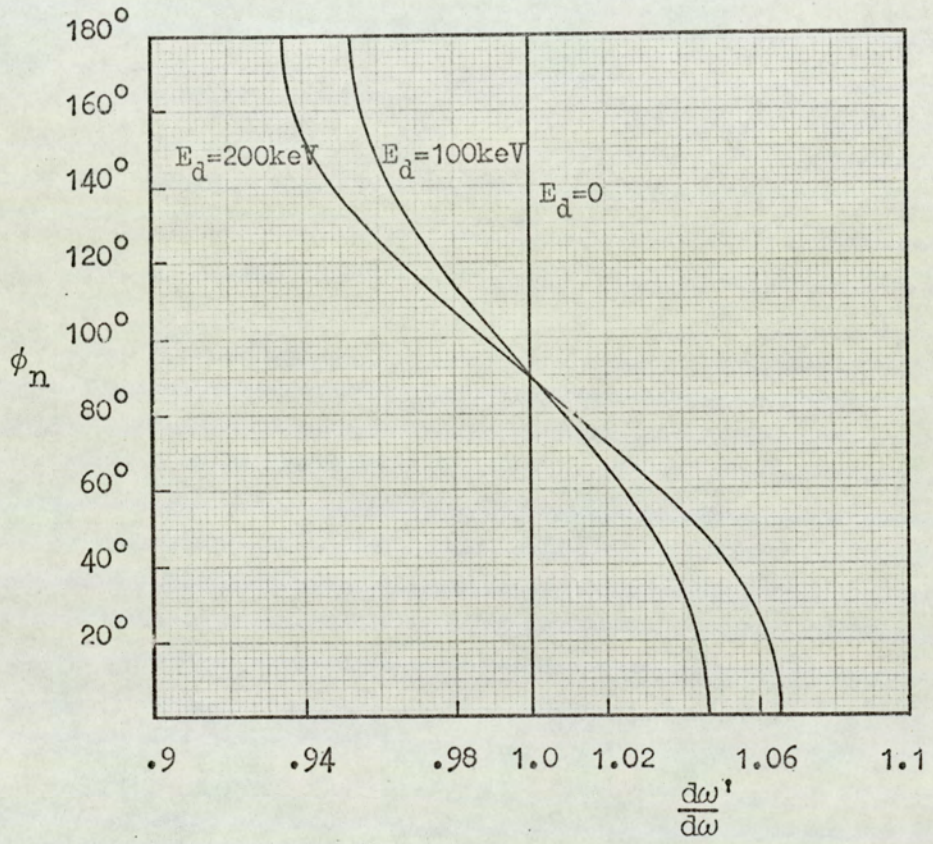


Figure 4.3. The neutron anisotropy factor as a function of neutron angle ϕ_n .

in KeV/mg/cm^2 for use in this equation. n represents the tritium loading factor, i.e. the number of tritium atoms per titanium and it is generally assumed to be constant with a value of unity. The numbers 48 and 3 are the mass numbers of titanium and tritium respectively.

The stopping power, $\frac{dE_d}{dx}$, has been calculated by Benveniste and Zenger⁽⁶⁸⁾. They interpolated the proton stopping power data of Warshaw⁽⁷¹⁾ for 50 KeV to 350 KeV protons in aluminium and copper with respect to the square root of the mass number to produce a proton stopping power curve in titanium. Then by assuming that the rate of energy loss is a function of the velocity of the particle,

$$\left(\frac{dE_p}{dx}\right)(E) = \left(\frac{dE_d}{dx}\right)(2E)$$

a deuteron stopping power curve in titanium was derived. Similarly, the rate of energy loss of deuterons in tritium was obtained using the proton data of Reynold et al.⁽⁷²⁾. Figure 4.4 shows the deuteron rate of energy loss in titanium tritide.

Gunnerson and James⁽⁷³⁾ have measured the stopping power of deuterons in titanium tritide for a limited deuteron energy range (50 KeV to 120 KeV) and they report good agreement with values calculated by the above method.

With this information the neutron yield as a function of deuteron energy can be calculated. The neutron yield, y , per unit solid angle, at an angle ϕ_n , from deuterons in the energy interval E_d to $E_d + \delta E_d$ is obtained using equation 4.7 and it gives

$$y(\phi_n, E_d) \propto \frac{\left(\frac{d\sigma}{d\omega'}\right) \left(\frac{d\omega'}{d\omega}\right) \delta E_d}{\frac{dE_d}{dx}} \dots \dots \dots 4.10$$

N the number of tritium atoms per unit volume is assumed constant. To obtain the relative neutron yield versus deuteron energy, expression 4.10 was evaluated in 10 KeV deuteron energy steps. The anisotropy was

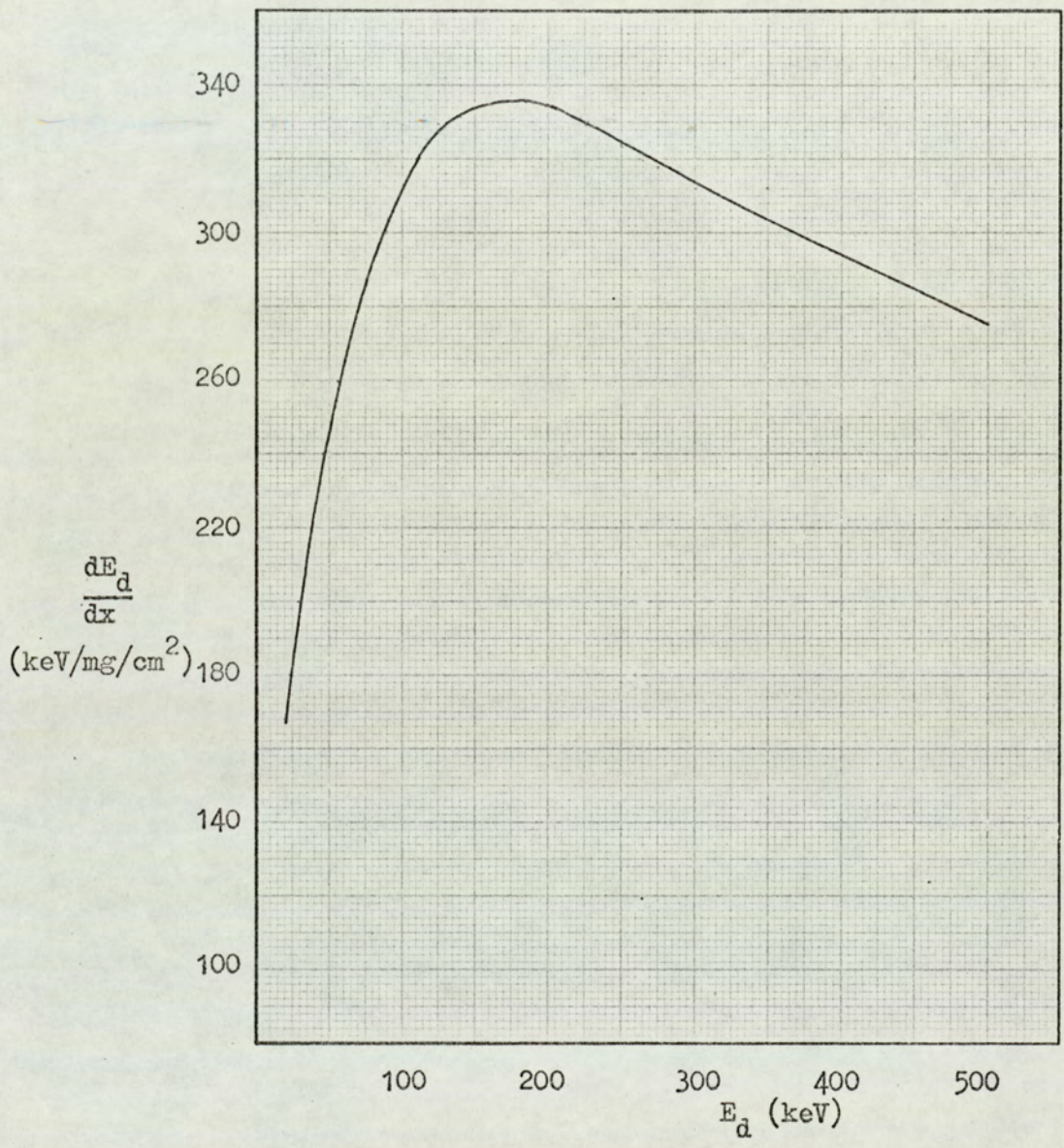


Figure 4.4. The stopping power curve of deuterons in titanium tritide, from Benveniste and Zenger⁽⁶⁸⁾.

taken as a constant with value unity, Figure 4.3. Mean values of the stopping power and the differential cross-section per steradian for each energy interval were taken from Figures 4.2 and 4.4. The relative neutron yield against deuteron energy is plotted in Figure 4.5.

4.2.3. The Neutron Beam Profile

The neutron beam profile, i.e. the relative neutron yield at each angle ϕ_n , as defined by the α -detector, can be calculated using the information given in Figures 4.1 and 4.5. Figure 4.1 gives the deuteron energy range contributing to the neutron yield at a given angle ϕ_n defined by the α -detector. The neutron yield for this deuteron energy range is proportional to the area under the curve of Figure 4.5 in the range under consideration. For example, from Figure 4.1 at $\phi_n = 80^\circ$ the emitted neutrons having detected associated α -particles, i.e. the useful neutrons, are only produced by deuterons in the energy interval 140 KeV to 80 KeV. Figure 4.5 shows that the intensity of the neutron yield is a function of deuteron energy. The area under the curve of Figure 4.5 in the energy interval 140 KeV to 80 KeV is proportional to the neutron yield for this deuteron energy interval. Thus the relative neutron yield at each angle ϕ_n , as defined by the α -detector, was calculated. The areas under the curve of Figure 4.5 for each deuteron energy interval were measured with a planimeter. The calculated neutron beam profile as defined by the $90^\circ \pm 4^\circ$ α -detector is shown in Figure 4.6. The full width at half maximum height of the neutron beam profile is exactly 8° which is the angle subtended in the horizontal plane by the α -detector.

The angular range of neutrons in the vertical plane is given by the angle subtended by the α -particle detector in the vertical plane, because in a reaction the deuteron, triton, neutron and alpha-particle must all be in the same plane for energy and momentum conservation. The angular range of the defined neutrons was $15\frac{1}{2}^\circ$

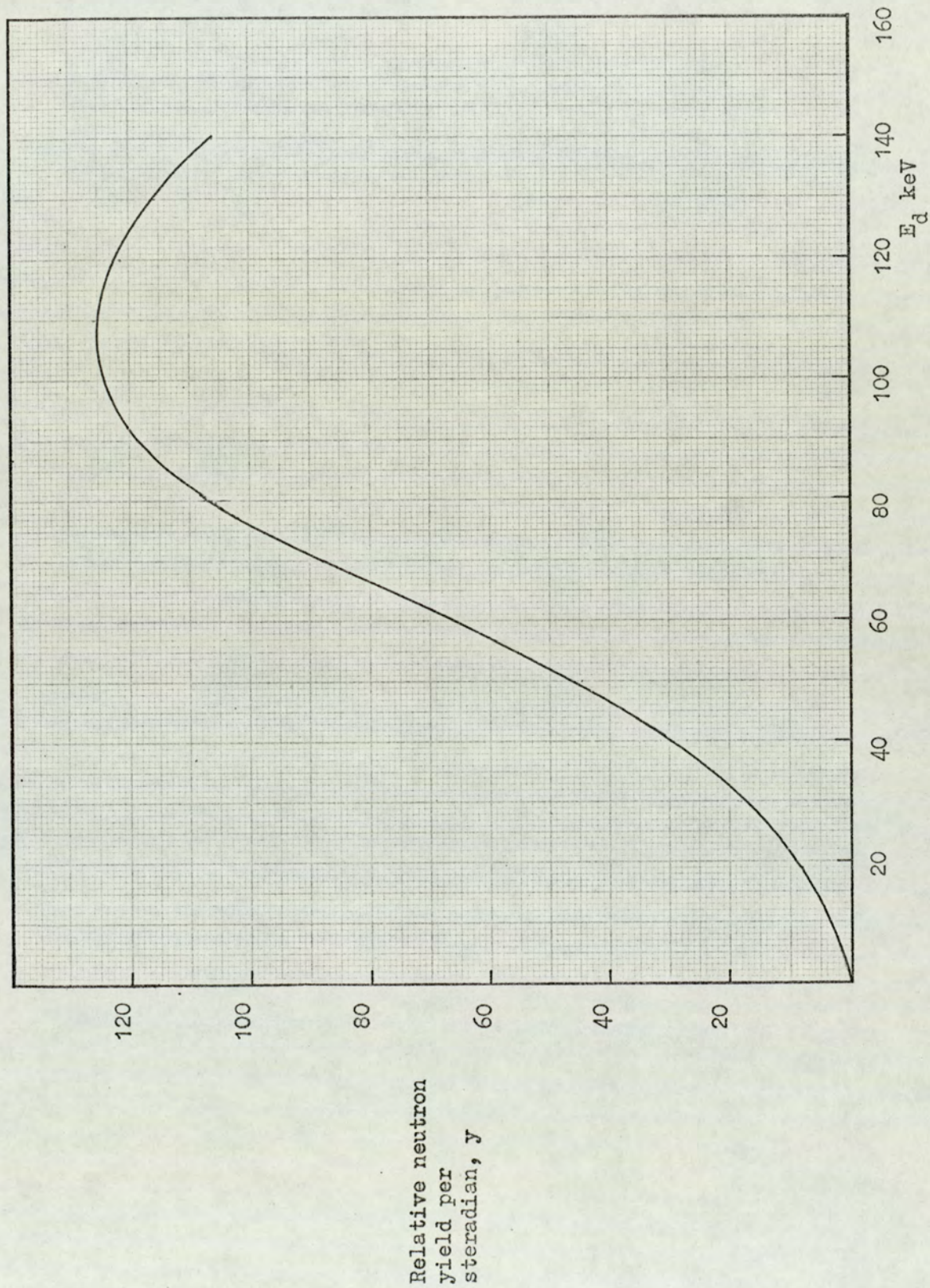
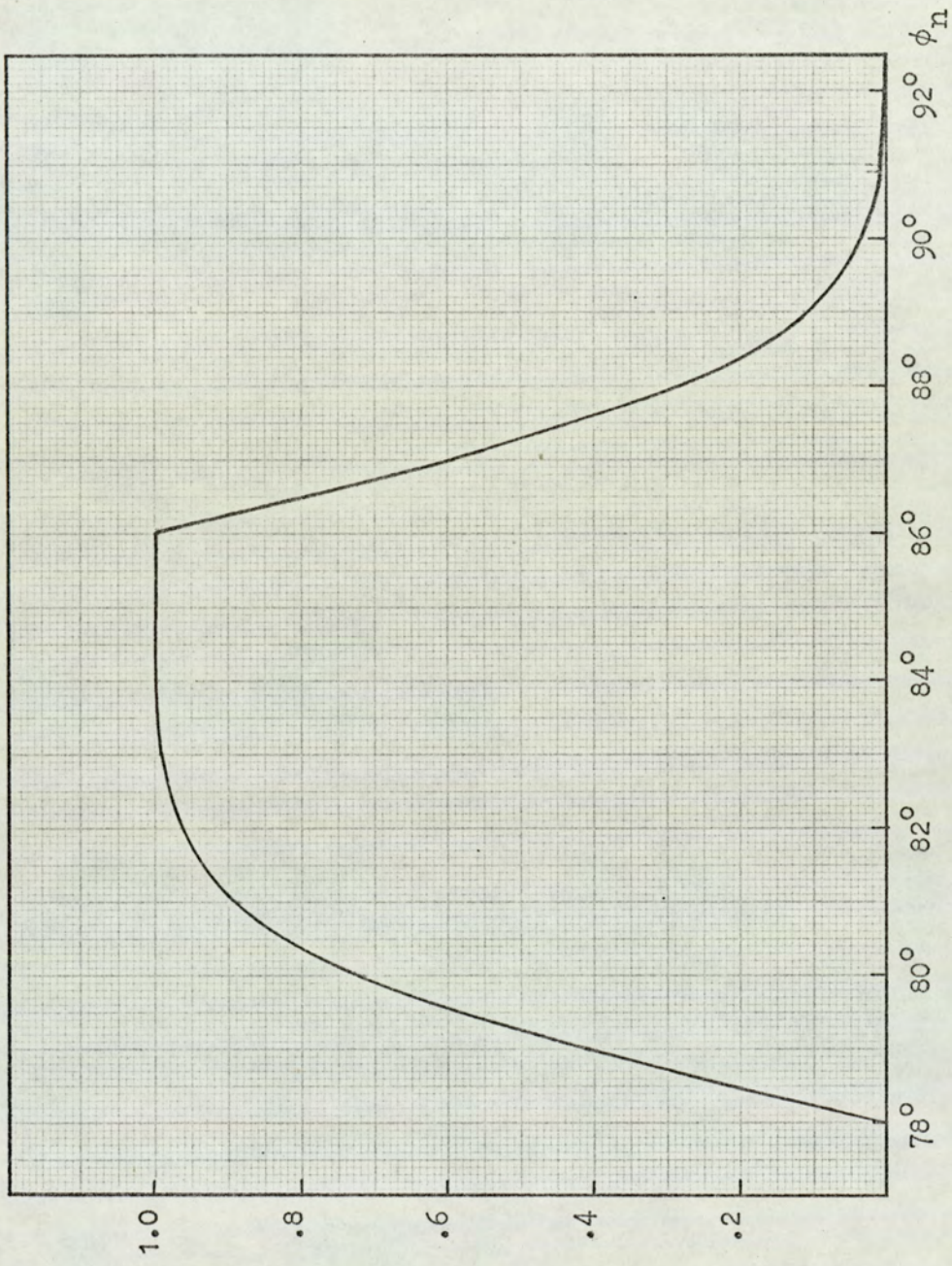


Figure 4.5. The relative neutron yield as a function of deuteron energy for $\phi_{\text{n}} = 78^{\circ}$ to 94° .



Relative neutron
yield per
steradian

Figure 4.6. The neutron beam profile, in the reaction plane, defined by the $90^\circ \pm 4^\circ$ alpha-detector.

in the vertical plane.

4.2.4. Assumptions in the Calculation of the Neutron Beam Profile

The two main assumptions in the previous calculations were

- (i) that the tritium loading factor was constant throughout the target and had a value of unity, and
- (ii) that the angular scattering of deuterons and alpha particles in the target was negligible.

These two assumptions are considered in detail with particular emphasis on their effect on the neutron beam profile.

The Loading Factor

There is some uncertainty as to the ratio of tritium to titanium in targets. A factor of one was used in the above calculations but Benveniste et al.⁽⁷⁴⁾ have reported loading factors varying from 0.5 to 1.2 and they explained anomalies in their results by suggesting a surface layer of the target depleted of tritium. Gunnensen and James⁽⁷³⁾ devised an experiment to measure the distribution of tritium in a target. A single target 1,500 nm thick was examined. The surface layer was found to contain very little tritium, but at a depth of 100 nm the tritium level rose sharply to a loading factor of about two. The loading factor remained fairly constant to a depth of 450 nm after which the tritium level began to fall off, the last 600 nm being devoid of tritium. The distribution of tritium gave an average loading factor of one.

The path length, x , of a deuteron in slowing down from an energy E_{d_1} to E_{d_2} is given by

$$x = \int_{E_{d_1}}^{E_{d_2}} \left(\frac{dE_d}{dx} \right)^{-1} dE_d \quad \dots \quad 4.11$$

The target used in the present work had a thickness of 2,000 nm. The target was positioned at an angle of 45° to the deuteron beam so that a deuteron path length, x , in the target was equivalent to a true depth

of penetration of $x/\sqrt{2}$. Using the stopping power values of deuterons in the target taken from Figure 4.4, equation 4.11 was solved numerically in 10 KeV deuteron energy steps; the results are given in Table 4.1

Table 4.1

Deuteron Energy (initially 140 KeV)	Depth of Penetration into target, $x/\sqrt{2}$
120 KeV	110 nm
110 KeV	150 nm
100 KeV	220 nm
50 KeV	520 nm

The non-uniform tritium distribution requires that equation 4.10 includes a term $n(x)$ for the variation of the loading factor with the depth of penetration into the target.

$$\text{i.e.} \quad y \propto n(x) \frac{\left(\frac{d\sigma}{d\omega'}\right) \left(\frac{d\omega'}{d\omega}\right)}{\frac{dE_d}{dx}} \delta E_d \dots \dots \dots 4.12$$

Assuming a tritium distribution in the target similar to that of Gunnensen and James and using the results of Table 4.1, then for the first 100 nm of the target, (i.e. for deuterons of 140 to 120 KeV) $n(x)$ is slowly increasing. Therefore the relative neutron yield from 140 KeV to 120 KeV deuterons is reduced. For deuterons with energies from 120 KeV to 50 KeV $n(x)$ is constant and the relative neutron yield is as calculated. At lower deuteron energies the loading factor begins to fall, but this has little effect on the relative neutron yield as the reaction cross-section falls off sharply, see Figures 4.2 and 4.5.

The deuteron stopping power to some extent depends on the loading factor, (equation 4.9). However, Beneveniste et al.⁽⁷⁴⁾ showed

that a 50% change in the loading factor gives only a 10% change in the stopping power. The relative neutron yield as a function of deuteron energy, (equation 4.10), is unaffected by the loading factor value used for the stopping power, because the shape of the stopping power vs. energy curve is a very weak function of the loading factor. Therefore, for deuterons below 120 KeV, for which the loading factor is constant, the relative neutron yield is approximately independent of the loading factor value.

The net effect of the variation of the loading factor is to reduce the neutron yield from deuterons with energies of 140 KeV to 120 KeV. A neutron beam profile was calculated for the extreme case in which no neutrons are produced by deuterons with energies between 140 KeV and 120 KeV. The beam profile was almost identical to that shown in Figure 4.6, except that the lowest neutron angle of emission was 78.5° as opposed to 78° in Figure 4.6.

Angular Straggling of Deuterons and Alpha-Particles

The path of a heavy particle through an absorber is practically rectilinear, however, the multiple collisions do tend to broaden out a collimated particle beam, producing what is termed angle straggling. Angle straggling can be calculated by an expression derived by Fermi⁽⁷⁵⁾ for the mean angle of divergence $\bar{\theta}$:

$$\bar{\theta}^2 = \frac{2\pi z^2 e^4}{\bar{E}^2} n_0 Z^2 x \ln \left(\frac{\bar{E} a}{z Z^{4/3} e^2} \right) \dots 4.13$$

where z is the particle charge,

e is the electronic charge

Z is the atomic number of the absorber,

n_0 is the number of absorber atoms per unit volume,

a is the Bohr radius, and

\bar{E} is the mean particle energy after traversing a thickness x of the absorber.

The angle straggling is proportional to the charge of the absorber, so to a first approximation, the effect was estimated by considering only the titanium in the target, which has an atomic number of 22 compared with 1 for tritium. $\bar{\theta}$ was calculated for deuterons slowing down from 140 KeV to 100 KeV and to 50 KeV. The path lengths, x , to reduce the energy to 50 KeV and 100 KeV can be obtained from Table 4.1. The mean value of the angle of divergence, $\bar{\theta}$, for 100 KeV deuterons was calculated to be 3° and for a 50 KeV deuteron it was 10° . This effect is however not as serious as it at first appears. For example consider a 50 KeV deuteron interaction. If the deuteron undergoes no angle straggling and the α -particle is emitted at 90° ($\phi_\alpha = 90^\circ$) then from Figure 4.1 the neutron angle ϕ_n relative to the beam tube current direction is 85.2° . However, if the deuteron is deflected through an angle of 10° before interacting the incident beam direction is effectively rotated by 10° . If the α -particle is again detected in the centre of the detector the angle ϕ_α is effectively 100° (allowing for the 10° incident direction rotation). From Figure 4.1 this corresponds to an angle $\phi_n = 75.2^\circ$ relative to the rotated beam direction. The angle ϕ_n relative to the beam tube current direction is however 85.2° which is the same as when no angle straggling occurs. Deuteron angle straggling would tend to broaden the defined neutron beam slightly for larger straggling angles because the relationship between ϕ_n and ϕ_α (at a given energy) is not linear over the larger angular interval.

The α -particles also undergo angle straggling in escaping the target. The mean values of $\bar{\theta}$ were calculated by the Fermi equation for two cases: for a 90° emitted α -particle in a 100 KeV deuteron interaction and for a 90° α -particle produced by a 50 KeV deuteron. To calculate the mean angle of divergence, $\bar{\theta}$, the energies with which the alpha-particles leave the target are required and also the depths, x , of the target they traverse. With the target plane at

45° to the incident beam the alpha path length in escaping the target is equal to the deuteron path length, so that the values of x can be obtained from Table 4.1.

The energy of an alpha-particle at production in the lab.system is given by $E_\alpha = 17.586 - E_n + E_d$ where E_α and E_n are the alpha-particle and neutron lab. energies.

The general expression for the neutron energy in the lab.system $E_n(\phi_n, E_d)$ is given by⁽⁶⁸⁾.

$$E_n(\phi_n, E_d) = \left(\frac{m_d}{m_d + m_t} \right)^2 \frac{m_n}{m_d} E_d \cos 2\phi_n + \frac{m_\alpha}{m_n + m_d} \left(\frac{m_t}{m_d + m_t} E_d + Q \right) + \frac{2 \cos \phi_n}{m_n + m_d} \left(m_d m_n \frac{m_\alpha}{(m_n + m_\alpha)} E_d \left(\frac{m_t}{m_d + m_t} E_d + Q \right) \right)^{\frac{1}{2}} \times \left(1 - \frac{m_d m_n}{m_d + m_t} \frac{E_d \sin^2 \phi_n}{m_\alpha \left(\frac{m_t}{m_d + m_t} E_d + Q \right)} \right)^{\frac{1}{2}} \dots \dots \dots 4.14$$

Equation 4.13 and 4.14 were evaluated for the two cases and the results are tabulated in Table 4.2.

Table 4.2

E_d	ϕ_α	ϕ_n	E_n	E_α
110 KeV	90°	83°	14.197 MeV	3.499 MeV
50 KeV	90°	85°	14.128 MeV	3.508 MeV

From the results of Table 4.2 both the 50 KeV and 100 KeV deuterons give 3.5 MeV α -particles. The energy with which these particles escape from the target was approximately estimated by the Bethe equation of the stopping power of non-relativistic heavy particles:

$$-\frac{dE}{dx} = \frac{4\pi z^2 e^4}{m_e v^2} n Z \ln \left(\frac{2m_e v^2}{I^2} \right) \dots \dots \dots 4.15$$

where m_e is the electron mass,

v is the particle velocity, and

I is the mean ionisation potential.

Again as an approximation, only the titanium in the target was considered.

The expression used to calculate the ionisation potential was,

$$I = 9.1Z(1 + 1.9Z^{-2/3}) \text{ eV}$$

taken from Sheldon and Marmier⁽⁷⁶⁾ and for titanium $I = 249$ eV. In the medium energy range, of the order MeV, the log. term of equation 4.15 varies slowly and may be considered as a constant. Alpha-particles below 2 MeV tend to pick up electrons so that the effective particle charge is less than two. However, 3.5 MeV alpha-particles are adequately described by the Bethe equation⁽⁷⁶⁾. Equation 4.15 for the passage of α - particles through titanium becomes,

$$-\frac{dE_\alpha}{dx} = \frac{4,042}{E_\alpha} \log_e(2.1903 E_\alpha)$$

where E_α is in MeV.

Assuming the log term varies very slowly with E_α and evaluating it with $E_\alpha = 3.5$ MeV gives,

$$-\frac{dE_\alpha}{dx} = \frac{8,232}{E_\alpha}$$

Integrating gives $\bar{E}_\alpha^2 = E_\alpha^2 - 16,464x \dots \dots \dots 4.16$

where E_α is the initial energy and \bar{E}_α is the mean α -particle energy after traversing a thickness x of the target.

Using equation 4.16 and the Fermi equation the mean angles of divergence were calculated for the two cases and the results are shown in Table 4.3.

Table 4.3.

E_d	x	\bar{E}	$\bar{\theta}$
110 KeV	220 nm	3.45 MeV	14'
50 KeV	730 nm	3.32 MeV	26'

The results show that the multiple scattering of the alpha particles in escaping the target introduces an angular uncertainty of about a quarter of a degree.

Angular straggling of the alpha-particles introduces a spread in the defined neutron cone, (neutron beam profile) of the order of $\frac{1}{4}^\circ$. This does to some extent compensate the loss of neutrons in the angular interval $\phi_n = 78^\circ$ to $\phi_n = 78\frac{1}{2}^\circ$ due to the depleted surface layer of tritium in the target.

In conclusion, the assumptions made in calculating the neutron beam profile, Figure 4.6 have little effect on the shape of the profile.

4.2.5. The Neutron Line Shape

The energy distribution of source neutrons at a given angle of production, ϕ_n , is termed the line shape. The neutron energy is a function of both the angle of production, ϕ_n , and the deuteron energy E_d . The ordinate of the neutron line shape is proportional to the neutron yield and it is given by the expression for the neutron yield as a function of angle ϕ_n and deuteron energy, $y(\phi_n, E_d)$, equation 4.10. The abscissa of the line shape, i.e. the neutron energy as a function of angle ϕ_n and energy E_d , $E_n(\phi_n, E_d)$, is given by equation 4.14.

Equations 4.10 and 4.14 were evaluated for a range of deuteron energies from zero to 140 KeV, for an angle $\phi_n = 84^\circ$. The neutron line shape is shown in Figure 4.7. The line shape is typical of the energy spread of the defined neutron beam because the neutron angular range of interest is limited. Neglected in the calculation of the line shape, equations 4.10 and 4.14, was the

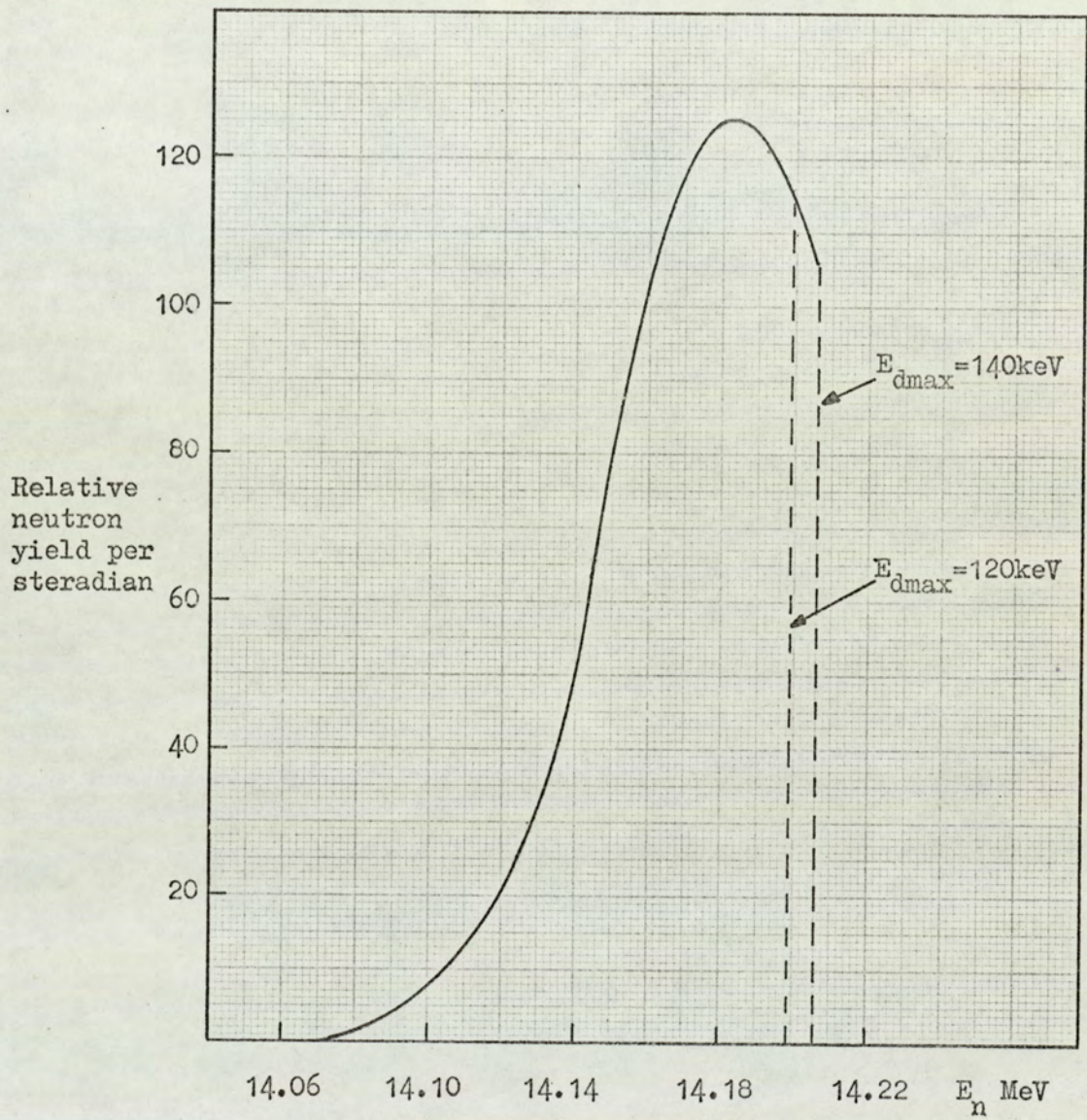


Figure 4.7. The neutron line shape, $\phi_n = 84^\circ$ and $E_d = 0$ to 140 keV.

variation of the tritium loading factor and the deuteron beam scattering. The variation of the loading factor would tend to reduce the number of neutrons produced by 120 KeV to 140 KeV deuterons. In Figure 4.7 the effect on the line shape is shown for a deuteron energy limit of 120 KeV. Deuteron scattering would tend to broaden the line shape slightly as effectively it increases the neutron angular production interval.

The total energy spread of the neutron beam, defined by the alpha-detector, was only 100 KeV.

4.3. Sample Size and Geometry

For a fixed neutron source to sample distance there are primarily three factors effecting the sample size and geometry. These are neutron multiple scattering, neutron attenuation and γ -ray absorption in the scattering sample.

4.3.1. Multiple Scattering

The expression for the calculation of the γ -ray differential cross-section, equation 4.4, assumes that the γ -ray yield is due to neutrons that have interacted only once in the scattering sample, so that there is an exponential fall off of the neutron flux through the sample. However, after a neutron has been scattered once, either elastically or inelastically, it is possible for the neutron to interact a second time. Neutron elastic scattering is very forward peaked and neutrons interacting by this process are only marginally reduced in energy, (except for scattering off light nuclei $A < 12$). The effect of multiple scattering, in γ -ray production cross-section measurements, is to cause an increase in the γ -ray yield, due to the effective increase in the neutron flux. Consequently the calculated cross-section is artificially high. The probability of multiple scattering depends on the dimensions of the sample and on the scattering cross-section.

Day⁽²⁷⁾ has investigated the dependence of neutron multiple

scattering on sample thickness with particular reference to the γ -ray production cross-section in inelastic scattering. Day measured the 0.847 MeV γ -ray production cross-section in the inelastic scattering of 2.6 MeV neutrons off iron with five different sized samples. The cross-sections, in each case, were calculated by two methods; firstly ignoring multiple scattering and secondly including a correction for the increased γ -ray yield from second neutron scattering events. Figure 4.8 shows the results; the total γ -ray production cross-section is plotted against the sample thickness in mm and mean-free path lengths both with and without the multiple scattering correction. (The mean-free path is the inverse of the total macroscopic cross-section). A significant result of this work is that multiple scattering is appreciable for thin scattering samples. This is in contrast to Walt⁽⁷⁷⁾ who states that multiple scattering is not appreciable for samples less than 0.2 mean-free paths thickness. From Figure 4.8 a scattering sample of 0.2 mean-free paths thickness causes an increase in the measured cross-section of 14%.

Multiple scattering corrections require a great deal of tedious computing; however Day found a simple alternative way of calculating the cross-section. He neglected multiple scattering and assumed that the neutron flux was constant throughout the sample. This assumes that the increased γ -ray yield from second scattering events is exactly compensated by neglecting the neutron beam attenuation. Provided that the sample thickness had a neutron transmission of not less than about 0.7, Day found that the cross-sections calculated in this way had a root mean square difference with those calculated with the multiple scattering corrections of only 3%, the simpler method generally giving smaller cross-sections. The validity of this approximation was verified by Nishimura et al.⁽⁷⁸⁾ who found that cross-section measurements agreed within 2% for different sized samples, with incident neutrons of 2.5 MeV. Martin and Stewart⁽¹⁴⁾ also obtained good

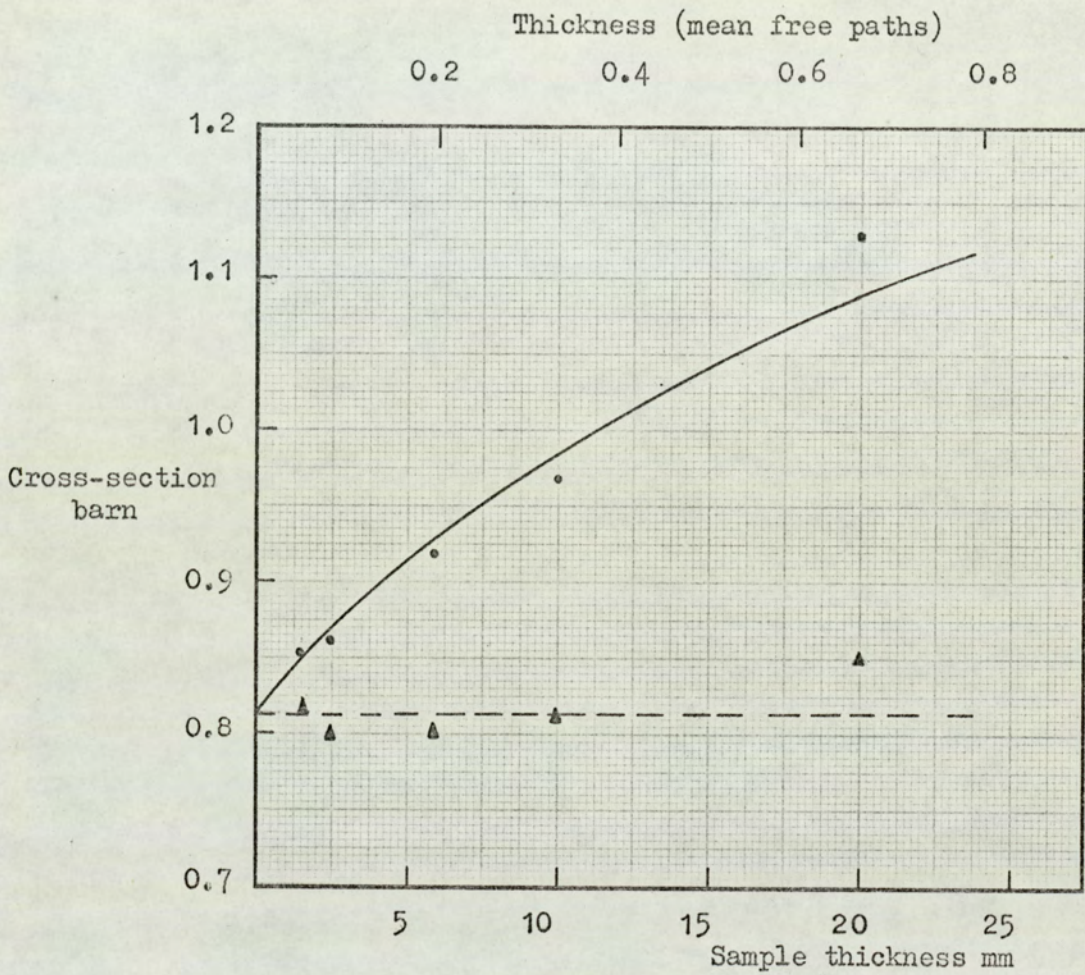


Figure 4.8. The effect of neutron multiple scattering on the gamma-ray production cross-section. $^{56}\text{Fe}(n,n'\gamma)^{56}\text{Fe}$ 0.847 MeV gamma-ray cross-section measured by Day⁽²⁷⁾ with different sized samples.

• Experimental.

▲ Corrected for multiple scattering.

agreement for cross-section measurements with different sized samples using 14 MeV neutrons.

The above method was adopted in the present measurements. Equation 4.4, for the calculation of the different cross-section, with the neutron flux remaining constant throughout the sample, becomes

$$\frac{d\sigma_{\gamma}}{d\Omega} = \frac{G(\theta)}{N\phi x \Delta\Omega \epsilon(E_{\gamma}) S(E_{\gamma}\theta)} \dots\dots\dots 4.16$$

The terms are as defined in section 4.1.

4.3.2. Choice of Sample Geometry

Two sample geometries, cylindrical and flat plate, can be used with the present experimental arrangement. With cylindrical geometry the sample is made in the form of a right solid cylinder and with flat plate geometry the sample is in the form of a thin rectangular slab of material. Flat plate geometry has several advantages for use with the associated particle method.

The scattering sample should completely subtend the neutron beam defined by the associated alpha-particles. This can easily be done with a slab sample but not always with a cylindrical sample. To use the method described in the previous section to correct for multiple scattering, the sample should have a neutron transmission of not less than 0.7 and this usually limits the sample thickness to a maximum of 20 mm to 30 mm depending on the total cross-section for the particular sample. The width at half maximum intensity of the neutron beam, as defined by a $90^{\circ} \pm 4^{\circ}$ alpha detector, with a 250 mm source to sample distance is 35 mm and the total width of the neutron beam is 56 mm (Figure 4.6). Clearly, multiple scattering becomes a problem if a cylindrical sample 56 mm in diameter is used. The signal to background ratio deteriorates if either a smaller diameter sample subtending a fraction of the defined beam is used, or if a narrower neutron beam is

defined. This problem does not arise with a slab sample as a thin slab can completely subtend the defined neutron beam without introducing multiple scattering difficulties. Another advantage of the flat plate geometry is that if the sample is made slightly wider than the defined neutron beam, then a small error in positioning the sample does not alter the effective sample thickness compared with the use of a cylindrical sample where an error in positioning the sample alters the effective sample thickness.

For these reasons the present measurements were made with flat plate geometry samples

4.3.3. Gamma-Ray Absorption in the Scattering Sample

The correction for self-absorption of γ -rays by the scattering sample is most important in cross-section measurements as it is of the order of 10%. The absorption depends on the sample size and the γ -ray absorption coefficient for the material. The absorption coefficient is a function of γ -ray energy and depends on the Z number of the sample as discussed in section 2.1.

To minimize γ -ray absorption the sample thickness has to be kept to a minimum, while maintaining a reasonable signal to background ratio. With flat plate geometry the positioning of the sample strongly effects the γ -ray absorption. If the sample is positioned so that the incident neutron flux is normal to the plane of the sample, then γ -rays escaping at a small scattering angle have a minimum thickness of material to penetrate, while γ -rays scattered at 90° have a maximum thickness to penetrate and are strongly absorbed. However, if the plane of the sample is placed at an angle of 45° to the incident neutron beam, as shown in Figure 4.9, the absorption is still a function of scattering angle but the magnitude of the correction does not change so much between 0° and 90° . The γ -ray absorption correction can be simply and accurately calculated with the flat plate sample so positioned.

To calculate the correction factor the irradiated portion of the sample is divided into elemental strips of width δx as shown in Figure 4.9. The γ -ray yield varies at points along an elemental strip particularly at the ends of the element because the relative neutron yield varies with the neutron angle, ϕ_n . In the calculation of the γ -ray production cross-section it is assumed that the neutron flux is constant throughout the sample (to correct for multiple scattering), so that the γ -ray yield from each element is constant. The fraction of the total γ -rays produced in any element is then given by $\frac{\delta x}{b}$, where b is the sample thickness. With the sample-detector geometry used the detector crystal face was positioned 1.39 m from the scattering sample. It is assumed that the detected γ -rays formed a parallel beam. This avoids the need to integrate along the length of an elemental strip for the change in scattering angle and yield along the strip. In view of the long flight path this is a good approximation. Thus the fraction of γ -rays produced in a single element, escaping the scattering sample at an angle θ , is given by

$$\exp \left[-\mu \left(\frac{b-x}{\cos(\theta-45^\circ)} \right) \right] \frac{\delta x}{b}$$

where μ is the γ -ray absorption coefficient and x is as shown in Figure 4.9. This assumes that all detected γ -rays escape through face A of the sample, Figure 4.9. The samples were made wide enough to meet this requirement. The total fraction of γ -rays escaping the sample, $S(\theta)$, is obtained by integration through the sample,

i.e.

$$S(\theta) = \int_0^b \exp \left[-\mu \left(\frac{b-x}{\cos(\theta-45^\circ)} \right) \right] \frac{dx}{b}$$

giving,

$$S(\theta) = \frac{\cos(\theta-45^\circ)}{\mu b} \left[1 - \exp \left(-\frac{\mu b}{\cos(\theta-45^\circ)} \right) \right] \quad 4.17$$

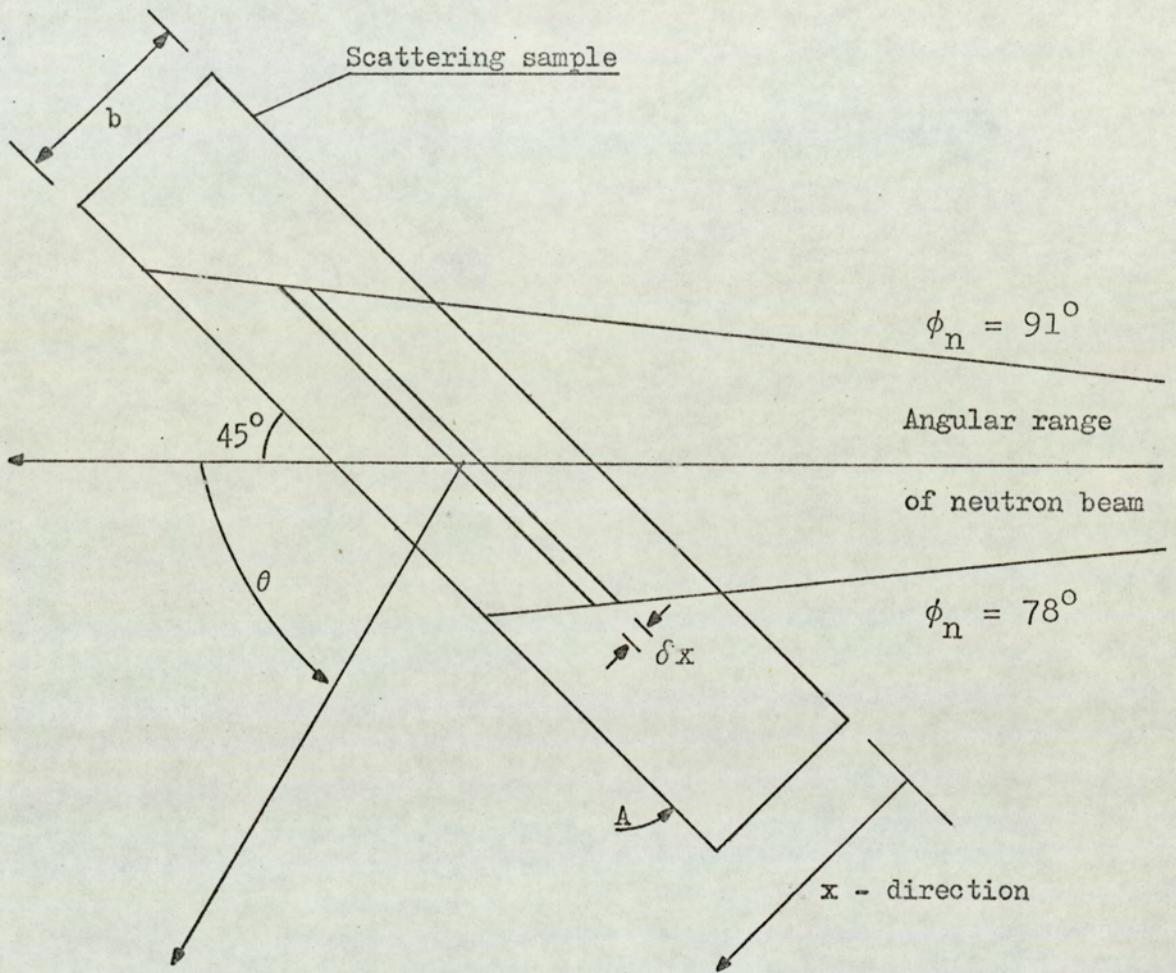


Figure 4.9. Sample geometry.

If the total γ -ray absorption coefficient is used in equation 4.17, $S(\theta)$ gives the fraction of γ -rays escaping the sample without interaction and it does not include degraded γ -rays from Compton scattering. Values for the total linear absorption coefficients (less coherent scattering) were obtained from Grodstein⁽⁴⁷⁾ who has tabulated the γ -ray mass absorption coefficients, (i.e. μ/ρ where ρ is the sample density), of most elements for γ -ray energies from 10 KeV to 100 MeV.

To illustrate how the absorption varies with γ -ray energy, Figure 4.10 shows the absorption correction plotted against γ -ray energy for a 19.8 mm thick titanium slab sample at a scattering angle of 45° , i.e. $\theta = 45^\circ$. The shape of the curve is typical of all elements. The γ -ray self-absorption is a minimum at $\theta = 45^\circ$ where 78% of 1 MeV γ -rays escape the titanium sample without interacting. At a 90° scattering angle the value drops to 71%.

4.3.4. Sample Thickness

Equation 4.16 for the calculation of the differential γ -ray production cross-section is derived assuming that a narrow parallel beam of neutrons is incident normally on a uniform scattering sample. However, the neutron beam diverges from a point target over an angular range of 13° , (Figure 4.6). The neutron flux as defined by the alpha-detector varies across this angular interval. As the neutron beam at 250 mm from the source is slightly diverging, the sample thickness varies with the neutron angle, ϕ_n , and with the plane of the sample at 45° to the beam the variation of sample thickness with neutron angle is more marked. From Figure 4.9 it can be seen that as ϕ_n increases, the sample thickness increases. To correct for this the sample thickness term, x , in equation 4.16 was replaced by a weighted term.

The neutron beam profile, i.e. the variation of the neutron yield with angle as defined by the alpha detector is divided into angular intervals $\delta\phi_n$ and the fraction of the neutron beam per unit

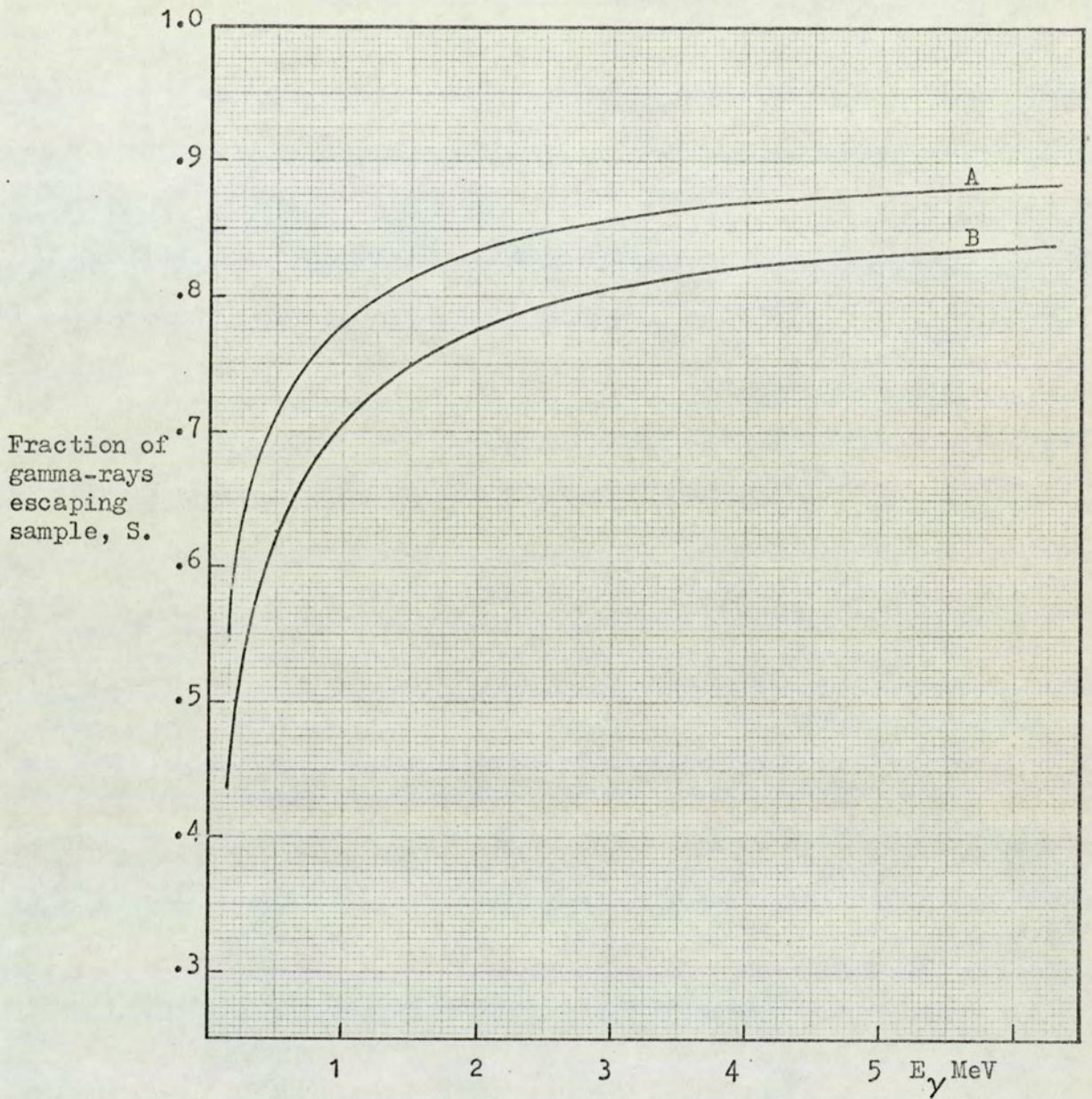


Figure 4.10. Gamma-ray absorption by a 19.8 mm titanium sample positioned at 45° to the neutron beam.

A _ at a 45° scattering angle and B _ at a 90° scattering angle.

beam, f_i , in the i^{th} angular interval is estimated. The fraction f_i is given by the ratio of the area under the neutron beam profile curve in the interval $(\delta\phi_n)_i$ to the total area under the neutron beam profile curve, and $\sum_i f_i = 1$. If x_i is the mean sample thickness in the interval $(\delta\phi_n)_i$ for a flat plate sample at 45° to the neutron beam, the effective sample thickness weighted by the incident neutron beam fraction per incident neutron is given by $\sum_i f_i x_i$.

The weighted sample thickness was evaluated using the neutron beam profile calculated in Figure 4.6. The beam profile was divided up into one degree intervals and the areas under the curve were measured with a planimeter to calculate the fractions f_i . The weighted sample thickness calculated in this way was only 1.2% higher than the sample thickness given by $\frac{b}{\cos 45^\circ}$, which is the sample thickness seen by the centre of the neutron beam.

4.4. The Integrated Neutron Flux,

One of the important advantages of the associated particle time of flight method is that it enables the neutron flux incident on the scattering sample to be accurately determined. The neutron flux is given by the α -monitor count. However, the α -monitor count has to be corrected for two effects. The corrections are for background radiation in the detector and for neutron absorption in the target assembly.

α - Monitor Background

The background correction can be divided into two parts. The first part is due to the detection of source neutrons and radiation promptly emitted in fast neutron interactions with the material of the target assembly. The second part of the correction is for the detection of γ -rays and β -particles resulting from the activation of the target assembly.

Immediately after switching off the deuteron beam, after each data cycle, the background count rate in the alpha-monitor was noted.

This background was entirely due to γ -rays and β -particles emitted by the active target assembly material, as prior to an experimental run the background count rate was zero. Provided the neutron yield remained constant, the correction for the activation background remained fairly constant for a period of up to eight hours. After a 1 h period of neutron production the activation background accounted for 1% of the α -monitor count. As this correction factor was checked regularly, the activation background was corrected for with a negligible experimental error. The γ -ray detector was used to investigate the source of the activation background observed by the α -detector. After a days experimental run the γ -ray detector was placed as close to the α -detector as possible to record the γ -ray spectrum of the active target assembly and to observe its rate of decay. The γ -ray spectrum fell from a maximum at zero pulse height to zero at 3 MeV pulse height with four prominent peaks superimposed at γ -ray energies of 0.511 MeV, 0.85 MeV, 1.81 MeV and 2.12 MeV. The 0.511 MeV γ -ray had a half life of approximately 10 min and the other γ -rays had half lives of several hours.

The sources of the γ -rays were identified using the table of isotopes⁷⁹ and the Barn cross-section book⁽³²⁾. The materials in the target assembly consisted mainly of iron, copper and zinc. The most probable activation reaction with iron is the $^{56}\text{Fe}(n,p)^{56}\text{Mn}$ reaction which has a cross-section of only 110 mb at 14 MeV. ^{56}Mn decays with a half life of 2.5 h and accounts for the three higher energy γ -rays mentioned above. The activation of both copper and zinc is predominantly by the (n,2n) reaction. A 0.511 MeV annihilation γ -ray is produced by the β^+ decay of ^{62}Cu following the $^{63}\text{Cu}(n,2n)^{62}\text{Cu}$ reaction which has a cross-section of 550 mb and ^{62}Cu has a half life of 10 min. The unstable products of the (n,2n) reaction with zinc and copper produce very few γ -rays.

Thin plastic scintillator sheet is an inefficient γ -ray and neutron detector. The efficiency of 0.5 mm NE 102A scintillator was estimated as 0.2% for 14 MeV neutrons: considering only (n,p) scattering with the hydrogen of the scintillator. The efficiency for γ -rays was calculated to be 0.6% at 0.3 MeV and 0.4% at 1 MeV γ -ray energies using the absorption coefficients of Grodstein⁽⁴⁷⁾ for carbon and hydrogen. One third of the scintillator area was exposed to α -particles and the whole area was effectively exposed to neutrons and γ -rays so the detection efficiencies must be multiplied by a factor of three for comparison with the α -efficiency. The direct neutron detection count is increased by neutrons elastically and inelastically scattered by the target assembly and by neutrons from (n,2n) reactions. The cross-sections for these processes with iron and copper are very large, and besides giving a flux of neutrons degraded in energy, the inelastic and (n,2n) reactions give rise to a large flux of prompt γ -rays. There is at present very little data on γ -ray production cross-sections in neutron reactions, but as an illustration of the magnitude of the processes the production cross-section of 0.85 MeV and 1.24 MeV γ -rays following neutron inelastic scattering from ^{56}Fe has been measured by Martin and Stewart⁽¹⁵⁾ as 1.95 barn. Thus in view of the prompt γ -rays emitted in activation reactions and the direct and scattered source neutrons the order of magnitude of this background correction must be several times greater than the activation background correction factor. Clearly the correction factor cannot be calculated in view of the difficult geometry and lack of cross-section data; the background was therefore measured experimentally.

To measure the neutron and γ -ray prompt background correction factor, the α -monitor count was first recorded for many different deuteron beam target currents, corresponding to neutron yields from 5×10^6 neutrons s^{-1} to 1.5×10^7 neutrons s^{-1} . The α -detector aperture was then replaced by a blank plate of the same thickness so that

all α -particles were completely shielded from the detector. The alpha-monitor count was then noted for the same target currents. This monitor count was entirely due to the neutron and γ -ray background. The monitor counts were corrected for the activation background giving a value of 5.5% for the percentage of the α -monitor count due to prompt neutrons and γ -rays. The value was the same for each neutron yield within $\pm 0.2\%$. As the blanking plate was only 1 mm thick it introduced a negligible amount of neutron and γ -ray shielding of the scintillator. Aluminium has low 14 MeV reaction cross-sections and coupled with its small thickness, it introduced a small amount of secondary radiation. It was assumed that this secondary radiation cancelled the loss of protons normally detected from the (n,p) reaction with iron, which also has a low cross-section. The estimated error in the determination of the neutron background was less than 0.5%. The prompt background correction factor, F_1 , was then equal to 0.945.

Absorption in the Target

The target assembly was designed to give minimum neutron absorption as the source neutrons had only a small thickness of material to penetrate. However, in the present use the neutron beam, defined by the associated α -particles, left the target at a mean angle of 38° to the normal to the plane of the target and this increased the neutron path length through the assembly. With information on the target holder supplied by the manufacturers the neutrons had to penetrate an estimated 5.5 mm of steel and 1.3 mm of water. The steel thickness was large because it included a path length of 3 mm through the strengthening rib across the back of the target holder which was penetrated because of the oblique angle of emission of the neutrons.

The intensity of the defined incident neutron flux on the scattering sample was reduced due to neutron elastic scattering and non-elastic reactions in escaping the target assembly. Neutron elastic

scattering is very forward peaked, for example the differential elastic scattering cross-section of iron, measured by Coon et al.⁽⁸⁰⁾, has a value of 2.7 barn/st. at a zero scattering angle and falls to a value less than 50 mb/st. at scattering angles greater than 35° . It would appear that a large fraction of the source neutrons elastically scattered in the target assembly would still pass through the scattering sample. A value of the elastic neutron scattering cross-section corrected for this effect was then calculated for each of the materials: hydrogen, oxygen and iron. Essentially the problem was to calculate the elastic cross-section for neutrons only scattered out of the solid angle subtended by the scattering sample.

The mean maximum scattering angle that neutrons could be scattered and still pass through the scattering sample was estimated as $8\frac{1}{2}^\circ$ for all the scattering samples used. The cross-section for neutrons elastically scattered by angles less than $8\frac{1}{2}^\circ$, σ_ℓ , using equation 4.2, is given by,

$$\sigma_\ell = 2\pi \int_0^{8\frac{1}{2}^\circ} \sigma(\theta) \sin\theta d\theta \quad \dots \quad 4.18$$

where $\sigma(\theta)$ is the differential elastic scattering cross-section in the angular interval between the integration limits. The corrected elastic cross-section is given by $\sigma_e - \sigma_\ell$ where σ_e is the elastic scattering cross-section.

Data on the total and non-elastic cross-sections was taken from the Barn book⁽³²⁾. The differential elastic scattering cross-section data for iron, oxygen and hydrogen was taken from Coon et al.⁽⁸⁰⁾, Bauer et al.⁽⁸¹⁾ and Murray⁽⁸²⁾. As differential elastic scattering cross-section data is always given in the centre of mass system of co-ordinates, the maximum laboratory system scattering angle of $8\frac{1}{2}^\circ$ was converted into the centre of mass system using equation (4.8). In the centre of mass system the maximum scattering angle for iron, oxygen and hydrogen becomes $8^\circ 36'$, 9° and 17° respectively. As the equations for

the differential cross-sections were not given in the literature, mean values of $\sigma(\theta)$ were used to solve equation (4.18). This introduced a negligible error as over the angular range of interest the differential cross-sections changed by less than the experimental error in the data points. The 14 MeV neutron cross-section data taken from the above references and calculated using equation 4.18 is summarised in Table 4.4.

Table 4.4

<u>Element</u>	σ_T	σ_e	$\overline{\sigma(\theta)}$	σ_l	corrected total cross-section
Hydrogen	0.66 barn	0.66 barn	<u>0.66</u> barn/st	0.014 b	0.646 b
Oxygen	1.6 "	0.88 "	1 " "	0.077 b	1.523 b
Iron	2.5 "	1.14 "	2.6 " "	0.184 b	2.316 b

The fraction of source neutrons escaping the target, F_2 , is then given by,

$$F_2 = \exp - \left(\Sigma_{Fe} x_1 + (\Sigma_o + \Sigma_H) x_2 \right) \quad 4.19$$

where $\Sigma_{Fe}, \Sigma_o, \Sigma_H$ are the corrected macroscopic total cross-sections for iron, oxygen and hydrogen respectively and x_1 and x_2 are the mean thicknesses of iron and water the neutrons penetrate.

The fraction of source neutrons escaping the target was calculated as 0.886.

The main uncertainty in this calculation was the mean $8\frac{1}{2}^\circ$ allowable angle for elastic scattering. However the neutron correction factor, F_2 , is rather insensitive to the value because the fraction F_2 calculated using the total neutron cross-section was only 1% lower.

The integrated neutron flux as determined by the α -monitor count was first corrected for the activation background in the α monitor detector and the corrected integrated flux was multiplied by the two

correction factors, F_1 and F_2 having values 0.945 and 0.886 respectively. In this way the integrated neutron flux was determined with an estimated error of less than 1%.

4.5. Gamma-ray Detector Efficiency

To determine the number of γ -rays emitted by the sample into the solid angle subtended by the detector crystal, the γ -ray spectrum has to be corrected for the detector efficiency. The absolute γ -ray detection efficiency, $T(E_\gamma)$, is the fraction of γ -rays, of energy E_γ , incident on the detector that interact with a finite loss of energy. The efficiency is a function of the source-detector geometry in that the path lengths through the crystal of the source γ -rays change with the source to detector separation.

To use the total absolute efficiency at a given energy, the integrated count in the pulse height response function of the detector is required. In the present work this information was impossible to obtain as the pulse height spectrum below the γ -ray discrimination level was not recorded. Even if the total spectrum could be recorded, the method has the draw back that the spectrum has to be corrected for radiation scattered into the detector by the collimator.

An alternative method is to use the full energy peak efficiency, $\epsilon(E_\gamma)$. The full energy peak efficiency is defined as the ratio of the number of counts within the full absorption peak, at energy E_γ , to the number of gamma-ray quanta of energy E_γ incident on the scintillator. It would be difficult to calculate the full energy peak efficiency directly because of the large number of multiple processes that occur in a scintillation detector. The peak efficiency was then determined by the following relationship

$$\epsilon(E_\gamma) = P(E_\gamma) T(E_\gamma) \dots \dots \dots 4.20$$

where $P(E_\gamma)$ is the peak to total ratio and it is defined as the fraction

of the total counts in the pulse height spectrum of a γ -ray line of energy E_γ which appear in the full energy peak. The peak to total ratio was measured experimentally and the absolute detection efficiency was calculated for the experimental geometry used.

With the detector crystal face positioned 1.39 m from the scattering sample, the detector subtended a very small solid angle at the sample and to a good approximation the source γ -rays incident on the crystal could be considered as a parallel beam. Assuming that the γ -ray flux is incident normally on the crystal face, the total efficiency is given by the fraction of interactions in the detector multiplied by the fraction of the incident radiation penetrating the detector entrance window,

$$T(E_\gamma) = e^{-\mu_A x_A} (1 - e^{-\mu_C x_C})$$

where x_A and x_C are the detector entrance window and crystal thicknesses respectively and μ_A and μ_C are the respective aluminium and crystal total linear γ -ray absorption coefficients. The use of the total absorption coefficient for the entrance window introduces an error into the absolute efficiency as degraded γ -rays from Compton interactions in the aluminium can still be detected. However this introduces no error in the full energy peak efficiency because any interactions in the entrance window produce degraded γ -rays of lower energy than the full absorption peak energy. The entrance window thickness consisted of the crystal packaging which the manufacturers stated as being equivalent to 280 mg/cm² of aluminium and the detector housing can which was 75 mg/cm² of aluminium. The total γ -ray absorption coefficients, less coherent scattering, were taken from values tabulated by Grodstein⁽⁴⁷⁾. Grodstein compared the calculated coefficients with the available experimental data and estimated the error in the calculated results. For γ -ray energies below 50 KeV the error was of the order 10%, however, with increasing energy the data

became more reliable and for the γ -ray energy range 0.5 MeV to several MeV the error was 2%. Considering the error in the dimensions of the machined crystal as being negligible, a 2% uncertainty in the absorption coefficients gave a 0.4% to a 1% error in the total efficiency for γ -ray energies varying from 0.5 MeV to 2 MeV.

4.5.1. Peak to Total Ratio and Full Energy Peak Efficiency

The peak to total ratio, $P(E_\gamma)$, depends in a complex manner on the incident γ -ray energy the absorption coefficients of the various interaction processes, the energy spectrum of the secondary photons, the crystal dimensions and the experimental geometry. It is better to measure the quantity experimentally, because of the many factors involved.

Suitable γ -ray sources for the measurement of the peak to total ratio must emit a single energy γ -ray, and this restricts the number of useful isotopic sources. However measurements were made at four γ -ray energies covering the energy range over which absolute differential cross-section measurements were made. The isotopic sources used were ^{137}Cs , ^{54}Mn , ^{22}Na , and ^{28}Al giving γ -ray lines of 0.662 MeV, 0.835 MeV, 1.28 MeV and 1.78 MeV respectively.

The spectra should be observed under scatter free and low background conditions. To keep the background low the detector must be shielded and to reduce scattering from the shield, the shield should be large and constructed of a dense material, usually lead. A shield was constructed of 50.8 mm thick lead bricks, and it measured 450 mm square by 750 mm tall. The detector was placed in the centre of the shield and the top of the shield was covered by a 25 mm thick lead sheet.

With an uncollimated source the peak to total ratio is independent of the source to detector distance for separations of 100 mm and greater. Heath⁽⁸³⁾ has shown that for a point source the peak to total ratio increases by less than 2% for a change in the source to detector distance from 30 mm to 100 mm. The thin disc shaped sources

were then positioned 120 mm above the crystal face. Finally the spectra were corrected for background radiation.

To determine the total count in the full energy peak the method suggested by Heath⁽⁸³⁾ was used, i.e. the low energy side of the peak was completed so that the peak was symmetrical. The total spectrum count was corrected for the back scatter peak, and the spectrum count of ^{22}Na , which decays by β^+ emission was corrected for the annihilation γ -ray spectrum. The subtraction of the 0.511 MeV annihilation spectrum did not introduce a large error as it sits on the flat part of the Compton spectrum of the 1.28 MeV γ -ray. The peak to total ratio had to be corrected for the increased spectrum count due to the detection of degraded γ -rays from the interaction of source γ -rays in the detector entrance window. At the energies peak to total ratio measurements were made, the interaction of γ -rays with aluminium is only by the Compton effect, Grodstein⁽⁴⁷⁾. To estimate the increase in the total spectrum count resulting from these interactions, it was assumed that the source γ -rays interacted only once in the aluminium crystal entrance window, and that half of the degraded γ -rays passed through the crystal. It was further assumed that the forward scattered γ -rays were detected with an efficiency given by $(1 - e^{-\mu_C x_C})$ where μ_C is the total linear absorption coefficient for the mean energy of the forward scattered γ -rays. This approximation was justified in that, at most, only 3% of the source γ -rays interacted in the aluminium entrance window and that the total spectrum count was corrected by only 1% or less. The measurements were made three times with each source and the results are shown in Table 4.5. The experimental error, due mainly to the backscattering correction was estimated as 3%.

Table 4.5

E_γ MeV	$P(E_\gamma)$ Measurements	Heath ⁽⁸³⁾	Borkowski ⁽⁸⁴⁾	Lazar ⁽⁸⁵⁾	Crumpton ⁽⁸⁶⁾
0.662	0.51 \pm 0.015	0.534	0.55	0.542	0.505
0.835	0.45 \pm 0.014	0.469	-	0.476	0.443
1.28	0.354 \pm 0.010	-	-	-	-
1.78	0.266 \pm 0.008	0.292	-	0.295	-

In table 4.5 the results are compared with the available experimental data obtained under similar conditions for 76.2 mm crystals. Heath's and Lazar's results are for a point source 100 mm above the crystal; Barowski's results are for a broad parallel beam and Crumpton's results are for a disc source 100 mm above the crystal. With the exception of the results due to Crumpton the present measurements are several percent lower than the other data. As the most extensive published work is due to Heath⁽⁸³⁾ a smooth curve was drawn through the measured points following Heath's curve; this is shown in Figure 4.11. The measured peak to total ratios were, on average, 4.5% lower than Heath's results.

With values of the peak to total ratio, $P(E_\gamma)$, taken from the curve drawn through the experimental results, the peak efficiency was calculated by the following equation,

$$\epsilon(E_\gamma) = P(E_\gamma) e^{-\mu_A x_A} (1 - e^{-\mu_C x_C}) \quad 4.22$$

The full energy peak efficiency vs. γ -ray energy curve is plotted in Figure 4.12. Jarczyk et al.⁽⁸⁷⁾ measured the peak efficiency for several different sized crystals for a broad parallel beam of radiation. They made measurements with a 76.2 mm crystal at two energies, 0.662 MeV and 2.75 MeV; their results are plotted in Figure 4.12. The results of Jarczyk et al. are in good agreement with the present peak efficiency results even though the peak to total ratio values used were generally lower than the comparison data.

The error in the peak efficiency owing to the errors in the peak to total ratio and γ -ray absorption coefficient data was estimated as 3.5% adding the errors quadratically.

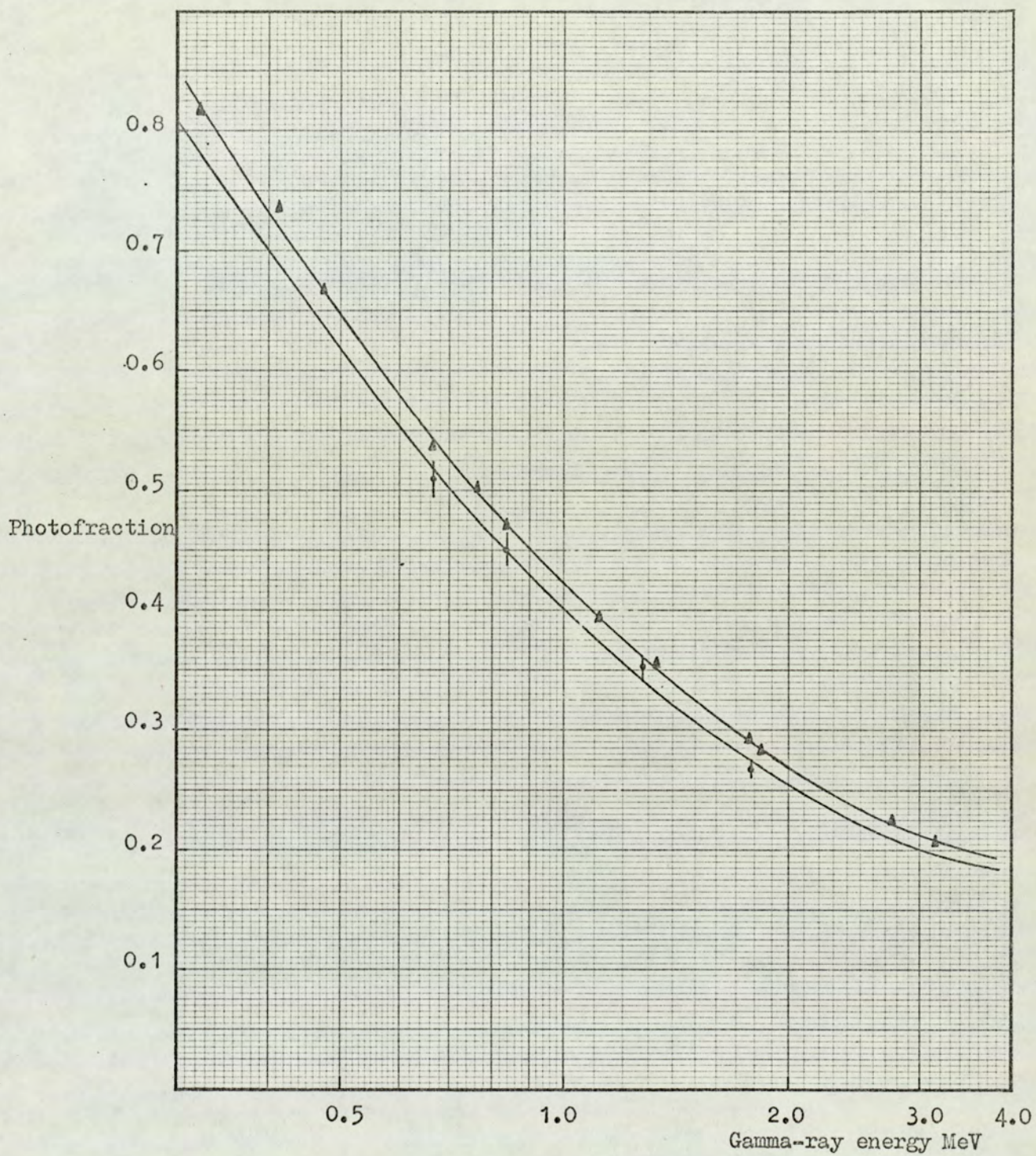


Figure 4.11. Peak to total ratio for a 76.2 mm (3in) sodium iodide crystal.

- Measured values.
- ▲ Heath's⁽⁸³⁾ results.

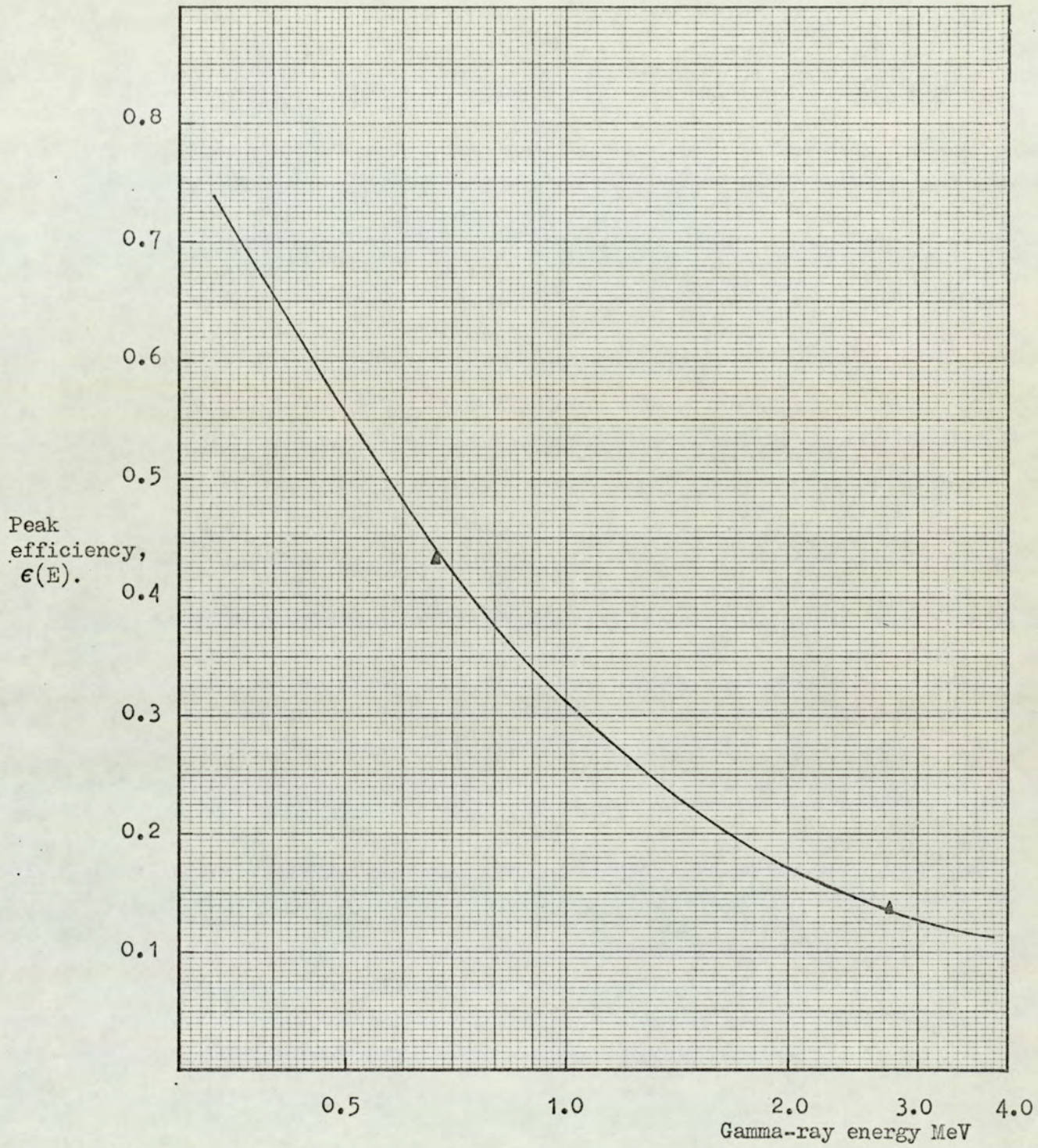


Figure 4.12. Peak efficiency of the 76.2 mm sodium iodide crystal.

▲ Peak efficiency measurements of Jarczyk et al. ⁽⁸⁷⁾

CHAPTER 5Absolute Cross-section Measurement Results5.1. Differential Cross-section Measurement Procedure

With the electronic system set as described in Chapter 3, γ -ray spectra were observed for differential cross-section measurements. The procedure adopted for taking measurements is described below.

The electronics was switched on at least $1\frac{1}{2}$ h prior to taking measurements to allow the system to stabilise. The neutron source was also run for a minimum of 45 min prior to an experimental run to allow the activity of the γ -ray detector and the target assembly to begin to level off.

Alternate runs were made with the scattering sample in position and with the sample removed for the background correction to the spectrum. The runs were made for the same integrated neutron yield as determined by the α -monitor. The magnitude of the background correction to the γ -ray spectrum was found to be dependent on the source strength, not simply the integrated neutron yield, so it was important to maintain a constant source strength to enable the correct background correction to be made; this point is discussed in section 5.1.1. The need to maintain a constant source strength limited the intensity of the neutron source. The α -detector photomultiplier could operate at count rates in excess of 10^5 counts s^{-1} . However, in practice the count rate was usually limited to between $3 \cdot 10^4$ to $3.5 \cdot 10^4$ counts s^{-1} , as this was the maximum neutron yield that could be maintained with good stability for long periods, up to eight hours, and this corresponded to a source strength of 10^7 neutrons s^{-1} .

A single data accumulation period was about 25 min. and corresponded to an α -monitor count of $5 \cdot 10^7$. After this period the multichannel analyser γ -ray spectrum was printed out on paper tape. The background was then subtracted with the sample removed and the

corrected spectrum was printed out. After this data cycle the deuteron beam was switched off and the background count rate in the α -monitor was noted. This count rate gave the activation background.

The accumulated γ -ray spectrum in the multichannel analyser was cleared after each data cycle to check the energy calibration because of the slowly varying gain of the γ -ray detector. The γ -ray energy calibration was checked by observing the channel about which the 1.28 MeV γ -ray peak of ^{22}Na was centred. The drift, usually less than half a channel, was corrected by adjusting the fine gain of the main amplifier.

The γ -ray spectra obtained from each data cycle were then added by hand. A final spectrum at a given scattering angle was obtained after about twenty such data cycles and it took two to three days to accumulate.

5.1.1. The need for Stability in the Neutron Source Strength

It follows from equation 4.16, in which $G(\theta) \propto \phi$, that the γ -ray signal count rate, $G(t)$ is proportional to the neutron source strength; i.e. $G(t) \propto S(t)$.

The recorded background results from random coincidences between the background flux incident on detector and the alpha-detector pulses. Thus the recorded γ -ray detector background count rate, $B(t)$, is proportional to the product of the background flux and the α -monitor count rate both of which are proportional to the neutron source strength, $S(t)$. It follows that: $B(t) \propto [S(t)]^2$.

This illustrates the necessity of keeping the neutron source strength, $S(t)$, constant because the recorded number of background counts, B , after a given integrated neutron yield, S , is then proportional to $S(t)$, whereas the signal count is simply proportional to S .

5.2. Silicon

5.2.1. The Scattering Sample

The scattering sample was made of powdered silicon because it

is a very hard material and difficult to machine. 99.9% pure silicon powder ($< 45 \mu\text{m}$) was packed into a thin walled rectangular vessel which was made of 0.5 mm tin plate. The sample measured 120 mm by 70 mm and was 32.4 mm thick. The sample had a density of $1,330 \text{ kg m}^{-3}$ which is considerably lower than the density of solid silicon ($2,400 \text{ kg m}^{-3}$). An identical empty vessel was used for the background subtraction runs so that the accumulated γ -ray spectrum was due to the silicon with no contribution from the iron vessel.

5.2.2. Gamma-Ray Spectra and Interpretation

Gamma-ray angular distribution measurements following the interaction of 14 MeV neutrons with many elements have shown that the shape of the distributions vary slowly with angle. For this reason, and in view of the good angular resolution, $\pm 4^\circ$, of the present method, differential cross-section measurements could be made at large angular intervals, i.e. 15° to 20° , to obtain an angular distribution. Spectra were accumulated at six scattering angles: 30° , 35° , 45° , 75° and 90° .

The use of a 100 channel analyser restricted the energy range over which the spectra could be recorded, without having too coarse an energy interval per channel. Spectra were recorded for the 1 MeV to 4 MeV pulse height region; the lower limit was set by the γ -ray discriminator. A spectrum is shown in Figure 5.1. This is typical of all the spectra obtained from silicon and the one shown was obtained at a 45° scattering angle. The spectrum is almost continuous with only a single γ -ray line resolved at 1.78 MeV. The first escape peak of the 1.78 MeV line is visible at 1.27 MeV. The error bars shown in the region of the full energy peak are discussed in section 5.2.3. The rather poor statistics result from the low spectrum counts, however the number of counts is approximately three times greater than typically obtained by Martin and Stewart⁽¹⁵⁾ who also used the associated particle method. Each spectrum took approximately 20 h to accumulate.

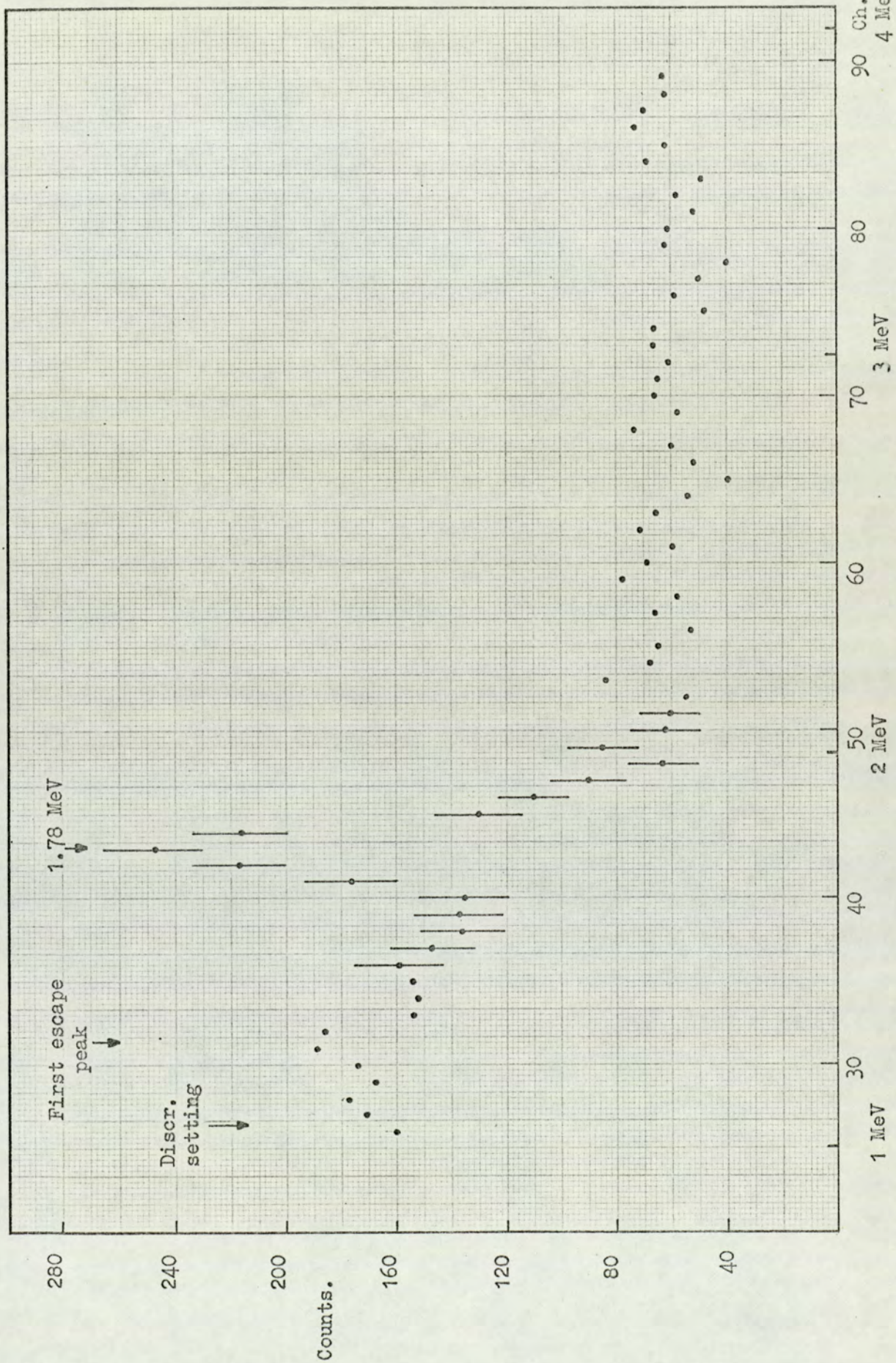
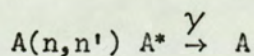


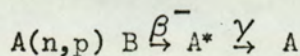
Figure 5.1. The gamma-ray spectrum for silicon, scattering angle 45° .

The three most probable reactions giving rise to the detected γ - rays are the (n,n') , (n,p) and (n,α) reactions. The silicon non-elastic cross-section, at 14 MeV is 1,020 mb and the (n,p) and (n,α) reactions have cross-sections of approximately 260 mb and 80 mb respectively ⁽³²⁾; therefore neutron inelastic scattering has the largest cross-section.

Natural silicon has three stable isotopes ^{28}Si , ^{29}Si and ^{30}Si with isotopic abundances of 92.18%, 4.71% and 3.12% respectively. The main source of γ - rays was therefore inelastic scattering with ^{28}Si . The level structure of the excited levels of ^{28}Si is shown in Figure 5.2 for the first levels with known spins and parities; the information is taken from Endt and Van der Leun ⁽⁸⁸⁾. The 1.78 MeV γ - ray is identifiable with the transition between the first excited state and ground state of ^{28}Si . This γ - ray is produced by neutron inelastic scattering exciting the first level and in cascade transitions of similarly excited higher levels. This is the only reaction mode producing 1.78 MeV prompt γ - rays. However, the same γ - ray can be produced not only promptly by a reaction of the type



but also by the reaction



In some cases the (n,p) reaction leads to a B which decays to the ground state of A or is long-lived compared with the duration of the run. In the case of the $^{28}\text{Si}(n,p)^{28}\text{Al}$ reaction, ^{28}Al has a half-life of only 2.3 min and it decays in 100% of its transitions to the 1.78 MeV level of ^{28}Si . Clearly the (n,p) contribution of the silicon sample must be considered.

The cross-section for the $^{28}\text{Si}(n,p)^{28}\text{Al}$ reaction is 260 mb ⁽³²⁾ so the scattering sample (in excess of 300 gm) becomes a strong source of 1.78 MeV γ - rays. The activity $A(t)$ at a time t , of the sample owing

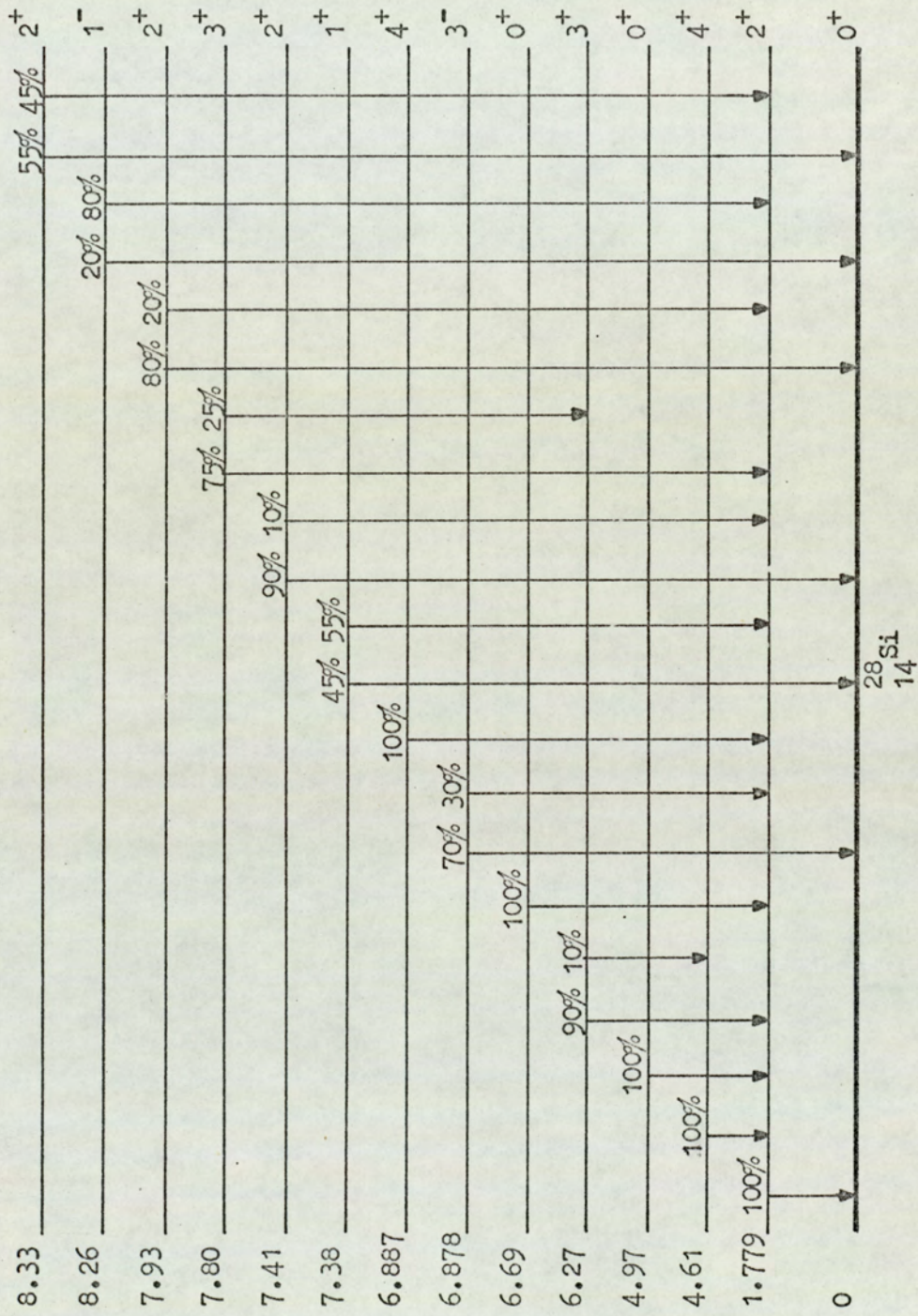


Figure 5.2. The level structure of $^{28}\text{Si}_{14}$, from Endt and Van der Leun (88).

to the formation of ^{28}Al is given by

$$A(t) = VN I_0 \sigma (1 - e^{-\lambda t})$$

where V is the sample volume, N is the number of ^{28}Si nuclei per unit volume, I_0 is the incident neutron flux, σ is the (n,p) reaction cross-section and λ the ^{28}Al decay time constant. The activity of the sample reaches equilibrium, given by $VN I_0 \sigma$, after approximately 7 min because of the short half-life of ^{28}Al . However, the accumulation of the ^{28}Al 1.78 MeV γ -rays in the pulse height spectrum is restricted by the time of flight discrimination system. The ^{28}Al decays randomly and thus only γ -rays in random coincident with an α -particle pulse are recorded in the spectrum. The number of ^{28}Al 1.78 MeV γ -rays recorded in the full energy peak C, is given by

$$C = A(t) \Delta t \alpha(t) \epsilon(E_\gamma) \frac{\Delta\Omega}{4\pi} T \quad 5.1$$

where Δt is the 25 ns time window of the single channel analyser $\alpha(t)$ is the α -detector count rate, $\epsilon(E_\gamma)$ is the full energy peak detector efficiency, $\Delta\Omega$ is the solid angle subtended by the detector, and T is the total running time with the sample in position which was ~ 10 h. Equation 5.1 was evaluated for the $^{28}\text{Si}(n,p)^{28}\text{Al}$ reaction assuming that the sample was always at the equilibrium activity. It gave a contribution in the 1.78 MeV γ -ray peak from ^{28}Al of only 2 counts after a period of 10 h compared with approximately 700 counts from inelastic scattering. Hence the (n,p) contribution could be neglected and the 1.78 MeV γ -ray in Figure 5.1 was solely attributed to inelastic scattering.

Estimation of the Full Energy Peak Count

The usual procedure for estimating the number of counts in a full energy peak in a spectrum containing many different energy γ -rays is referred to as the graphical stripping technique. In this method, the full energy peak count of the highest energy γ -ray present is directly

determined, as the peak base line is the abscissa, and then a point by point subtraction of the spectral shape corresponding to the intensity of the γ -ray is made from the composite spectrum. When this subtraction has been completed, the γ -ray of the next highest energy has its total absorption peak resting on the abscissa and its intensity can be estimated by the counts in the peak. The spectral shape corresponding to this second γ -ray is then subtracted from the remaining distribution, and the process is continued. For this method monoenergetic γ -ray response functions for each of the γ -rays present must be known. However, it was impossible to use this procedure with the spectra obtained from the silicon sample for two reasons: firstly because only a single γ -ray line was resolved in a spectrum with poor statistics and secondly because the highest energy γ -rays were not recorded.

To estimate the full energy peak counts a method similar to that suggested by Covell⁽⁸⁹⁾ was used. Covell's method for estimating the intensity of a single γ -ray in a complicated spectrum is to measure a calibrated fraction of the area of the total absorption peak. In the present work the peak count was low so that as large a fraction as possible of the full energy peak was used. A line was drawn across the base of the photopeak, as shown in Figure 5.3. The events above the line are a fixed fraction of the total peak count.

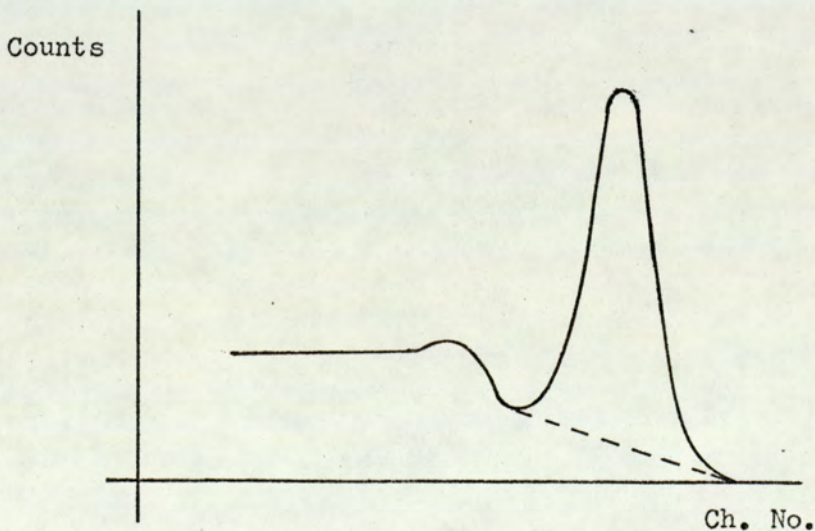


Figure 5.3

The correction factor to relate the fractional peak count to the true peak count is obtained by observing the γ -ray spectra of isotopic sources emitting γ -rays of the energy of interest. In this way the peak correction factor could be measured with an uncertainty of less than 1%. In using this method to estimate the full energy peak count it is assumed that the peak does not sit on any sharp irregularities in the spectrum. The method has the advantage that the fractional peak count is independent of whether the peak of interest sits on a flat continuous spectrum or on a smoothly increasing spectrum.

An ^{28}Al source which emits a 1.78 MeV γ -ray was used to measure the peak correction factor for the estimation of the silicon spectrum peak intensity. The ^{28}Al spectrum was recorded with the source placed at the the collimator entrance so that the correction factor accounted for any distortion to the spectrum owing to the γ -rays scattered into the detector by the collimator. The spectrum also gave the number of channels over which a 1.78 MeV γ -ray peak spreads.

5.2.3. Differential Gamma-Ray Production Cross-Sections

The final equation used to evaluate the absolute differential γ -ray production cross-sections was:

$$\frac{d\sigma_{\gamma}}{d\Omega} = \frac{p g(\theta)}{N F_1 F_2 \phi \left(\sum_i f_i x_i \right) \epsilon(E_{\gamma}) S(E_{\gamma}, \theta) \frac{\pi r^2}{\rho^2}} \quad 5.2$$

where p is the γ -ray peak correction factor, defined in section 5.2.2, $g(\theta)$ is the fractional peak counts, ϕ is the integrated neutron flux given by the α -monitor count corrected for the activation background detected by the monitor, ρ is the sample to detector face flight path, r is the crystal radius and the remaining terms are as defined previously.

The measured values of the differential production cross-sections of the 1.78 MeV γ -ray following the inelastic scattering of 14.2 MeV neutrons from ^{28}Si are given in Table 5.1. The experimental errors in

the results are given for completeness before they are discussed at the end of this section.

Table 5.1

$^{28}\text{Si}(n,n'\gamma)^{28}\text{Si}$; $E_n = 14.2$ MeV; $E_\gamma = 1.78$ MeV

θ	$\cos\theta$	$\frac{d\sigma_\gamma}{d\Omega}$
90°	0.0	33.1 ± 4.5 mb/st
75°	0.2588	32.2 ± 4.4 " "
60°	0.5	36.9 ± 5.0 " "
45°	0.7071	40.6 ± 5.5 " "
35°	0.8192	34.7 ± 4.7 " "
30°	0.8660	32.8 ± 4.4 " "

In Table 5.2. all the 90° differential cross-section measurements are compared and brief details of the different experimental methods used are given. Although all the results agree within the large quoted errors, there are two low values for the differential cross-section, 23.8 mb/st and 26.2 mb/st and two high values, 31.5 mb/st and 33.6 mb/st. There is no obvious reason for this discrepancy, and it cannot be attributed to methods employing time of flight discrimination as a high and low result were obtained with systems employing time of flight discrimination. The present result for the 90° differential cross-section, 33.1 ± 4.5 mb/st is in good agreement with the higher values. One other point apparent from the comparison of results in Table 5.2. is the comparatively excellent angular resolution of the present method which was achieved maintaining a relatively good experimental error.

The Experimental Error

The errors in many of the terms of equation 5.2, which was used to calculate the absolute differential cross-sections, have been discussed

Table 5.2 $^{28}\text{Si}(n,n'\gamma)^{28}\text{Si}$; $E_\gamma = 1.78 \text{ MeV}$

$\left(\frac{d\sigma_\gamma}{d\Omega}\right)_{90^\circ}$ mb/st	E_n MeV	Angular resolution degrees	Comment on method
33.1 ± 4.5	14.2	$\pm 4^\circ$	Present work
$26.2 \pm 4.4^{(b)}$	14.8	$\pm 18^\circ$	Nellis et al. (8) Time of flight discrimination pulsed beam method. Anti-coincidence NaI(Tl) spectrometer
$31.5 \pm 7^{(a,b)}$	14.7	$\pm 20^\circ$	Thompson and Engesser (5) No time of flight discrimination small sample with a massive shield, NaI(Tl) single crystal.
33.6 (c)	14.1		Martin and Stewart (15) Time of flight discrimination associated particle method, single NaI(Tl) crystal.
$23.8 \pm 7^{(d)(b)}$	14	$60^\circ \rightarrow 140^\circ$	Caldwell et al. (26) Open geometry, no time of flight discrimination, large scattering sample; Single NaI(Tl) crystal.

- (a) Corrected for $^{28}\text{Si}(n,p)^{28}\text{Al}$ contribution.
- (b) Converted to isotopic cross-section by dividing by the isotopic abundance of ^{28}Si .
- (c) Calculated from least squares fit equation.
- (d) Corrected for neutron attenuation and γ -ray absorption in the large scattering samples, but not clear whether corrected for the $^{28}\text{Si}(n,p)^{28}\text{Al}$ contribution, which would reduce the value.

throughout the text. The remaining terms are now considered.

The largest single source of error was the estimation of the full energy γ -ray peak intensity. If C_i is the spectrum count in a single channel in the region of the full energy γ -ray peak, then the standard error in C_i , given by c_i , is

$$c_i = (C_i + S_i)^{1/2}$$

where S_i is the total background counts subtracted from the i^{th} channel with the scattering sample removed. The total spectrum count in the region of the full energy peak is then

$$\sum_1^n C_i \pm \left(\sum_1^n c_i^2 \right)^{1/2}$$

where the peak extends over n channels. The fraction error in $\sum_1^n C_i$ was typically 3%. However a much larger error arose in estimating the fractional peak count. The fractional peak count, $g(\theta)$, is given by $\frac{\sum_1^n C_i}{\sum_1^n C_i - \sum_1^n B_i}$ where B_i is the base line counts per channel on which

the peak sits. The error in $\sum_1^n B_i$, given by b , was typically

estimated as 6%. The standard error in peak counts $g(\theta)$ is then given

by
$$\left(\sum_1^n c_i^2 + b^2 \right)^{1/2}$$

For the 1.78 MeV γ -ray from the silicon sample, the fractional error in $g(\theta)$ was estimated as 12%.

The angle between the scattering sample and the neutron beam could be positioned to one degree and this introduced an uncertainty in the sample thickness $\sum_1^n f_i x_i$ of 1.5%. The solid angle, $\Delta \Omega$, subtended by the detector is given by $\pi r^2 / \rho^2$. Owing to the sample thickness, ρ was uncertain by ± 15 mm giving an error in $\Delta \Omega$ of 2%. The number of ^{28}Si nuclei per unit volume had an estimated uncertainty of 3.5% owing to variations in the homogeneity of the sample.

The errors in each term of equation 5.1 are summarised in

Table 5.3.

Table 5.3.

Term	Estimated fractional error
Peak Counts, $g(\theta)$	12%
Peak efficiency $\epsilon(E_\gamma)$	3.5%
Sample thickness $\sum_i f_i x_i$	1.5%
Peak correction factor, p	0.7%
Corrected integrated flux, $F_1 \cdot F_2 \phi$	1.0%
Nuclei/unit vol., N	3.5%
γ -ray absorption, S	0.5%
Solid angle, $\Delta\Omega$	2.0%

The error in the differential cross-section was obtained by adding the errors in each term quadratically, to give an estimated experimental error in the results for silicon of 13.5%. The fractional error in the present results is smaller than the errors in the other results given in Table 5.2. This is undoubtedly due to the accuracy with which the integrated neutron flux can be estimated using the associated particle time of flight method.

5.2.4. The Angular Distribution and Integrated Cross-Section of the $^{28}\text{Si}(n,n'\gamma)^{28}\text{Si}$ 1.78 MeV γ -ray

Owing to the limited laboratory space differential cross-section measurements could not be made at scattering angles greater than 90° . However, whether the interaction mechanism is described by a direct interaction or compound nucleus theory; the theories predict that the γ -ray angular distributions are symmetrical about the 90° scattering angle⁽²³⁾. Furthermore, all γ -ray production angular distribution measurements, in the interaction of 14 MeV to 15 MeV neutrons in the 0° to 180° angular interval, have shown the angular distributions to be symmetrical about 90° . It was, therefore, assumed that the measured

distributions are symmetrical about 90° . The experimental work referred to in support of this assumption was for the elements ^{12}C , ^{14}N , ^{16}O , ^{24}Mg investigated by Ashe et al.⁽¹⁰⁾, Benetskii⁽¹³⁾, Martin and Stewart⁽¹⁴⁾ Benveniste⁽¹⁶⁾ and Anderson⁽¹²⁾. Some of the distributions were found to be isotropic.

The angular distribution was obtained by a least squares fit of a polynomial expression to the experimental differential cross-section measurements. Gamma-ray angular distributions predicted by the theory are of the form

$$\sigma(\theta) = A_0 + A_2 P_2(\theta) + A_4 P_4(\theta)$$

where $P_2(\theta)$ and $P_4(\theta)$ are the second and fourth order Legendre polynomials and A_0 , A_2 and A_4 are constants. This equation reduces to the form

$$\sigma(\theta) = a_0 + a_2 \cos^2 \theta + a_4 \cos^4 \theta \dots \quad 5.3$$

where a_0 , a_2 and a_4 are new constants.

A least squares fit of equation 5.3 was made to the differential production cross-section measurements of the $^{28}\text{Si}(n,n'\gamma) ^{28}\text{Si}$, 1.78 MeV γ -ray as described in appendix 1. The equation of the angular distribution is,

$$\sigma(\theta) = 31.5 \pm 1.6 + (38.4 \pm 11.7) \cos^2 \theta - (48.5 \pm 13.4) \cos^4 \theta$$

The differential cross-section measurements for the 1.78 MeV γ -ray and the fitted curve are plotted in Figure 5.4. Also plotted in Figure 5.4 is the angular distribution of Martin and Stewart⁽¹⁵⁾. The fitted distribution to the present results is in good agreement with their curve. The anisotropy in the angular distribution is not very marked and a straight line, giving an isotropic distribution, could be drawn through the data points within the error bars. However, the similarity of the fitted curve with the distribution of Martin and Stewart suggests that the angular distribution is anisotropic. The

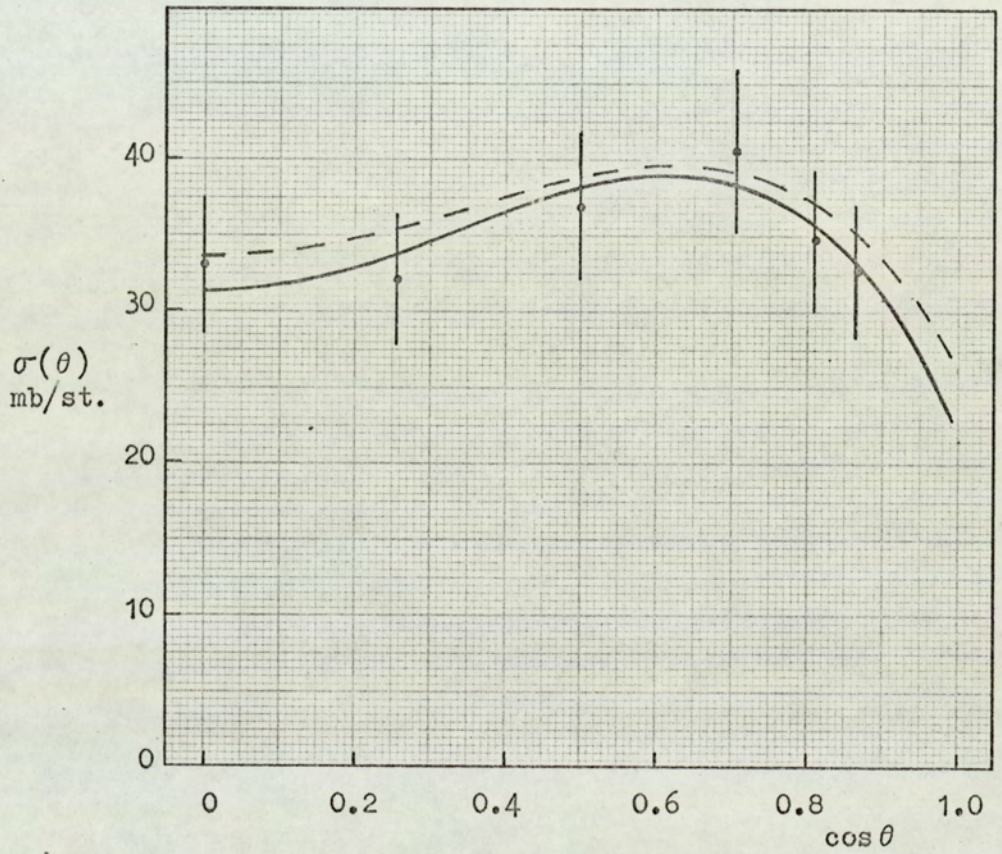


Figure 5.4. The angular distribution of the 1.78 MeV gamma-ray from ^{28}Si . ($E_n = 14.2$ MeV)

--- Distribution due to Martin and Stewart⁽¹⁵⁾.

The equation of the fitted curve was therefore used to calculate the integrated cross-section.

As discussed in section 4.1 the integrated γ -ray production cross-section is given by

$$\sigma(n, n'\gamma) = 4\pi \int_0^{\pi/2} \sigma(\theta) \sin\theta \, d\theta$$

so that

$$\begin{aligned} \sigma(n, n'\gamma) &= 4\pi \int_0^{\pi/2} (31.5 + 38.4 \cos^2\theta - 48.5 \cos^4\theta) \sin\theta \, d\theta \\ &= 434 \text{ mb} \end{aligned}$$

Error in the Integrated Cross-Section

The integrated cross-section is given by

$$\sigma = 4\pi \int_0^{\pi/2} (a_0 + a_2 \cos^2\theta + a_4 \cos^4\theta) \sin\theta \, d\theta$$

where a_0 , a_2 and a_4 are the coefficients obtained from a least squares fit to the measured differential cross-sections. Integrating this expression between the limits gives

$$\sigma = 4\pi \left(a_0 + \frac{a_2}{3} + \frac{a_4}{5} \right)$$

If α is the error in a_i the cross-section is given by

$$\sigma = 4\pi \left(a_0 \pm \alpha_0 + \frac{a_2 \pm \alpha_2}{3} + \frac{a_4 \pm \alpha_4}{5} \right)$$

The error, $\delta\sigma$, in the integrated cross-section is then given by,

$$\delta\sigma = \pm 4\pi \left(\alpha_0^2 + \frac{\alpha_2^2}{9} + \frac{\alpha_4^2}{25} \right)^{\frac{1}{2}}$$

The total cross-section measurements for the production of 1.78 MeV γ -rays by the $^{28}\text{Si}(n, n'\gamma)^{28}\text{Si}$ reaction are compared in Table 5.4. The present result is approximately mid-way between the two reported cross-section measurements and it agrees with the reported values within the experimental errors.

Table 5.4.

$\sigma(n, n'\gamma), {}^{28}\text{Si}$ $E_\gamma = 1.78 \text{ MeV}$	Reference
$434 \pm 63 \text{ mb}$	Present work
$471 \pm 70 \text{ mb}$	Martin and Stewart ⁽¹⁵⁾
$370 \pm 60 \text{ mb}$	Benetskii ⁽⁹⁰⁾

5.3. Sulphur5.3.1. The Scattering Sample

Sulphur is readily available in powdered form, flowers of sulphur, and as its melting point is only 120°C a solid scattering sample was cast. The sulphur was melted in an open aluminium container. The molten sulphur on cooling formed a solid surface crust and as the main body of the sulphur crystallised cavities were formed throughout the block. To overcome this problem the liquid sulphur was stirred until its temperature was just above its melting point and then the container was lowered into a cold water bath while a stream of hot air from a 1 kW hot air blower was played on the surface. The rather rapid cooling discouraged the growth of large crystals and the stream of hot air prevented a surface crust forming. The sulphur block after cooling was machined to a uniform thickness and then an X-ray radiograph was made of the sample to inspect it for cavities. Six attempts were required before a large enough uniform sample was made. The sample used was 100 mm by 120 mm and it was $27.7 \pm 0.1 \text{ mm}$ thick. The density of the sample was measured as $1,980 \pm 10 \text{ kg m}^{-3}$ and this is in good agreement with the published value, which is given as 2,000 to $2,100 \text{ kg m}^{-3}$.

The total 14.2 MeV neutron cross-section for sulphur is 1.92 barns⁽³²⁾ and this gives a neutron transmission for the scattering sample of 76% with the sample positioned at 45° to the beam. Sulphur

has four stable isotopes, ^{32}S , ^{33}S , ^{34}S and ^{36}S and the two most abundant are ^{32}S and ^{34}S with isotopic abundances of 95.0% and 4.22% respectively.

5.3.2. Gamma-Ray Spectra

The γ -ray spectra were recorded for the 1 MeV to 4 MeV pulse height region. Spectra were accumulated at five scattering angles: 90° , 70° , 60° , 40° and 25° . Figure 5.5. shows the 90° γ -ray spectrum. This is typical of the γ -ray spectra except that at the lower scattering angles the intensity of the high energy peak was noticeable larger and this is illustrated in Figure 5.6 which shows the 40° γ -ray spectrum. The running time taken to accumulate each spectrum was ~ 20 h. Each spectrum shows three peaks clearly resolved above the continuous spectrum at energies of 2.24 MeV, 1.7 MeV and 1.27 MeV. The two lower energy peaks coincide with the first and second escape peaks of the 2.24 MeV γ -ray and the 1.27 MeV peak also coincides with the first escape peak of the 1.7 MeV γ -ray.

To estimate the full energy peak count of the 2.24 MeV γ -ray, the method described for the silicon results was used, i.e. a line was drawn across the base of the peak and the fractional peak count was multiplied by a correction factor. The nearest energy γ -ray emitted by an isotopic source that could be used to measure the peak correction factor was 2.16 MeV from ^{38}Cl which has a 37 min half-life. The ^{38}Cl was made by irradiating a sample of potassium metal with 14 MeV neutrons; the isotope is produced by the $^{41}\text{K}(n, \alpha)^{38}\text{Cl}$ reaction. Unfortunately ^{41}K has an isotopic abundance of only 6.9% and the isotope could not be produced with an intense activity. The irradiated potassium sample gave three γ -ray lines at 1.29 MeV, 1.59 MeV and 2.16 MeV. The 2.16 MeV γ -ray was completely resolved from the lower energy γ -rays thus enabling the peak correction factor to be measured; it was measured as 1.44 ± 0.015 .

Before the 1.7 MeV peak intensity was estimated the 2.24 MeV

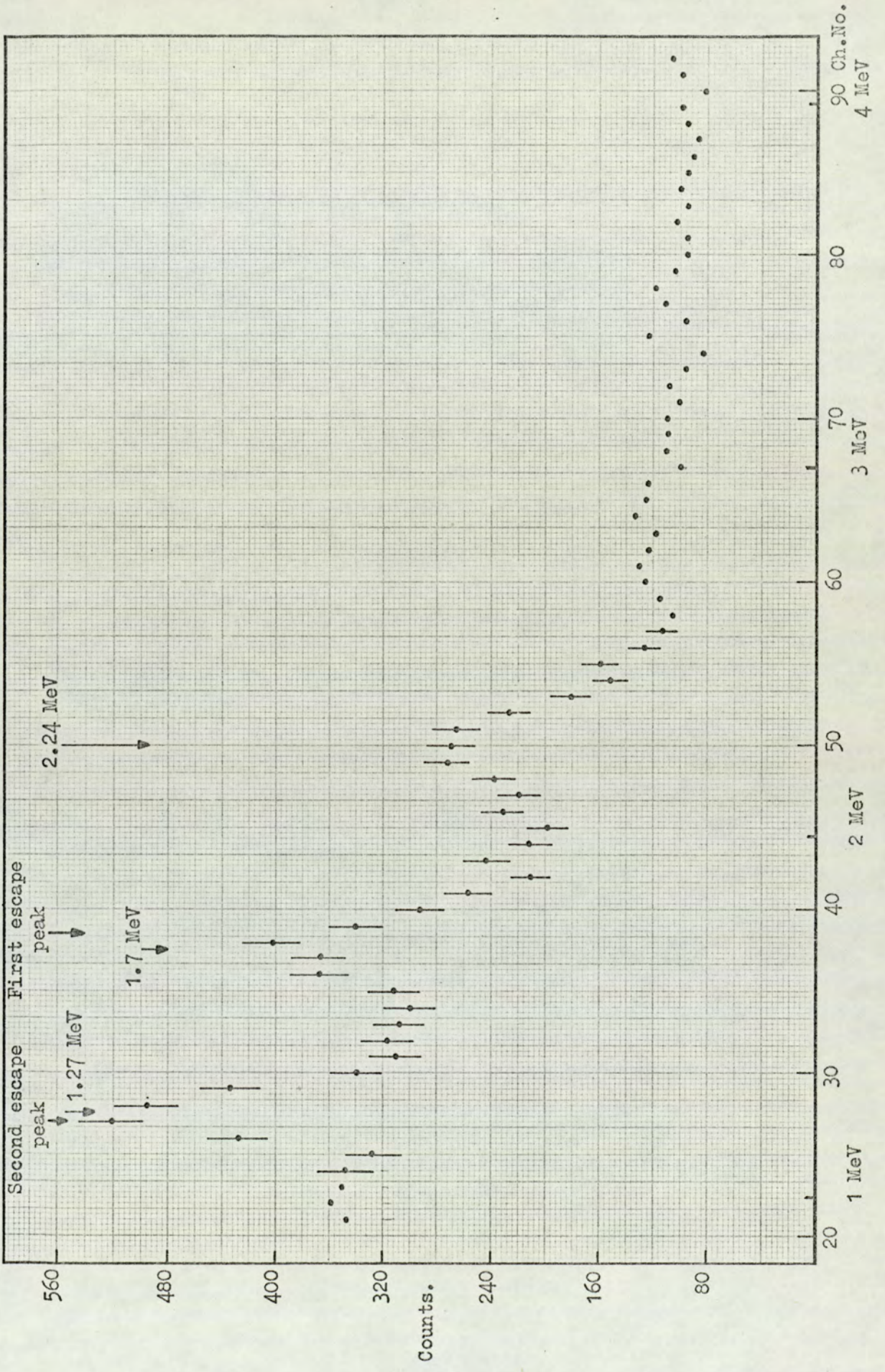


Figure 5.5. The gamma-ray spectrum for sulphur, (scattering angle 90°).

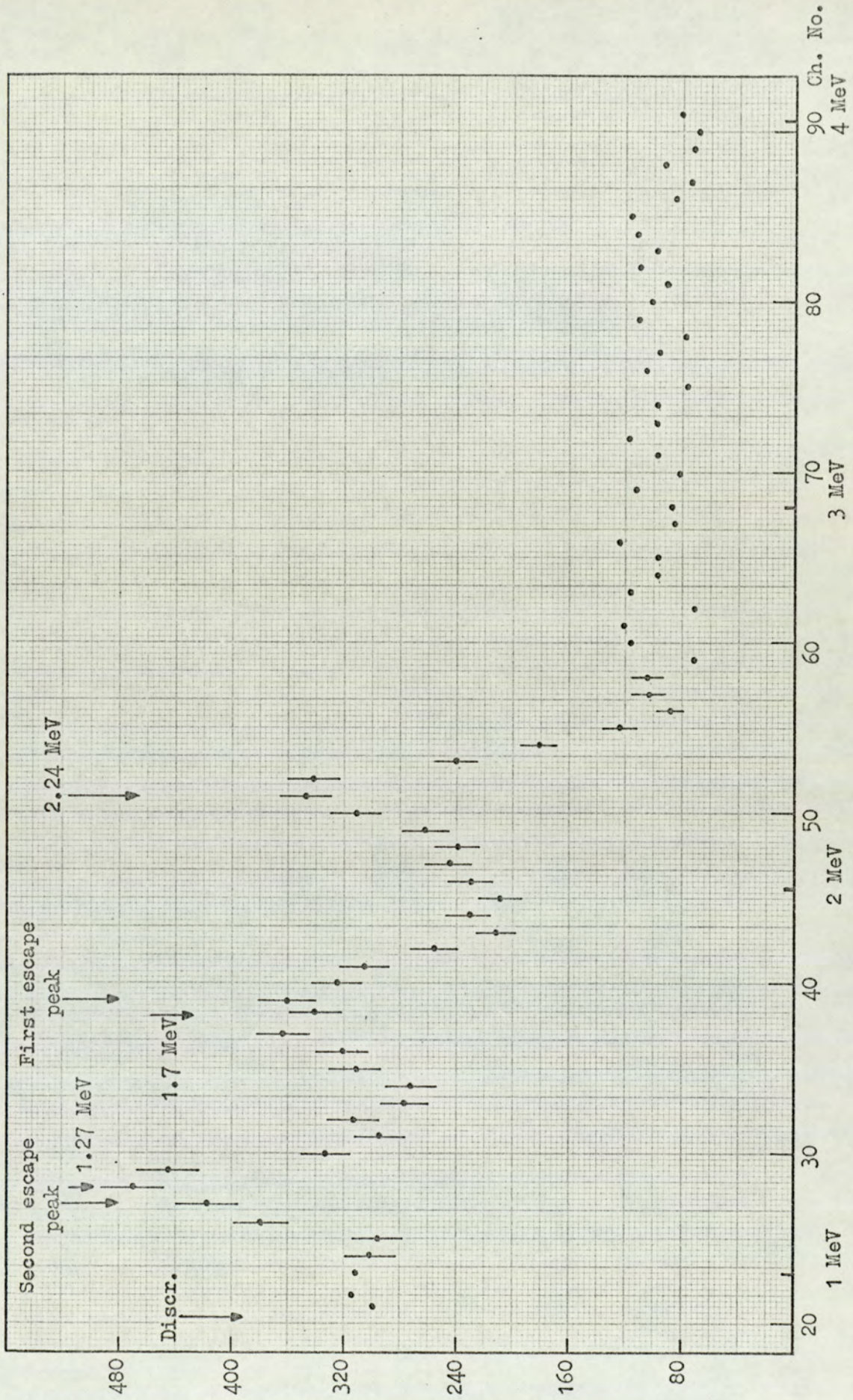


Figure 5.6. The spectrum for sulphur, (scattering angle 40°).

γ -ray spectral shape was stripped off. There is no monoenergetic isotopic γ -ray source emitted a 2.24 MeV γ -ray whose spectral shape could be used for the stripping procedure. The two nearest energy sources are ^{28}Al and ^{24}Na emitting γ -rays of 1.78 MeV and 2.75 MeV respectively. Gamma-ray spectra of the 1.78 MeV and 2.75 MeV lines were recorded with the same energy interval per channel of the analyser as used in the sulphur scattering experiment. The amplitudes of the 1.78 MeV and 2.75 MeV peaks were normalised and plotted on one piece of graph paper and a 2.24 MeV spectral shape was drawn midway between these two spectra. The estimated 2.24 MeV spectral shape was used to strip the 2.24 MeV line from the sulphur spectrum. The number of counts per channel to be stripped off the sulphur spectrum was calculated by normalising the intensities of the 2.24 MeV sulphur peak and the peak of the stripping spectrum. Figure 5.7 shows the 90° sulphur spectrum with the 2.24 MeV spectrum stripped off.

The intensity of the 1.7 MeV peak was then estimated by the same method. The peak correction factor was 1.3 ± 0.015 and it was calculated using the 1.78 MeV γ -ray of ^{28}Al . Before the intensity of the 1.27 MeV peak was estimated the 1.7 MeV peak was stripped off and the ^{28}Al 1.78 MeV γ -ray spectrum was used. Figure 5.8 shows the final 90° sulphur spectrum with both the higher energy γ -ray peaks stripped off. The peak correction factor for the estimation of the intensity of the 1.27 MeV peak was calculated from the 1.274 MeV γ -ray spectrum of ^{22}Na as 1.153 ± 0.005 .

5.3.3. The 2.24 MeV Gamma-Ray

The 2.24 MeV peak was attributed to the γ -ray transition between the first excited level and ground state of ^{32}S . The level structure of ^{32}S for the first levels with known spins and parities is shown in Figure 5.9 taken from Endt and Van der Leun⁽⁸⁸⁾. Many of the excited levels produce the 2.24 MeV γ -ray in cascade transitions to

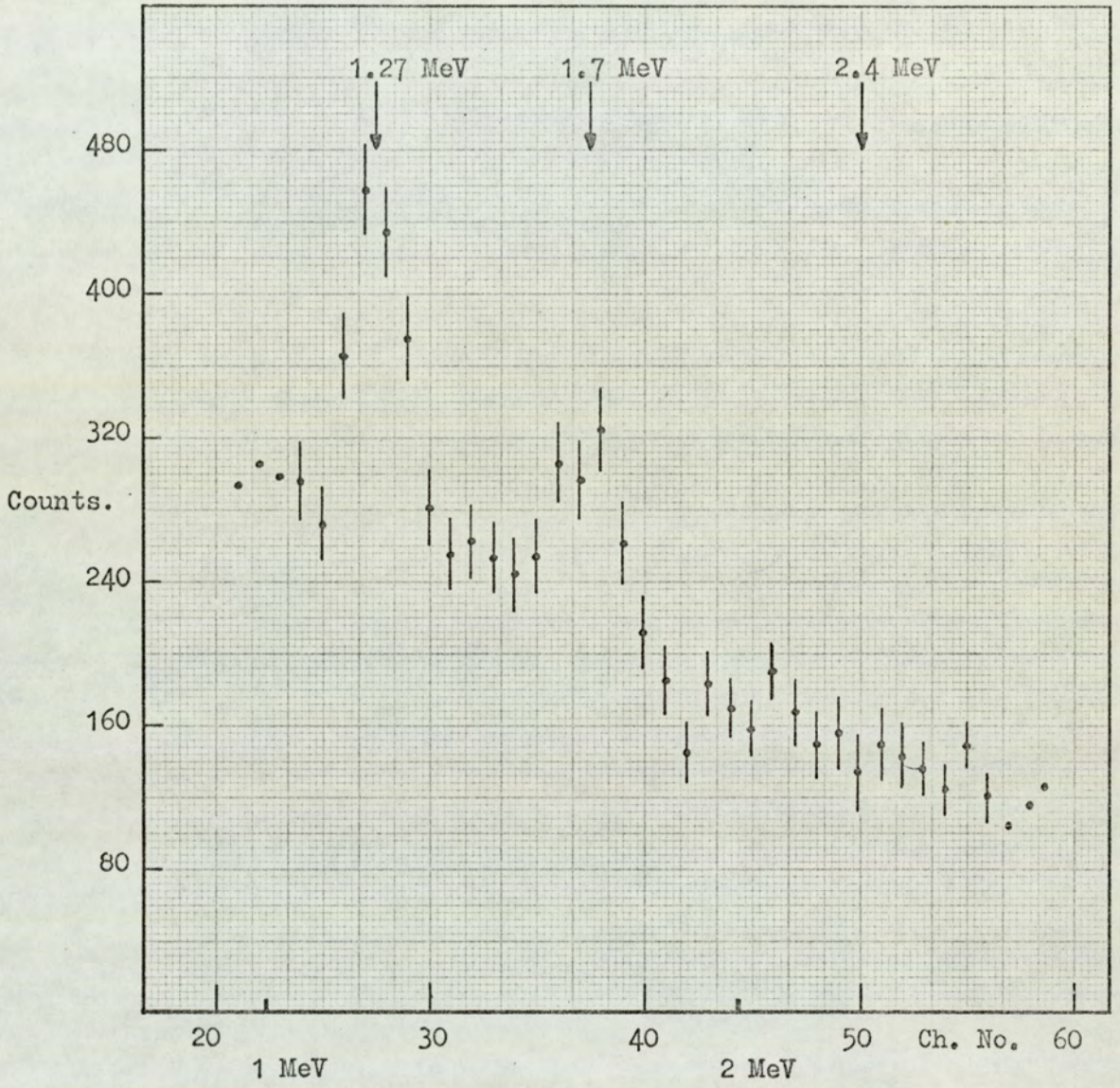


Figure 5.7. The 90° sulphur spectrum with the 2.24 MeV gamma-ray spectrum stripped off.

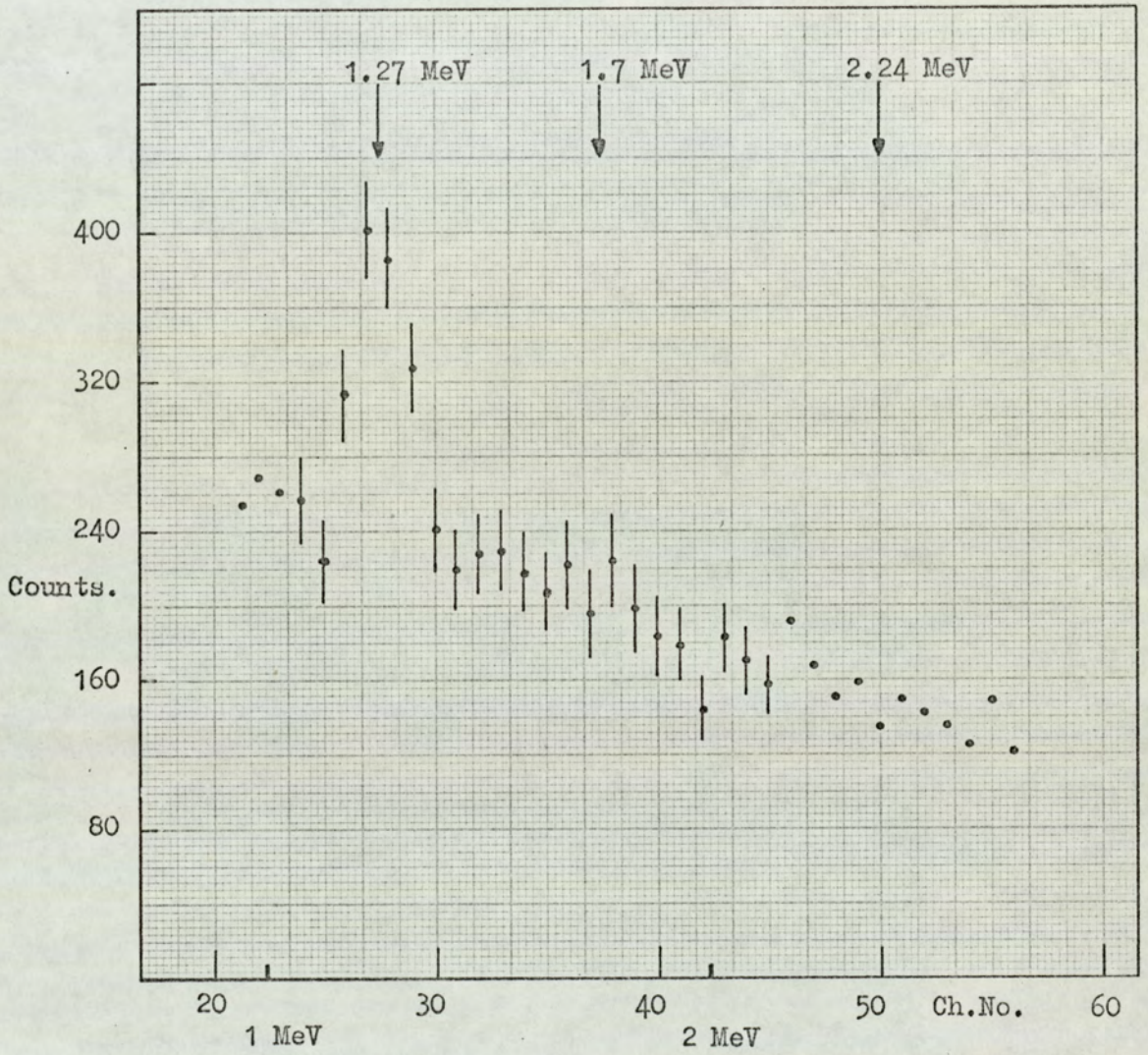


Figure 5.8. The ^{90}S sulphur spectrum with the 2.24 MeV and 1.7 MeV gamma-ray spectra stripped off.

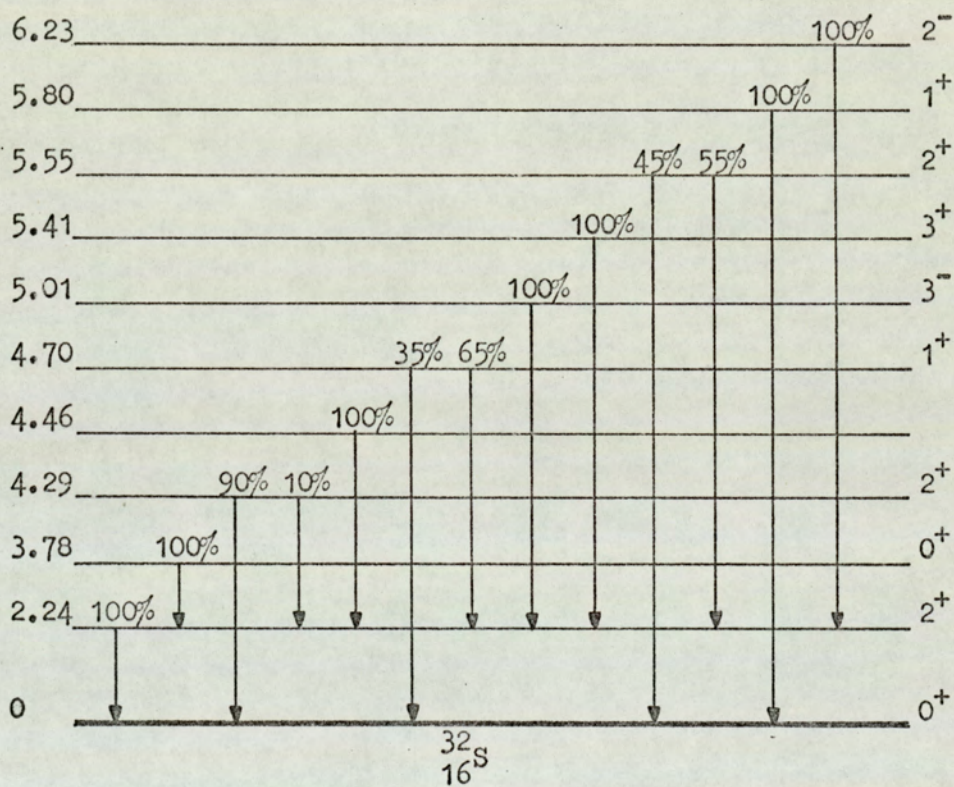


Figure 5.9. The level structure of ^{32}S , taken from Endt and Van der Leun⁽⁸⁸⁾.

the ground state. However, inelastic scattering is not the only production mode possible for this energy γ -ray. A 2.23 MeV γ -ray can be promptly emitted in the following reactions: $^{32}\text{S}(n, d\gamma)^{31}\text{P}$, $^{32}\text{S}(n, np\gamma)^{31}\text{P}$ and $^{32}\text{S}(n, ^3\text{He}\gamma)^{30}\text{Si}$.

In the formation of ^{31}P in an excited state a 2.23 MeV γ -ray is emitted in a transition between the second level and ground state and in the formation of ^{30}Si in an excited state the γ -ray is emitted in a first level to ground state transition. At 14 MeV neutron energy all three reactions are energetically possible, but only the $^{32}\text{S}(n, np)^{31}\text{P}$ reaction cross-section has been measured ⁽³²⁾, and it has a value of 100 mb.

There is no contribution possible via the $^{32}\text{S}(n, p)^{32}\text{P}$ reaction as ^{32}P decays by β^- emission to the ground state of ^{32}S .

The 2.24 MeV γ -ray peak cannot be assigned to a single reaction mode, but the most probable of the four possible reactions is inelastic scattering.

5.3.3(i) Differential γ -ray Production Cross-Sections

The differential cross-section results for the production of 2.24 MeV γ -rays in the interaction of 14.2 MeV neutrons with ^{32}S are given in Table 5.5.

Table 5.5

$$^{32}\text{S}(n, n'\gamma)^{32}\text{S}; E_n = 14.2 \text{ MeV}; E_\gamma = 2.24 \text{ MeV}$$

θ	$\cos\theta$	$\frac{d\sigma}{d\Omega}$
90°	0.0	$19.0 \pm 2.4 \text{ mb/st}$
70°	0.342	$23.0 \pm 2.9 \text{ mb/st}$
60°	0.5	$26.8 \pm 2.9 \text{ mb/st}$
40°	0.660	$31.9 \pm 2.9 \text{ mb/st}$
25°	0.906	$26.4 \pm 2.9 \text{ mb/st}$

Table 5.6

E_{γ}	Author's assigned production mode	E_n	Ang. Res.	90° differential cross-section	Comment on Method
2.24 MeV	$^{32}\text{S}(n,n')$, ^{32}S $^{32}\text{S}(n,np)$, ^{31}P $^{32}\text{S}(n,d)$, ^{31}P $^{32}\text{S}(n,^3\text{He})$, ^{30}Si	14.2 MeV	$\pm 4^\circ$	19.0 ± 2.4 mb/st	Present Work
2.24 MeV	$^{32}\text{S}(n,n')$, ^{32}S $^{32}\text{S}(n,d)$, ^{31}P	14.7 MeV	$\pm 20^\circ$	16.1 ± 1.7 mb/st 3.5 ± 1.2 (a) 3.2 ± 1.1 (a)	Engesser and Thompson (5) No time of flight discrimination; small sample; massive shield; NaI(Tl) single crystal.
2.1 MeV 2.03 MeV	$^{34}\text{S}(n,n')$, ^{34}S $^{32}\text{S}(n,\alpha)$, ^{29}Si				
2.23 MeV	$^{32}\text{S}(n,n')$, ^{32}S $^{32}\text{S}(n,np)$, ^{31}P $^{32}\text{S}(n,d)$, ^{31}P $^{32}\text{S}(n,^3\text{He})$, ^{30}Si	14 MeV		24.2 ± 6.3 mb/st	Bocharov and Nefedov (6) Pulse shape discrimination; Stilbene crystal; ring geometry
1.95 to 2.5 MeV	$\text{S}(n,xy)\text{S}$	14.8 MeV	$\pm 20^\circ$	35.4 (a) mb/st	Morgan et al. (9) Time of flight discrimination. Anti-coincidence NaI(Tl) spectrometer
2 MeV to 3 MeV	$\text{S}(n,n'\gamma)\text{S}$	14 MeV	60° to 140°	26.4 mb/st (a)	Caldwell et al. (26) Open geometry. No time of flight discrimination; large scattering sample, single NaI(Tl) crystal.
2.24 MeV	$^{32}\text{S}(n,n'\gamma)$, ^{32}S	14.1 MeV		14.7 mb/st (b)	Martin and Stewart (15) Time of flight discrimination. NaI(Tl) single crystal

(a) Not isotopic cross-sections

(b) Calculated from least squares fit equation

The results of all the known measurements for the 2.24 MeV γ -ray 90° differential production cross-section are compared in Table 5.6 in which brief experimental details and the authors' suggested production modes are given. The results of Morgan et al.⁽⁹⁾ and of Caldwell et al.⁽²⁶⁾ are not for a single energy γ -ray; the present result is mid-way in the range of values of the other three authors' work listed in Table 5.6. However, Bocharov and Nefedov's result probably contains a contribution from a line at approximately 2.1 MeV owing to the poor energy resolution of the organic scintillator used.

Morgan et al.⁽⁹⁾ who used an anti-coincidence spectrometer, observed two unresolved peaks at 2.1 MeV and 2.24 MeV. The largest peak was at 2.24 MeV. If Morgan's value of 35.4 mb/st is corrected for the ~ 2.1 MeV γ -ray contribution with the data of Engesser and Thompson⁽⁵⁾, the cross-section for the 2.24 MeV peak becomes 29.7 mb/st, which becomes 31.2 mb/st when corrected to an isotopic cross-section. This is considerably larger than the present result. Caldwell et al.⁽²⁶⁾ give the cross-section for γ -rays produced in the 2 MeV to 3 MeV energy interval and considering that the 2.24 MeV peak only covers a fraction of this range the agreement with the present work is reasonable.

Evidence for the presence of a 2.1 MeV γ -ray peak from the sulphur sample is just visible in Figure 5.8, which shows the sulphur spectrum with the 2.24 MeV peak stripped off. There is a slight rise about channel 46 which corresponds to 2.1 MeV, but as no peak was resolved no measurement was possible.

The angular resolution of the present method is again considerably better than that of the other groups. This was achieved maintaining an experimental accuracy similar to that of Engesser and Thompson⁽⁵⁾.

The Experimental Error

The estimated errors in the terms of equation 5.2 which was used to calculate the results for the 2.24 MeV γ -ray are summarised in Table 5.7.

Table 5.7

Term	Error
Peak efficiency, $\epsilon(E_\gamma)$	3.5%
Sample thickness $\sum_i f_i x_i$	1.5%
Solid angle, $\Delta\Omega$	2.0%
Gamma-ray absorption, S	0.5%
Nuclei/cm ³ (density) N	0.5%
Corrected integrated flux $F_1 F_2^\phi$	1.0%
Peak correction factor P	1.0%
Fractional peak counts $g(\theta)$:-	
$\theta = 90^\circ, 70^\circ$	12 %
$\theta = 60^\circ, 25^\circ$	10 %
$\theta = 40^\circ$	8 %

Most of the errors are as described for silicon, with the following exceptions. The density of the sulphur sample was measured with a 0.5% error giving a similar error in the number of ^{32}S nuclei per unit volume. The single largest source of error was again due to the poor spectrum statistics, however the error in the fractional peak counts improved at lower scattering angles and it was estimated as described for the silicon case. The experimental errors were added quadratically to give values of 12.8% for 90° and 70° scattering angles, 11% at 60° and 25° and 9.2% at 40° .

5.3.3(ii) Angular Distribution and Integrated Cross-Section

The angular distribution of the 2.24 MeV γ -ray from sulphur, which shows a definite anisotropy, is shown in Figure 5.10. The equation of the angular distribution obtained by a least squares fit (appendix 1) to the experimental data is,

$$\sigma(\theta) = 18.4 \pm 0.9 + (48.2 \pm 6.6) \cos^2 \theta - (46.2 \pm 7.8) \cos^4 \theta$$

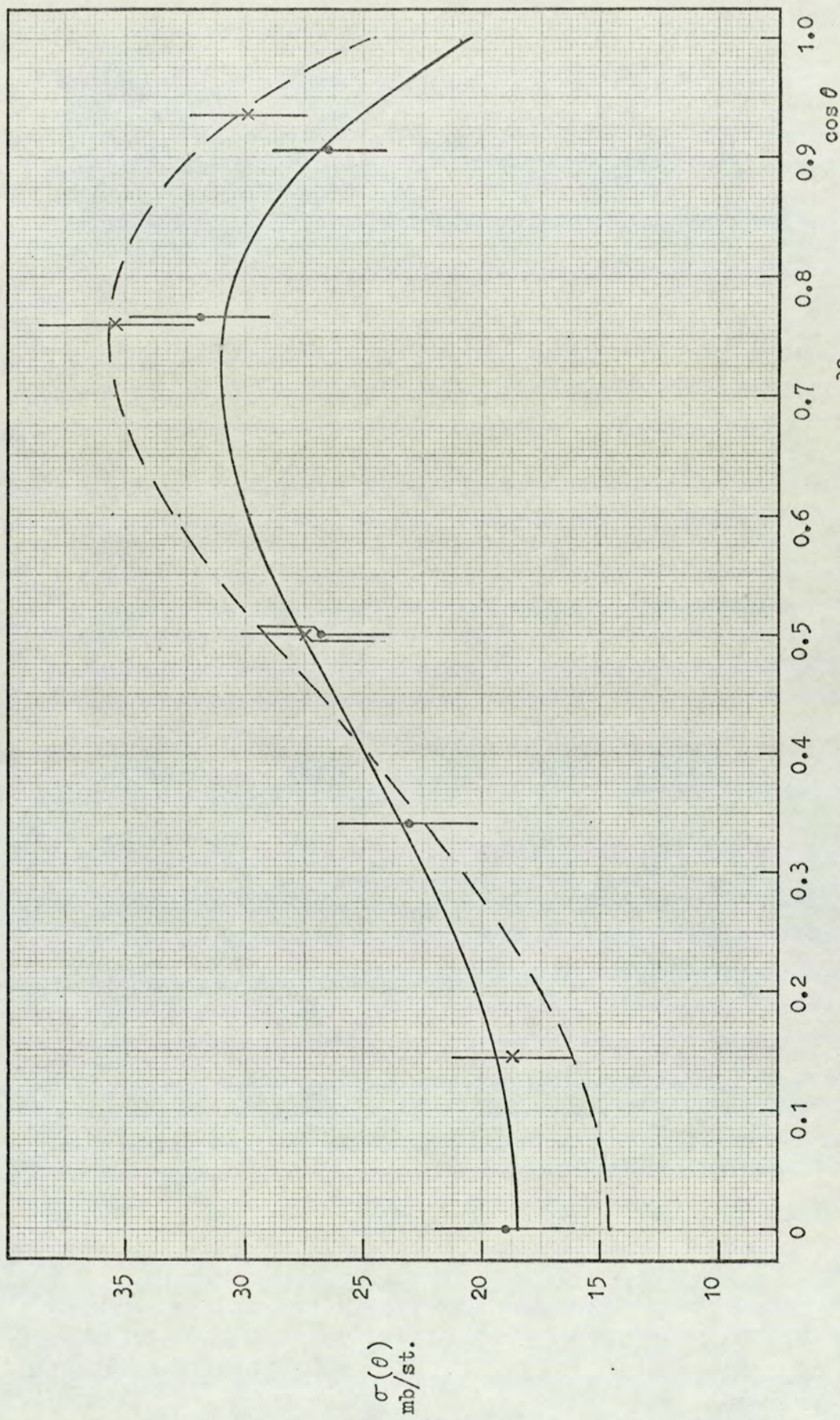


Figure 5.10. The angular distribution of the 2.24 MeV gamma-ray from ^{32}S , ($E_{\gamma} = 14.2 \text{ MeV}$).

- — Present measurements.
- X — Martin and Stewart (15).

The experimentally measured differential cross-section and the fitted angular distribution of Martin and Stewart⁽¹⁵⁾ for the 2.24 MeV γ -ray are also shown in Figure 5.10. Theirs is the only other reported angular distribution measurement for this γ -ray.

The integrated production cross-section for the 2.24 MeV γ -ray calculated from the fitted curve, is 318 ± 36 mb and this agrees favourably with the integrated cross-section, 332 ± 50 mb, given by Martin and Stewart⁽¹⁵⁾.

Although there is good agreement in the two measurements of the integrated cross-sections, there is a marked difference in the shape of the angular distributions. The anisotropy ratio, $\sigma(40^\circ)/\sigma(90^\circ)$ in the angular distribution of the present work has a value of 1.7 but for Martin and Stewart's distribution the ratio has a value of 2.5

5.3.4. The 1.7 MeV Gamma-Ray

The origin of the 1.7 MeV γ -ray peak is more uncertain than the 2.24 MeV γ -ray. On the basis of the nuclear level schemes and transition probabilities of End and Van der Leun⁽⁸⁸⁾, a 1.7 MeV γ -ray cannot be assigned to transitions between the levels of either ^{32}S or ^{34}S excited by neutron inelastic scattering. This energy γ -ray was therefore due only to neutron reactions with charged particle emission. Excluding neutron elastic and inelastic scattering, the (n,p) and (n, α) reactions with sulphur have the largest cross-sections, with reported values of 235 mb and 110 mb respectively. Gamma-rays of approximately 1.7 MeV can be attributed to both of these reactions and also to the (n,n' α) and (n,2p) reactions. Although the last two reactions are energetically possible at 14 MeV, cross-section measurements have not been reported for them. In Table 5.8 the reactions producing γ -rays of approximately 1.7 MeV are listed with the reaction Q-values.

Table 5.8

E_{γ} MeV	Reaction	Reaction Q value MeV	Q-value for the γ -ray production MeV
1.68	$^{32}\text{S}(n,p)^{32}\text{P}$ 1.755(6) \rightarrow 0.0781 (1)	-0.928	-2.683
1.79	$^{32}\text{S}(n,\alpha)^{29}\text{Si}$ 3.07(4) \rightarrow 1.27(1)	-1.528	-4.6
1.58	" 3.63(5) \rightarrow 2.03(2)	-1.528	-5.15
1.69	$^{32}\text{S}(n,2p)^{31}\text{Si}$ 1.693(2) \rightarrow 0.	-9.56	-11.25
1.78	$^{32}\text{S}(n,n'\alpha)^{28}\text{Si}$ 1.78(1) \rightarrow 0.	-6.95	-8.73

The most probable reaction made for the production of γ -rays of approximately 1.7 MeV is via the (n,p) and (n, α) reactions with ^{32}S .

5.3.4.(i) Differential γ -ray Production Cross-Sections

The 1.7 MeV γ -ray differential production cross-section results for the sulphur sample are listed in Table 5.9.

Table 5.9

1.7 MeV differential γ -ray production cross-section measurements - ^{32}S

θ	$\cos \theta$	$\frac{d\sigma}{d\Omega}$
90°	0.0	11.0 ± 2.4 mb/st
70°	0.342	14.3 ± 2.9 " "
60°	0.5	12.6 ± 2.6 " "
40°	0.766	10.3 ± 2.1 " "
25°	0.906	9.2 ± 1.9 " "

There are three other 90° differential cross-section measurements reported, and these are compared in Table 5.10. Engesser and Thompson⁽⁵⁾ measured differential cross-sections for three γ -rays at approximately 1.7 MeV.

Table 5.10

E_γ	Author's assigned production mode	E_n	Ang. Res.	90° differential cross-section (isotopic)	Comment on Method
~ 1.7 MeV	As in Table 5.7	14.2 MeV	$\pm 4^\circ$	11.0 ± 2.4 mb/st	Present work
1.77 MeV	$^{32}\text{S}(n, \alpha)^{29}\text{Si}$ 3.07(4) \rightarrow 1.27(1)	14.7 MeV	$\pm 20^\circ$	4.1 \pm 1.4 mb/st	(5) Engesser and Thompson No time of flight discrimination; Small sample; Massive shield; single NaI(Tl) crystal.
1.67 MeV	$^{32}\text{S}(n, n'\alpha)^{28}\text{Si}$ 1.78(1) \rightarrow 0	"	"	Total) 10.5) mb/st	
1.58 MeV	? $^{32}\text{S}(n, \alpha)^{29}\text{Si}$ 3.62(5) \rightarrow 2.03(2)	"	"	5.2 \pm 1.7 mb/st 1.2 \pm 0.4 mb/st	
1.66 MeV	$^{32}\text{S}(n, 2p)^{31}\text{Si}$ 1.70(2) \rightarrow 0	14 MeV		12.3 \pm 3.7 mb/st	(6) Bocharev and Nefedov Pulse Shape discrimination; Stilbene crystal; ring geometry.
1.68 MeV	$\text{S}(n, x\gamma)\text{S}$	14.8 MeV	$\pm 20^\circ$	22.1 mb/st(a)	(9) Morgan et al. Time of flight discrimination; anti-coincidence NaI(Tl) Spectrometer

(a) Not an isotopic cross-section.

They assigned production modes to two of the γ -rays. If the three differential cross-sections for these γ -rays are summed, a value of 10.5 mb/st is obtained and this is in good agreement with the result of the present work for the approximately 1.7 MeV γ -ray peak. The differential cross-section measurement of Bocharov and Nefedov⁽⁶⁾ is in good agreement with the present result.

Morgan et al.⁽⁹⁾, using an anticoincidence spectrometer, resolved only a single peak at 1.68 MeV and their result for this γ -ray, 22.1 mb/st, is considerably larger than all the other reported values. This is consistent with the large value reported for their measurement of the 2.24 MeV 90° differential γ -ray production cross-section for sulphur.

The Experimental Error

The experimental errors in the determination of the ~ 1.7 MeV γ -ray differential production cross-sections are as listed in Table 5.7 with the exception of the error in the fractional peak counts.

The error in the total counts per channel in the region of the 1.7 MeV peak is given by,

$$(C_i + S_i + S_{li})^{1/2}$$

where C_i and S_i are as defined in section 5.2.2 and S_{li} is the counts per channel subtracted in the stripping of the 2.24 MeV spectral shape. This clearly increases the error in the fractional peak intensity which was estimated as 20%. The errors were added quadratically to give an error in the differential cross-section measurements of 20.5%

5.3.4.(ii) The Angular Distribution and Integrated Cross-Section

The angular distribution of the ~ 1.7 MeV γ -ray from sulphur is given in Figure 5.11. The distribution was taken to be isotropic as there is no apparent (or marked) anisotropy. The mean value of the differential cross-section is 11.6 mb/st.

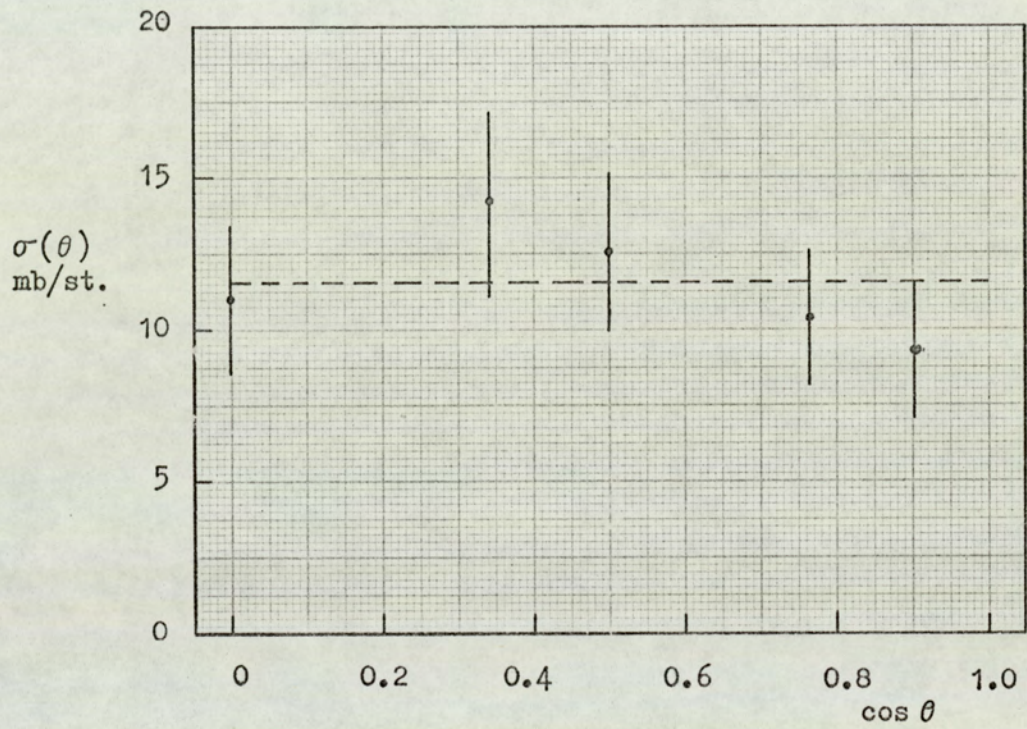


Figure 5.11. The angular distribution of the 1.7 MeV gamma-ray from ^{32}S , ($E_n = 14.2$ MeV).

The standard error in an isotropic differential cross-section, $\delta\sigma(\theta)$, is given by

$$\delta\sigma(\theta) = \left[\frac{\sum_{i=1}^n \left([\sigma(\theta)]_i - \overline{\sigma(\theta)} \right)^2}{n} \right]^{\frac{1}{2}}$$

where $\overline{\sigma(\theta)}$ is the mean differential cross-section, $[\sigma(\theta)]_i$ is the i^{th} experimental data point and n is the number of measurements.

The mean differential cross-section is 11.6 ± 1.8 mb/st.

The integrated cross-section is given by $4\pi\overline{\sigma(\theta)}$, with an error of $\pm 4\pi\delta\sigma(\theta)$.

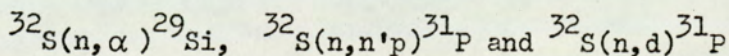
The integrated cross-section for the production of ~ 1.7 MeV γ -rays for ^{32}S , is 145 ± 23 mb.

There are no reported angular distribution and integrated cross-section measurements with which to compare these results.

5.3.5. The 1.27 MeV Gamma-Ray

The 1.27 MeV γ -ray peak from sulphur, Figure 5.4 cannot be assigned to inelastic scattering reactions with either ^{32}S or ^{34}S on the basis of the level structure data of Endt and Van der Leun⁽⁸⁸⁾.

However, a first excited state to ground state transition in both ^{29}Si and ^{31}P produces a 1.27 MeV γ -ray. These two isotopes can be produced in the following three reactions:



The (n, α) and $(n, n'p)$ reactions for ^{32}S have been measured⁽³²⁾ and each has a 110 mb cross-section. The 1.27 MeV γ -ray was assigned to these reactions.

5.3.5.(i) Differential γ -ray Production Cross-Sections

The 1.27 MeV γ -ray differential production cross-section measurements for ^{32}S at $E_n = 14.2$ MeV are listed in Table 5.11.

Table 5.11

1.27 MeV γ -ray differential production cross-sections for $^{32}\text{S}; E_n = 14.2\text{MeV}$

θ	$\cos\theta$	$\frac{d\sigma}{d\Omega}$
90°	0.0	11.2 ± 1.7 mb/st
70°	0.342	12.8 ± 2.0 "
60°	0.5	10.1 ± 1.6 "
40°	0.766	9.8 ± 1.5 "
25°	0.906	9.0 ± 1.4 "

There are three other reported 90° differential cross-section measurements for this γ -ray and the results are compared in Table 5.12. The energy of the γ -ray and its production mode are not compared as there is general agreement on these points. The present result agrees with that of Engesser and Thompson⁽⁵⁾ and with that of Bocharov and Nefedov⁽⁶⁾ within the quoted errors. Consistent with the results of Morgan et al.⁽⁹⁾ for the other γ -ray lines produced in 15 MeV neutron interactions with sulphur, their differential cross-section measurement for the 1.27 MeV γ -ray is considerably larger than the other reported results.

The Experimental Errors

The experimental errors in the measurement of the 1.27 MeV γ -ray differential production cross-section are as listed in Table 5.7. with the exception of the error in the fractional peak count. The spectrum statistics further deteriorated with the stripping of the second, 1.7 MeV spectrum. The error in the fractional peak count was estimated as 15%. The errors in each term were added quadratically to give an estimated error in the differential cross-section measurements of 15.5%.

5.3.5(ii) Angular Distribution and Integrated Cross-Section

The angular distribution for the production of the 1.27 MeV γ -ray in the interaction of 14.2 MeV neutrons with sulphur is plotted in Figure 5.12. The distribution was assumed isotropic as there is no marked anisotropy apparent. The mean value of the angular distribution is 10.6 ± 1.3 mb/st. This gives an integrated cross-section for the 1.27 MeV γ -ray production cross-section of 133 ± 16 mb. Again there is no data with which to compare the angular distribution.

Table 5.12

Comparison of 90° differential cross-section measurements for the 1.27 MeV γ -ray produced by 14 MeV neutron interactions with ^{32}S

$\left(\frac{d\sigma}{d\Omega}\right)_{90^\circ}$	E_n	Ang. Res.	Comment on Method
11.2 ± 1.7 mb/st	14.2 MeV	$\pm 4^\circ$	Present work
9.5 ± 1.1 mb/st	14.7 MeV	$\pm 20^\circ$	Engesser and Thompson ⁽⁵⁾ No time of flight discrimination; Small sample; Massive shield; Single NaI(Tl) crystal.
7.5 ± 2.6 mb/st	14 MeV	?	Bocharev and Nefedov ⁽⁶⁾ Pulse shape discrimination; Stilbene crystal; ring geometry.
$17.6 \pm$ mb/st	14.8 MeV	$\pm 20^\circ$	Morgan et al. ⁽⁹⁾ Time of flight discrimination; anti-coincidence NaI(Tl) spectrometer

5.4. Titanium

5.4.1. The Scattering Sample

The titanium scattering sample was a slab of natural titanium measuring 100 mm by 120 mm. The sample was machined to a thickness of 19.8 ± 0.05 mm. The density of the sample was measured as $4,510 \pm 30$ kg.m⁻³. This is in good agreement with the stated density $4,540$ kg.m⁻³.

Natural titanium has five stable isotopes listed as follows

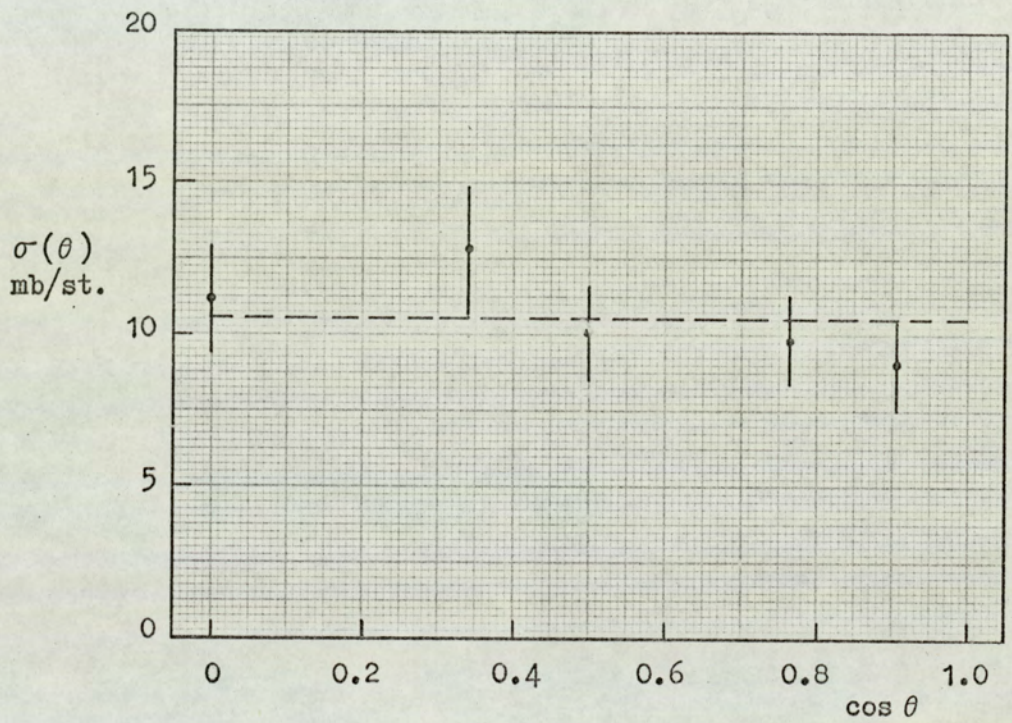


Figure 5.12. The angular distribution of the 1.27 MeV gamma-ray from ^{32}S , ($E_n=14.2$ MeV).

with their isotopic abundances: ^{46}Ti , 7.99%; ^{47}Ti , 7.32%; ^{48}Ti , 73.99%; ^{49}Ti , 5.46%; ^{50}Ti , 5.25%.

The total 14.2 MeV neutron cross-section for natural titanium is 2.26 barns. This gives a neutron transmission (without interaction) for the scattering sample of 70% with the sample positioned at 45° to the neutron beam, so that the multiple scattering correction is valid.

5.4.2. Gamma-Ray Spectra and Interpretation

Gamma-ray spectra for the 0.7 MeV to 3.0 MeV pulse height region were accumulated at six scattering angles: 90° , 75° , 60° , 45° , 30° and 20° . Figure 5.13 shows the γ -ray spectrum accumulated at a 90° scattering angle and this is typical of all six spectra obtained. The running time to accumulate each spectrum was 10 h which is much less than for the other samples studied. The reduced running time was possible because of the large γ -ray production cross-sections.

The titanium γ -ray spectra each have an intense peak resolved at 1.3 MeV. The non-elastic neutron cross-section for titanium is 1.22 barn and as the (n,p), (n,np) (n, α) and (n,2n) reactions are very low, the main reaction is inelastic scattering. In particular, the (n,p), (n,np) and (n, α) cross-sections for ^{48}Ti are only 64 mb, 12 mb, and 48 mb respectively. The two γ -ray lines were therefore attributed to neutron inelastic scattering and correspond to two low level transitions in ^{48}Ti . The level structure of the first few levels of ^{48}Ti is shown in Figure 5.14 and the data is taken from Nuclear Data Sheets⁽⁹¹⁾. A 0.99 MeV γ -ray is produced in the first level to ground state transition in ^{48}Ti and a 1.31 MeV γ -ray is produced in a second level to first excited level transition in ^{48}Ti . The two γ -rays, 0.99 MeV and 1.31 MeV, were solely assigned to neutron inelastic scattering with ^{48}Ti . The contribution from the activation of the sample via the $^{48}\text{Ti}(n,p)^{48}\text{Sc}$ reaction was negligible because of the low reaction cross-section and because ^{48}Sc has a 1.8 day half-life.

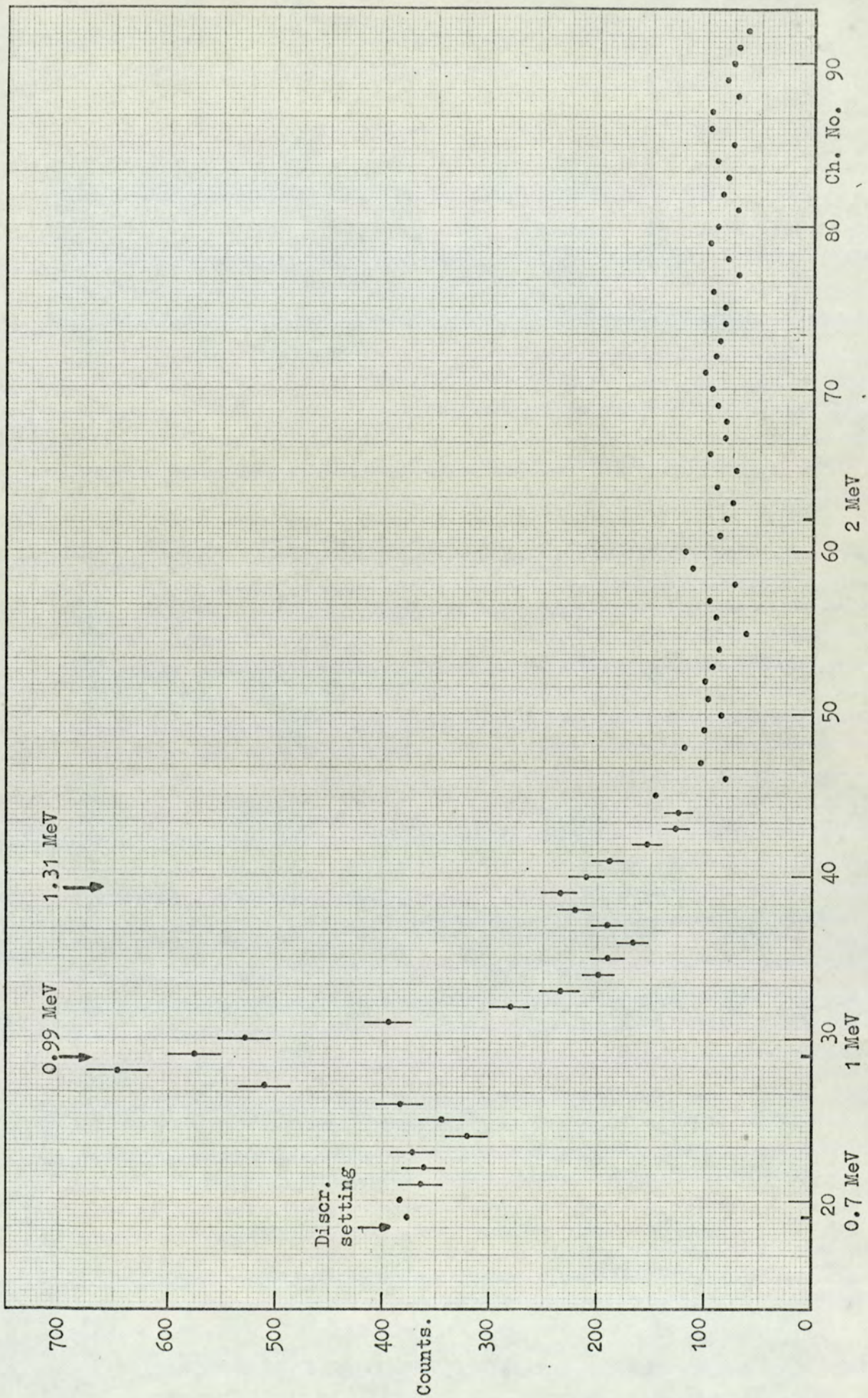


Figure 5.13. The gamma-ray spectrum for titanium, scattering angle 90°.

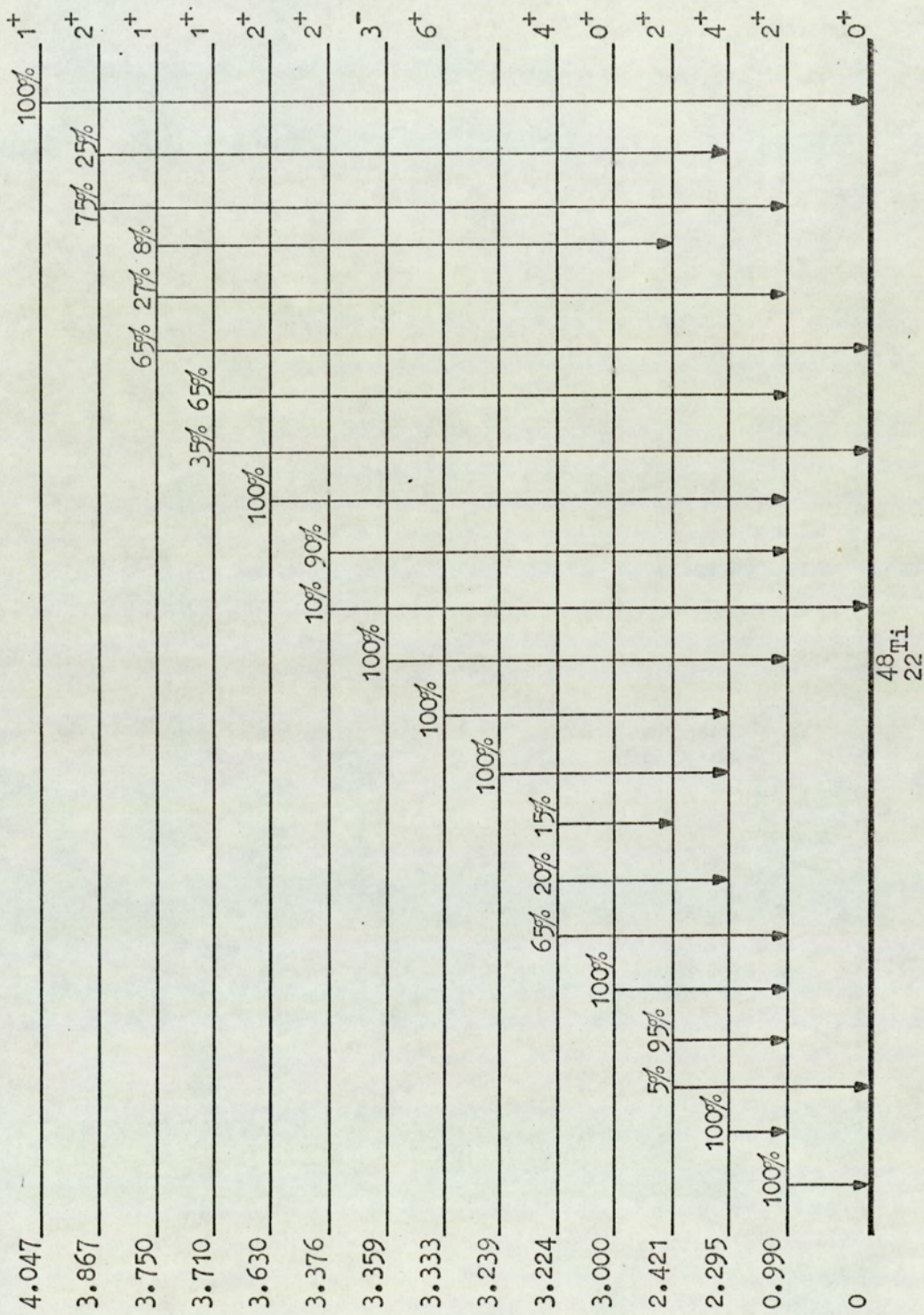


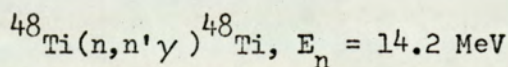
Figure 5.14. The level structure of ^{48}Ti , from Nuclear Data Sheets (91).

The fractional peak count method, described in section 5.2.2 was used to estimate the intensities of the two γ -ray peaks. The 1.31 MeV peak was compared with the 1.27 MeV peak of ^{22}Na , for which the peak correction factor is 1.153 ± 0.005 . As the 0.99 MeV peak sits on the Compton edge of the 1.31 MeV peak the higher energy peak was stripped off before estimating the intensity of the 0.99 MeV γ -ray peak. A ^{22}Na γ -ray spectrum was used for the stripping procedure. The intensity of the 1.27 MeV ^{22}Na γ -ray was normalised to the 1.31 MeV peak intensity and a channel by channel subtraction of the stripping spectrum from the titanium spectrum was made. Figure 5.15 shows the 90° titanium γ -ray spectrum with the 1.31 MeV peak stripped off. The peak correction factor for the 0.99 MeV γ -ray was estimated as 1.12 ± 0.006 and it was obtained by a linear interpolation between the peak correction factors measured for the 0.835 MeV and 1.27 MeV γ -rays of ^{54}Mn and ^{22}Na .

5.4.3. Differential Gamma-Ray Production Cross-Sections

The differential production cross-section results for both the 0.99 MeV and 1.31 MeV γ -rays are listed in Table 5.13.

Table 5.13



Angle θ	$\cos \theta$	$\sigma(\theta)$ for $E_\gamma = 0.99 \text{ MeV}$	$\sigma(\theta)$ for $E_\gamma = 1.31 \text{ MeV}$
90°	0.0	$75.4 \pm 5.6 \text{ mb/st}$	$22.1 \pm 3.4 \text{ mb/st}$
75°	0.259	$81.9 \pm 6.0 \text{ mb/st}$	$26.4 \pm 3.8 \text{ mb/st}$
60°	0.5	$89.9 \pm 6.6 \text{ mb/st}$	$23.1 \pm 3.6 \text{ mb/st}$
45°	0.707	$88.8 \pm 6.6 \text{ mb/st}$	$22.5 \pm 3.5 \text{ mb/st}$
30°	0.866	$81.0 \pm 6.0 \text{ mb/st}$	$21.5 \pm 3.3 \text{ mb/st}$
20°	0.940	$70.5 \pm 5.2 \text{ mb/st}$	$19.5 \pm 3.0 \text{ mb/st}$

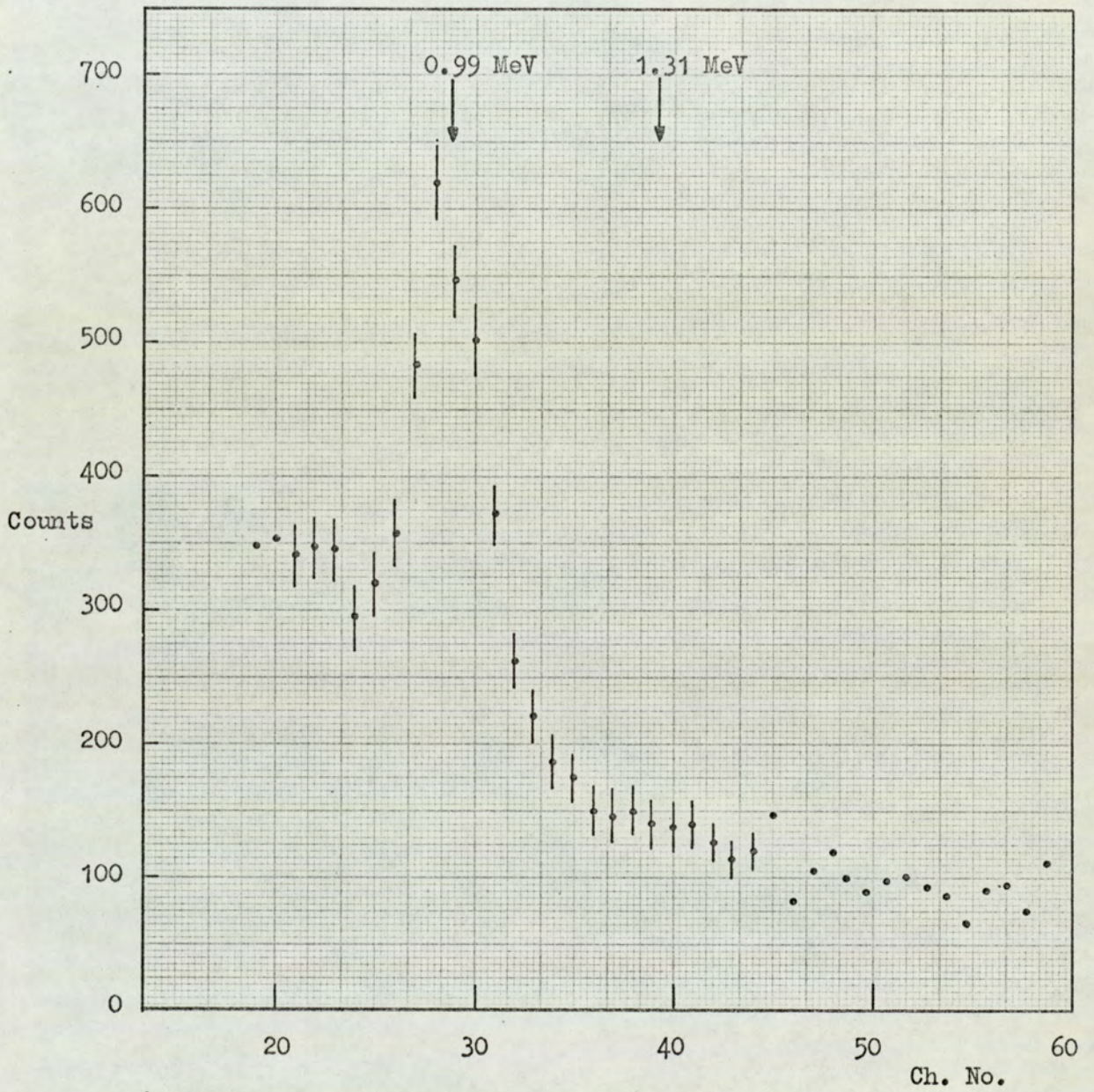


Figure 5.15. The 90° Titanium spectrum with the 1.31 MeV gamma-ray spectrum stripped off.

Engesser and Thompson⁽⁵⁾ measured the differential production cross-sections of both the 1.31 MeV and 0.99 MeV γ -rays at a $90^\circ \pm 20^\circ$ scattering angle for 14.7 MeV neutrons. They measured the 90° differential cross-sections as 70.1 ± 6.8 mb/st for the production of 0.99 MeV γ -rays and 23.2 ± 2.4 mb/st. for the production of 1.31 MeV γ -rays. The present result for the 1.31 MeV γ -ray is in good agreement with the value obtained by Engesser and Thompson. The results for the 0.99 MeV γ -ray agree within the experimental errors. The magnitude of the experimental error is approximately the same for both sets of results, however the angular resolution of the present measurements, $\pm 4^\circ$, is considerably better than the $\pm 20^\circ$ for Engesser and Thompson's measurements.

The Experimental Error

The experimental errors in the determination of the differential production cross-sections are listed in Table 5.14 for both the 0.99 MeV and 1.31 MeV γ -rays from ^{48}Ti .

Table 5.14

Term	Error
Peak efficiency $\epsilon(E_\gamma)$	3.5%
Sample thickness, (positioning) $\sum f_i x_i$	0.9%
Solid angle, $\Delta\Omega$	2.0%
Gamma-ray absorption, S	0.5%
No. of nuclei/unit vol. N	0.6%
Corrected integrated flux, $F_1 F_2 \phi$	1.0%
Peak correction factor, p	0.5%
Fractional peak counts, $g(\theta)$	
for 1.31 MeV γ -ray	15.0%
for 0.99 MeV γ -ray	6.0%

Most of the errors are as given previously. However, the intensity of the 0.99 MeV γ -ray peak enabled the fractional peak counts to be estimated with a relatively small error, 6%. The error in the 1.31 MeV γ -ray peak count was estimated as 15%. Adding the errors quadratically gives overall errors in the 1.31 MeV and 0.99 MeV γ -ray cross-section measurements of 15.6% and 7.4% respectively.

5.4.4. Angular Distributions and Integrated Cross-Sections of the $^{48}\text{Ti}(n,n'\gamma)^{48}\text{Ti}$ 0.99 MeV and 1.31 MeV γ -rays

The 0.99 MeV γ -ray differential cross-section measurements and the curve obtained by a least squares fit are plotted in Figure 5.16. The equation of the angular distribution is,

$$\sigma(\theta) = 76.5 \pm 1.1 + (72.0 \pm 6.8)\cos^2\theta - (89.0 \pm 7.6)\cos^4\theta$$

A definite anisotropy in the angular distribution is clearly resolved. The anisotropy ratio $\sigma(45^\circ) : \sigma(90^\circ)$ has a value of 1.19.

Using the fitted angular distribution equation, the integrated cross-section for the production of 0.99 MeV γ -rays in 14.2 MeV neutron inelastic scattering from ^{48}Ti was calculated as $1,039 \pm 107$ mb.

The differential cross-section measurements for the production of the 1.31 MeV γ -ray are plotted in Figure 5.17. The distribution was considered to be isotropic as there is no definite anisotropy. The mean isotropic differential production cross-section for the 1.31 MeV γ -ray is 22.5 ± 2.1 mb/st. The integrated cross-section for the production of the 1.31 MeV γ -ray in 14.2 MeV neutron inelastic scattering was calculated as 283 ± 26 mb.

There are no other reported angular distribution measurements with which to compare these results.

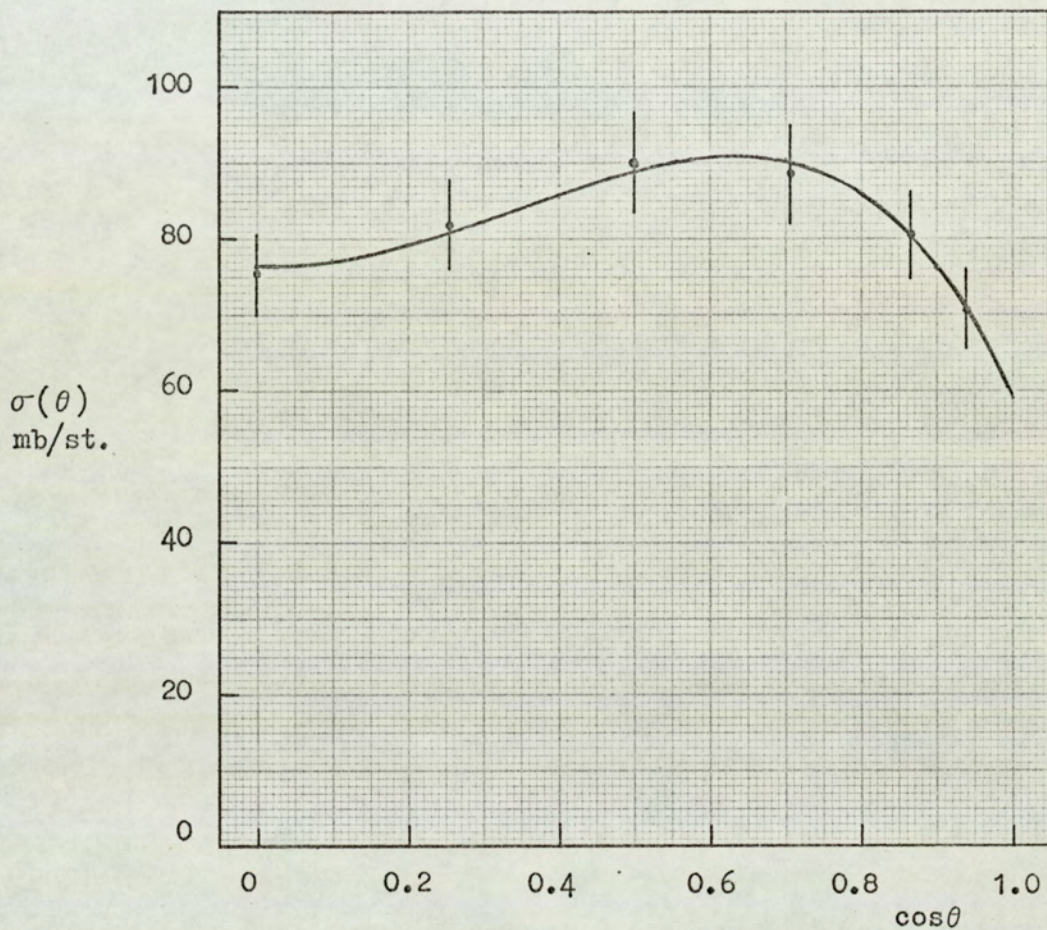


Figure 5.16. The angular distribution of the 0.99 MeV gamma-ray from titanium, ($E_n = 14.2$ MeV).

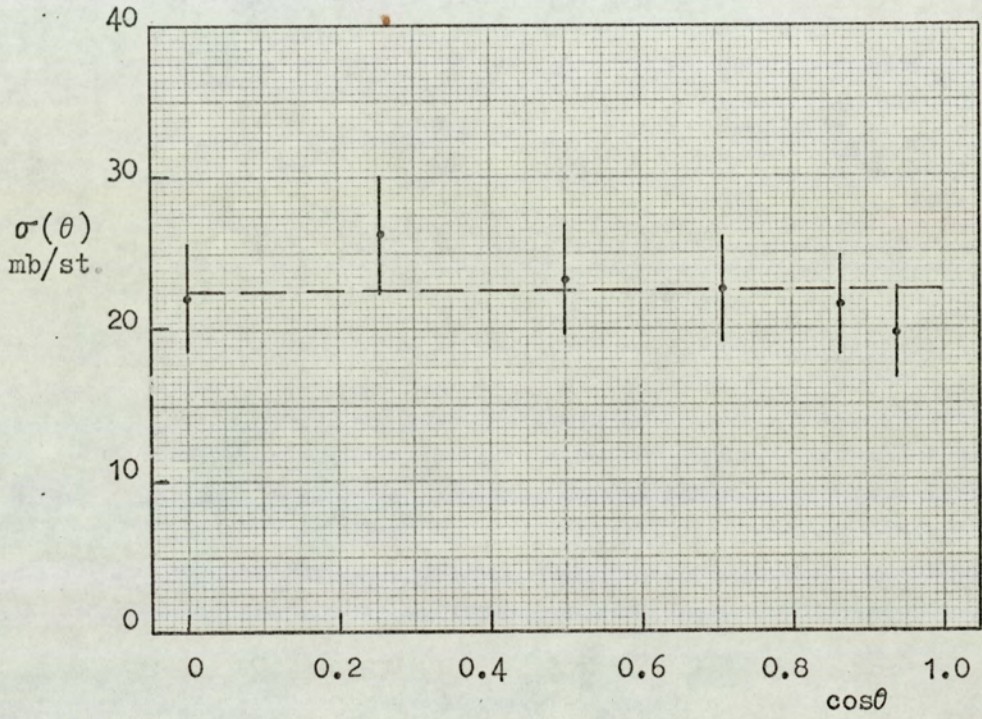


Figure 5.17. The angular distribution of the 1.31 MeV gamma-ray from titanium, ($E_n = 14.2$ MeV).

CHAPTER 6

Theoretical Comparison of Results6.1 The Optical Model

A neutron reaction can be described by the Schrodinger wave equation if the target (the scattering centre) is represented by a complex potential. The steady state wave equation for the neutron wave incident on the scattering centre is of the form

$$\nabla^2 \psi + \frac{8\pi^2 \mu}{h^2} \left(E' - V(r) - V_1(r) \underline{s} \cdot \underline{\ell} \right) \psi = 0 \quad 6.1$$

where E' is the total energy in the centre of mass system, $V(r)$ is the nuclear potential of the scattering centre, μ is the reduced neutron mass, h is Planck's constant and $V_1(r) \underline{s} \cdot \underline{\ell}$ is a spin-orbit interaction potential which may or may not be included. There is no Coulomb potential term as neutrons are uncharged.

If spin-orbit coupling is neglected, the asymptotic solution of the wave equation is of the form

$$\psi(r) = e^{ikz} + f(\theta) \frac{e^{ikr}}{r}$$

which represents a plane wave travelling in the positive z -direction, with wave number $K = \frac{1}{\lambda}$ in the centre of mass system incident on the scattering centre and an outgoing spherical wave with a scattering amplitude $f(\theta)$.

Asymptotically the incident wave, ψ_{INC} , can be expressed as a series of spherical waves as follows

$$\psi_{\text{INC}} = \frac{1}{kr} \sum_{\ell=0}^{\infty} (2\ell+1) i^{\ell} P_{\ell}(\cos\theta) \frac{e^{i(kr - \frac{\ell\pi}{2})} - e^{-i(kr - \frac{\ell\pi}{2})}}{2i}$$

where ℓ is the orbital angular momentum quantum number which designates the incoming partial wave. The interaction potential may effect the outgoing waves in phase or in amplitude and phase, corresponding to elastic or non-elastic processes respectively. The solution then has the form

$$\psi(\mathbf{r}) = \frac{1}{kr} \sum_{\ell=0}^{\infty} (2\ell+1) i^{\ell} P_{\ell}(\cos\theta) \frac{\eta_{\ell} e^{i(kr - \frac{\ell\pi}{2})} - e^{-i(kr - \frac{\ell\pi}{2})}}{2i} \quad 6.2$$

where η_{ℓ} is a complex constant representing the affect of the scattering centre. The solution may be considered as arising from the superposition of a scattered wave, ψ_{SC} , on the incident wave,

$$\text{i.e.} \quad \psi = \psi_{INC} + \psi_{SC}$$

The loss of particles from the state of incident energy E (with a particle velocity v) in the scattered wave corresponds to compound nucleus formation. The cross-section for the formation of the compound nucleus, σ_r , (or the reaction cross-section, compound elastic scattering not occurring) is determined by the ratio of the absorbed current to the incident flux.

Thus

$$\sigma_r = \frac{\int_{\Omega} v r^2 (|\psi_{INC}|^2 - |\psi_{SC}|^2) d\Omega}{v}$$

where the numerator gives the absorbed current, and the number of neutrons crossing unit surface area per unit time in the incident plane wave is v .

Using equation 6.2 this gives

$$\sigma_r = \frac{\pi}{k^2} \sum_{\ell=0}^{\infty} (2\ell+1) (1 - |\eta_{\ell}|^2) \dots \dots \dots 6.3$$

The term $1 - |\eta_{\ell}|^2$ can be identified as the barrier transmission

coefficient, $T_{\ell}(E)$. It gives the fraction of neutrons with energy, E , and angular momentum, ℓ , incident on the nucleus that enter the nucleus. If spin-orbit coupling is considered the transmission coefficients become a function of the neutron intrinsic spin, or total angular momentum j where $j = \ell \pm \frac{1}{2}$, for spin $\frac{1}{2}$ particles. The reaction cross-section is then given by

$$\sigma_{\text{r}} = \frac{\pi}{k^2} \sum_{\ell=0}^{\infty} \left\{ (\ell+1) T_{\ell j}^{+}(\text{E}) + \ell T_{\ell j}^{-}(\text{E}) \right\} \dots \dots \dots 6.4.$$

where $T_{\ell j}^{+}(\text{E})$ and $T_{\ell j}^{-}(\text{E})$ are the transmission coefficients for particles with total spin $j = \ell + \frac{1}{2}$ and $j = \ell - \frac{1}{2}$ respectively.

The transmission coefficients, which are required for compound nucleus calculations, can be obtained by solving the wave equation for the complex scattering coefficient η_{ℓ} or if spin-orbit coupling is considered by solving for $\eta_{\ell j}$. Two separate optical model computer programmes, due to Smith⁽⁹²⁾ and Wilmore⁽⁹³⁾, were used to calculate transmission coefficients for the present work. The main difference in the two programmes, when used for this purpose, is that Smith's programme makes provision for spin-orbit interaction.

The optical model potential describing the nucleon-nucleus interaction, neglecting spin-orbit interaction which is considered below, comprises a real and an imaginary part as follows

$$V(r) = Uf(r) + iWg(r),$$

Each part is expressed as the product of a depth, U or W , and a radial form factor, $f(r)$ or $g(r)$. The real potential shape in the above computer programmes is described by the Wood-Saxon form, illustrated in Figure 6.1(a), and given by,

$$f(r) = \frac{1}{1 + \exp\left(\frac{r-R_u}{a_u}\right)}$$

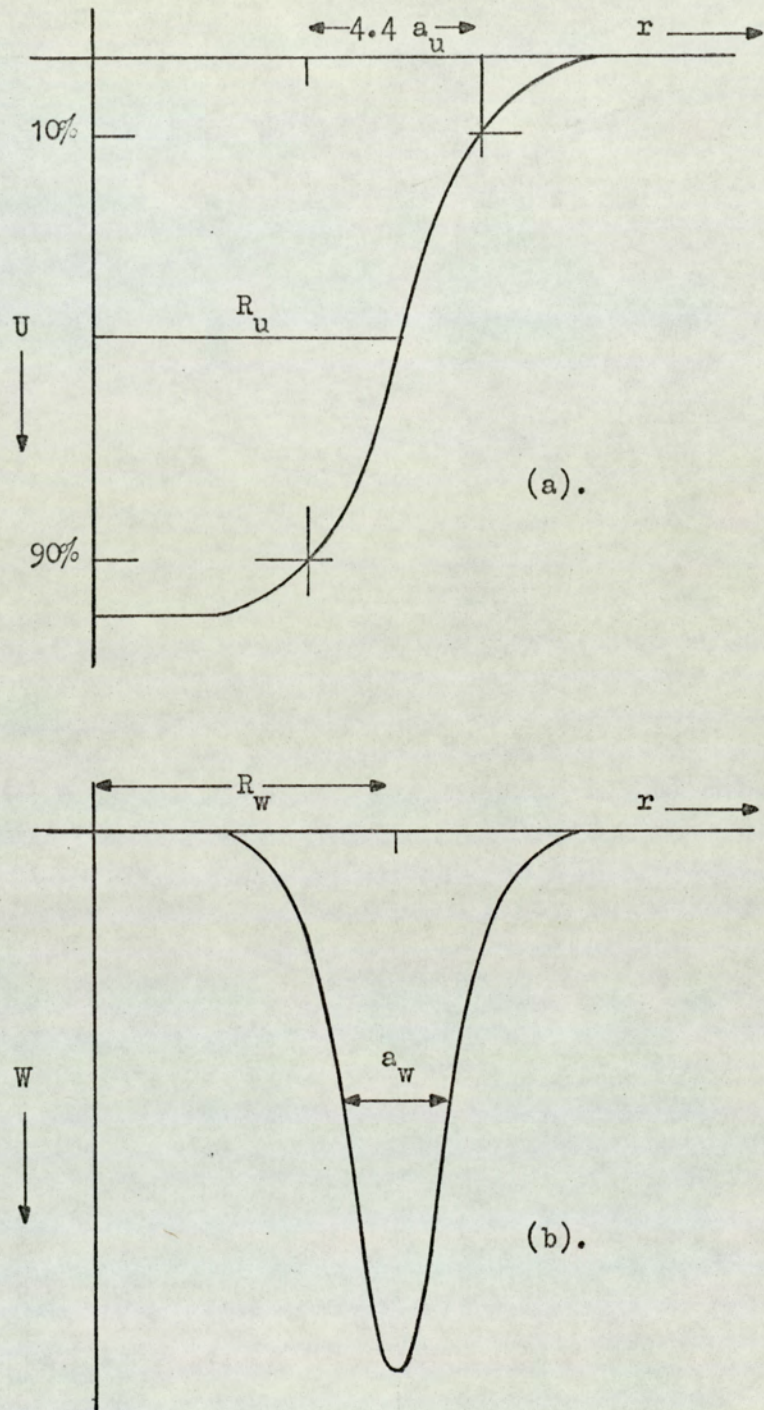


Figure 6.1. The nuclear potential form factors.

(a). Wood-Saxon real potential shape.

(b). Wood-Saxon derivative imaginary potential shape.

where R_u is the nuclear radius and a_u is the surface diffuseness parameter. The imaginary potential shape is described by the Wood-Saxon derivative form, illustrated in Figure 6.2(b) and given by

$$g(r) = \frac{4 \exp\left(\frac{r - R_w}{a_w}\right)}{1 + \exp\left(\frac{r - R_w}{a_w}\right)}$$

where R_w is the radius parameter and a_w is proportional to the full width of half maximum height of the surface absorption peak. Non-elastic processes at neutron energies of 14 MeV and less are considered as being solely due to a surface absorption peak; at higher energies a volume absorption form factor is also included. The non-central spin-orbit interaction potential, when it is included, is given by the real potential

$$V_1(r) \underline{s} \cdot \underline{\ell} = \left(\frac{\hbar}{m_\pi c}\right)^2 U_S \left(-\frac{1}{r} \frac{d}{dr} f(r)\right) \underline{s} \cdot \underline{\ell}$$

where U_S is the depth of the potential, $f(r)$ is the Wood-Saxon form factor and $\left(\frac{\hbar}{m_\pi c}\right)^2$ is the square of the pion's Compton wavelength. Although theoretical calculations have indicated the presence of an imaginary spin-orbit potential all practical analyses have dispensed with it.

Optical model calculations can be made with 'particular' or 'overall' potentials. A particular potential gives parameters which best fit the scattering data for a particular sample. An overall potential gives an averaged set of parameters suitable for describing many nuclei. Overall potentials are found to give good fits to the data that are not markedly inferior to those given by appropriate particular potentials. In view of the approximations required in the use of the compound nucleus theory at 14 MeV neutron energies (section 6.3) there was little to be gained by searching the literature for particular model

parameters for 14 MeV neutron interactions with ^{28}Si , ^{32}S and ^{48}Ti and so an overall potential was used to calculate the transmission coefficients.

Optical model parameters due to Agee and Rosen⁽⁹⁴⁾ which include spin-orbit interaction, were mainly used. They obtained the set by systematically varying the parameters to give the best fit to 14 MeV neutron scattering data for elements with mass numbers greater than $A=20$. The overall potential is described by

$$U = 49 - 0.33E \text{ MeV, where } E \text{ is the incident neutron energy in the centre of mass system,}$$

$$W = 5.7 \text{ MeV}$$

$$r_u = 1.25 \text{ fermi, where } R_u = r_u A^{1/3},$$

$$r_w = 1.25 \text{ " , " } R_w = r_w A^{1/3}$$

$$a_u = 0.65 \text{ " ,}$$

$$a_w = 0.7 \text{ " ,}$$

$$U_s = 5.5 \text{ MeV.}$$

These parameters were used with Smith's programme. Transmission coefficients were also calculated with the parameters of Wilmore and Hodgson⁽⁹⁵⁾. These parameters are the local potential equivalent of the non-local potential of Perey and Buck⁽⁹⁶⁾ who deduced them by an extensive analysis of neutron scattering. This set of parameters which does not contain a spin-orbit interaction potential was used with Wilmore's programme and the potential is given by

$$U = 47.01 - 0.267E - 0.00118E^2$$

$$W = 9.52 - 0.053E ,$$

$$r_u = 1.322 - 0.00076A + (4.10^{-6}) A^2 - (8.10^{-9}) A^3,$$

$$r_w = 1.266 - 0.00037A + (2.10^{-6}) A^2 - (4.10^{-9}) A^3,$$

$$a_u = 0.66$$

$$a_w = 0.48$$

Details of the running of the programmes and the transmission coefficients obtained are given in Appendix 2.

6.2. The Compound Nucleus Theory

The Hauser-Feshbach, compound nucleus theory is based on three assumptions.

- (i) **Compound Nucleus Formation.** The incident nucleon forms a compound nucleus whose life time is long compared with the nucleon period within the nucleus.
- (ii) **Continuum of Compound Nucleus Levels.** The excitation of the compound nucleus corresponding to the incident nucleon energy is taken to be so high that levels formed overlap strongly forming a continuum.
- (iii) **Independence Hypothesis.** The mode of decay of the compound nucleus is taken to be independent of its method of formation, but to depend only on the quantum parameters of the system-energy, spin, parity etc., and the properties of the particular decay channel involved.

On the basis of these assumptions the cross-section for a reaction involving a particular compound nucleus level can be factorised into the cross-section for the formation of the level times the probability of the level decaying through the required reaction channel. In a reaction of the type $A(a,b)B$, the sum of these product terms for all compound nucleus levels gives the reaction cross-section. For spinless particles, the reaction cross-section $\sigma(a,b)$ is given by

$$\sigma(a,b) = \frac{\pi}{k^2} \sum_{l_a} (2l_a+1) \frac{T_{l_a}(E_a) T_{l_b}(E_b)}{\sum_{l_c} T_{l_c}(E_c)} \dots 6.5$$

where $\frac{\pi}{k^2} (2l_a+1) T_{l_a}(E_a)$ is the compound nucleus formation cross-section for the incident particle with angular momentum l_a , energy E_a and transmission coefficient $T_{l_a}(E_a)$, (equation 6.3) and

$$\frac{T_{l_b}(E_b)}{\sum_{l_c} T_{l_c}(E_c)}$$

is the probability of the level decaying by emission of particle b and it

is given by the ratio of the transmission coefficient for the emission of particle b, with angular momentum ℓ_b and energy E_b to the sum of the transmission coefficients for all modes of decay of the level.

More generally, the angular distribution of γ -rays produced in neutron reactions on the Hauser-Feshbach-Satchler theory is, following Sheldon⁽²³⁾, given by a Legendre polynomial expansion of even order:

$$\frac{d\sigma}{d\Omega} = \sum_{\nu} a_{\nu} P_{\nu}(\cos\theta) \dots \dots \dots 6.6$$

where ν has a maximum value of four. The expression is of even order Legendre polynomials because the theory requires the γ -ray, or particle, distribution to be symmetric about the 90° scattering angle. The weighting coefficients of equation 6.6. are energy and momentum dependent and the angular distribution can be expanded as follows

$$\frac{d\sigma}{d\Omega} = \frac{1}{8} \lambda^2 \sum_{i,\nu} \alpha_{i\nu} \tau_i P_{\nu}(\cos\theta) \dots \dots \dots 6.7$$

where $\alpha_{i\nu}$ are spin and angular momentum terms and τ_i are energy dependent terms which are given by the transmission coefficients. The summation index i is over all possible compound nucleus levels and each level corresponds to a different spin sequence.

The spin and angular momentum sequence in a reaction is shown diagrammatically in Figure 6.2.

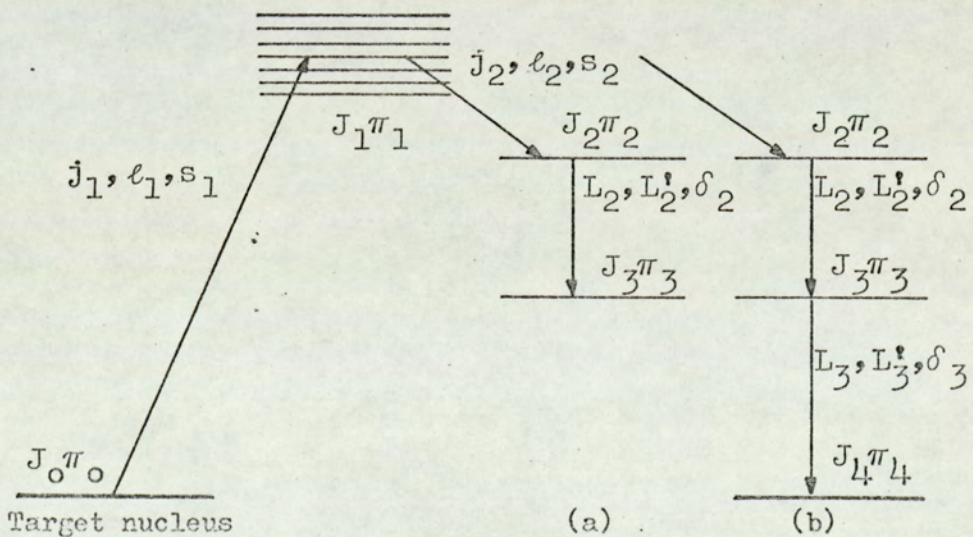


Figure 6.2

$J\pi$ represents the spin and parity of a level and the subscripts 0 and 1 refer to the target and compound nucleus levels respectively; subscripts 2, 3 and 4 refer to levels of the product nucleus. j_1 and j_2 are the total angular momenta of the incident and exit particles respectively. If ℓ is the angular momentum of a particle with intrinsic spin s , then the total angular momentum of the particle, j , has $(2s+1)$ values for each ℓ value, e.g. for a neutron with $s = \frac{1}{2}$, then $j = \ell \pm \frac{1}{2}$. L represents the multipole order of the γ -ray emitted in a transition between levels of the final nucleus. In mixed multipolarity γ -ray transitions $L' = L + 1$ and δ is the amplitude multipolarity mixing ratio where δ^2 is the ratio of the intensities of L' to L multipolarity γ -rays.

The coefficients $\alpha_{i\nu}$ in equation 6.7 are products of transition parameters; one for each step of the sequence shown in Figure 6.2. The transition parameter values are dictated by the nature and angular momentum of the particles effecting the transitions as well as the initial and final nuclear spins involved. The coefficients, $\alpha_{i\nu}$, which are given by numerical, Clebsch-Gordon and Racah coefficients have been tabulated for hand calculations by Sheldon⁽²³⁾ for many spin sequences. In the calculation of an angular distribution, the coefficients are calculated by a subroutine of the programme MANDY for each possible spin sequence involving a different compound nucleus level.

The possible spin sequences are not unlimited but subject to selection rules. The compound nucleus level spin is given by

$$J_1 = J_0 + j_1$$

so for a given j_1 value there are $(2j_1 + 1)$ values of J_1 which satisfy the inequality

$$|J_0 - j_1| < J_1 < J_0 + j_1$$

The j_1 values are limited by the maximum value of ℓ_1 , i.e. $\ell_{1\max}$. The

The parity of the compound nucleus level is given by $\pi_1 = (-1)^{\ell_1} \pi_0$. Parity conservation requires the sum $\ell_1 + \ell_2$ to be even if $\pi_0 = \pi_2$ and odd if $\pi_0 \neq \pi_2$. This restricts the values of ℓ_2 and thus the outgoing particle angular momentum j_2 which must satisfy the inequality,

$$|J_1 - J_2| < j_2 < J_1 + J_2$$

j_2 is also restricted by the maximum outgoing particle angular momentum $\ell_{2\max}$.

The energy or penetrability term τ_i of equation 6.7 is given by

$$\tau_i = \frac{T_{\ell_1 j_1}(E_1) T_{\ell_2 j_2}(E_2)}{\sum_{\ell j E} T_{\ell j}(E)}$$

$T_{\ell_1 j_1}(E_1)$ is the transmission coefficient of the incident particle with total angular momentum j_1 and energy E_1 . $T_{\ell_2 j_2}(E_2)$ is the coefficient for the decay of the compound nucleus in the spin sequence i to the particular level $J_2 \pi_2$. The summation in the denominator extends over all open channels (including elastic scattering) by which the particular intermediate state $J_1 \pi_1$, in the sequence i , can decay. To evaluate the terms τ_i the transmission coefficients are supplied as input data to the programme MANDY.

Equation 6.7 integrated over all solid angle gives the production cross-section for a particular γ -ray as

$$\sigma = \pi \lambda^2 \sum_{J_1 \ell_1 j_1} \frac{(2J_1 + 1)}{(2J_0 + 1)(2s_1 + 1)} \frac{T_{\ell_1 j_1}(E_1) T_{\ell_2 j_2}(E_2)}{\sum_{\ell j E} T_{\ell j}(E)}$$

If the spin of the incident particle is neglected this reduces to equation 6.5

The shape of particle and γ -ray angular distributions at neutron energies less than 7 MeV, are well predicted by the theory, but the magnitudes of the distributions are found to be too high at neutron energies near the reaction threshold. The Hauser-Feshbach theory makes the assumption that transmission coefficients (and therefore the widths) are the same for all the compound nucleus states in the same energy region. Moldauer⁽²¹⁾ modified the theory by considering the compound nucleus levels as having a distribution of widths. This "level width fluctuation correction" appears as correction factors to the Hauser-Feshbach penetrability terms, τ . It has the effect of reducing the inelastic cross-section magnitudes and improving the fit to experimental data, and it increases the compound elastic scattering cross section as the compound nucleus formation cross-section is unaltered by the correction. The effect of the correction decreases with increasing neutron energy⁽⁹⁷⁾ and it is not used at higher energies⁽⁹⁸⁾ (above 7 MeV). Therefore, although the programme MANDY has the option of including the correction, it was not used in the calculations at 14 MeV neutron energies.

Details of the programme are given in Appendix 3.

6.3. The Use of the Programme MANDY at 14 MeV Neutron Energy

In measuring the γ -ray production cross-section for a transition between a low lying excited nuclear level and the ground state, following 14 MeV neutron inelastic scattering, the γ -rays observed are produced by two reaction modes: by the direct excitation of the particular level, and by cascade transitions from higher excited levels. In the latter case the cascade may involve the emission of two or more cascade γ -rays. The programme MANDY can at most only deal with a two stage cascade reaction, Figure 6.2(b). At 14 MeV incident neutron energy, for all but the lightest elements, many levels of the scattering nucleus can be excited and it is impossible to consider all of the levels because of the lack of data on the spins, parities and branching modes of the higher

energy levels.

At the higher incident neutron energies, besides scattering reactions, usually several of the following have appreciable cross-sections - the (n,p) , (n,α) , $(n,n'p)$, (n,d) and $(n,2n)$ reactions. Reactions such as the $(n,2n)$ and $(n,n'p)$ in which two light reaction products are emitted cannot be accounted for by the programme MANDY. The (n,p) , (n,α) and (n,d) reactions are accounted for as extra exit channels by which the compound nucleus can decay and the relevant transmission coefficients are required to evaluate the denominator of the penetrability terms, equation 6.7. Again, owing to a lack of data on the energy levels, spins and parities of the final nuclei, it is only possible to account for a small fraction of the different energy protons, α -particles and deuterons that may be emitted.

Thus, only γ -ray production cross-sections may be calculated for a single or two stage γ -ray cascade transition. Secondly, it is impossible to include all of the energetically possible modes of decay of the compound nucleus not only because of the lack of data but also because the number of channels involved is too great for the programme to handle.

MANDY was then used to estimate the normalised γ -ray angular distributions of the predominantly excited first level in inelastic scattering. In these calculations the cascade contributions from as many excited levels of the scattering nucleus as there is data for were considered. The effect on the shape of the angular distribution due to neglecting compound nucleus decay channels was also investigated. With the additional aid of published cross-section for the (n,p) , (n,α) etc., reactions, the magnitudes of the γ -ray production cross-sections were estimated.

6.4. Results

In Figure 6.3 the calculated normalised angular distributions

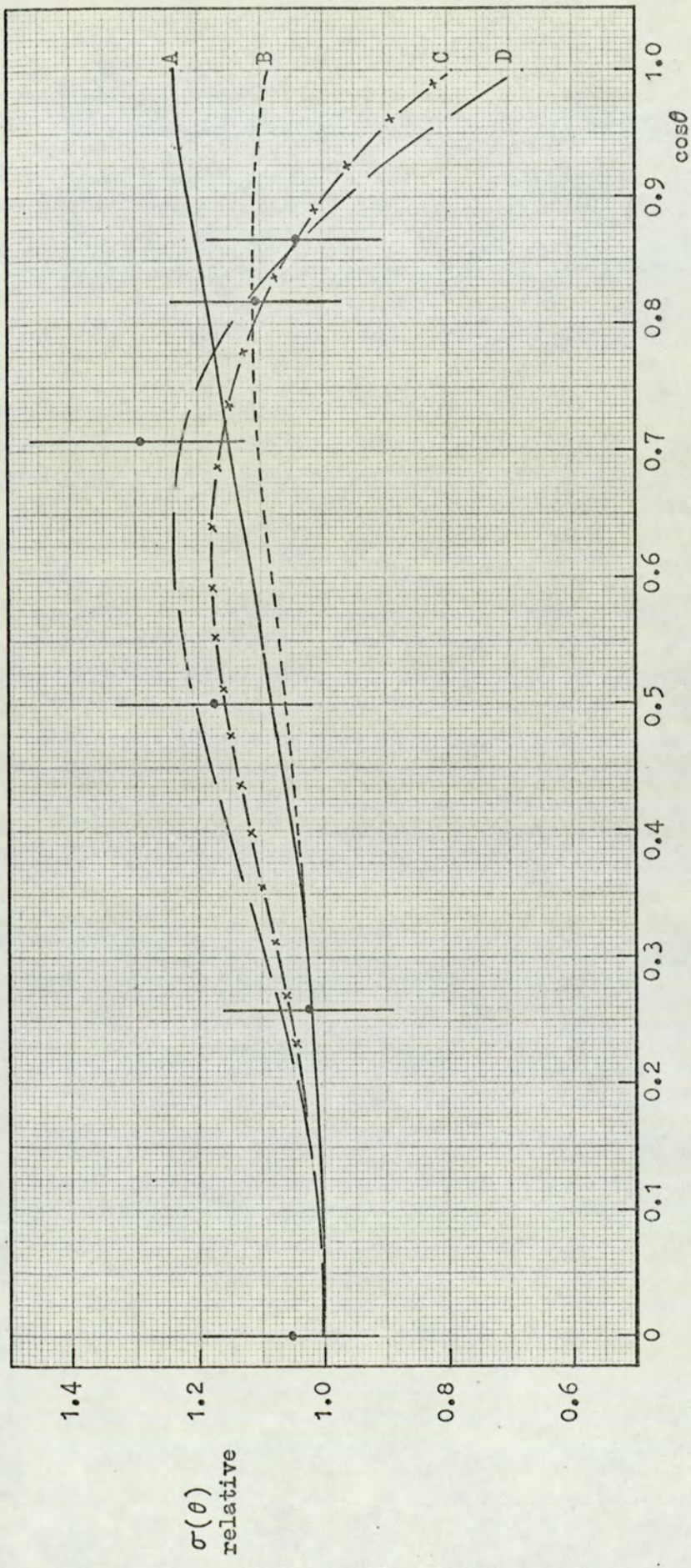


Figure 6.3. Comparison of the normalised theoretical and experimental angular distributions for the 1.78 MeV gamma-ray from silicon.

- A - The 13 channel approximation, Mandy.
- B - The 2 channel approximation.
- C - Calculated by Drake (25).
- D - Least squares fit to experimental data.

are shown for the production of 1.78 MeV γ -rays in the $^{28}\text{Si}(n,n'\gamma)^{28}\text{Si}$ reaction. There are two calculated curves shown, A and B, these are compared with the normalised experimental results, curve D, and the normalised angular distribution calculated by Drake⁽²⁵⁾ curve, C.

Curve B is the two channel approximation in which the compound nucleus is considered to decay by inelastic scattering to the 1.78 MeV level of ^{28}Si or by compound elastic scattering. The transmission coefficients for both curves were calculated using the optical model parameters of Agee and Rosen⁽⁹⁴⁾ and included spin-orbit coupling. Curve A was calculated considering thirteen compound nucleus inelastic scattering channels, this is the maximum number of levels for which there is sufficient data and includes all excited levels below 8.4 MeV. The energy, spin, parity and branching modes of the levels of ^{28}Si are given in Figure 5.2, taken from Endt and Van der Leun⁽⁸⁸⁾. In calculating the contribution of each level, the other twelve levels were included as extra exit channels by which the compound nucleus can decay. The effect of neglecting charged particle emission is considered below. In cases where levels decay by mixed multipole transitions, i.e. a mixture of dipole and quadrupole radiations, with unknown mixing ratio, the transitions were taken as being pure dipole transitions. The calculated differential cross-sections for the cascade contributions from each of the excited levels were then summed in accordance with the branching modes given in Figure 5.2. In the few cases where a level has a three stage cascade contribution, such as the 7.41 MeV level of ^{28}Si in which 25% of its transitions decay in a three stage cascade, the level was considered as decaying only by the two stage cascade mode.

The angular distribution was also calculated considering the excitation of fewer levels of ^{28}Si . The first seven levels of ^{28}Si , which includes all levels below 7 MeV excitation energy, were considered and this is approximately half the number considered above. The

normalised angular distribution was almost identical to curve A shown in Figure 6.3. The similarity can be explained because the shapes of the contributing distributions from each level were very similar, tending to increase smoothly from $\theta = 90^\circ$ to $\theta = 0^\circ$, with a few exceptions: contributions from levels with $J_3^\pi = 0.0$ were isotropic and the first excited level distribution tended to dip slightly at $\theta = 0^\circ$.

The effect of compound nucleus exit channels other than inelastic scattering on the shape of the angular distribution was investigated by considering proton exit channels. Transmission coefficients for proton emission in the $^{28}\text{Si}(n,p)^{28}\text{Al}$ reaction were calculated using Wilmore's programme with optical model parameters due to Perry⁽⁹⁹⁾. As there is little data on the level structure of ^{28}Al given by Endt and Van der Leun⁽⁸⁸⁾ only five proton energies could be considered. The inclusion of the proton exit channels decreased the magnitude of the γ -ray production cross-sections, but the shape of the normalised angular distributions changed by less than 1%. From this it was assumed that the omission of proton and alpha particle compound nucleus exit channels made a negligible error to the shape of the normalised angular distribution.

Normalised angular distributions calculated using the neutron optical model parameters of Wilmore and Hodgson⁽⁹⁵⁾ in which spin-orbit coupling is neglected were very similar to the above results.

The calculated angular distributions do not agree well with the least squares fitted curve to the experimental data, in particular they are less anisotropic. However, the calculated distributions pass through the error bars of most of the data points. There is good agreement between the calculated curve given by Drake⁽²⁵⁾ and the fitted curve to the experimental results. The agreement is hard to explain as Drake also used a translation of the MANDY code with transmission coefficients calculated with the optical model parameters of Agee and Rosen. However, Drake gives no further details of the calculation such

as whether the curve is a two channel approximation or what assumptions were made. Martin and Stewart⁽¹⁴⁾ calculated the angular distribution of the 1.27 MeV γ -ray produced in the $^{24}\text{Mg}(n,n'\gamma)^{24}\text{Mg}$ reaction using compound nucleus theory. ^{24}Mg is an even-even nucleus and the incident neutron energy was 14 MeV, so the shape of the distribution might well be expected to be similar to that of the 1.78 MeV γ -ray from ^{28}Si . The shape of the distribution was in fact similar to curve A of the present work as opposed to that given by Drake.

The normalised γ -ray angular distributions for a first excited level to ground state transition were calculated for ^{32}S and ^{48}Ti by the two channel approximation and by considering as many neutron inelastic scattering channels as possible in each case. Agee and Rosen's optical model parameters were used to calculate the transmission coefficients. It was assumed that compound nucleus exit channels other than inelastic scattering have a negligible effect on the shape of the calculated distributions.

In Figure 6.4 the theoretical results for the 2.24 MeV γ -ray produced in the $^{32}\text{S}(n,n'\gamma)^{32}\text{S}$ reaction are compared with the experimental results. The excited level structure and branching modes of ^{32}S necessary for the calculations are given in Figure 5.9. In the calculation of the distribution labelled B in Figure 6.4 the contributions of nine levels of ^{32}S were considered and included all but one level below 6.3 MeV excitation energy of ^{32}S . The distributions were normalised to $\theta = 60^\circ$ because of the anisotropy in the experimentally fitted curve. The slightly anisotropic theoretical distributions do not agree with the experimental curve which shows a marked anisotropy.

A comparison of the results for the production of the 0.99 MeV γ -ray in the $^{48}\text{Ti}(n,n'\gamma)^{48}\text{Ti}$ reaction is made in Figure 6.5. In the calculation of distribution B, Figure 6.5, twelve inelastic scattering channels were considered and the level structure data is given in

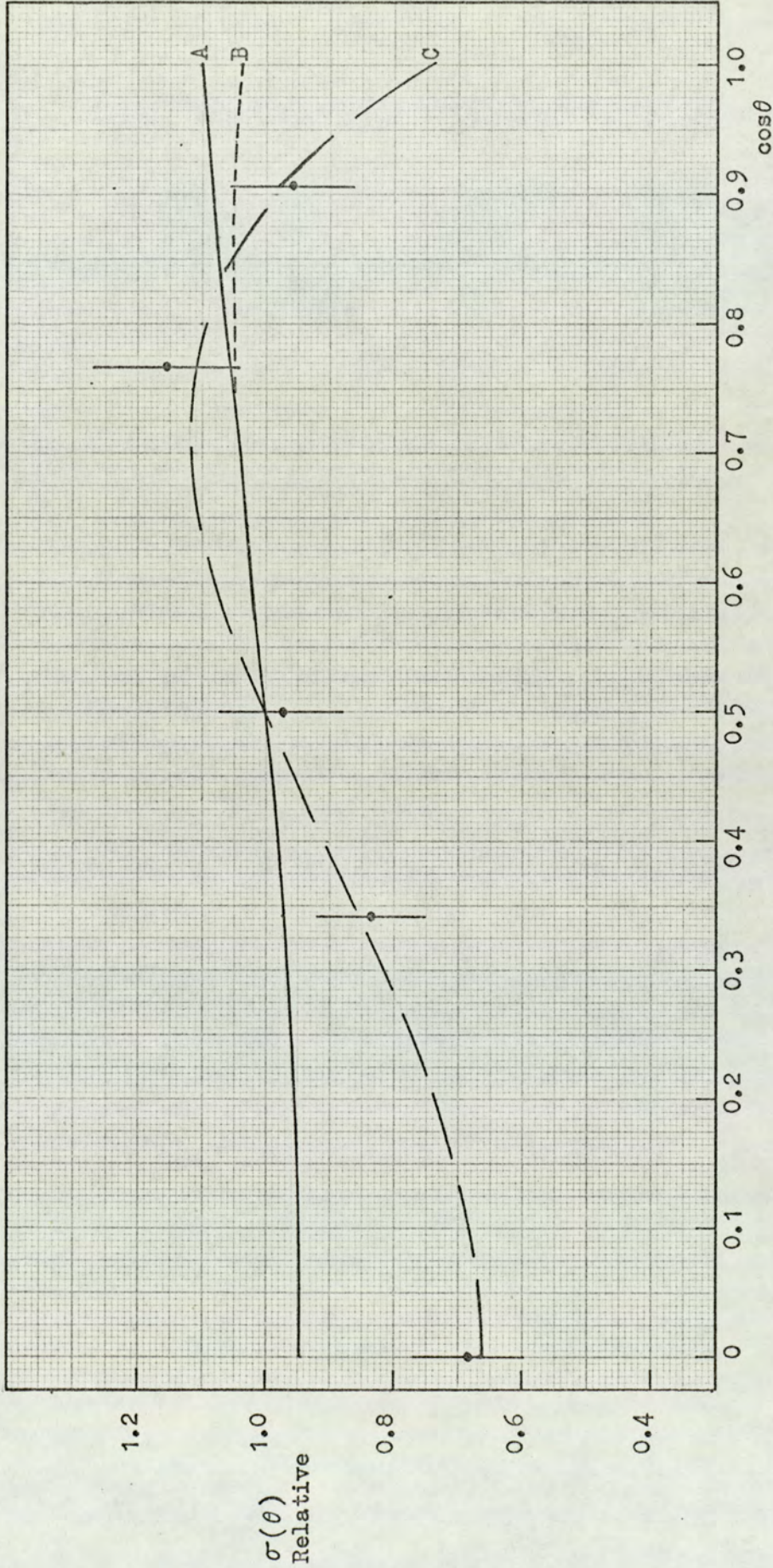


Figure 6.4. Comparison of the normalised theoretical and experimental angular distributions for the 2.24 MeV gamma-ray from sulphur.

- A - The 10 channel approximation.
- B - The 2 channel approximation.
- C - Least squares fit to experimental data.

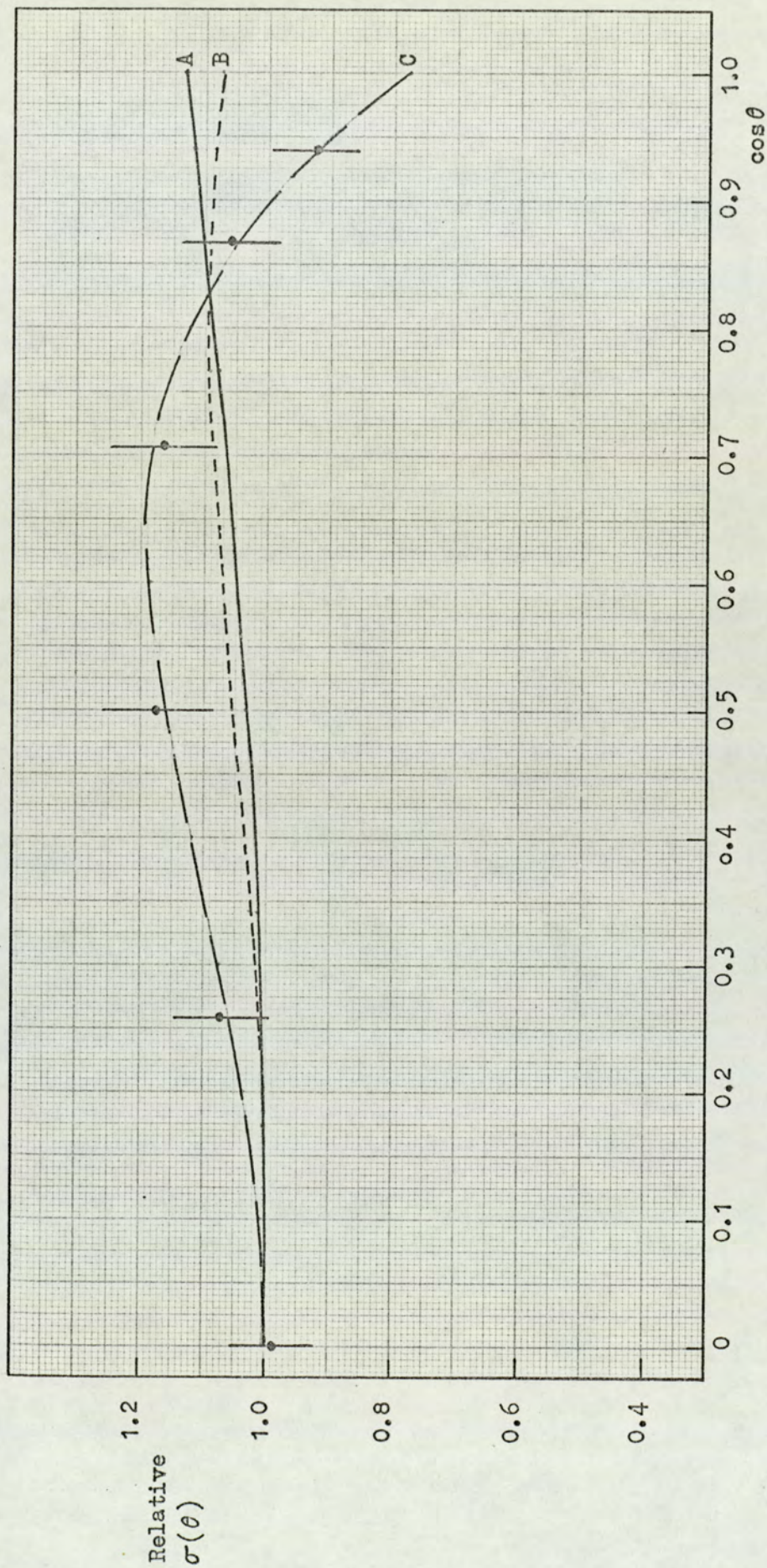


Figure 6.5. Comparison of the normalised theoretical and experimental angular distributions for the 0.99 MeV gamma-ray from titanium.

A - The 13 channel approximation.

B - The 2 channel approximation.

C - Least squares fit to experimental data.

Figure 5.14. In the many channel approximation the maximum energy level of ^{48}Ti considered was 4.05 MeV above which the level structure tends to become continuous. The theoretical distributions have the familiar shape and are in poor agreement with the least squares fitted curve to the experimental results.

The total neutron reaction cross-section can be calculated by equation 6.4 using the optical model transmission coefficients. If, for a particular scattering nucleus, the (n,α) , (n,p) , (n,d) , $(n,n'p)$ and $(n,2n)$ etc. cross-sections are subtracted from the calculated reaction cross-sections, the result gives the total neutron inelastic scattering cross-section. This estimation of the neutron inelastic scattering cross-section is generally larger than the production cross-section for the first excited level to ground state transition γ -ray. However, Figures 5.2, 5.9 and 5.14 which give the level structure of ^{28}Si , ^{32}S and ^{48}Ti , show that in these even-even nuclei having a ground state spin of +0.0 and a first level spin of +2.0, there is a strong tendency for excited levels to decay via the first excited level rather than directly to the ground state. Thus the magnitude of the γ -ray production cross-section for this particular γ -ray would be expected to approach the value of the total inelastic neutron scattering cross-section.

The results of the compound nucleus calculations were used to estimate a correction factor by which the total neutron inelastic scattering cross-section can be multiplied to give the production cross-section for the first excited state to ground state transition γ -ray. The correction factor was taken as the ratio of the calculated cross-section for the production of the γ -ray in question, summing the contributions of each level in the many channel approximation, to the total inelastic scattering cross-section.

The results for the three samples considered are given in Table 6.1. For the three samples, at 14 MeV, the $(n,2n)$ reaction is

Table 6.1

Sample	Calculated reaction cross-section σ_r	Charged particle reaction cross-sections, $E_n = 14$ MeV	Estimated total inelastic scattering cross-section	Correction factor	Estimated production cross-section for 1st level to g.s transition γ -ray	Experimentally measured γ -ray production cross-section
^{28}Si	1,100 mb	440 mb	660 mb	$\frac{784}{1,066}$	485 mb (1.78 MeV γ -ray)	434^{+63} mb
^{32}S	1,150 mb	460 mb	690 mb	$\frac{769}{1,110}$	480 mb (2.24 MeV γ -ray)	317^{+34} mb
^{48}Ti	1,395 mb	1,125 mb	1,270 mb	$\frac{1,195}{1,357}$	1,120 mb (0.99 MeV γ -ray)	$1,039^{+107}$ mb

below its threshold, so only charged particle reaction cross-sections were subtracted from the calculated total reaction cross-sections. The charged particle reaction cross-sections given are the sums for the (n,p) , (n,α) and $(n,n'p)$ reactions taken from the Barn book⁽³²⁾ - the cross-sections were not given for any other reactions. The numerator of the correction factor in the case of ^{28}Si , for example, is the cross-section sum for all inelastic scattering channels producing a 1.78 MeV γ -ray in the 14 channel approximation in accordance with the decay scheme of ^{28}Si and the denominator is the sum of the calculated inelastic scattering cross-sections to all thirteen levels of ^{28}Si considered.

The estimated γ -ray production cross-sections for ^{28}Si and ^{48}Ti agree with the experimental results within the estimated errors. The agreement in the case of ^{32}S is rather poor. In section 5.3.3 it was noted that a 2.24 MeV γ -ray can be produced by reactions other than inelastic scattering with ^{32}S though inelastic scattering was the major production mode. If the experimentally measured 2.24 MeV γ -ray production cross-section could be corrected for these other processes the agreement would further deteriorate. The probable reason for the poor agreement in the case of ^{32}S is that the data on neutron reactions emitting charged particles given in the Barn book⁽³²⁾ is rather inadequate, for example there is no cross-section measurement for the (n,d) reaction with ^{32}S given.

CHAPTER 7Conclusions and Recommendations

The work has demonstrated that the time-of-flight spectrometer is well capable of observing the γ -ray spectra produced in the interaction of 14.2 MeV neutrons and that absolute differential production cross-sections may be measured with considerable accuracy. It is useful here to make a general comparison of the present system with other arrangements.

Only the associated particle and pulsed beam time-of-flight techniques have been used to make γ -ray production angular distribution measurements at 14 MeV; however pulse shape discrimination using a stilbene crystal, massive shielding with a small sample and open geometry with a large sample have all been used for differential cross-section measurements with poor angular resolution at a single scattering angle. The massive shielding approach, used by Engesser and Thompson⁽⁵⁾, is the most successful of these methods in terms of the quality of the γ -ray spectra obtained. However the relatively simple methods often require large corrections to be made to the spectra to correct for the γ -rays produced in the decay of the activated scattering samples. The open geometry method has a severe neutron background problem and the results obtained by Caldwell et al.⁽²⁶⁾ using this method require difficult corrections to be made for neutron multiple scattering and γ -ray absorption. While pulse shape discrimination, used by Bocharov and Nefedov⁽⁶⁾, largely overcomes the background problem the low γ -ray detection efficiency and poor spectral response of the stilbene crystal cause large errors in the measurements. The main advantages of the associated particle method are a good γ -ray signal to background

ratio due to the fact that a start signal is only obtained when a neutron penetrates the scattering sample, an excellent angular resolution (on average a factor of five better than the other methods), and the accuracy with which the neutron flux incident on the scattering sample can be determined. The associated particle method is in addition a relatively simple and economic way of dispensing with the heavy and complex equipment required in a pulsed beam system. The main disadvantage of the associated particle method is the low signal count rate. However, the estimated experimental errors in the present measurements are as good as, or better than quoted for results obtained by the other techniques.

Certain modifications to the system can improve the signal count rate and the γ -ray spectra fairly easily. The signal count rate can be improved by increasing the intensity of the neutron source. The source strength was limited in the present case to 10^7 neutrons s^{-1} , because of the need to maintain a constant neutron yield. However a higher neutron yield with good stability can be obtained if the aperture plate, defining the neutron source, is replaced by a plate with a thin vertical hole to define a vertical line neutron source. The neutron cone defined by the associated alpha-particles would still have the same profile in the horizontal plane and to maintain the same yield in the vertical plane the height of the alpha-detector scintillator would simply have to be reduced. With a 10 mm neutron line source, a stable neutron yield a factor of three up on the present value should easily be obtained without increasing the deuteron beam current. This would increase the signal count rate by a factor of 3. To prevent the alpha-detector background count rate increasing with the higher neutron yield, the 0.5 mm thick plastic scintillator can be replaced by a 0.05 mm thick scintillator. This would have a 100% alpha-particle detection efficiency but would have a lower neutron and γ -ray efficiency. The time resolution of the spectrometer may be improved to ~ 7 ns (f.w.h.m.) if the fast amplifier

in the γ -ray timing line is replaced by a more sophisticated, high gain, wide band amplifier producing a standard sized fast rising output pulse for γ -ray energies between 50 KeV to 100 KeV. This would enable a shorter sample to detector flight path to be used, e.g. ~ 0.9 m. As the solid angle subtended by the detector at the sample is proportional to the inverse square of the flight path length, the signal count rate would improve by a factor of ~ 2.5 for a 0.9 m flight path. The signal to background ratio also improves with sharper time resolution. Better γ -ray detector energy resolution improves the accuracy with which the γ -ray spectra can be interpreted and this can be obtained by coupling the scintillation crystal directly onto a 127 mm (5 in) photomultiplier tube. This should give an energy resolution of 10% at 0.66 MeV γ -ray energy. Finally a wider alpha-particle detector *aperture* defining an angular resolution of $\pm 6^\circ$ would increase the signal count rate without any increase in neutron yield thus improving the signal to background ratio. The angular resolution would still be superior to the other methods by at least a factor of three.

These modifications should give an overall improvement in signal count rate of at least a factor of 5 and at best a factor of 8 to 10 depending on the time resolution obtained. Gamma-ray production cross-sections of the order millibarns may then be accurately determined.

The production of the intense resolved γ -ray lines from ^{28}Si , ^{32}S and ^{48}Ti in 14.2 MeV neutron irradiation is only by inelastic scattering with the exception of ^{32}S for which two lines attributed to charged particle emission reactions are resolved. In the case of ^{32}S the results suggest that there are γ -ray lines present in the energy interval between the 1.27 MeV and 2.24 MeV peaks other than the 1.7 MeV peak. This point should be clarified by further investigation.

The published γ -ray production cross-section data is rather sparse; however the available 90° differential production cross-section

is in reasonable agreement with the present results. The angular distributions of the first level to ground state transition γ -rays for ^{28}Si , ^{32}S and ^{48}Ti excited by inelastic neutron scattering are all anisotropic and show the same general shape; the anisotropy is most marked in the case of ^{32}S . The shape of the angular distributions for the 1.78 MeV and 2.24 MeV γ -rays from ^{28}Si and ^{32}S respectively, are similar to those reported by Martin and Stewart⁽¹⁵⁾; however there is disagreement on the anisotropy of the 2.24 MeV γ -ray, the present result being relatively less anisotropic. The results indicate the usefulness of the associated particle method for γ -ray spectroscopy and for cross-section measurements.

The γ -ray angular distributions calculated by the Hauser-Feshbach-Satchler compound nucleus theory have to be normalised for comparison with the experimental results because of the large number of compound nucleus decay channels, at 14 MeV, which cannot all be considered. The theoretical distributions show rather less anisotropy than the least squares fitted distributions to the experimental measurements; however the theoretical curves do pass through the error bars of many of the experimental results. The coefficients of the $\cos^2\theta$ and $\cos^4\theta$ terms of the theoretical distributions are numerically smaller than the least squares fit coefficients. It appears that the averaging effect of the compound nucleus theory over the many reaction channels tends to smooth out the anisotropy in the distributions. This effect may be removed by the direct interaction theory. A modified version of a (p,p' γ) direct interaction programme would appear to be the most likely way of obtaining such a programme.

Least Squares Fit

The γ -ray angular distribution in the $X(a,\gamma)Y$ reaction is described by an equation of the form

$$\sigma(\theta) = A_0 + A_2 \cos^2 \theta + A_4 \cos^4 \theta \quad \dots \quad A.1$$

In fitting a curve to differential cross-section measurements it is assumed that there is only an experimental error in the values of the differential cross-section, $\sigma(\theta)$ and not in the values of the scattering angle θ .

Let $y_i = \sigma(\theta)$ and $x_i = \cos \theta$, then the coefficients of the polynomial can be estimated, using the least squares principle, by minimizing

$$\sum_{i=1}^n \left[y_i - (A_0 + A_2 x_i^2 + A_4 x_i^4) \right]^2$$

for the n data points (x_i, y_i)

Differentiating this expression partially with respect to A_0 , A_2 and A_4 , equating the partial derivatives to zero and letting a_i be the best estimate of A_i gives

$$\begin{aligned} \sum y_i &= n a_0 + a_2 \sum x_i^2 + a_4 \sum x_i^4 \\ \sum y_i x_i^2 &= a_0 \sum x_i^2 + a_2 \sum x_i^4 + a_4 \sum x_i^6 \quad \dots \quad A.2 \\ \sum y_i x_i^4 &= a_0 \sum x_i^4 + a_2 \sum x_i^6 + a_4 \sum x_i^8 \end{aligned}$$

where the summation extends from 1 to n in each case. The coefficients a_0 , a_2 , and a_4 of the polynomials fitted to the measured γ -ray angular distributions were calculated using equations A.2. As the number of data points for each angular distribution was only six, equations A.2 were solved by Cramer's rule with the aid of a desk calculator.

Estimation of error in fitted curve

If a_0 , a_2 and a_4 are the coefficients of the fitted polynomial to the measured angular distribution, then the residuals, d_i , are given by

$$d_i = y_i - (a_0 + a_2 x_i^2 + a_4 x_i^4) \dots \dots \dots A.3$$

The standard error, α , in the expression

$$y_i - (a_0 + a_2 x_i^2 + a_4 x_i^4)$$

is given by

$$\alpha^2 = \frac{\sum_{i=1}^n d_i^2}{n - m} \dots \dots \dots A.4$$

where m is the number of calculated coefficients, a_i , and in this case $m = 3$.

If α_i is the standard error in a_i , then following Topping⁽¹⁰⁰⁾, the errors α_i are given by

$$\frac{\alpha_0^2}{\begin{vmatrix} \sum x_i^4 & \sum x_i^6 \\ \sum x_i^4 & \sum x_i^8 \end{vmatrix}} = \frac{\alpha_2^2}{\begin{vmatrix} n & \sum x_i^4 \\ \sum x_i^4 & \sum x_i^8 \end{vmatrix}} = \frac{\alpha_4^2}{\begin{vmatrix} n & \sum x_i^2 \\ \sum x_i^2 & \sum x_i^4 \end{vmatrix}} = \frac{\alpha^2}{\Delta} \quad A.5$$

where $\Delta = \begin{vmatrix} n & \sum x_i^2 & \sum x_i^4 \\ \sum x_i^2 & \sum x_i^4 & \sum x_i^6 \\ \sum x_i^4 & \sum x_i^6 & \sum x_i^8 \end{vmatrix} \dots \dots \dots A.6$

and where the summations, Σ , in equations A.5 and A.6 are from 1 to n .

The equation for the angular distribution is then given by

$$\sigma(\theta) = a_0 \pm \alpha_0 + (a_2 \pm \alpha_2) \cos^2 \theta + (a_4 \pm \alpha_4) \cos^4 \theta$$

APPENDIX 2Transmission Coefficients

The optical model programmes of Smith⁽⁹²⁾ and Wilmore⁽⁹³⁾ are in the Atlas Nuclear Physics Programme Library. Consequently both programmes were run on the Atlas computer.

The input data required for the programmes is the lab. energy, spin and charge of the incident particle, the mass, charge and excited level structure of the target nucleus and the values of the optical model parameters. The input data format is described in the Library reports^(92,93).

The transmission coefficients obtained with the optical model parameters of Agee and Rosen⁽⁹⁴⁾ using Smith's programme are reproduced in Table A.1 should they be required for further calculations. The transmission coefficients are given for the excitation of all levels considered of the three elements.

Table 1

Calculated neutron transmission coefficients, including spin-orbit coupling, $E_n = 14.2$ MeV(lab)

28 Silicon											
Level	Spin	$\ell=0$	$\ell=1$	$\ell=2$	$\ell=3$	$\ell=4$	$\ell=5$	$\ell=6$	$\ell=7$	$\ell=8$	$\ell=9$
g.s	T^+	0.6969	0.7018	0.8033	0.6416	0.9800	0.2554	0.0403	0.0074	0.0013	0.0002
	T^-		0.7479	0.7542	0.8072	0.6980	0.1611	0.0343	0.0070	0.0013	0.0002
1.78 Mev	T^+	0.6797	0.7170	0.8115	0.6186	0.9294	0.1525	0.0221	0.0037	0.0006	
	T^-		0.7704	0.7447	0.8336	0.5455	0.1033	0.0195	0.0035	0.0006	
4.61 Mev	T^+	0.6923	0.7485	0.8064	0.5612	0.5861	0.0514	0.0064	0.0008	0.0001	
	T^-		0.8160	0.7061	0.8659	0.2797	0.0392	0.0058	0.0008	0.0001	
4.98 Mev	T^+	0.6907	0.7533	0.8028	0.5511	0.5243	0.0435	0.0052	0.0007		
	T^-		0.8229	0.6980	0.8656	0.2489	0.0336	0.0048	0.0006		
6.27 Mev	T^+	0.6826	0.7723	0.7799	0.5066	0.3111	0.0220	0.0024	0.0003		
	T^-		0.8501	0.6599	0.8402	0.1517	0.0178	0.0022	0.0003		
6.69 Mev	T^+	0.6790	0.7791	0.7682	0.4888	0.2521	0.0171	0.0018	0.0002		
	T^-		0.8598	0.6440	0.8195	0.1257	0.0140	0.0017	0.0002		
6.878 Mev	T^+	0.6772	0.7822	0.7620	0.4801	0.2278	0.0152	0.0015	0.0002		
	T^-		0.8643	0.6360	0.8074	0.1148	0.0125	0.0014	0.0002		
6.887 Mev	T^+	0.6771	0.7824	0.7617	0.4797	0.2266	0.0151	0.0015	0.0002		
	T^-		0.8645	0.6357	0.8068	0.1143	0.0125	0.0014	0.0002		
7.38 Mev	T^+	0.6717	0.7910	0.7422	0.4544	0.1698	0.0108	0.0010	0.0001		
	T^-		0.8768	0.6124	0.7648	0.0886	0.0091	0.0010	0.0001		
7.41 Mev	T^+	0.6713	0.7916	0.7408	0.4526	0.1664	0.0106	0.0010	0.0001		
	T^-		0.8776	0.6107	0.7615	0.8070	0.0089	0.0009	0.0001		

Table A.1 continued

Level	Spin	$\ell=0$	$\ell=1$	$\ell=2$	$\ell=3$	$\ell=4$	$\ell=5$	$\ell=6$	$\ell=7$	$\ell=8$	$\ell=9$
7.80 MeV	T^+	0.6663	0.7986	0.7218	0.4302	0.1300	0.0080	0.0007	0.0001		
	T^-		0.8876	0.5899	0.7170	0.0700	0.0068	0.0007	0.0001		
7.93 MeV	T^+	0.6644	0.8012	0.7143	0.4218	0.1186	0.0072	0.0006	0.0001		
	T^-		0.8912	0.5820	0.6989	0.0646	0.0061	0.0006	0.0001		
8.26 MeV	T^+	0.6593	0.8074	0.6939	0.3997	0.0939	0.0055	0.0005			
	T^-		0.9002	0.5611	0.6491	0.0525	0.0048	0.0004			
8.34 MeV	T^+	0.6582	0.8088	0.6892	0.3949	0.0892	0.0052	0.0004			
	T^-		0.9020	0.5566	0.6378	0.0502	0.0045	0.0004			
$^{32}\text{Sulphur}$											
6.5	T^+	0.7289	0.6708	0.8259	0.6541	0.8801	0.3823	0.00565	0.0102	0.0019	0.0003
	T^-		0.7063	0.8071	0.7074	0.8613	0.2154	0.0458	0.0095	0.0018	0.0003
2.24 MeV	T^+	0.7375	0.6795	0.8636	0.6122	0.8968	0.1976	0.0260	0.0041	0.0006	0.0001
	T^-		0.7252	0.8098	0.7101	0.6698	0.1224	0.0223	0.0039	0.0006	0.0001
3.78 MeV	T^+	0.7413	0.6865	0.8704	0.5785	0.8374	0.1104	0.0135	0.0019	0.0003	
	T^-		0.7411	0.8033	0.7103	0.4949	0.0740	0.0119	0.0018	0.0003	
4.29 MeV	T^+	0.7420	0.6890	0.8749	0.5538	0.7931	0.0888	0.0106	0.0014	0.0002	
	T^-		0.7470	0.7988	0.7094	0.4349	0.0611	0.0094	0.0014	0.0002	
4.70 MeV	T^+	0.7423	0.6911	0.8779	0.5389	0.7460	0.0736	0.0085	0.0011	0.0001	
	T^-		0.7519	0.7940	0.7079	0.3868	0.0517	0.0077	0.0011	0.0001	
5.01 MeV	T^+	0.7424	0.6927	0.8796	0.5267	0.7033	0.0634	0.0072	0.0009	0.0001	
	T^-		0.7559	0.7896	0.7063	0.3509	0.0452	0.0065	0.0009	0.0001	

Table A.1 continued

Level	Spin	$\ell=0$	$\ell=1$	$\ell=2$	$\ell=3$	$\ell=4$	$\ell=5$	$\ell=6$	$\ell=7$	$\ell=8$	$\ell=9$
5.41 MeV	π^+	0.7422	0.6948	0.8811	0.5101	0.6416	0.0519	0.0057	0.0007	0.0001	
	π^-		0.7611	0.7828	0.7032	0.3070	0.0378	0.0052	0.0007	0.0001	
5.55 MeV	π^+	0.7421	0.6956	0.8814	0.5038	0.6176	0.0482	0.0053	0.0006	0.0001	
	π^-		0.7630	0.7800	0.7018	0.2917	0.0353	0.0048	0.0006	0.0001	
5.80 MeV	π^+	0.7418	0.6969	0.8815	0.4925	0.5745	0.0423	0.0045	0.0005		
	π^-		0.7664	0.7748	0.6989	0.2661	0.0313	0.0041	0.0005		
6.23 MeV	π^+	0.7409	0.6993	0.8805	0.4715	0.4960	0.0333	0.0035	0.0004		
	π^-		0.7725	0.7641	0.6921	0.2242	0.0251	0.0032	0.0004		
$^{48}\text{Titanium}$											
g.s	π^+	0.7373	0.6947	0.7221	0.8375	0.6087	0.8990	0.1899	0.0290	0.0053	0.0009
	π^-		0.6828	0.7978	0.7553	0.8010	0.5637	0.1169	0.0245	0.0050	0.0009
0.99 MeV	π^+	0.7492	0.6931	0.7328	0.8394	0.5866	0.8499	0.1359	0.0201	0.0035	0.0006
	π^-		0.6805	0.8143	0.7424	0.8139	0.4659	0.0881	0.0174	0.0033	0.0006
2.295 MeV	π^+	0.7667	0.6893	0.7493	0.8353	0.5514	0.7142	0.0823	0.0116	0.0018	0.0003
	π^-		0.6758	0.8389	0.7179	0.8264	0.3386	0.0571	0.0103	0.0018	0.0003
2.42 MeV	π^+	0.7685	0.6888	0.7511	0.8344	0.5476	0.6969	0.0781	0.0109	0.0017	0.0003
	π^-		0.6752	0.8414	0.7151	0.8269	0.3270	0.0546	0.0098	0.0017	0.0003

Table A.1. continued.

Level	Spin	$\ell=0$	$\ell=1$	$\ell=2$	$\ell=3$	$\ell=4$	$\ell=5$	$\ell=6$	$\ell=7$	$\ell=8$	$\ell=9$
3.0 MeV	T^+	0.7771	0.6862	0.7596	0.8287	0.5292	0.6100	0.0610	0.0084	0.0013	0.0002
	T^-		0.6724	0.8535	0.7005	0.8271	0.2757	0.0439	0.0075	0.0012	0.0002
3.22 MeV	T^+	0.7805	0.6851	0.7630	0.8257	0.5216	0.5739	0.0552	0.0075	0.0011	0.0002
	T^-		0.6711	0.8584	0.6942	0.8258	0.2569	0.0401	0.0068	0.0011	0.0002
3.359 MeV	T^+	0.7826	0.6843	0.7652	0.8237	0.5169	0.5517	0.0519	0.0070	0.0010	0.0001
	T^-		0.6704	0.8614	0.6903	0.8246	0.2458	0.0380	0.0063	0.0010	0.0001
3.376 MeV	T^+	0.7829	0.6842	0.7654	0.8234	0.5163	0.5489	0.0515	0.0069	0.0010	0.0001
	T^-		0.6703	0.8617	0.6898	0.8244	0.2445	0.0377	0.0063	0.0010	0.0001
3.630 MeV	T^+	0.7869	0.6828	0.7696	0.8191	0.5072	0.5066	0.0458	0.0061	0.0009	0.0001
	T^-		0.6687	0.8674	0.6819	0.8209	0.2244	0.0339	0.0055	0.0008	0.0001
3.71 MeV	T^+	0.7882	0.6823	0.7709	0.8176	0.5042	0.4933	0.0441	0.0058	0.0008	0.0001
	T^-		0.6682	0.8693	0.6793	0.8195	0.2162	0.0328	0.0053	0.0008	0.0001
3.75 MeV	T^+	0.7888	0.6820	0.7716	0.8168	0.5027	0.4866	0.0432	0.0057	0.0008	0.0001
	T^-		0.6680	0.8702	0.6779	0.8188	0.2152	0.0322	0.0052	0.0008	0.0001
3.867 MeV	T^+	0.7908	0.6813	0.7736	0.8144	0.4982	0.4671	0.0409	0.0054	0.0007	0.0001
	T^-		0.6672	0.8729	0.6740	0.8163	0.2065	0.0306	0.0049	0.0008	0.0001
4.047 MeV	T^+	0.7937	0.6800	0.7767	0.8104	0.4912	0.4372	0.0374	0.0048	0.0007	
	T^-		0.6660	0.8771	0.6677	0.8117	0.1934	0.0283	0.0044	0.0007	

APPENDIX 3The Angular Distribution Programme "MANDY"

The programme MANDY had to be run on the S.R.C's Atlas Computer. This required a complete translation of the published Algol - 64 code⁽²⁰⁾. The translated Atlas Algol version was thoroughly tested under all options using data supplied by Sheldon⁽¹⁰¹⁾. The Atlas version functioned correctly if the Moldauer correction was omitted. The output data was sometimes in error if the correction was included, but this did not affect the present calculations as the correction was not used.

In calculating an angular distribution the programme MANDY first tabulates all the possible momentum sequences compatible with the momentum and parity selection rules. The momentum and energy weighting coefficients, $\alpha_{i\nu}$ and τ_i (see section 6.2) are evaluated for each possible spin sequence. The overall sums of these coefficients give the Legendre polynomial weighting coefficients, a_ν , from which the differential cross-sections are derived over the desired range of angles.

The input data and the data order for the Atlas Algol version of MANDY follow that for the published version⁽²⁰⁾, except that no provision has been made for a title card. There are three steering options: o1, o2 and o3. Option o1 = 1 corresponds to a particle distribution; o1 = 2 is for a γ -ray distribution of either pure or mixed multipolarity in a single transition; and o1 = 3 and 4 are for γ -ray distributions resulting from a two stage cascade of pure and mixed multipolarities respectively. Option o2 is used to specify whether the Moldauer correction is required and allows the omission of the lengthy momentum sequence tabulation. Finally option o3 specifies

the number of extra exit channels to be considered, the maximum number being 40. The bulk of the input data is concerned with the level spins and parities of the target nucleus; the spin, mass and energy of the incident and emergent particles and the transmission coefficients. Specimen MANDY input data is shown in Table A.2 for the calculation of the γ -ray differential cross-section in the $^{28}\text{Si}(n,n'\gamma)^{28}\text{Si}$ reaction at 14.2 MeV (lab.) considering the excitation of the first 1.78 MeV level, with two extra inelastic scattering channels. The corresponding output data is given in Table A.3: the input data is first reproduced, then the Legendre Polynomial weighting coefficients and normalised coefficients are given and this is followed by the integrated cross-section, angular distribution and normalised angular distribution.

Table A.2

Mandy Input data for $^{28}\text{Si}(n,n'\gamma)^{28}\text{Si}$ reaction with 2 extra exit channels.

Card No.	Input data (Free field format)	Comment
1	2	Option ol
2	0.5, 0.5, 0, 28	In/out particle spins and target mass. 0 interpreted as neutron mass.
3	+0.0, +2.0, +0.0, 99.9 2, 2, 0.0	Spin sequence, γ -ray multipolarity and mixing ratio* $\pi_0^{J_0}, \pi_2^{J_2}, \pi_3^{J_3}, \pi_4^{J_4}, L_2, L_2^*, \delta_2$ $\pi_4^{J_4} = 99.9$ for ol = 1 and 2
4.	8, 8, 1	$\ell_{1\text{max}}, \ell_{2\text{max}}$ and option o2 o2 = 1 - omit Moldauer correction and momentum tabulation.
5.	14.2, 11.51, 10.	n, n' energies, E_n in lab. energy, $E_{n'}$ is just a label. $\Delta\theta$ for required angular interval of results.
6.	0.6969, 0.7479, 0.7542, 0.8072, 0.6980, 0.1611, 0.0343, 0.0070, 0.0013	<u>Transmission Coefficients.</u> <u>Incident channel</u> $T_0^- \dots$ to $T_{\ell_{1\text{max}}}^-$
7.	0.6969, 0.7018, 0.8033, 0.6416, 0.9800, 0.2554, 0.0403, 0.0074, 0.0013.	$T_0^+ \dots$ to $T_{\ell_{1\text{max}}}^+$
8.	0.6978, 0.7704, 0.7447, 0.8336, 0.5455, 0.1033, 0.0195, 0.0035, 0.0006	<u>Emergent channel</u> $T_0^- \dots$ to $T_{\ell_{2\text{max}}}^-$
9.	0.6978, 0.7170, 0.8115, 0.6186, 0.9294, 0.1525, 0.0221, 0.0037, 0.0006	$T_0^+ \dots$ to $T_{\ell_{2\text{max}}}^+$

Table A.2 continued

Card No.	Input data	Comment
10.	2	Option 03
11.	0.5, +4.0, 8.78, 8.	Spin of particle, parity and spin of level, energy label of level or particle, and angular momentum cut off. $s, \pi J, E, \ell_{\max}^{28\text{Si}}$ (Second level of ^{28}Si)
12.	0.6923, 0.8160, 0.7061, 0.8659, 0.2797, 0.0392, 0.0058, 0.0008, 0.0001.	Transmission coefficients, $T_0^- \dots \text{to } T_{\ell_{\max}}^-$
13.	0.6923, 0.7485, 0.8064, 0.5612, 0.5861, 0.0514, 0.0064, 0.0008, 0.0001.	$T_0^+ \dots \text{to } T_{\ell_{\max}}^+$
14.	0.5, +0.0, 8.43, 8	$s, \pi J, E, \ell_{\max}^{28\text{Si}}$ (third level of ^{28}Si)
15.	0.6907, 0.8229, 0.6980, 0.8656, 0.2489, 0.0336, 0.0048, 0.0006, 0.0001.	$T_0^- \dots \text{to } T_{\ell_{\max}}^+$
16.	0.6907, 0.7533, 0.8028, 0.5511, 0.5243, 0.0435, 0.0052, 0.0007, 0.0001	$T_0^+ \dots \text{to } T_{\ell_{\max}}^+$

* Symbols as defined in 6.2

Table A.3.
MANDY output data for the input data given in Table A.2.

OPTION 01 = 2		OPTION 02 = 1		NR = 7					
S1 = 0.5	S2 = 0.5	MI = 1.00866540	MT = 28.00000000						
J0 = 2.0	J2 = 2.0	J3 = 0.0							
L2 = 2.0	L2* = 2.0								
D2 = 0.0000α	0								
L1MAX = 8.0	L2MAX = 8.0								
E1LAB = 14.2	E1 = 13.23	E2 = 11.51							
T(-)	L = 0	6.969000α	-1	L = 1	7.479000α	-1	L = 2	7.542000α	-1
	L = 3	8.072000α	-1	L = 4	6.980000α	-1	L = 5	1.611000α	-1
	L = 6	3.430000α	-2	L = 7	7.000000α	-3	L = 8	1.300000α	-3
T(+)	L = 0	6.969000α	-1	L = 1	7.018000α	-1	L = 2	8.033000α	-1
	L = 3	6.416000α	-1	L = 4	9.800000α	-1	L = 5	2.554000α	-1
	L = 6	4.030000α	-2	L = 7	7.400000α	-3	L = 8	1.300000α	-3
T(-)	L = 0	6.978000α	-1	L = 1	7.704000α	-1	L = 2	7.447000α	-1
	L = 3	8.336000α	-1	L = 4	5.455000α	-1	L = 5	1.033000α	-1
	L = 6	1.950000α	-2	L = 7	3.500000α	-3	L = 8	6.000000α	-4
T(+)	L = 0	6.978000α	-1	L = 1	7.170000α	-1	L = 2	8.115000α	-1
	L = 3	6.186000α	-1	L = 4	9.294000α	-1	L = 5	1.525000α	-1
	L = 6	2.210000α	-2	L = 7	3.700000α	-3	L = 8	6.000000α	-4

THE EFFECT OF THE FOLLOWING 2 EXTRA EXIT CHANNELS IS TAKEN INTO ACCOUNT:

S = 0.5	E* = 8.780		MEV		TRANSHISSION COEFFICIENTS				
J = 4.0									
T(-)	L = 0	6.923000α	-1	L = 1	8.160000α	-1	L = 2	7.061000α	-1
	L = 3	8.659000α	-1	L = 4	2.797000α	-1	L = 5	3.920000α	-2
	L = 6	5.800000α	-3	L = 7	8.000000α	-4	L = 8	1.000000α	-4
T(+)	L = 0	6.923000α	-1	L = 1	7.485000α	-1	L = 2	8.064000α	-1
	L = 3	5.612000α	-1	L = 4	5.861000α	-1	L = 5	5.140000α	-2
	L = 6	6.400000α	-3	L = 7	8.000000α	-4	L = 8	1.000000α	-4

Table A.3. cont.

S = 0.5		E* = 0.0		8.430 MEV		TRANSMISSION COEFFICIENTS			
J =	L =	F =	L =	L =	L =	L =	L =		
T(-)	0	6.907000α	-1	1	8.229000α	-1	2	6.980000α	-1
	3	8.656000α	-1	4	2.489000α	-1	5	3.360000α	-2
	6	4.800000α	-3	7	6.000000α	-4	8	8.000000α	-5
T(+)	0	6.907000α	-1	1	7.533000α	-1	2	8.028000α	-1
	3	5.511000α	-1	4	5.243000α	-1	5	4.350000α	-2
	6	5.200000α	-3	7	7.000000α	-4	8	8.000000α	-5
LAMBDA	A (D=0)	A* (D=0)	A (D)	A* (D)	A (D)	A* (D)	A (D)	A* (D)	A (D)
0	3.4747665α	1	1.0000000	3.4747665α	1	1.0000000	3.4747665α	1	1.0000000
2	2.6544532		7.6392276α	2.6544532	-2	7.6392276α	2.6544532		7.6392276α
4	-1.5831556		-4.5561497α	-1.5831556	=2	-4.5561497α	-1.5831556		-4.5561497α
6	0.000000α	0	0.000000α	0.000000α	0	0.000000α	0.000000α	0	0.000000α
8	0.000000α	0	0.000000α	0.000000α	0	0.000000α	0.000000α	0	0.000000α
10	0.000000α	0	0.000000α	0.000000α	0	0.000000α	0.000000α	0	0.000000α
12	0.000000α	0	0.000000α	0.000000α	0	0.000000α	0.000000α	0	0.000000α
14	0.000000α	0	0.000000α	0.000000α	0	0.000000α	0.000000α	0	0.000000α
16	0.000000α	0	0.000000α	0.000000α	0	0.000000α	0.000000α	0	0.000000α
TOTAL CROSS SECTION = 0.43665 BARNS									
THETA (DEG)	DESIGMA (D=0) (MB/SR)	W(THETA)(D=0)	DESIGMA (D) (MB/SR)	W(THETA)(D)	DESIGMA (D) (MB/SR)	W(THETA)(D)	DESIGMA (D) (MB/SR)	W(THETA)(D)	DESIGMA (D) (MB/SR)
0	3.5818963α	1	1.0911515	3.5818963α	1	1.0911515	3.5818963α	1	1.0911515
10	3.5931293α	1	1.0945734	3.5931293α	1	1.0945734	3.5931293α	1	1.0945734
20	3.6184387α	1	1.1022834	3.6184387α	1	1.1022834	3.6184387α	1	1.1022834
30	3.6369593α	1	1.1079253	3.6369593α	1	1.1079253	3.6369593α	1	1.1079253
40	3.6262018α	1	1.1046403	3.6262018α	1	1.1046403	3.6262018α	1	1.1046403
50	3.5742427α	1	1.0882000	3.5742427α	1	1.0882000	3.5742427α	1	1.0882000
60	3.4873490α	1	1.0523496	3.4873490α	1	1.0523496	3.4873490α	1	1.0523496
70	3.3892223α	1	1.0324573	3.3892223α	1	1.0324573	3.3892223α	1	1.0324573
80	3.3119538α	1	1.0069190	3.3119538α	1	1.0069190	3.3119538α	1	1.0069190
90	3.2826755α	1	1.0000000	3.2826755α	1	1.0000000	3.2826755α	1	1.0000000

REFERENCES

1. R.B. Day. "Progress in Fast Neutron Physics", edited by G. Philips, J. Marion, and J. Risser. University of Chicago Press (1963)
2. A.T.G. Ferguson. Proceedings of the International Conference on the Study of Nuclear Structure with Neutrons. Antwerp. July (1965).
3. M.T. McEllistrem. "Nuclear Research with low energy accelerators" edited by J. Marion and D. Van Patter. Academic Press (1967).
4. W.M. Deuchars and D. Dandy. Proc. of Phys. Soc. 75, 855, (1965).
5. F.C. Engesser and W.E. Thompson. Journal of Nucl. Energy. 21, 487, (1967)
6. V.N. Bochkarev and V.V. Nefedov. Soviet Journal of Nucl. Physics, 1, No. 5., 574, (1965).
7. D.O. Nellis, R.W. Benjamin, J.B. Ashe, J.T. Prud'homme and I.L. Morgan. Texas Nucl. Corp. Report. TID-20689 (1962)
8. D.O. Nellis, R.W. Benjamin, J.H. Henderson, R.L. Pewett, J.B. Ashe, I.L. Morgan and J.T. Prud'homme. Texas Nucl. Corp. Report. TID-20657 (1962).
9. I.L. Morgan, J.B. Ashe, D.O. Nellis. Texas Nucl. Corp. Report. TID-20658 (1963).
10. I.L. Morgan, J.B. Ashe, D.O. Nellis. Texas Nucl. Corp. Report. TID-22012. (1964)
11. I.L. Morgan, J.B. Ashe, J.D. Hall and others. Texas Nucl. Corp. Report. ORO-2791-19 (1966)
12. J.D. Anderson, C.C. Gardener, J.W. McClure, M.P. Nakada, C. Wong. Phys. Rev. 111, 572, (1958).

13. B.A. Benetskii, Yu.P. Betin, Ya. Gonzatko.
Soviet Physics JEPT. 18, 640, (1964)
14. D.T. Stewart and P.W. Martin, Nucl. Phys. 60, 349, (1964).
15. P.W. Martin and D.T. Stewart. Journal of Nucl. Energy
Parts A/B. 19, 447, (1965).
16. J. Benveniste, A.C. Mitchell, C.D. Schrader and J.H. Zenger.
Nucl. Phys. 19, 448, (1960).
17. W. Hauser and H. Feshbach. Phys. Rev. 87, 366, (1952).
18. G.R. Satchler. Phys. Rev. 104, 1198, (1956): errata Phys. Rev.
III, 1747, (1958)
19. E. Sheldon and P. Gantenbein. J. Appl. Math. Phys (ZAMP).
18, 397, (1967).
20. E. Sheldon and R.M. Strang. Computer Phys. Communications,
1, 35, (1969).
21. P.A. Moldauer, Phys. Rev. 123, 968, (1961); 135, B642, (1964);
Rev. Mod. Phys. 36, 1079, (1964).
22. S.C. Mathur, P.S. Buchanan and I.L. Morgan.
Nucl. Phys. 81, 468, (1966).
23. E. Sheldon and D.M. Van Patter, Rev. Mod. Physics, 38, 143 (1966)
24. R.W. Benjamin, P.S. Buchanan and I.L. Morgan.
Nucl. Phys. 79, 241, (1966).
25. M.K. Drake, Gulf General Atomic Inc. AD 679907
26. R.L. Caldwell, W.R. Mills, Jr. and J.B. Hickman, Jr.
Nucl. Sci. and Eng. 8, 173, (1960)
27. R.B. Day. Phys. Rev. 102, 767, (1956).
28. D.M. Van Patter, N. Nath, S.M. Shafroth, S.S. Malik and
M.A. Rothman. Phys. Rev. 128, 1246, (1962).
29. F.S. Eby and W.K. Jentschke, Phys. Rev. 96, 911, (1954).
30. J.C. Robertson and J.G. Lynch, Proc. Phys. Soc. 77, 751, (1961).

31. K.P. Nicholson and G.F. Snelling, Brit. J. Appl. Phys 6, 104, (1955).
32. Neutron Cross-Sections, BNL-325 (1964) Supplement No. 2.
33. L.V. Grosher et al. Atlas of γ -ray spectra from radiative capture of thermal neutrons. Pergamon Press (1959).
34. S.M. Shafroth, E.N. Strait and Carpenter, Nucl. Instr. and Methods, 3, 298 (1958).
35. J.J. Van Loef and D.A. Lind, Phys. Rev. 101, 103, (1956).
36. Neutron Cross-Sections, BNL-325 (1958).
37. J.H. Aitken and W.R. Dixon, Nucl. Phys. 67, 395, (1965).
38. H.M. Mann and J.L. Yntema, I.E.E.E. Trans. Nucl. Sci. NS.11, No. 3, 201, (1964).
39. C.C. Trail and S. Raboy, Rev. of Sci. Instr. 30, 425, (1959).
40. R.B. Nichols, K.D. Klein and M.T. McEllistrem, Phys. Rev. 151, 879, (1966).
41. J.B. Ashe, J.D. Hall, and I.L. Morgan, Rev. Sci. Instr. 37, 1559, (1966).
42. R.K. Swank. Liquid Scintillation Coating, ed. C. Bell and F.N. Hayes. Pergamon Press (1958).
43. W.J. Van Sciver, High Energy Physic. Lab. Report No. 38, Stanford University (1955).
44. R.W. Engstrom et al. Nucleonics, 10, No. 4, 58, (1952).
45. R. Connor and M. Hussain, Nucl. Instr. and Methods, 6, 337, (1960).
46. R.B. Murray and J.J. Manning, I.R.E. Trans. Nucl. Sci. NS-7, No. 2-3, 80 (1960)
47. G.W. Grodstein, National Bureau of Standards Circular NBS-583.
48. W.E. Kreger and R.L. Mather, Scintillation Spectroscopy of Gamma-Radiation, ed. S.M. Shafroth. Gordon and Breach
49. J.C. Hopkins, J.T. Martin and J.D. Seagrave, Nucl. Instr. and Methods, 56, 175, (1967).

50. L. Cranberg and J.S. Levin, Phys. Rev., 100, 435 (1955)
103, 343, (1956).
51. V.E. Parker and R.F. King, Bull. Am. Phys. Soc., 1, 70, (1956).
52. C.M. Turner and S.D. Bloom, Rev. Sci. Instr. 29, 480, (1958)
53. R.C. Mobley. Phys. Rev., 88, 360, (1952).
54. P.H. Stelson, R.L. Robinson, H.J. Kin, J. Rapaport and
G.R. Satchler, Nucl. Phys. 68, 97, (1965).
55. V.E. Scherrer, R. Theus and W.R. Faust, Phys. Rev. 89, 1268 (1953)
56. D.E. Baynham, Ph.D. Thesis, University of Aston in Birmingham (1971)
57. I.M. Rozman and K.G. Zimmer, Intern. J. Appl. Radn. Isotopes,
3, 36, (1958).
58. J.B. Birks and F.A. Black, Proc. Phys. Soc. A64, 511, (1951).
59. G.K. O'Neill, Phys. Rev. 95, 1235, (1954).
60. J.B. Marion and F.C. Young, Nuclear Reaction Analysis,
published North-Holland, (1968).
61. W. Whaling. Handbuch der Physik, Vol. XXXIV, 193.
62. J.E. Strain, Guide to Activation Analysis, edited by
S.Lyon Jr. U.S.A.E.C.
63. G.A. Morton, Nucleonics, 10, No. 3, 39, (1952).
64. R.F. Post and C.I. Schiff, Phys. Rev. 80, 1113, (1950).
65. A.K. Gupta and N. Nath, Nucl. Instr. and Methods, 53, 352, (1967).
66. C. Cernigoi, I. Gabrielli and G. Ternetti, Nucl. Instr.
and Methods, 6, 193, (1960).
67. C.J. Oliver, B. Collinge and G. Kaye, Nucl. Instr. and
Methods, 50, 109, (1967).
68. J. Benveniste and J. Zenger. UCRL-4266 (1954)
69. Allen and Poole, Proc. Roy. Soc. A204, 500, (1951).
70. S.J. Bame and J.E. Perry, Phys. Rev. 107, 1616, (1957).
71. S.D. Warshaw, Phys. Rev. 76, 1759, (1943).

72. H.K. Reynolds, D.N.F. Dunbar, W.A. Wenzel and W. Whaling, Phys. Rev. 92, 742, (1953).
73. E.M. Gunnerson and G. James, Nucl. Instr. and Methods, 8 173, (1960).
74. J. Benveniste, A.C. Mitchell, C.D. Schrader and J.H. Zenger, Nucl. Instr. and Meth., 7, 306, (1960).
75. E. Fermi, Nuclear Physics: Notes Compiled by J. Orear, A.H. Rosenfeld, and R.A. Schluter. Univ of Chicago Press, 1950.
76. P. Marmier and E. Sheldon, Physics of Nuclei and Particles, Vol. 1, Academic Press 1969.
77. M. Walt, Fast Neutron Physics, Vol. IV, part II edited by J.B. Marion and J.L. Fowler. Interscience (1963).
78. K. Nishimura, K.O. Kano and S. Kikuchi, Nucl. Phys. 70, 421, (1965).
79. C.M. Lederer, J.M. Hollander and I. Perlman, "Table of Isotopes", J. Wiley (1967).
80. J.H. Coon, R.W. Davis, H.E. Felthouser and D.B. Nicodemus, Phys. Rev. 111, 250, (1958).
81. R.W. Bauer, J.D. Anderson, L.J. Christensen, Nucl-Phys. 47, 241, (1963).
82. M.D. Goldberg et al. BNL-400
83. R.L. Heath, Scintillation Spectrometry IDO-16880-1 (1964)
84. C.J. Borkowski, I.R.E. Transact. on Nucl.Sci., NS-3, 71, (1956).
85. N.H. Lazar, I.R.E. Transact on Nucl.Science, NS-5, 138, (1958)
86. D. Crumpton, Ph.D. Thesis University of Aston in Birmingham (1967)
87. L. Jarczyk, H. Knoepfel, J. Lang, R. Muller, W. Wolfli Nucl. Inst. and Methods, 17, 310, (1962).
88. P.M. Endt and C. Van der Leun, Nucl.Phys. A105, 134, (1967).
89. D.F. Covell, Anal. Chem. 31, 1785, (1959).
90. B.A. Benetskii, Tr. Fiz. Inst. Akad. Nauk. SSSR, 33, 123, (1965).
91. Nucl. Data B. 3, (1970).

92. W.R. Smith, Nuclear Physics Theoretical Group Report No. 37,
University of Oxford, Program Library Report No. 8.
Atlas Computer.
93. D. Wilmore, A.E.R.E. - R5053, Atlas Computer Program
Library Report No. 2.
94. F.P. Agee and L. Rosen, LA-3538, Vol.1. (1966).
95. D. Wilmore and P.E. Hodgson, Nucl. Phys. 55, 673 (1964).
96. F.G. Perry and B. Buck, Nucl. Phys. 32, 353 (1962).
97. S.C. Mathur, P.S. Buchanan and I.L. Morgan, Phys. Rev. 160,
816 (1967)
98. D.M. Drake, J.C. Hopkins and C.S. Young, Nucl. Phys.
A128, 209 (1969).
99. F.G. Perry, Phys. Rev. 131, 745 (1963).
100. J. Topping, "Errors of Observation and their Treatment".
The Institute of Physics and the Physical Society Monograph.
101. E. Sheldon, private communication (1971).